Nano Energy 104 (2022) 107917

Contents lists available at ScienceDirect

Nano Energy

journal homepage: www.elsevier.com/locate/nanoen

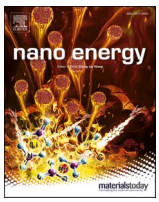

Review

Strain related new sciences and devices in low-dimensional binary oxides

Jie Jiang [a,*], Saloni Pendse [a], Lifu Zhang [a], Jian Shi [a,b,**]

[a] Department of Materials Science and Engineering, Rensselaer Polytechnic Institute, Troy, NY 12180, USA
[b] Center for Materials, Devices, and Integrated Systems, Rensselaer Polytechnic Institute, Troy, NY 12180, USA

ARTICLE INFO

Keywords:
Binary oxides
Low-dimensional materials
Elastic strain engineering

ABSTRACT

The possibility of generating a large range of elastic strain in low-dimensional materials offers a vast design space that has led to a plethora of scientific and technological breakthroughs in the field of materials science. The concept of using the elastic strain to engineer physical properties of materials has been found extremely useful in many areas such as enhancing the charge mobility in microelectronics and ionics, inducing new physical properties, regulating phase transitions in complex materials, band dispersion engineering in quantum well lasers, semiconductor band gap engineering and improving electrochemical performance of materials. Throughout these progresses in elastic strain engineering, low-dimensional binary oxides have demonstrated their unique advantages over other materials systems: high electron/hole mobility, high optoelectronic quantum efficiency, low defects density, simple thermodynamics/kinetics, versatile functionality and intriguing responses to elastic strain. This article reviews the most significant milestones of elastic strain engineering in low-dimensional binary oxides. It provides reports and analyses of model binary oxide materials, strain-related phenomena, methods of introducing and characterizing strains in low-dimensional materials and strain engineered physical properties. It is our hope that this review can inspire more researchers seeking new scientific understanding as well as technological breakthroughs to explore this rich field of low-dimensional strained binary oxides.

1. Motivation

Strain engineering is a research field that utilizes strain (elastic or inelastic) to tune the properties of a material by modifying its structural attributes. Effects of hydrostatic strain (stress tensor $\varepsilon_{11} = \varepsilon_{22} = \varepsilon_{33} < 0$) on properties of materials have been studied since the 17th century with plenty of progress being made in the associated field of high-pressure physics [1]. This review instead focuses on the progress made in studying effects of non-hydrostatic elastic strain on properties of materials. Unlike hydrostatic stress, non-hydrostatic elastic tensile and shear stresses in crystalline materials can be relaxed by plastic deformation or fracture. Traditional bulk materials, e.g., Si, Ge and SiC, can only sustain elastic strains less than 0.5% before inelastic relaxations from plasticity or fracture set in [2], as shown by the crack in a three-dimensional (3D) bulk material in the bottom left panel of Fig. 1. On the other hand, low dimensional materials (one dimensional (1D) and two dimensional (2D)), which have received increasing research focus over the past few decades, have been shown to sustain elastic strains larger than 1% without undergoing plastic deformation or fracture in their crystalline form. Since effective strain engineering, i.e., manipulation of functional properties (e.g., electronic, magnetic, optical and catalytic properties) of a material with elastic strain, is largely dependent on the magnitude of elastic strain introduced in and sustained by a material, it can be said that low-dimensional materials serve as good candidates for elastic strain engineering hence providing an impetus to the field. Low-dimensional materials (e.g., nanowires, nanosheets and thin films) have been found to sustain large elastic strains (tensile or compressive) introduced by various approaches such as bending [3] and tensile loading in nanowires [4], nanoindentation in monolayers [5], buckling in membranes [6] as well as heteroepitaxy in nanostructures [7], as shown in the top panels of Fig. 1. So far, elastic strain engineering in low-dimensional materials has led to significant progress in terms of functionality as well as materials in a variety of research fields, including piezotronics [8,9], ferroelectrics [10], catalysts [11], 2D crystals [12,13], semiconductors [14] and even organic materials [15]. Hence, the rich field of elastic strain engineering, with its promising applications in energy harvesting, conversion and computing [16,17], was chosen as the topic for this review. In this article, we focus on elastic strain

* Corresponding author.
** Corresponding author at: Department of Materials Science and Engineering, Rensselaer Polytechnic Institute, Troy, NY 12180, USA.
E-mail addresses: jiangj2@rpi.edu (J. Jiang), shij4@rpi.edu (J. Shi).

https://doi.org/10.1016/j.nanoen.2022.107917
Received 25 July 2022; Received in revised form 17 October 2022; Accepted 18 October 2022
Available online 27 October 2022

engineering as enabled by a specific class of low-dimensional materials – the binary oxides. Within the field of elastic strain engineering, strained oxides (binary, ternary and even quaternary), have been extensively studied both in terms of fundamental properties and technological applications. Elastic strain engineering in low-dimensional ternary oxides received an impetus partially due to the demonstration of room temperature ferroelectricity in strained $SrTiO_3$ films even though the bulk $SrTiO_3$ crystal does not exhibit ferroelectricity [18]. Since then, research on elastic strain engineering in low-dimensional ternary oxides has been exhaustively discussed and reviewed in many articles [10,19]. However, to the best of our knowledge, an article specifically and comprehensively reviewing or highlighting elastic strain engineering in low-dimensional binary oxides can hardly be found in literature.

Binary oxides exhibit a range of advantageous properties. These include their ease of processing (ZnO nanobelts [20], nanowires [3], nanohelice [21], nanotubes [22], monolayers [23] and microspheres [24]), high carrier mobility [25] and high dielectric constant *K* [26,27]. Binary oxides are also compatible with complementary metal oxide semiconductor (CMOS) systems [28] and support the possibility of developing high performance transparent thin film transistors (TFTs)/CMOS [25]. Some binary oxides are even multifunctional [29,30] and superconducting [31]. Similarly, low-dimensional materials also possess unique characteristics such as the size effect [32] and the electronic confinement effect [33,34]. Consequently, low-dimensional binary oxides, which combine the advantages of low dimensions with those of a binary oxide system as shown in Fig. 1, deserve a special mention in the field of elastic strain engineering. The next few paragraphs (Sections 1.1 and 1.2) describe the motivation behind combining properties stemming from low dimensions with those of binary oxides.

1.1. Low-dimensional materials

Since 1970, when electron resonant tunneling was achieved and the first laser based on quantum well structures was developed [35–37], low-dimensional materials have attracted increasing interest in terms of both fundamental studies and technological applications [34]. Low-dimensional materials can be defined as materials with an atomic or nanometer size in one (2D materials such as quantum wells, graphene and layered semiconductors), two (1D materials such as quantum wires or nanowires) or three (0D materials such as quantum dots) spatial dimensions, possessing physical properties different from their bulk counterparts. For example, the spatial confinement in low-dimensional materials leads to quantum confinement of the electronic state wave function as illustrated in the left panels of Fig. 1 which show the density of states (DOS) for 3D crystalline materials, 2D quantum wells, 1D nanowires and 0D quantum dots. Such electronic confinement in low-dimensional materials significantly changes their electronic band structure and these materials exhibit extraordinary electronic and optical properties that can be harnessed for a wide range of potential applications. Detailed physics of size effects and electronic properties in low-dimensional materials have been summarized in the review article Ref. [33].

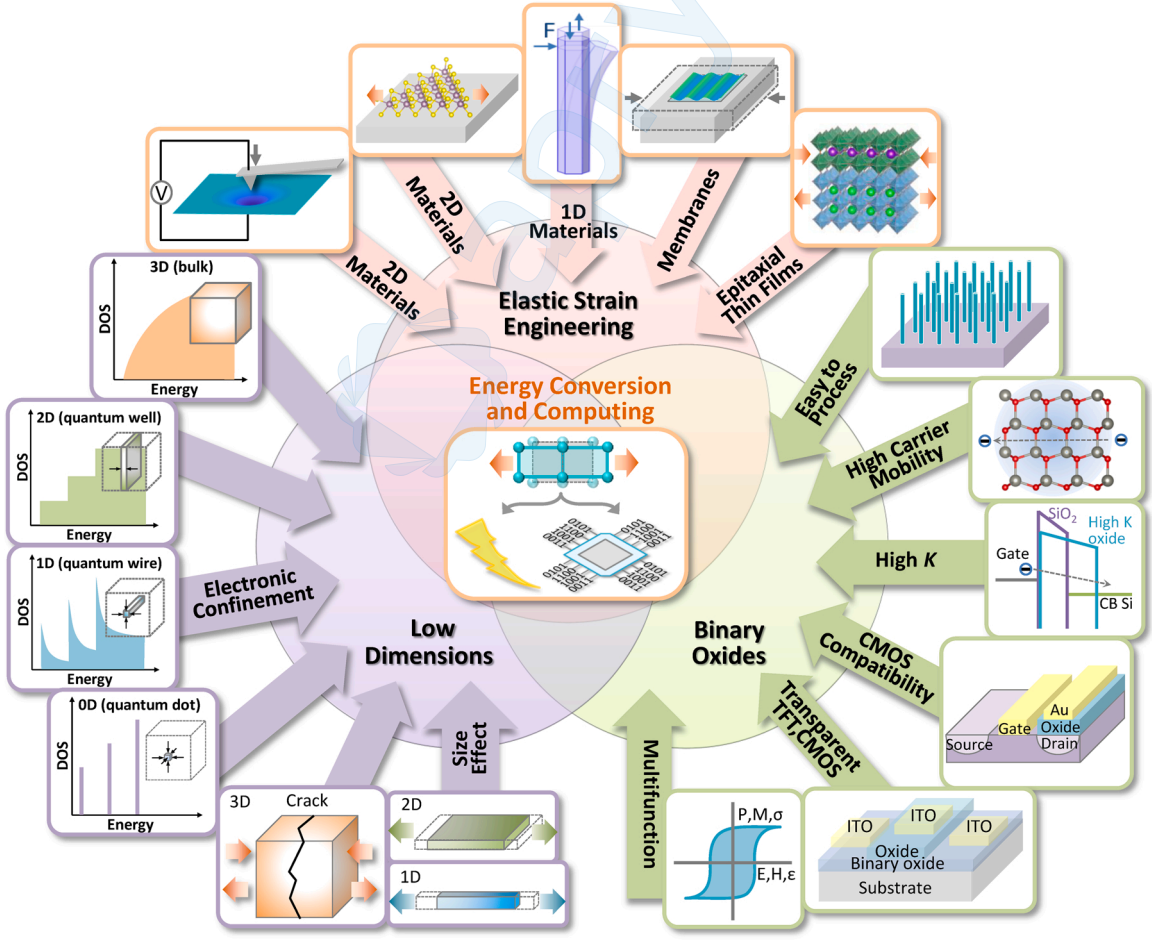

Fig. 1. The new research field of elastic strain engineering in low-dimensional binary oxides with applications such as energy conversion and computing. Unique characteristics of low dimensions (e.g., size effect and electronic confinement) and binary oxides (e.g., ease of processing, high carrier mobility, high *K*, CMOS compatibility, transparent TFT and CMOS, and multifunction) are shown in the left panels and the right panels, respectively. Some approaches to sustain tensile and compressive elastic strains in low-dimensional materials are shown in the top panels, e.g., nanoindentation, tensile loading, bending, buckling and epitaxy.

In addition to possessing intriguing physical properties, low-dimensional materials also serve as useful candidates for elastic strain engineering due to their ability to sustain large values of elastic strains unlike their bulk counterparts. Bulk crystals, which typically contain a large number of in-grown defects such as dislocations or cracks, can only sustain yield strains that are far (a factor of 100) below the ideal or theoretically expected value. Even in well-annealed crystals with a low dislocation density, plastic deformation can be induced by double cross slip and other Frank-Read type multiplication processes much before the theoretically expected elastic strain is reached [38]. On the other hand, in low-dimensional materials, a larger elastic deformation can be tolerated before yielding [39], which may be attributed to factors such as limited defect (e.g., dislocation) density [40] and surface dislocation nucleation and kinetics [152]. Hence, low-dimensional materials, as compared to bulk materials, can be subjected to a broader range of elastic strains, enabling effective elastic strain engineering. Details of maximum values of elastic strain sustained and experimentally realized in various low-dimensional materials are reviewed in Section 2.2. Additionally, an inhomogeneous strain field (strain gradient) can also be generated in low-dimensional materials, providing unprecedented opportunities to explore novel functional properties. Therefore, based on the large range of elastic strain or strain gradient that can be sustained by low-dimensional materials, along with their inherent functional properties arising from surface effects and electronic confinements, it can be anticipated that elastic strain engineering would be very intriguing and profitable in materials with low dimensions.

1.2. Binary oxides – advantages

Within the class of inorganic materials, oxides display perhaps the most diverse range of functionalities [41], including hard oxides [42], dielectric and ferroelectric oxides [43,44], magnetic oxides [45,46], multiferroic oxides [7,47], semiconducting oxides [20], etc. There is a wide range of studies and review articles on oxides [41,48,49], including binary oxides (e.g., ZnO [50], SnO_2 [51,52], TiO_2 [53], copper oxides [54], transition metal oxides [55,56] and tungsten oxides [57]), ternary ferroelectric oxides [19,58,59] and complex oxides [48,60]. Among oxides, low-dimensional binary oxides, which combine the intrinsic bulk properties of binary oxides with properties enabled by reduced dimensions, demonstrate several unique advantages over other materials systems. In addition to the advantages mentioned in Fig. 1, low-dimensional binary oxides demonstrate thermodynamic and kinetic stability in contact with silicon [26,61], high optoelectronic quantum efficiency [62–64], versatile functionality [65,66], and intriguing

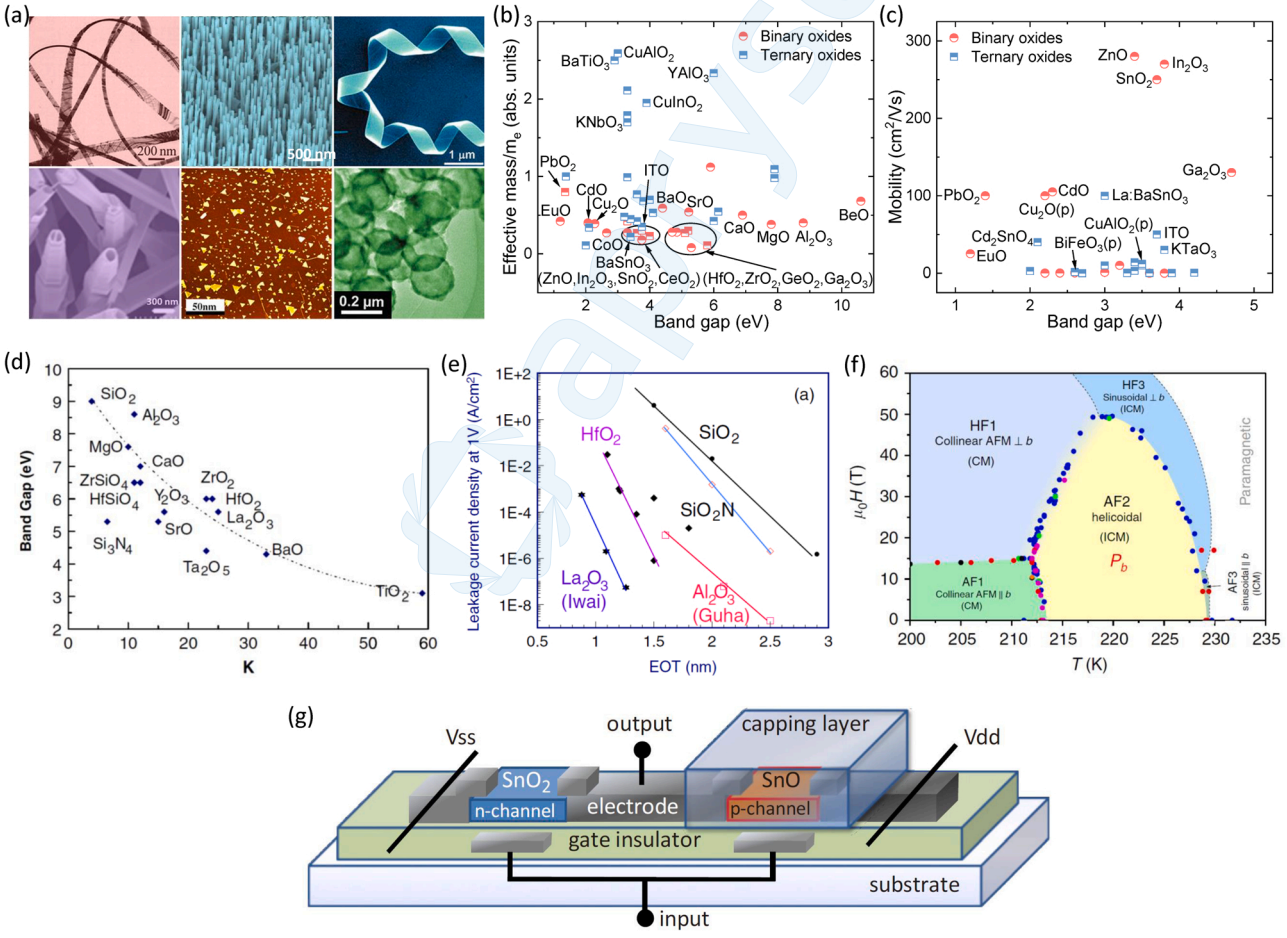

Fig. 2. A summary of scientifically and technologically important physical properties of binary oxides. (a) Typical morphologies of ZnO nanostructures, e.g., nanobelt [20], nanowire [72], nanohelice [21], nanotube [22], monolayer [23], and microsphere [24]. (b,c) Effective mass (b) and room-temperature carrier mobility (c) as a function of band gap in both binary (red) and ternary oxides (blue). Data points are taken from the references in Table 1. (d) Static dielectric constants for gate oxides as a function of their band gaps. (e) Leakage current density as a function of "equivalent (to SiO_2) oxide thickness" (EOT) for binary oxides including HfO_2, Al_2O_3, La_2O_3, SiO_2 and SiO_2N. (f) Magnetoelectric phase diagram of CuO. The critical magnetic field is recorded based on pyrocurrent (blue dots), capacitance (green dots), magnetostriction (pink dots), sound velocity (red dots), and bulk magnetization data (black dots). The expected hypothetical phase boundaries are predicted from theoretical analysis (dashed lines). (g) Schematic illustration of a conceptual design of a CMOS inverter based on n-type SnO_2 TFTs and p-type SnO TFTs. Reprinted by permission of Wiley-VCH, American Chemical Society, American Institute of Physics, IOP Publishing and Elsevier.
(a) is adapted from Ref. [20–24,72]. (d) and (e) are adapted from Ref. [26]. (g) adapted is from Ref. [86].

responses to strain [67] (details are reviewed in Section 6).

Binary oxides in a low-dimensional form are also easy to be synthesized via various techniques. Techniques for depositing epitaxial thin films (or layers) of oxides, e.g., pulsed laser deposition (PLD), molecular beam epitaxy (MBE), metal-organic chemical vapor deposition (MOCVD) and sputtering, have been well summarized in the review article Ref. [41]. Binary oxides have also been synthesized in nanostructured forms via liquid phase techniques such as the sol-gel and Pechini methods (summarized in the review article Ref. [6,8]), as well as vapor-phase methods such as chemical vapor deposition (CVD) [69]. Further improvements in synthesis techniques have also led to successful synthesis of low-dimensional binary oxides in unique morphologies and heterostructure forms, e.g., core/shell nanowires [70–74]. Fig. 2a shows typical morphologies of ZnO nanostructures, including nanobelts [20], nanowires [3], nanohelice [21], nanotubes [22], monolayer [23] and microspheres [24]. Such single-crystal metal-oxide nanostructures have a high crystalline quality and a low defect density [75].

Another significant advantage of binary oxides is their intriguing electronic properties. Table 1 summarizes the effective mass, mobility and band gaps of typical oxide materials (both binary and ternary). Fig. 2b and c respectively present the effective mass and mobility of binary and ternary oxides as a function of their band gap. The lower electron effective mass in many metal binary oxides is a result of hybridization of metal *s* orbitals with oxygen *p* orbitals [76]. On the other hand, in ternary oxides, the second metallic element (often a transition metal) has very localized *d* or *f* orbitals which affect the band structure and are partially responsible for a large effective electron mass and a low mobility. Thus, in general, as shown in Fig. 2b and c, the effective mass of typical non-transition metal binary oxides (e.g., ZnO) is lower than that of ternary oxides carrying a transition metal element.

Furthermore, oxides such as HfO_2 and ZrO_2 have high dielectric constants *K*. Both HfO_2 and ZrO_2 exhibit better performance than SiO_2 to serve as gate oxides in the miniaturization of CMOS transistors and have attracted increasing attention for both fundamental research and commercial applications [26,27]. Fig. 2d presents the static dielectric constants for gate oxides as a function of their band gap. As shown in Fig. 2d,

Table 1
Summary of band gaps, effective mass, and mobility of oxide materials. Abbreviations: experimental (expt.), calculation (cal.), n (n-type), p (p-type), i (indirect band gap). All the listed oxides are direct band gap materials except the ones indicated with (i). The symbol "-" represents data that is not reported in literature.

Oxides	Band gap (eV)	m_e^*/m_0	m_h^*/m_0	Mobility at RT (cm^2/Vs)	Reference
CdO	2.31(expt.)	0.27(expt.)	–	75—135(n)	[91]
ZnO	3.3(expt.)	0.3(expt.)	–	120—440(n)	[50]
BeO	10.6(cal.)	0.65—0.80(cal.)	–	238(n)	[92]
α-PbO	1.78(i)(cal.)	0.4(cal.)	2.44(cal.)	–	[93]
MgO	7.8(exp.)	0.38(cal.)	–	–	[94,95]
CaO	3.55(cal.)	0.33(cal.)	1.25(cal.)	–	[96]
NiO	4.3(expt.)		0.8—1.0(expt.)	–	[97,98]
MnO	3.6(exp.)	1.08(cal.)	–		[99,100]
EuO	1.1(exp.)	0.4(cal.)	–	~20(n)	[101,102]
Cu_2O	2.2(expt.)	0.99(expt.)	0.58(expt.)	100(p)	[54]
β-PbO_2	1.4(expt.)	0.8(expt.)	–	~100(n)	[103]
CeO_2	3.15(expt.)	0.42(expt.)	0.42(expt.)	–	[104]
TiO_2(rutile)	3.0(i)(expt.)	0.09(cal.)	0.56(cal.)	~1(n)	[105,106]
TiO_2(anatase)	3.2(i)(expt.)	0.09(cal.)	0.8(expt.)	~10(n)	[105,107]
HfO_2	5.5(i)(expt.)	0.11(expt.)	–	–	[108,109]
ZrO_2	4.7(expt.)	0.6—2.0(cal.)	0.3(cal.)	–	[110]
SnO_2	3.7(expt.)	0.23—0.3(expt.)	–	250(n)	[111]
α-Al_2O_3	6.3(cal.)	0.4(expt.)	0.36(expt.)	–	[112,113]
β-Ga_2O_3	4.7(expt.)	0.28(expt.)	–	130(n)	[114]
In_2O_3	2.9(expt.)	0.3(expt.)	–	270(n)	[115,116]
$In_{2-x}Sn_xO_3$(ITO)	3.75(expt.)	0.35(expt.)	–	~50(n)	[117]
$BaTiO_3$	2.6(cal.)	1.1—4(cal.)	7—8(cal.)	–	[118]
Ce:$YAlO_3$	7.9(cal.)	2.34(cal.)	1.94(cal.)	–	[119]
Ce:$LuAlO_3$	6.1(cal.)	0.42(cal.)	2.09(cal.)	–	[119]
Ce:$Y_3Al_5O_{12}$	7.9(cal.)	1.09(cal.)	1.98(cal.)	–	[119]
Ce:$Lu_3Al_5O_{12}$	7.9(cal.)	0.98(cal.)	2.43(cal.)	–	[119]
Ce:Y_2SiO_5	6.14(cal.)	0.70(cal.)	3.80(cal.)	–	[119]
Ce: Lu_2SiO_5	4(cal.)	0.50(cal.)	3.60(cal.)	–	[119]
$Bi_4Ge_3O_{12}$	4(cal.)	0.60(cal.)	3.02(cal.)	–	[119]
Ce:$BaHfO_3$	–	0.65(cal.)	3.68(cal.)	–	[119]
Ce:$SrHfO_3$	–	0.66(cal.)	2.39(cal.)	–	[119]
$SrGeO_3$	3.5(expt.)	–	–	12(n)	[120]
La:$BaSnO_3$	3(expt.)	0.19(expt.)	–	100(n)	[121]
Sr:$LaCoO_3$	2(expt.)	0.1—10(expt.)	–	0.1—5(n)	[122]
$AgInO_2$	4.2(expt.)	–	–	0.47(n)	[41]
$CuGaO_2$	3.6(expt.)	0.42(cal.)	0.58—2.04(cal.)	0.23(p)	[41]
$SrTiO_3$	3.4(expt.)	5.0(expt.)	–	3(n)	[41]
$MgIn_2O_4$	3.4(expt.)	–	0.45(expt.)	14(n)	[41,123]
$SrCu_2O_2$	3.3(expt.)	0.99(expt.)	0.58—0.69(expt.)	0.46(p)	[41]
Cd_2SnO_4	2.1(expt.)	0.33—0.35(expt.)	–	40(n)	[41,124]
$CuInO_2$	3.9(expt.)	0.37(cal.)	0.68—3.22(cal.)	0.2(p)	[125,126]
$CuScO_2$	3.3(expt.)	0.56—1.08(cal.)	0.45—3.12(cal.)	0.14(p)	[125,127]
$NaNbO_2$	1.38(cal.)	–	0.64—1.36(cal.)	–	[128]
$PbTiO_3$	3.2(cal.)	–	0.48(cal.)	–	[128]
$PbZrO_3$	3.6(cal.)	–	0.44—1.09(cal.)	–	[128]
$CuAlO_2$	3(expt.)	–	2.53—2.64(cal.)	10(p)	[128]
$SrCu_2O_2$	3.3(expt.)	–	2.01—2.22(cal.)	0.46(p)	[128,129]
$ZnRh_2O_4$	2.7(expt.)	–	3.47(cal.)	2.8×10^{-4}(p)	[128,130]
$KTaO_3$	3.8(expt.)	0.55—0.8(expt.)	–	–	[131,132]
$KNbO_3$	3.3(expt.)	1.7(cal.)	–	–	[133]
$BiFeO_3$	2.6(expt.)		5—6.7(expt.)	0.1—3(p)	[134,135]

binary oxides, e.g., Al_2O_3, HfO_2, ZrO_2, Y_2O_3 and La_2O_3, show high K and reasonably large band gaps. Due to a high heat of formation and a wide band gap, these oxides are thermodynamically and kinetically stable in contact with silicon [61]. In addition, as plotted in Fig. 2e, the leakage current density as a function of "equivalent oxide thickness" or "EOT" (defined as $(3.9/K) \times t$, where 3.9 is the static dielectric constant of SiO_2 and t is the film thickness, giving a thickness of the gate oxide in terms of its equivalent silicon dioxide thickness) for binary oxides (HfO_2, Al_2O_3 and La_2O_3) is lower than that for SiO_2. Hence, binary oxides such as Al_2O_3, HfO_2, ZrO_2, Y_2O_3 and La_2O_3 can replace SiO_2 as the gate oxide in COMS devices. Moreover, some binary-oxide based devices, e.g., resistive random access memories [28,77] and gas sensors [78], have already been fully integrated into CMOS technology.

Additionally, the transparent nature of many oxides, especially when combined with their excellent electronic properties (e.g., high mobility) has rendered oxide-based TFT and CMOS devices as one of the most promising technologies leading the next generation of flat panel displays [49,79]. These oxides include both the n-type oxides such as ZnO [80, 81] and SnO_2 [82] and p-type oxides such as Cu_2O [83] and SnO [84, 85]. Both n-type SnO_2 TFTs and p-type SnO TFTs can be fabricated on the same substrate and a corresponding conceptual design of a CMOS inverter has been proposed by Yabuta et al. [86], as shown in Fig. 2g.

Another interesting property of binary oxides is their high photoluminescence (PL) quantum efficiency (the absolute yield within a material from exciton creation to photon emission). A value of up to 20 % has been observed in single-crystal ZnO nanowires [64] and a high external quantum efficiency (EQE, defined as the number of electrons detected per light photon) of up to 10^8 % has been reported in photodetectors based on metal oxide nanostructures [62,63]. In addition, some binary oxides, such as EuO [30,66,87,88] and CuO [89] which are multiferroic as well as semiconducting, exhibit versatile functionalities. Wang et al. plotted the magnetoelectric phase diagram of CuO as shown in Fig. 2f based on pyrocurrent (blue dots), capacitance (green dots), magnetostriction (pink dots), sound velocity (red dots), bulk magnetization data (black dots) and expected hypothetical phase boundaries predicted from theoretical analysis (dashed lines) [90], uncovering a remarkable hidden magnetoelectric effect in the multiferroic oxide CuO [89].

The physical properties of binary oxides mentioned above can be further combined with elastic strain to discover various intriguing phenomena. One of the most well-known examples is that bending a piezoelectric ZnO nanowire by using a conductive atomic force microscopy (AFM) tip enables energy conversion from nanoscale mechanical energy into electrical energy [67] (details are reviewed in Sections 6.1 and 6.3).

Beginning from the next section, we briefly introduce the concept of elastic strain engineering with a focus on low-dimensional materials (Section 2) and some common crystal structures of binary oxides (Section 3), summarize approaches to introduce elastic strain in low-dimensional materials (Section 4) and techniques to characterize elastic strain (Section 5), then comprehensively review the physical properties of binary oxides tuned by elastic strain and the corresponding applications (Section 6). These include piezoelectricity (Section 6.1), the piezoresistive effect (Section 6.2), the piezotronic and piezo-phototronic effects (Section 6.3), ferroelectricity (Section 6.4), metal-insulator transition (Section 6.5), band gap engineering (Section 6.6), magnetic properties (Section 6.7), chemical reactivity (Section 6.8), ionic conductivity (Section 6.9) and others (Section 6.10). Finally, challenges, unresolved issues (Section 7.1) and perspectives (Section 7.2) are presented in Section 7. It is our hope that this review can inspire more material scientists, in pursuit of scientific understanding as well as technological breakthroughs, to explore the rich field of elastic strain engineering of low-dimensional binary oxides.

2. Introduction to strain engineering

2.1. Basic principles

Strain engineering is defined as achieving the desired functional properties in a material by controlling strain $\varepsilon(x)$, where x denotes the position vector in a material [136]. Here we briefly introduce some basic concepts of this field. For a more detailed description, one can refer to Ref. [137]. Strain ε can be represented as a 3×3 symmetric tensor with six independent components. While high-pressure physics deals with a single hydrostatic degree of freedom, strain engineering focusses on the non-hydrostatic part of ε. The total strain ε at a given point is a sum of the elastic strain (the recoverable part when the material returns to a stress-free state) and the inelastic strain (the residual strain): $\varepsilon = \varepsilon_e + \varepsilon_i$, where ε_e and ε_i are the elastic and inelastic strains, respectively [137]. ε_e represents the distortion of lattice vectors and can be measured by selected-area X-ray or electron diffraction. ε_i represents changes related to phase transformation or bonding topology which are difficult to be quantified experimentally. Strain engineering includes elastic strain engineering as well as inelastic strain engineering. In elastic strain engineering, one aims to introduce and sustain an unconventionally large elastic strain ε_e (normally larger than 1 %) in a material, so as to control the functional properties of materials. In inelastic strain engineering, inelastic strain ε_i, localized in microstructural features such as dislocation-swept areas, deformation twinning [138], multiferroic domain patterns [139] or new phases [140], is used to modify the physical properties of materials. In many applications, especially where phase transformations are involved, elastic strain engineering and inelastic strain engineering often get coupled together. In the present review, we focus on elastic strain engineering.

2.2. Elastic strain in low-dimensional materials

Bulk crystals can only withstand a maximum elastic strain of much less than 1% due to the large number of in-grown defects (e.g., dislocations or cracks) either inside or on the surface of the material [141]. Although the in-grown defect density can be reduced after annealing [142], it increases rapidly once deformation occurs due to processes such as dislocation generation by Frank-Read type multiplication typically seen in metals [38] and brittle fracture (Dugdale-Barenblatt model of the crack tip) typically seen in ceramics [143], as shown in Fig. 3a and b. With a decrease in size or volume of crystals to microscale or nanoscale, the defect (e.g., vacancy [40]) density decreases due to increased formation energy. In other words, during crystal growth, low-dimensional materials easily reach their thermodynamic equilibrium shape, and can be expected to contain less defects as compared to bulk materials, as shown in Fig. 3c. Additionally, due to the increased surface area to volume ratio in low-dimensional materials, surface dislocation nucleation and dislocation kinetics may play a critical role in their deformation, as shown in Fig. 3d. Zhu et al. developed a reaction pathway modeling of surface dislocation nucleation from a Cu nanowire under uniaxial compression, revealing a possible mechanism of deformation in low-dimensional materials [144]. Such a mechanism of defect creation, controlled by surface nucleation, makes low-dimensional materials such as a nanowire, much stronger than their bulk counterparts in which defect creation is controlled by growth/propagation (e.g., dislocation generation by Frank-Read source). Hence, low-dimensional materials are likely to sustain elastic strains of 1 % and more [145–148].

The maximum elastic strain sustained by a low-dimensional material depends on its size, as can be found in various metals. With decreasing diameter, metal nanowires (e.g., Cu [149], Au [141,150] and Ag [151]) exhibit ultrahigh elastic strains that even approach the theoretically expected maximum elastic strain in the given material. The dimensionality effect can also be observed in ceramics, but with a different mechanism – defect statics. For example, Wei et al. reported that the maximum elastic strain sustained in ZnO nanowires increased up to 7.8

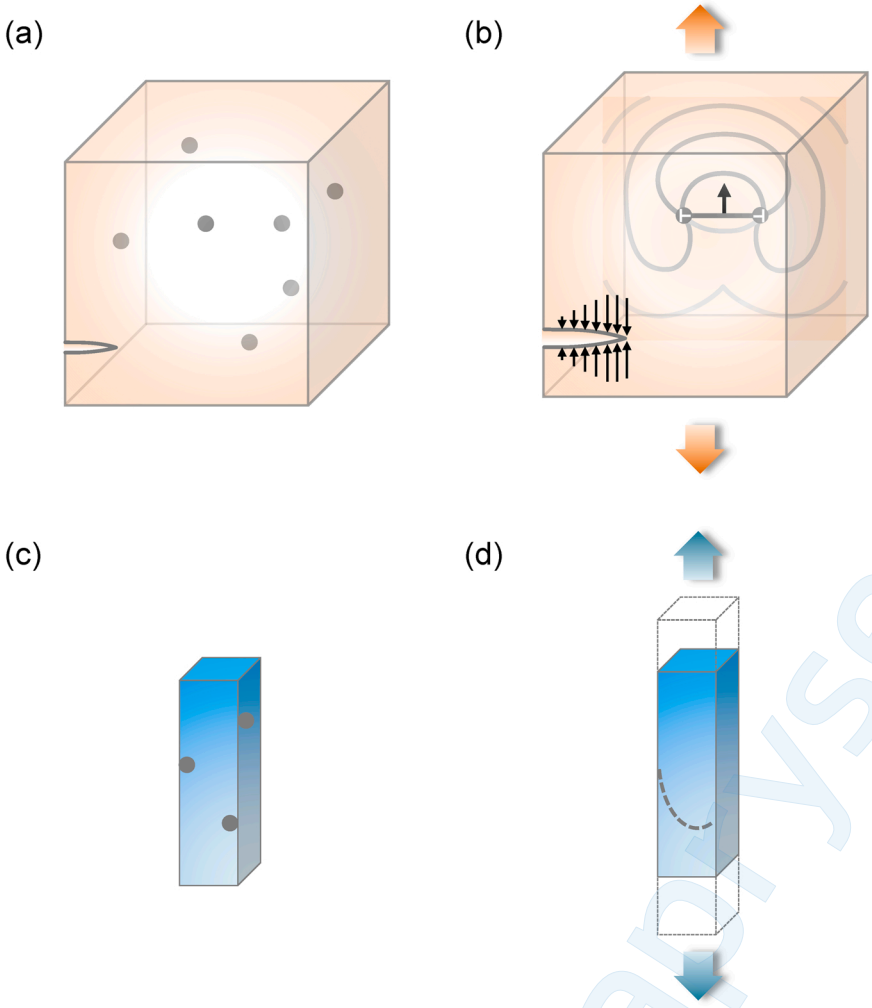

Fig. 3. Schematic illustrations of the dimensionality effect on dislocation development under a deviatoric stress. (a,b) Schematics of a bulk crystal with in-grown defects (e.g., dislocations (marked as gray circles) and cracks) before (a) and after (b) applying a deviatoric stress. Dislocation generation by a Frank-Read type multiplication process (inside the material) and a brittle fracture (at the surface) due to a crack tip (Dugdale-Barenblatt model) during deformation in the bulk crystal. (c,d) Schematics of a low-dimensional material (here a nanowire) with surface defects (marked as gray circles) before (c) and after (d) applying a deviatoric stress. An initial mobile dislocation (gray line in (d)) can be nucleated during deformation. Much larger maximum elastic strains can be sustained in low-dimensional materials than their bulk counterparts, due to less defects and a mechanism of defect creation that is controlled by surface nucleation as opposed to growth/propagation typically seen in bulk materials.

% with decreasing diameter of the nanowires, as shown in Fig. 4a [152]. A linear relationship between the maximum elastic strain and the inverse of the diameter ($1/D$) was found in these nanowires, as shown in Fig. 4b.

The dimensionality effect can also be observed in heteroepitaxial thin films in which elastic strains are induced due to the film/substrate lattice mismatch. However, such epitaxial films suffer from the presence of misfit dislocations that are formed during growth to relax the strain energy. By varying the film thickness in heteroepitaxy, Shi et al. have demonstrated large biaxial elastic strains up to 5% in ultrathin CeO_2 films on (001)-oriented single crystal yttria-stabilized zirconia (YSZ) [153]. Reciprocal space mapping revealed that the ultrathin CeO_2 films were gradually relaxed while they remained coherently strained. Fig. 4c shows the in-plane and out-of-plane lattice parameters for epitaxial

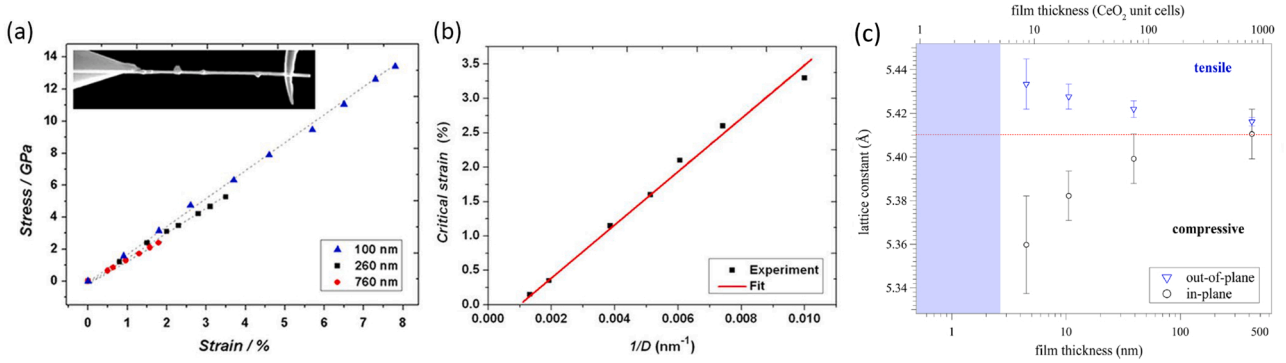

Fig. 4. Dimensionality effects on maximum elastic strains in binary oxides (e.g., ZnO (a,b) and CeO_2 (c)). (a) Stress–strain curves of ZnO nanowires with different diameters (100, 260 and 760 nm) and a secondary electron image of an individual nanowire (inset). (b) Critical strain (or maximum elastic strain) versus $1/D$ in ZnO nanowires. (c) In-plane and out-of-plane lattice parameters versus film thickness in relaxed CeO_2 films epitaxially grown on YSZ substrates. Coherent films lie in the shaded region. [152]. [153]. Reprinted by permission of American Chemical Society.
(a) (a) and (b) are adapted from Ref. (b) (c) is adapted from Ref.

CeO_2 films, revealing the dependence of strain on the thickness of heteroepitaxial CeO_2 thin films.

In general, a reduction in either dimensions of an internal feature or structure or in overall physical dimensions of a low dimensional material can lead to an increase in the maximum elastic strain. The ability to introduce larger elastic strains in low-dimensional materials as compared to their bulk counterparts widens the design space for elastic strain engineering in these materials.

Large elastic strains can be introduced in various low-dimensional materials by using different approaches, e.g., tensile loading [149–152, 154–157], bending [6, 158–163], heterostructures in nanocomposites [164–168], heteroepitaxy [153, 169–180], and doping [181–184]. These approaches are reviewed in Section 4. We have summarized the experimentally measured elastic strain limits in typical low-dimensional materials in Table 2 and Fig. 5 with binary oxides highlighted in bold face. It can be seen that some low-dimensional materials can sustain elastic strains of more than 20 %. For instance, Lee et al. reported an elastic strain up to ~25 % in freestanding graphene membranes measured by nanoindentation in an AFM system [185]. Similarly, foam like carbon nanotube films have been shown to exhibit a high compressibility of ~22 % [186].

However, these large values of elastic strains only exist in certain materials with specific morphologies. Different morphologies, sizes and testing methods can lead to different experimental values of elastic strains in low-dimensional materials. For instance, for low-dimensional Si, Domenicucci et al. reported an epitaxial tensile strain of 1.08 % in a Si thin film in the channel direction of an n-type FET device fabricated on s-Si/SiGe-on-insulator [187], while Zhang et al. reported that single-crystalline Si nanowires grown by the vapor-liquid-solid approach and having diameters of ~100 nm can reach ~16 % tensile strain [154]. In most materials listed in Table 2, the measured elastic strain limits are larger than 1 %, while annealed bulk crystals usually yield an elastic strain limit of less than 0.1 % [188].

2.3. Elastic strain engineering in low-dimensional materials

Strain can modify the electronic properties of materials. For instance, elastic strain can enhance the electron mobility in a Si layer grown on a $Si_{1-x}Ge_x$ substrate [221], increase ferroelectric Curie temperature [178, 222], tune the tunneling electroresistance effect in $BaTiO_3$ thin films [223], and argument the superconducting transition temperature in superconductors such as $La_{1.9}Sr_{0.1}CuO_4$ [224] and $(Ln_{1-x}M_x)_2CuO_4$ [225]. In addition, elastic strain can open a band gap in a metallic carbon nanotube [226] and modify the nature of the band transition (direct versus indirect) in strained Ge layers [173], MoS_2 monolayers [163], WSe_2 multilayers [227], and atomically thin arsenene and antimonene layers [228]. Moreover, elastic strain can be used to modulate the piezo-resistive effect in black phosphorus FETs [229], the high-temperature zero-field quantum valley Hall effect in twisted graphene bilayers [230], the giant piezoresistance effect in Si nanowires [231] and room-temperature ferroelectricity in strained $SrTiO_3$ [18].

Elastic strain also modifies the optical properties of low-dimensional materials, as observed by PL or cathodoluminescence (CL) spectroscopy [161, 172, 193, 232–239]. The emission peak energy can be shifted at a rate of ~-210 meV/% strain (redshift) in AlInGaN/InGaN quantum well structures [236], -45—99 meV/% uniaxial or biaxial strain in MoS_2 layers [163,194,238,240], ~95 meV/% strain in WS_2 monolayers [241], ~-27 meV/% strain in $MoSe_2$ monolayers [161], ~-120 meV/% strain in multi-layer black phosphorus [192] and ~-80 meV/% strain in GaAs/$Al_{0.3}Ga_{0.7}As$/GaAs core/shell nanowires [172]. Elastic strain can improve electro-optical properties as well. For instance, a rapid decrease in resistivity and a redshift in photocurrent spectra were observed in Ge nanowires with a high tensile strain [242] and a significant linear electro-optic effect was induced in a silicon electrooptic modulator by adding a strained layer on top of a silicon waveguide [243].

Elastic strain engineering with respect to magnetic properties in low-dimensional materials includes generation or tuning of different spin states in $LaCoO_3$ thin films [244], spin splitting in GaAs and InGaAs epitaxial layers [245], the magnetocaloric effect in MnAs epitaxial layers [246] and selective orbital occupancy in epitaxial $La_{2/3}Ca_{1/3}MnO_3$ films [247]. Recently, Hong et al. reported that tensile strains (up to 8 %) in nanoscale $La_{0.7}Ca_{0.3}MnO_3$ membranes can induce a phase transition from the ferromagnetic metal phase to the insulator phase [189].

Additionally, chemical properties can be affected by elastic strain. Elastic strain can modify the surface reactivity in Ru (0001) [248], CoO [218], TiO_2 [249] and (100) epitaxial $La_{1-x}Sr_xCoO_{3-\delta}$ (LSC) thin films [250], the number of oxygen vacancies in MnO thin films [251], superconducting $EuBa_2Cu_3O_{7-\delta}$ films [252] and $SrCoO_x$ films [176,253], and ionic transport in $Ce_{0.8}Gd_{0.2}O_{1.9-x}$ electrolyte films [6], $SrZrO_3$-RE_2O_3 nanocomposite films [167], cuboid Fe nanoparticles [254], and $Gd_{0.1}Ce_{0.9}O_{2-\delta}/Er_2O_3$ multilayers [174].

It has also been found that elastic strain can help to stabilize metastable phases of some materials. For example, metastable phases of halide perovskites such as black $CsPbI_3$ [255] and α-$FAPbI_3$ [215] can be stabilized by epitaxial strain. Topological structures such as polar meron in ferroelectric oxides can also be stabilized by epitaxial strain [213].

Elastic strain engineering has been widely utilized in technologically practical devices. A successful example of this is the strained Si technology [256–259]. The carrier mobility in silicon-based devices can be greatly enhanced by up to a hundred percent by introducing a few percent epitaxial strain in films on $Si_{1-x}Ge_x$ substrates [256]. Using embedded SiGe in p-type FET devices, a uniaxial compressive strain can be directly imparted to the channel region, resulting in more than 50 % enhancement in hole mobility [260]. Further, using an ultrathin tensile strained Si layer directly on insulator structures, IBM fabricated transistors exhibiting enhancement in both electron and hole mobility without the SiGe layer and avoiding the related process integration problems [257,261]. It was predicted that Moore's law would eventually break down due to physical limits on transistor scaling, but this was delayed by introducing elastic strain engineering in silicon technology over the last decade [137]. For a detailed review on strained silicon technology, one may refer to the article written by Bedell et al. [262].

Detailed effects of elastic strain on various properties of low-dimensional binary oxides are comprehensively reviewed in Section 6.

3. Binary oxides – Crystal structures

To study the effect of elastic strain on material properties, some familiarity with the symmetry of relevant crystal structures is necessary. Crystal structure of a material is determined by the cation-anion bond length and coordination. There are several common crystal structures in binary or ternary oxides.

For monoxide (MO) type binary oxides (M=metal cation), common structures are rock salt (Fig. 6a) and wurtzite (Fig. 6b). Examples of rock-salt MO oxides include alkaline earth metal oxides (MgO, BaO and CaO) and some transition metal oxides (TiO, FeO and MnO). Examples of wurtzite MO oxides include ZnO and BeO. In terms of electronic (or magnetic) properties, MO oxides can be metals (LaO, NdO and TiO), semiconductors (BeO, CdO, CoO, FeO, MnO, NiO, PbO and ZnO), insulators (BaO, CaO, MgO, SrO), superconductors (NbO), or even magnets (EuO). For dioxides (MO_2), the common structures include fluorite (Fig. 6c) and rutile (Fig. 6d). Examples of fluorite MO_2 oxides include CeO_2, PrO_2, and HfO_2, which are typically insulators. Examples of rutile MO_2 oxides include ferromagnetic CrO_2, semiconducting SnO_2 and TiO_2, and metallic IrO_2 and RuO_2. For M_2O_3-type oxides having trivalent cations, common structures include bixbyite and corundum (Fig. 6e). M_2O_3-type oxides with bixbyite structures are typically insulating, including Er_2O_3, La_2O_3, Nd_2O_3, Sm_2O_3 and Gd_2O_3. M_2O_3 oxides with corundum structures include metals (V_2O_3), semiconductors (In_2O_3, Beta-Ga_2O_3 and Ti_2O_3), and insulators (Al_2O_3, Cr_2O_3 and Fe_2O_3).

Table 2
Summary of experimentally reported elastic strains (either intentionally introduced or left behind after fabrication as residual strain) in low-dimensional materials. The corresponding growth method and source of strain are also included. Here positive values represent tensile elastic strains, while negative values represent compressive elastic strains. "IP" represents strain along the in-plane direction of the substrate. "OOP" represents strain along the out-of-plane direction of the substrate. Binary oxides are in bold font.

Materials	Morphology	Growth methods	Maximum elastic strain/%	Methods to generate/sustain elastic strain	Ref.
Recoverable					
ZnO	**Nanowire**	**PVD**	**7.3**	**Tensile testing**	[152]
$La_{0.7}Ca_{0.3}MnO_3$	Freestanding membrane	PLD	8.2	Tensile testing	[189]
Si	Nanowire	VLS technique	16	Tensile testing	[154]
Au	Nanowire	Chemical reduction	7.2	Tensile testing	[155]
Ag	Nanowire	Chemical reduction	1.6	Tensile testing	[156]
Cu	Nanowire	FIB	7.2	Tensile testing	[149]
MoS_2	Monolayer	CVD	4.8	Tensile testing	[4]
Cu-Zr	Nanowire	FIB	4.4	Tensile testing	[190]
Nb	NiTi:Nb nanocomposite	Vacuum induction melting	5.6	Tensile testing	[164,165]
SnO_2	**Microwire**	**CVD**	**1.7**	**Bending**	[191]
GaAs	Nanowire	MOVPE	3.5(−1)	Bending	[172]
MoS_2	Monolayer	Mechanical exfoliation	2.2	Bending	[163]
$MoSe_2$	Monolayer	Mechanical exfoliation	1.1	Bending	[161]
CeO_2:Gd	**Freestanding membrane**	**PLD**	**2(−2.7)**	**Buckling**	[6]
Graphene	Monolayer	CVD	7.8(−7.8)	Buckling	[162]
Black P	Sheet	Mechanical exfoliation	5(−5)	Buckling	[192]
$ReSe_2$	Sheet	Mechanical exfoliation	1.6	Buckling	[193]
MoS_2	Monolayer	CVD, Mechanical exfoliation	5.6	Buckling	[194]
GaAs	Ribbon	Wet chemical etching	2.5	Buckling	[195]
Graphene	Monolayer	Mechanical exfoliation	25	Nanoindentation	[185]
Carbon	Nanotube	Pulsed laser vaporization	5.8	Nanoindentation	[196]
MoS_2	Monolayer	Mechanical exfoliation	11	Nanoindentation	[197]
VO_2	**Nanowire**	**Vapor transport**	**-1.9**	**Compressive testing**	[198]
Carbon	Nanotube film	CVD	-22	Compressive testing	[186]
W	Nanowire	In situ welding	-4.9	Compressive testing	[199]
GaAs	Nanowire	MOCVD	-11	Compressive testing	[200]
CeO_2-ZrO_2	**Pillar**	**FIB**	**-7**	**Compressive testing**	[201]
$BiFeO_3$	Film	PLD	-14	Compressive testing	[202]
Cu-Al-Ni	Pillar	FIB	-4	Compressive testing	[203]
Irrecoverable					
Ge	InAlAs:Ge nanocomposite	MBE	5.3	Nanocomposite	[166]
$SrZrO_3$	$SrZrO_3$:Sm_2O_3 nanocomposite	PLD	1.3(OOP)	Nanocomposite	[167]
$BaTiO_3$	$BiTiO_3$:Sm_2O_3 nanocomposite	PLD	2.35(OOP)	Nanocomposite	[168]
$BiFeO_3$	$BiFeO_3$:Sm_2O_3 nanocomposite	PLD	1.5(OOP)	Nanocomposite	[204]
$BaZrO_3$	$Ba_2Cu_3O_7$:$BaZrO_3$ nanocomposite	PLD, MOCVD	1.9(OOP)	Nanocomposite	[205]
$CoFe_2O_4$	$CoFe_2O_4$:$BiFeO_3$ nanocomposite	PLD	-6(OOP)	Nanocomposite	[206]
ZrO_2:Y_2O_3	**ZrO_2:Y_2O_3/$SrTiO_3$ film**	**RF sputtering**	**7(IP)**	**Heteroepitaxy**	[169]
CeO_2	**CeO_2/YSZ film**	**PLD**	**-5(IP)**	**Heteroepitaxy**	[153]
CeO_2:Gd	**CeO_2:Gd/Er_2O_3 film**	**PLD**	**-1.16(IP)**	**Heteroepitaxy**	[174]
CeO_2:Gd	**CeO_2:Gd/$SrTiO_3$/MgO film**	**PLD**	**1.9(OOP)**	**Heteroepitaxy**	[175]
VO_2	**VO_2/TiO_2(001) film**	**PLD**	**-1.8(OOP)**	**Heteroepitaxy**	[207]
VO_2	**VO_2/TiO_2(100) film**	**Ion-beam deposition**	**3.7(IP)**	**Heteroepitaxy**	[208,209]
HfO_2	**HfO_2/Si(100) film**	**RF sputtering**	**-4(IP)**	**Heteroepitaxy**	[171]
EuO	**EuO/BaO superlattice**	**MBE**	**6.4(IP)**	**Heteroepitaxy**	[210]
Ge	Ge/InGaAs/GaAs(100) film	MBE	2.33(IP)	Heteroepitaxy	[173]
$SrTiO_3$	$SrTiO_3$/Si(001) film	MBE	-1.7(IP)	Heteroepitaxy	[177]
$BaTiO_3$	$BaTiO_3$/$DyScO_3$ film	MBE, PLD	-1.7(IP)	Heteroepitaxy	[178]
$BiFeO_3$	$BiFeO_3$/$YAlO_3$ film	MBE	-4.5(IP)	Heteroepitaxy	[211]
$CaTiO_3$	$CaTiO_3$/$NdGaO_3$ film	PLD	1.1(IP)	Heteroepitaxy	[179]
$EuTiO_3$	$EuTiO_3$/$DyScO_3$ film	MBE	1.1(IP)	Heteroepitaxy	[180]
$HoMnO_3$	$HoMnO_3$/Pt/c-Al_2O_3 film	PLD	1.2(IP)	Heteroepitaxy	[212]
$SrCoO_x$	$SrCoO_x$/$KTaO_3$ film	PLD	4.2(IP)	Heteroepitaxy	[176]
$PbTiO_3$	$PbTiO_3$/$PrScO_3$ film	PLD	3.5(IP)	Heteroepitaxy	[213]
$Bi_5Ti_3FeO_{12}$	$Bi_5Ti_3FeO_{12}$/$LaAlO_3$ film	PLD	2.2(IP)	Heteroepitaxy	[214]
α-$FAPbI_3$	α-$FAPbI_3$/$MAPbCl_{1.5}Br_{1.5}$	Vapor transport	-2.4(IP)	Heteroepitaxy	[215]
ZnO:Br	**Nanowire**	**RF sputtering**	**0.45**	**Doping**	[183]
CeO_2:Sc	**Film**	**PLD**	**-1.7**	**Doping**	[184]
MoS_2:N	Sheet	N_2 plasma treatment	-1.7	Doping	[181]
SnO_2	**Film**	**PLD**	**1.7(OOP)**	**He implantation**	[182]
$LaSrMnO_3$	Film	PLD	0.94(OOP)	He implantation	[216]
HVO_2	**Film**	**PLD**	**10.2**	**Hydrogenation**	[217]
CoO	**nanorod**	**Cation exchange**	**4**	**Stoichiometry**	[218]
Pt	Pt/Cu(111) core/shell nanopartical	Impregnation	-3.3	Core/shell	[219]
GaAs	GaAs/InGaAs core/shell nanowire	MBE	7	Core/shell	[220]

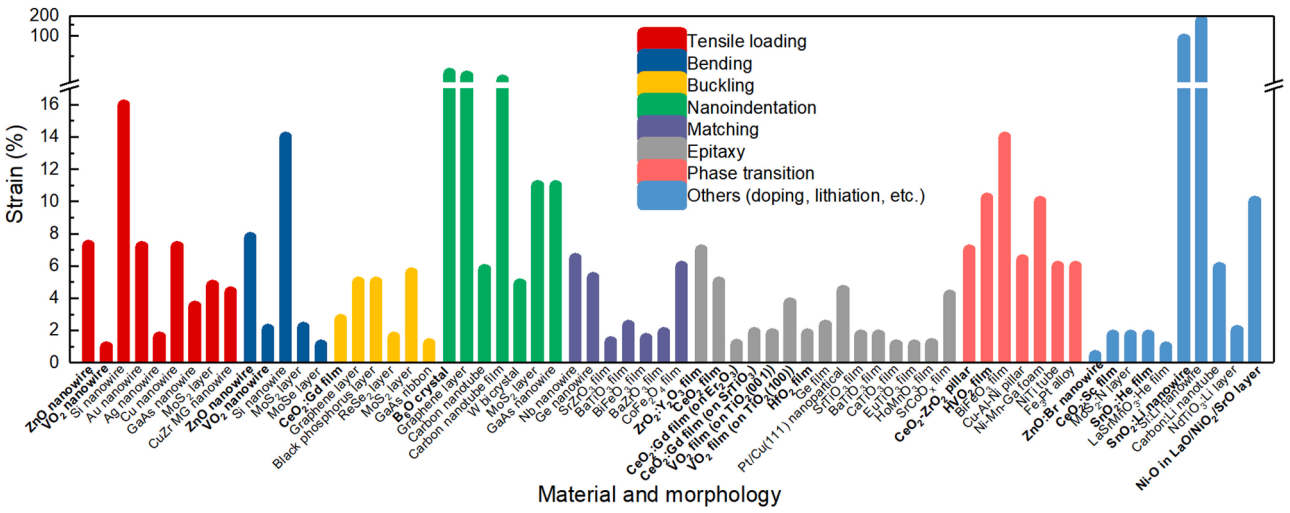

Fig. 5. Summary of experimentally measured elastic strain limits (absolute values) in typical low-dimensional materials. Binary oxides are in bold font.

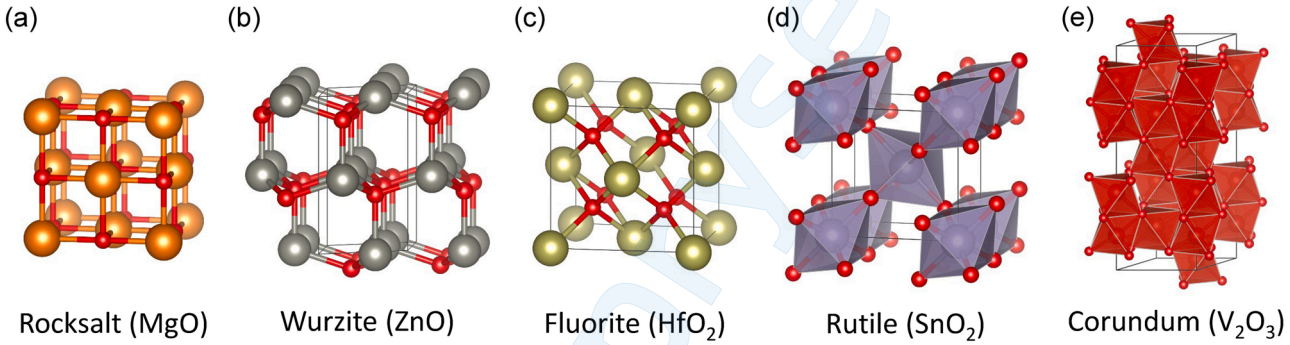

Fig. 6. Common crystal structures of binary oxides, including (a) rocksalt (MgO), (b) wurtzite (ZnO), (c) fluorite (HfO_2), (d) rutile (SnO_2), and (e) corundum (V_2O_3).

4. Methods to introduce or sustain elastic strains

To successfully modify or tune material properties via elastic strain engineering, control over the elastic strain introduced in a material is crucial. In this section, we summarize different methods adopted by different research fields to introduce and sustain elastic strains in low-dimensional materials. These include reversible as well as irreversible methods, as explained below.

4.1. Reversible methods

Reversible methods, in which the introduced elastic strain can also be removed, mainly include the mechanical, electrical, thermal and optical methods. In mechanical methods, strain (e.g., tensile and compressive) can be generated either directly by loading nanowires [152, 200, 263–265] and nanotubes [266] or indirectly by loading substrates with the target nanostructures on their surface [267,268]. Bending nanowires [3, 67, 269–272], nanotubes [273], and monolayers [163,238], and buckling ribbons [195,274,275], layers [162, 192–194, 240] and thin films [279] can generate compressive, tensile and shear strains. Nanoindentation can generate compressive strains in nanowires or nanobelts [276,277] and tensile strains in nanotubes [196] and monolayers [185,197,278].

Electrical methods of introducing elastic strain include application of an external bias to control biaxial strain in epitaxial thin films grown on piezoelectric crystals, e.g., VO_2 films on 0.72Pb(Mg1/3Nb2/3)−0.28$PbTiO_3$ (PMN-PT) crystals [279] or the use of electromechanical resonators to dynamically generate tensile strains in VO_2 nanobeams [280].

Thermal methods of introducing elastic strain include the thermal expansion of substrates to generate elastic strain in overlying nanostructures, e.g., VO_2 thin films [281] and transition metal dichalcogenide (TMD) monolayers (MoS_2, $MoSe_2$, WS_2, WSe_2) [241]. A dynamic phase transition triggered by temperature in VO_2 microbeams can generate elastic strain in a CdS or halide perovskite film grown on the beam [282,283] and in a MoS_2 sheet stacked on the beam [284]. Additionally, temperature-induced phase separation (spinodal decomposition) can be observed in alloy compounds like Li_xFePO_4 [285,286], $V_{1-x}Ti_xO_2$ [287], and $Ti_xSn_{1-x}O_2$ [288], generating strains at phase interfaces due to a lattice mismatch between different phases.

Optical methods of introducing elastic strain include the use of femtosecond lasers to induce a dynamic structural response and elastic strain waves in low-dimensional materials, e.g., MoS_2 layers [289,290]. Laser-induced spinodal decomposition in $MAPbBr_3$/$MAPbI_3$ [291] and a phase transition in VO_2 films [292] can also generate strains at phase interfaces.

In chemical methods, strains (i.e., chemical strains) can be generated by chemical processes, e.g., ion diffusion. In lithium-ion batteries, lithiation-induced strains have been observed in high-energy density anodes such as SnO_2 nanowires [293,294], Co_3O_4 hollow spheres [295], Si nanowires [296] and nanoparticles [297,298], multiwalled carbon nanotubes [299], Ge nanowires [300], $LiCoO_2$ layers [301], and LiNd-TiO_3 layers [302]. Transfer of oxygen and hydrogen ions can generate strains during phase transition in $SrCoO_x$ thin films [303,304] and VO_2 thin films [217].

4.2. Irreversible methods

Irreversible methods, in which the introduced elastic strain cannot be removed, include interfacial bonding (e.g., heteroepitaxy) and growth and post processing (e.g., doping). Typically, elastic strains in epitaxial thin films originate from the lattice mismatch in heteroepitaxy. Materials strained by such an approach include semiconductors such as Ge [173] and GaN [234], binary oxides such as ZrO_2 [169], CeO_2 [153, 174,175], VO_2 [207–209] and HfO_2 [171], ferroic oxides such as $SrTiO_3$ [10,177], $BaTiO_3$ [178] $CaTiO_3$ [179], $EuTiO_3$ [180] and $HoMnO_3$ [212], and transition metal oxides such as $SrCoO_x$ [176].

For heterostructures in nanocomposites, where one material is embedded in the matrix of another material, both materials have elastic strains. For instance, elastic strains have been observed in $(La_{0.67}Ca_{0.33}MnO_3)_{1-x}$:$(MgO)_x$ composite films consisting of MgO clusters formed around the $La_{0.67}Ca_{0.33}MnO_3$ grains [305], in $YBa_2Cu_3O_{7-\delta}$ films containing self-aligned nanodots and nanorods of $BaZrO_3$ [306], in a ferromagnetic $CoFe_2O_4$ film containing vertically aligned multiferroic $BiFeO_3$ nanopillars [206], and in films containing vertically self-assembled nanocolumns such as $BaTiO_3$:$CoFe_2O_4$ (film:nanocolumn) [7], $La_{0.70}Sr_{0.3}MnO_3$:ZnO [204], $BiFeO_3$:Sm_2O_3 [204,307], $BaTiO_3$:Sm_2O_3 [168], RE(rare earth)-$Ba_2Cu_3O_{7-\delta}$:$BaZrO_3$ [205], GaSb:ErSb [308], $SrZrO_3$:Sm_2O_3 [167] and $SrTiO_3$:yttria-stabilized ZrO_2 [309].

Irreversible strain can also be introduced by vdW epitaxy/growth. Although the vdW interaction at such an interface is much weaker than ionic or covalent bonding in conventional epitaxy, it can lead to elastic strains in as-grown layers, e.g., PbI_2/muscovite (Mica) [310], MoS_2/-SiO_2 [311], and Pb(Zr,Ti)O_3 (PZT)/Mica [312]. In vdW heterostructures formed by mechanical transfer, e.g., graphene/hydrogen silesquioxane [313] and graphene/SiO_2 [162,314], large elastic strains have been observed due to the vdW interaction between carbon atoms from the overlying graphene and oxygen atoms from the underlying patterned hydrogen silesquioxane or SiO_2 substrate.

Additionally, growth and post processing can lead to elastic strains in thin films. For instance, by doping or alloying, elastic strains can be introduced in perovskite oxides [315], superconductors [225], monolayer MoS_2 [181], binary oxide thin films such as SnO_2 [316] and CeO_2 [184], and ZnO nanowires [183]. In films grown by hybrid MBE, stoichiometry and oxygen partial pressures can be controlled, leading to tensile elastic strains in $CaTiO_3$ films [317] and large strains and strain gradients in epitaxial ferroelectric $HoMnO_3$ thin films [212], respectively. Other growth strategies involving control over growth temperature, growth modes and growth time (film thickness), can help to generate elastic strains and large strain gradients in epitaxial thin films including HfO_2 [318], VO_2 [319] and $La_{0.7}Sr_{0.3}MnO_3$/$PbZr_{0.2}Ti_{0.8}O_3$ [320]. Post-processing, e.g., annealing and helium implantation, can generate compressive elastic strain in acceptor doped CeO_2 films [184] and lead to strain in $La_{0.7}Sr_{0.3}MnO_3$ [216] and SnO_2 [182] thin films.

All the methods of introducing or sustaining elastic strain mentioned above are summarized in Table 3 and typical ones are schematically illustrated in Fig. 7a—j, including both reversible (Fig. 7a—g) and irreversible (Fig. 7 h—j) methods. Reversible methods include direct (Fig. 7a—d) and indirect (Fig. 7e—g) methods. For instance, tensile loading (a), compressive loading (b), bending of a nanowire (c) and nanoindentation on a nanosheet (d) are direct approaches. Tensile loading (e), bending (f) and compressive loading (g) of a substrate to generate tensile (e—f) and compressive strains (g) in a nanosheet via vdW interaction are indirect methods. Irreversible methods to introduce strain due to interfacial bonding include epitaxial strains in heteroepitaxy (h), epitaxial strains in vdW epitaxy (i) and strains induced by doping or alloying (j).

5. Characterization of strain

The various experimental techniques for characterizing strain are

Table 3
Summary of methods to introduce and sustain elastic strain, including reversible and irreversible methods.

Methods		Materials and references
Reversible methods		
Mechanical stimulation	Tensile loading	Si nanowires[263], ZnO nanowires [152], VO_2 nanowires[264], carbon nanotubes[266], graphene[321], MoS_2 monolayers[4]
	Compressive loading	TiO_2 nanotubes[265], GaAs nanowires [200], MoS_2 layers[267], graphene[268]
	Bending	Si nanowires[270], Ag nanowires[269], carbon nanotubes[273], MoS_2 monolayers[163,238], ZnO nanowires [3,67,271,272], VO_2 nanowire[198]
	Buckling	Si ribbons[274], GaAs ribbons[195], graphene ripples[275], graphene[162], MoS_2 layer[194,240], $ReSe_2$ layer[193], black phosphorus multi-layers[192], CeO_2 thin films[279]
	Nanoindentation	Carbon nanotubes[196], Graphene [185], MoS_2 layers[197,278], ZnO nanowires[276,277]
Electrical stimulation	Electrical field	VO_2 films[279], VO_2 nanobeams[280], $BiFeO_3$ films[202,322], yttrium-stabilized ZrO_2 films[323], $LiCoO_2$ layers[301], $BaTiO_3$ crystals [324]
Thermal stimulation	Temperature	VO_2 films[281], CdS/VO_2 microbeams [283], Li_xFePO_4 crystals[285,286], $V_{1-x}Ti_xO_2$ crystals[287], $Ti_xSn_{1-x}O_2$ crystals[288], TMD layers[241], $CsPbBr_3$/VO_2 microbeams[282], MoS_2/VO_2 microbeams[284]
Optical stimulation	Light	CdS and CdSe nanocrystals[325], MoS_2 layers[289,290], WSe_2 layer[326], $MAPbBr_3$/$MAPbI_3$ rods and films[291], VO_2 films[292]
Ion diffusion	Lithiation	Lithium alloy films[327], SnO_2 nanowires[293,294], Co_3O_4 hollow spheres[295], Si nanowires[296] and nanoparticles[297,298], multiwalled carbon nanotubes[299], Ge nanowires [300], $LiCoO_2$ layers[301], $LiNdTiO_3$ layers[302]
	Hydrogen and oxygen ion transfer	$SrCoO_x$ films[303,304], VO_2 films[217]
Irreversible methods		
Interfacial bonding	Heteroepitaxy (horizontal interface)	Ge layers[173], ZrO_2[169], CeO_2[153, 174,175], VO_2[207–209], HfO_2[171], $SrTiO_3$[10,177], $BaTiO_3$[178] $CaTiO_3$ [179], $EuTiO_3$[180], and $HoMnO_3$[212], $SrCoO_x$[176], GaN[234] films
	Nanocomposite (vertical interface)	$(La_{0.67}Ca_{0.33}MnO_3)_{1-x}$:$(MgO)_x$[305], $YBa_2Cu_3O_{7-\delta}$:$BaZrO_3$[306], $BaTiO_3$:$CoFe_2O_4$[7], $La_{0.70}Sr_{0.3}MnO_3$:ZnO[204] and $BiFeO_3$:Sm_2O_3[204,307], $BaTiO_3$:Sm_2O_3[168], RE(rare earth)-$Ba_2Cu_3O_{7-\delta}$:$BaZrO_3$[205], GaSb:ErSb[308], $SrZrO_3$:Sm_2O_3[167]and $SrTiO_3$:yttria-stabilized ZrO_2[309] films
	VdW interaction	PbI_2 films[310], MoS_2 layers[311], PZT layers[312], graphene/hydrogen silesquioxane[313], graphene/SiO_2[162, 314]
Growth strategy and post-processing	Doping or alloying	Perovskite oxides films[315], superconductors films[225], MoS_2 monolayer[181], SnO_2 films[316], CeO_2 films[184], and ZnO nanowires[183]
	Stoichiometry	$CaTiO_3$ films[317]
	Oxygen partial pressure	$HoMnO_3$ films[212]
	Polar cation ordering	layered oxide films[328]
	Growth temperature	HfO_2 films[318]
	Growth mode	VO_2 films[319]

(continued on next page)

Table 3 (*continued*)

Methods		Materials and references
	Annealing	CeO_2 films[184]
	Buffer layer	VO_2 films[329], $HoMnO_3$ films[212]
	Thickness	ZrO_2 films[169], CeO_2 films[153], EuO films[330], Pt/Cu(111) core-shell nanoparticle[219], $La_{0.7}Sr_{0.3}MnO_3/PbZr_{0.2}Ti_{0.8}O_3$ films [320]
	Ion implantation	$La_{0.7}Sr_{0.3}MnO_3$ films[216], SnO_2 films [182], VO_2 films[331]

summarized in Table 4. Different variants of X-ray diffraction (XRD) [332–338], several modes of electron diffraction [339–350], neutron diffraction [351] and spectroscopy (e.g. Raman spectroscopy) [352–355] are common techniques for characterizing strains.

Transmission electron microscopy (TEM) techniques including convergent-beam electron diffraction (CBED) [346,347], nano-beam electron diffraction (NBED) [348,349], high-resolution TEM (HRTEM) [340,341] and dark-field electron holography (DFEH) [345] are also often used for characterizing strain. In situ TEM mechanical tests can measure the real-time strain imposed on a material [155, 190, 356–363]. Besides, by fabricating electromechanical devices like resonators [280], the strain state can be dynamically tracked.

By integrating the time dimension into electron microscopy, ultrafast electron microscopy (UEM) expands static imaging to dynamic imaging. UEM can match the ultrashort time resolution of atomic motions while also providing atomic-scale spatial resolution. This technique has been used to study graphite in four dimensional (4D) space, functional nanomechanical systems, and irreversible phase transitions and crystallization [364]. Particularly, elastic modulation in materials that occurs at the speed of sound can be probed by UEM. For instance, by using in situ femtosecond photoexcitation, dynamics of in-plane photo-induced wrinkling in MoS_2 occurring on a picosecond time-scale have been visualized [289]. Further, UEM has been used to reveal the spatiotemporal evolution of photoexcited high-velocity elastic strain waves in MoS_2 [290]. UEM is one of the most powerful tools available to the materials science community for studying strain dynamics.

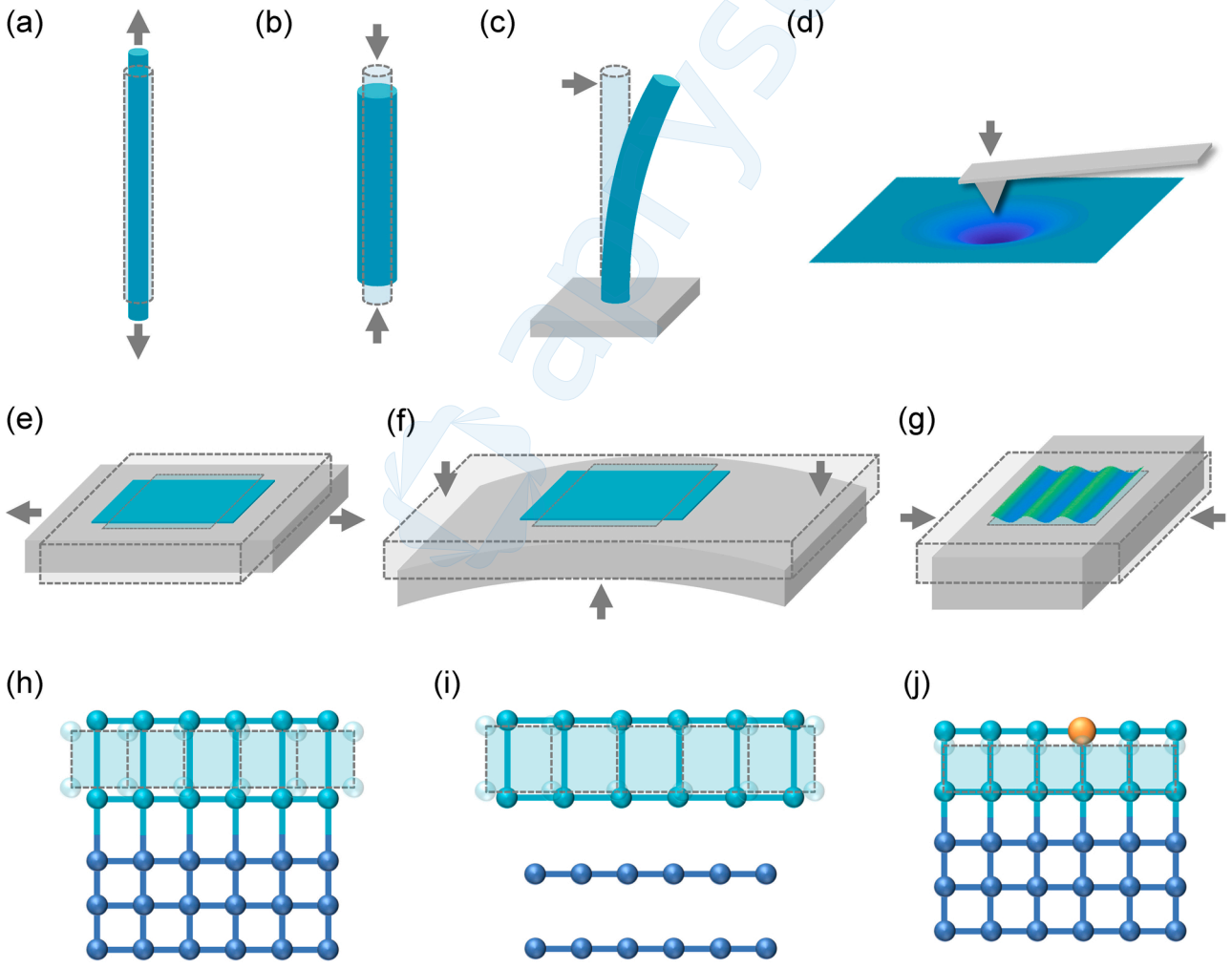

Fig. 7. Schematic illustrations of representative methods of introducing/sustaining elastic strain in low-dimensional materials (1D (a—c) and 2D (d—j)), including reversible (a—g) and irreversible (h—j) methods. (a—d) Direct reversible approaches to introduce/sustain elastic strain in a nanowire, e.g., tensile loading (a), compressive loading (b), bending (c), and nanoindentation of a nanosheet (d). (e—g) Indirect reversible approaches to introduce/sustain elastic strain in a nanosheet on top of a substrate, e.g., tensile loading (e), bending (f) and compressive loading (g) of the substrate leading to tensile (e—f) and compressive strain (g) in the nanosheet via vdW interaction. (h—j) Irreversible methods of introducing/sustaining elastic strain in an epitaxial thin film via interfacial bonding (h and i) and doping or alloying (j). (h) Epitaxial strain in heteroepitaxy. (i) epitaxial strain in vdW epitaxy. (j) Strain induced by doping or alloying.

Table 4
Summary of characterization techniques for strain.

Experimental techniques	Characterizations	Spatial resolution	References
Using Electrons			
Aberration-corrected TEM	Structure, elemental composition and chemical bonding	Atomic-scale	[339–341, 344]
Off-axis electron holography	Nanoscale electrostatic and magnetic fields	Nanoscale	[342]
Electron tomography	3D structural and chemical information	Nanoscale	[343]
Dark-field electron holography (DFEH)	Micrometer fields of view	Nanoscale	[345]
Convergent-beam electron diffraction (CBED) and nano-beam electron diffraction (NBED)	2D strain mapping	Nanoscale	[346–349]
Electron backscattering diffraction (EBSD)	Strain mapping and 3D microscopy	~20 nm	[350,365]
Reflection high-energy electron diffraction (RHEED)	Surface strain	Beam size	[366]
Ultrafast electron microscope (UEM)	Strain dynamics	Atomic scale	[364]
Using X-ray			
XRD	Strain and composition analysis	10 μm	[332,333]
3D X-ray microscopy	Elastic strain tensors	Submicrometer	[334,335]
Coherent X-ray diffraction (CXD)	Quantitative 3D images of strain	Nanoscale	[336,367]
Femtosecond XRD	Strain dynamics	Femtosecond (temporal)	[337]
X-ray absorption spectroscopy	Interatomic distance determination	Submicrometer	[34]
Using photons within ultraviolet-visible regime			
Micro-Raman spectroscopy	Strain distribution based on the Raman shift	Submicrometer	[352,368]
PL spectroscopy	Strain mapping by measuring degree of polarization	Submicrometer	[353]
Digital image correlation	In-plain strain mapping	Micrometer	[355]
Other			
Electrochemical strain microscopy	Nanoscale mapping of ion diffusion	Tens of nanometer	[301,323]

6. Elastic strain-tuned properties and applications of binary oxides

6.1. Piezoelectricity

Piezoelectricity, a phenomenon where the electrical and the mechanical state of a material are coupled, was first demonstrated by French physicists Jacques and Pierre Curie in 1880 [369]. In a piezoelectric material, the application of mechanical stress or pressure leads to accumulation of electric charge. Alternatively, an applied electric field can induce mechanical deformation of a piezoelectric material [370]. The first application of piezoelectricity was an ultrasonic submarine detector invented by Langevin with Chilowski in 1916 and 1917 [371] and later developed by Robert Boyle using quartz crystals [372]. Langevin's successful application of piezoelectricity in the generation and detection of ultrasonic waves created an intense interest in further development of devices, such as the invention of the first piezoelectric crystal oscillator in 1921 by Cady [373]. Due to limited sources of natural piezoelectric crystals, scientists searched for artificial piezoelectric materials in the form of ceramics. $BaTiO_3$, the first piezoelectric ceramic, was discovered in 1946 by Arthur von Hippel at MIT [374]. Subsequently, PZT, first reported by Shirane et al. at the Tokyo Institute of Technology, became the prevalent piezoelectric ceramic material due to its better reproducibility and higher speed of wave propagation over $BaTiO_3$ [375]. Because of the growing concern regarding toxicity of lead-containing devices, there has been a strong push over the years to explore lead-free piezoelectric materials. Sodium potassium niobate ((K, Na)NbO_3), known as NKN, was discovered by a group of Japanese researchers led by Yasuyoshi Saito in 2004 and is a promising candidate with properties close to those of PZT.[44].

Low-dimensional materials that exhibit piezoelectricity, e.g., semiconducting wurtzite compounds (such as ZnO [67,376] and GaN [377]), perovskite ferroelectrics (such as PZT nanowires [378,379] and nanofibers [380], $BaTiO_3$ nanowires [381] and thin films [382], $NaNbO_3$ thin films [383] and nanowires [384]) and oxides (such as SiO_2 crystals [385], MoO_2 sheets [386], PbO sheets [387] and silicon-doped HfO_2 thin films [388]), have received increased attention for use in piezoelectric nanosystems [389]. A measure of piezoelectricity involves direct measurement of the electric charges generated or the electric potential produced under mechanical deformation, e.g., tensile loading [381] or bending [67]. In bending experiments, a conductive AFM probe bends a nanowire (ZnO [67] and GaN [390]), and the generated electric potential across the nanowire is measured with the same conductive probe. Piezoelectric properties of typical low-dimensional materials have been well summarized in the review article Ref. [389].

Among binary oxides having a non-central symmetry as is necessary for the piezoelectric effect, ZnO is a typical example [391]. Piezoelectric properties of various type of ZnO nanostructures have been extensively explored during the last decade. Zhao et al. reported the effective piezoelectric coefficient of ZnO nanobelts (d_{33}^{eff}), obtained by piezoresponse force microscopy (PFM) in the strong indentation mode and measured according to the equation

$$A_f = V_f \delta = d_{33}^{eff} U_f, \quad (1)$$

where A_f is the vibration amplitude, V_f is the vertical deflection signal of the cantilever, δ is the calibration constant of the photodetector sensitivity and U_f is the amplitude of the testing AC voltage. The authors found the effective piezoelectric coefficient of nanobelts to be much larger than the value for bulk wurtzite ZnO [376]. In contrast, Fan et al. showed that the piezoelectric coefficient for ZnO nanopillars with a diameter of about 300 nm was smaller than the bulk value [392]. Scrymgeour and Hsu reported a similar study for ZnO nanorods obtaining a variation of the piezoelectric coefficient from 0.4 to 9.5 pm/V [393]. Besides, Gao et al. reported the growth of piezoelectric ZnO nanohelice [394] and a nonlinear electronic transport behavior of the nanohelice was observed [395].

Various nanodevices employ low-dimensional materials, including low-dimensional binary oxides with piezoelectric properties. The photovoltaic effect observed in strained core−shell compound semiconductor nanowires was attributed to a piezoelectric field [396]. Photovoltaic performance was also enhanced by piezoelectric polarization in depletion-heterojunction ZnO/PbS quantum dot solar cells (QDSC), as reported by Shi [397]. Besides, strain sensors based on piezoelectric semiconductor nanowires with high sensitivity have also been fabricated [398]. Liao et al. recently fabricated a highly stretchable and multifunctional nanosensor consisting of ZnO nanowires and polyurethane fibers with three different sensing capabilities, i.e., strain, temperature and ultraviolet (UV) [399]. Due to its portability and fiber layout, this stretchable and multifunctional sensor is a promising candidate for diverse smart sensing applications and multiparametric sensing platforms.

Low-dimensional piezoelectric materials are also of importance for use in piezoelectric nanogenerators (PENG) which convert mechanical energy to electrical energy for the operation of low-power electronics. PENGs have attracted significant attention and have been manufactured based on ZnO nanowires [67,400], PZT [401] and flexible piezoelectric polymers such as polyvinylidene fluoride (PVDF) [402]. In 2006, Wang and Song first demonstrated PENGs based on ZnO nanowire arrays that

harvested microscale and nanoscale mechanical energy [67]. Bending a ZnO nanowire creates a strain field and charge separation across the nanowire. The bent wire displays a rectifying effect, characteristic of a Schottky barrier between the metal tip and the nanowire and leads to the generation of an electrical current. The output of electrical energy from one nanowire based on one piezoelectric discharge (PZD) event is calculated as

$$\Delta W_{PZD} = \quad V_0^2 C/2 \tag{2}$$

where V_0 is the peak voltage of the discharge output. The elastic deformation energy created due to displacement of the nanowire by the AFM tip is calculated as

$$W_{ELD} = 3YIy_m^2/2L^3 \tag{3}$$

where Y is the elastic modulus, I is the moment of inertia, L is the length of the nanowire and y_m is the maximum deflection of the nanowire. The efficiency of electric power generation is then determined by the ratio

$$Efficiency = \Delta W_{PZD}/\Delta W_{ELD} \tag{4}$$

Where, ΔW_{ELD} is the energy dissipated by the nanowire in the first cycle of vibration. The authors reported high efficiencies in the range of 17–30% which they attributed to the large deformation that could be borne by the ZnO nanowires. Gao and Wang proposed the original mechanism for a PENG based on ZnO nanowires, as shown in Fig. 8a-c, suggesting that for a nanowire having a diameter of 50 nm and a length of 600 nm, a piezoelectric potential of ~0.3 V was enough to drive the metal-semiconductor Schottky diode at the interface of the AFM probe and the nanowire [403]. The behavior of free charge carriers in the PENG under thermodynamic equilibrium conditions was investigated as well [404].

Meanwhile, Wang et al. developed a PENG driven by an ultrasonic wave and producing a continuous direct-current output [405]. Liu et al. further improved the performance of direct-current PENGs to obtain an output current density of 8.3 μA/cm^2 by tuning the carrier density and the characteristics of the Schottky barrier at the interface between the metal electrode and the nanowire [406]. Subsequently, the performance of PENGs with a Schottky contact structure, in terms of the open circuit (OC) voltage, was improved from the original 9 mV to 1 V [400,407]. In 2010, Hu et al. introduced a sandwich structure to PENGs by combining piezoelectric ZnO nanowires with a dielectric and sandwiching them in between two electrodes [408]. The output performance of PENGs with the sandwich structure was further improved and the OC voltage was raised from 2 V to 58 V [409,410]. Additionally, piezoelectric performance of ZnO-based flexible nanogenerators can also be remarkably

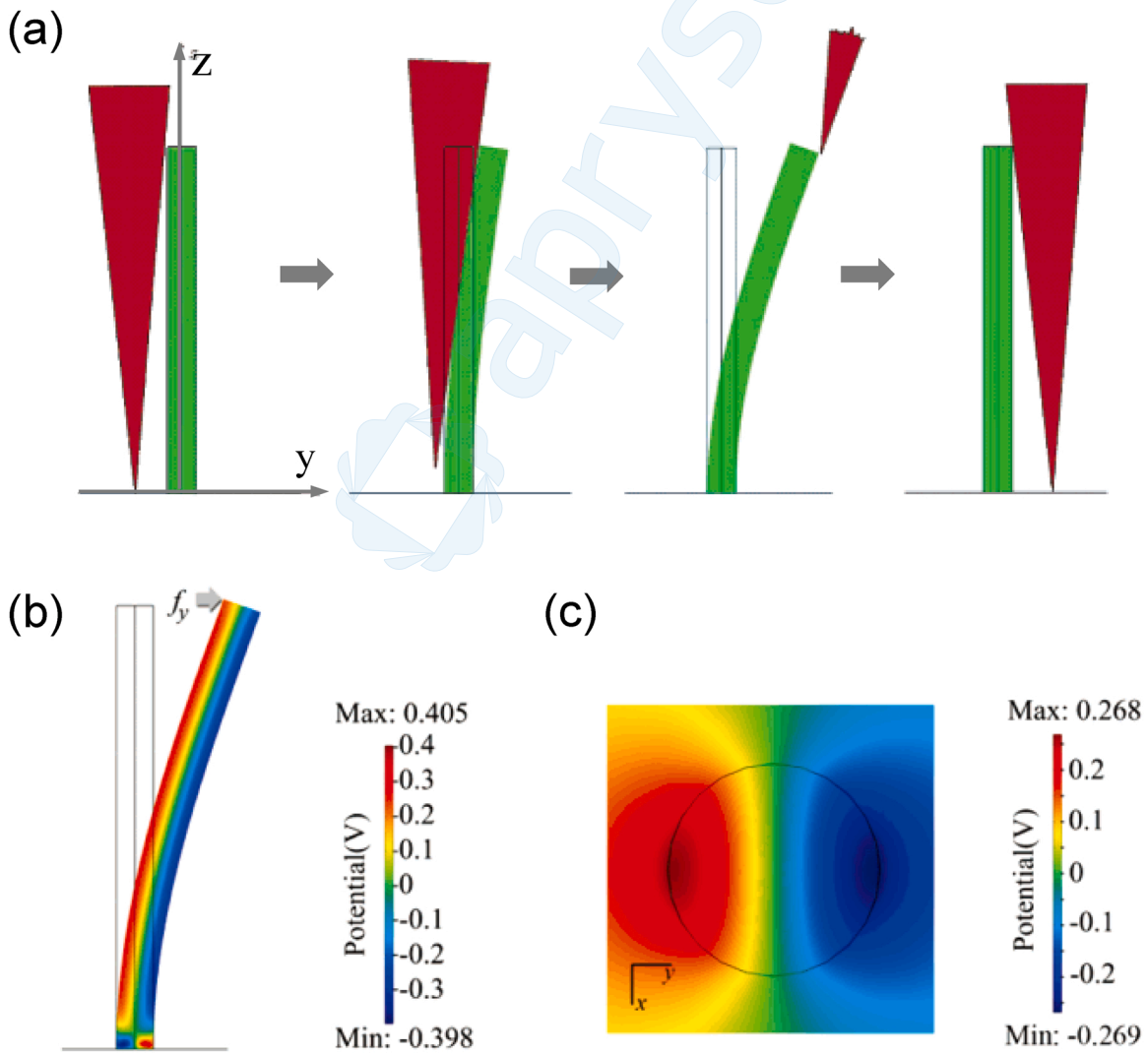

Fig. 8. Fundamental theory of nanogenerator. (a) Schematic of a ZnO nanogenerator. Bending a ZnO nanowire creates an electric field and a potential distribution. (b,c) Perturbation theory calculation of the piezoelectric potential distribution along the side (b) and at the top (c) of a nanowire pushed by a lateral force at the tip. (a—c) are adapted from Ref. [403]. Reprinted by permission of American Chemical Society.

enhanced by doping halogen elements which in turn introduce a lattice strain [183]. Many applications based on high output performance PENGs have been demonstrated, such as photon detection [409], environmental monitoring [411], vehicle monitoring [412] and deformation sensors [413–415].

Computational studies have also been undertaken to explore piezoelectricity in low-dimensional binary oxides. However, computational investigations of piezoelectricity are limited to nanowires with diameters below 4 nm due to the associated computational cost [389]. Xiang et al. studied piezoelectricity in ZnO nanowires with diameters up to 2.8 nm using DFT calculations and found that their effective piezoelectric constants were larger than that of the bulk ZnO due to their free boundaries [416]. The size-dependence of piezoelectricity in GaN and ZnO nanowires with diameters in the range of 0.6—2.4 nm was also studied by Agrawal and Espinosa based on first principle-based DFT calculations [417]. Apart from benchmark DFT calculations, classical polarizable core-shell interatomic potentials were also applied to analyze piezoelectric properties of ZnO [418]. Moreover, Sun et al. numerically estimated the potential, the output power and the energy conversion efficiency of piezoelectric nanostructures, including rectangular nanowires ($BaTiO_3$ nanowires), hexagonal nanowires (ZnO nanowires) and two-dimensional vertical thin films (ZnO nanofins) [419].

Recently, computational investigations of piezoelectricity in monolayers have been carried out. Piezoelectric coefficients for multiple 2D material systems have been calculated by DFT and large in-plane piezoelectric coefficients (d_{11}) have been found in 2D metal oxides, e.g., MgO (6.63 pm/V), CdO (21.7 pm/V), CaO (8.47 pm/V), and ZnO (8.65 pm/V) [420]. Similar first-principles calculations focused on monolayer II–VI group oxides (MO where M= Be, Mg, Ca, Sr, Ba, Zn, and Cd) have also been reported, revealing that group II–VI oxides exhibit highly promising piezoelectric properties, e.g., the highest e_{11} and d_{11} relaxed-ion coefficients are in BeO and BaO, respectively [421]. Single layer transition metal dioxides (MO_2 where M=Cr, Mo, W, Ti, Zr, Hf, Sn) have been theoretically investigated as well, having comparable or larger relaxed-ion piezoelectric coefficients (e.g., ~7 pm/V for TiO_2 and ~ pm/V for ZrO_2) compared to traditional bulk materials (e.g., 2.3 pm/V for α-quartz [422] and 3.1 pm/V for wurtzite GaN [423]) [424]. Considering the large piezoelectric coefficient of ~114 pm/V in PZT nanowires, the development of lead-free piezoelectric materials, although much needed due to environmental concerns, has a long way to go before they become comparable to PZT [378].

As reviewed above, piezoelectric properties of low-dimensional ZnO have been extensively investigated and their application in electronic nanodevices has been demonstrated. Additionally, low-dimensional CdO may prove to be a promising candidate for future nanoscale piezoelectric applications due to its much higher in-plane piezoelectric coefficients over ZnO [420] and reasonably low formation energy with respect to its bulk structure [425]. Although the formation energies of 2D MgO and CaO are higher, it may be possible to stabilize their 2D structures via methods such as interfacial strain engineering. Low-dimensional transition metal dioxides, such as TiO_2 and ZrO_2, are good candidates for studying piezoelectric properties as well. Once 2D structures can be achieved in these oxides, their piezoelectric properties and applications will be very attractive.

6.2. Piezoresistive effect

The piezoresistive effect is a phenomenon in which mechanical strain (ε) can affect the electrical resistance (R) of a material. R of a homogeneous structure is defined as:

$$R = \rho l/a, \tag{5}$$

where ρ is the resistivity, l is the length and a is the average cross-sectional area. The piezoresistive sensitivity, known as the gauge factor (GF), describes the fractional change in resistance ($\Delta R/R$) under applied strain ε, which is expressed as [426]:

$$GF = \frac{\Delta R/R}{\varepsilon}. \tag{6}$$

The fractional change in resistance with strain ($\Delta R/R$) is calculated from the following relation [427]:

$$\frac{\Delta R}{R} = (1 + 2\nu - K_T)\varepsilon + \frac{\Delta \rho}{\rho}, \tag{7}$$

where $(1+2\nu)$ accounts for geometric effects (ν is the Poisson's ratio) and K_T is a constant related to the change in temperature with strain. In semiconductors such as silicon, the change in carrier mobility due to strain dominates the piezoresistive performance, while the geometric effects can be neglected. Thus, the GF in semiconductors is orders of magnitude larger than in metals (typically less than 2) [426]. In ZnO nanobelts or nanowires, a GF varying from 300 to 1250 has been reported [398,428].

A change in resistance with elongation was first observed in iron and copper by William Thomson (Lord Kelvin) in 1856 [429]. In 1935, adapted from analogous work on piezoelectricity, Cookson coined the term 'piezoresistance' to describe the change in conductivity with stress, distinct from the total fractional change in resistance [369,430]. In 1950, Bardeen and Shockley predicted relatively large piezoresistance in single-crystal semiconductors [431]. Later in 1954, Smith reported the first measurement of exceptionally large piezoresistive shear coefficients in silicon and germanium [432].

Based on Bardeen and Shockley's model, more refined models of transport and energy band structure were proposed, e.g., Herring's Many-Valley model that explained the piezoresistance in n-type silicon and germanium [433]. On the other hand, gaining an understanding of the piezoresistance theory for p-type semiconductors was difficult due to the complexity of their valence band structure and was improved upon in late 1990's due to computational advances [434,435]. Theoretically, the piezoresistive effect originates from variation of the electronic structure with strain, which changes the concentration, the effective mass and the mobility of charge carriers, as well as the quantization effect that occurs in the first few atomic layers of low-dimensional materials at the sub-10 nm scale [436].

Piezoresistive sensors were among the first micro-electro-mechanical-systems (MEMS) devices [426]. The first silicon piezoresistive device, i.e., a diffused piezoresistive pressure sensing diaphragm, was realized by Tufte et al. in 1962 [437]. Piezoresistive sensors were the first commercial devices that emerged in the 1980's [438]. Later, developments in silicon processing and modeling for the integrated circuits (IC) industry allowed significant improvements in sensitivity, resolution, bandwidth, and miniaturization of piezoresistive devices [439]. Detailed history of the piezoresistive effect can be found in the review article written by Barlian et al. [426].

When it comes to low-dimensional binary oxides, e.g., ZnO, great emphasis has been laid on the piezoelectric effect in nanostructures with a Schottky contact, as reviewed in the last section (Section 6.1). Essentially, in semiconductors with a non-centrosymmetric crystal structure, both the piezoelectric effect and the piezoresistive effect exist when measured with a Schottky contact. Based on four-point measurements, Zhu and Yang separated both effects and found that the resistivity in ZnO nanowires decreases due to tensile strains [440]. By using a focused ion beam (FIB) to deposit Pt electrodes, Han et al. achieved ohmic contacts in ZnO nanowires and reported that up to a 113% increase in conductance can be induced by bending [441].

Recently, Wang et al. studied the effect of elastic strain on the electrical resistivity of ZnO nanowires with different sizes and cross-sectional morphologies [442]. Fig. 9a shows the corresponding mechanoelectrical testing device for ZnO nanowires. Perfect ohmic contacts were achieved by ion-beam Pt deposition, as shown in Fig. 9b. Schottky contacts fabricated by e-beam Pt deposition were also studied for

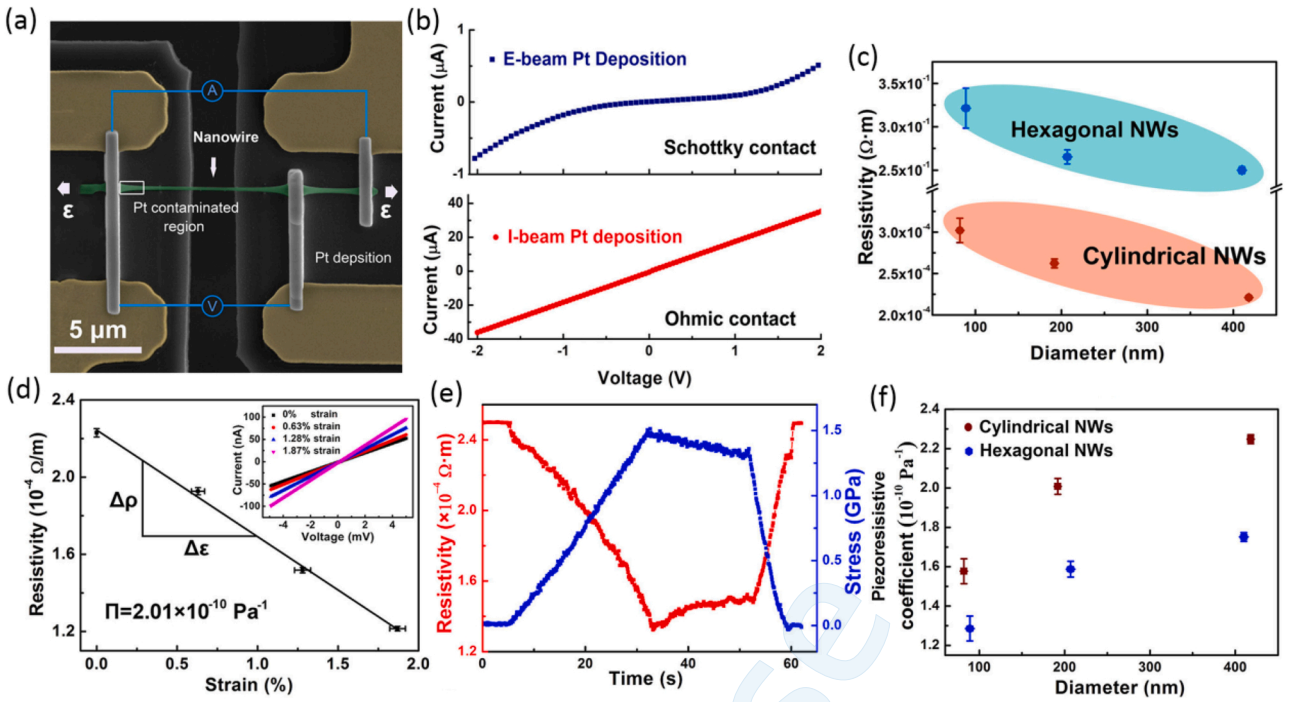

Fig. 9. Piezoresistivity in ZnO nanowires [442]. Experimental setup (a) and electrical measurement (b) of individual ZnO nanowires. Good ohmic contacts were secured and retained, excluding the piezoelectric effect. (c) Electrical resistivity of cylindrical and hexagonal ZnO nanowires with different diameters without any intentionally applied strain. (d) Effect of uniaxial tensile strain on the resistivity of a cylindrical ZnO nanowire. (e) Real-time resistivity response under applied stress. (f) Piezoresistive coefficient of both types of nanowires with different sizes. The piezoresistive coefficient of cylindrical nanowires is generally higher than that of hexagonal ones. Reprinted by permission of American Chemical Society.

comparison to exclude the piezoelectric effect. The contact made by ion-beam Pt deposition exhibited superior performance probably due to increased tunneling across the Schottky barrier caused by high energy Ga ions injected on the surface [443]. Fig. 9c shows the size dependence of the resistivity of ZnO nanowires and it can be seen that a much higher resistivity was observed in hexagonal nanowires than cylindrical ones with a similar sample diameter. The effect of elastic strain on the electrical resistivity of a cylindrical ZnO nanowire is illustrated in Fig. 9d. With increasing tensile strain, the resistivity shows a linear drop with a piezoresistive coefficient of 2.01×10^{-10} Pa^{-1}. Fig. 9e and f show the real-time resistivity response under an applied stress and the piezoresistive coefficient of both types of nanowires with different sizes, respectively. It can be found that the piezoresistive coefficient of cylindrical nanowires is generally higher than that of hexagonal ones. Both types of nanowires shown in Fig. 9c and f show similar trends, i.e., the piezoresistive coefficient increases and the resistivity decreases as the diameter increases [231].

In addition to nanowires, piezoresistivity in ZnO thin films [444] and Al-doped ZnO-polydimethylsiloxane nanocomposites [445] have also been reported. Based on the piezoresistive effect in ZnO, piezoresistive sensors have been fabricated, e.g., a poly(3,4-ethylenedioxythiophene) polystyrene sulfonate (PEDOT:PSS)/$Zn_{0.85}Mn_{0.15}O$ Schottky diode based piezoresistive sensor with high pressure sensitivity and a fast response [446], and an Al-doped ZnO thin-film transistor based strain sensor with high deflection sensitivity [447].

Piezoresistivity has also been reported in other binary oxides. Li et al. fabricated an ultrasensitive tactile sensor based on free standing VO_2 nanomembranes, exhibiting giant electrical responses to external strains [448]. Cao et al. reported a significant change in resistance in M1, M2 and R phases of VO_2 microbeams at different strain states [449]. The metal-insulator transition in VO_2 will be reviewed in detail in Section 6.5. In the M2 phase of VO_2 nanowires, Sedlmayr et al. reported a strong piezoresistive effect with an increase in resistivity of 51% per 1% of strain [450]. Onuma et al. reported in 1998 that the piezoresistive property of polycrystalline SnO_2 films is comparable to that of polycrystalline Si thin films [451]. Recently, Sakurai et al. reported a reversible and nonvolatile semiconductor-insulator transition in SnO_2 microrods under an applied mechanical strain resulting from lattice defects induced by the strain [452]. In low-dimensional monolayer MoO_3, DFT calculations suggested a profound piezoresistive effect due to an elastic strain effect on bandgap modulation [453]. Later, Wen et al. experimentally reported presence of significant piezoresistivity in MoO_3 nanobelts and its application in strain-enhanced oxygen sensors [454]. The piezoresistive effect has been found in Cu_2O/CuO nanorods as well and has been shown to enhance their photocatalytic property [455].

Strain sensitivity is an essential phenomenon for nanoscale device applications since intrinsic strain can exist in most low-dimensional materials [456]. The underlying mechanism of the piezoresistive effect in low-dimensional materials, particularly in binary oxides, requires further systematic theoretical study. When the sample size is beyond the range of quantum confinement, the intrinsic band structure and the surface state contribute to the enhancement of the piezoresistive coefficient. However, for low-dimensional materials at the sub-10 nm scale, the quantum confinement effect may play a substantial role and affect the corresponding piezoresistive effect. Due to the presence of both quantum confinement effect and an effect from the surface state in low-dimensional materials, a giant piezoresistive effect might be observed.

6.3. *Piezotronic and piezo-phototronic effect*

The piezotronic effect can be defined as the use of inner crystal piezoelectric potential (piezopotential) as a “gate” voltage to tune or control charge carrier transport properties in a piezoelectric material-based device. The piezotronic effect has triggered numerous studies ever since its discovery in 2006 [67]. The term ‘piezotronics’ refers to electronics that harvest the piezotronic effect and have applications in strain/force/pressure triggered/controlled electronic devices, sensors

and logic units [457]. The fundamental principle of piezotronics was first introduced by Prof. Zhong Lin Wang in 2007 [458]. Wurtzite and zinc blende structured semiconductors with piezoelectric properties, e.g., ZnO, GaN, InN, ZnS, CdS and CdSe, have attracted immense attention since they exhibit the piezotronic effect and have potential in enabling novel applications for sensors [459,460], transistors [461], electronics [462], optoelectronics [463–465], smart MEMS [466] and human-machine interfacing [467].

The theory of charge transport in piezotronic devices has been investigated and numerical calculations have been performed for predicting the current-voltage characteristics of a general piezotronic transistor i.e., a metal-ZnO nanowire-metal device [468]. As can be seen in Fig. 10a, the piezotronic effect is observed when the gate voltage that controls the channel length in metal-oxide-semiconductor (MOS) FET is replaced by a piezopotential that controls transport across the metal-semiconductor (M-S) interface. Fig. 10b and c show the ideal models of charge, electric field and energy distributions of piezoelectric M-S Schottky contacts and p-n junctions. Band structure engineering at heterojunction interfaces, an important aspect of piezotronics, has been summarized by Shi et al. [469].

The piezo-phototronic effect results from a three-way coupling among piezoelectricity, photonic excitation and semiconductor transport. In the piezo-phototronic effect, strain induced piezopotential can tune and control electro-optical processes [8, 458,470]. The fundamental theory of piezo-phototronics, especially for light-emitting diodes (LEDs) [471], nanoLEDs [472], and photodetectors [473], has been intensively studied by Wang's group, and has been reviewed by Liu et al. [470]. Based on analytical calculations and numerical simulations, Liu et al. have proposed that piezoelectric polarization charges can induce a change in the Schottky barrier height, the depletion region shift and/or the formation of a charge channel, hence effectively enhancing the efficiency of LEDs, solar cells and photon detectors [470]. Many review articles are available in literature on piezotronics [8,468,474–476] and piezo-phototronics [9,17,457,470,477,478].

Devices based on the piezotronic and piezo-phototronic effect can be categorized into several representative heterojunction systems based on their different interfacial band structures engineered by the remnant piezopotential. These include the metal-piezoelectric semiconductor system (Schottky contact), the semiconductor-piezoelectric semiconductor system (p-n junction and other heterogeneous semiconductor interfaces), and the electrolyte-piezoelectric semiconductor system.

6.3.1. *M-S Schottky contact*

The M-S contact is a fundamental construction in semiconductor-based electronics and optoelectronics [479]. The piezotronic and piezo-phototronic effect in devices with a Schottky contact formed between a metal and a semiconductor are of high interest [477]. Strain-induced piezoelectric polarization charges present in the vicinity of a local Schottky contact in piezoelectric semiconductors can effectively modulate the Schottky barrier height (SBH) and thereby tune or control the transport properties of the device [457,480,481].

In 2010, Yang et al. found an asymmetric change in the *I-V* curve of a single ZnO micro/nanowire metal-semiconductor-metal (MSM) photodetector when external strains were applied [464]. The authors observed an enhancement in performance of this photodetector under compressive strain. This observation has proved to be one of the most important criteria to distinguish the contribution of the piezo-phototronic effect from non-polarity factors [482] in further investigations [483,484]. A theoretical model for describing the characteristics of a metal-nanowire-metal structured piezo-phototronic photodetector has been constructed by Liu et al., fitting well to the experimental results of a CdS-based visible detector and a ZnO-based UV detector [473]. Han et al. have reported that by introducing the piezo-phototronic effect, the performance of a large array of Schottky UV photodetectors, based on vertically aligned ZnO nanowires, can be enhanced up to seven times in photoresponsivity, six times in sensitivity, and 2.8 times in the detection limit [485]. Zhang et al. have reported a similar enhancement of photo response in ZnO nanorods-based photodetector [486].

In addition to photodetectors, the performance of sensors with a Schottky contact can also be enhanced by the piezotronic effect, e.g., a ZnO nanowire-based strain sensor reported by Zhou et al. [398], a ZnO thin film-based UV sensor reported by Wen et al. [487], a ZnO nanowire-based protein sensor reported by Yu et al. [460], a flexible oxygen sensor based on an individual ZnO nanowire reported by Niu et al. [459], a ZnO micro/nanowire-based pH sensor et al. [488], a strain sensor based on tunneling junction Ag/HfO_2/n-ZnO [489], H_2/NO_2 gas sensors based on ZnO micro/nanowires reported by Zhou et al. [490] and DNA sensors based on a Schottky-contacted ZnO nanowire reported by Cao et al. [491]. Fig. 11a shows that the sensitivity (change of current) of an oxygen sensor based on a ZnO nanowire can be enhanced by increasing the tensile strain. The working mechanism of this flexible oxygen sensor can be understood by considering the piezoelectric

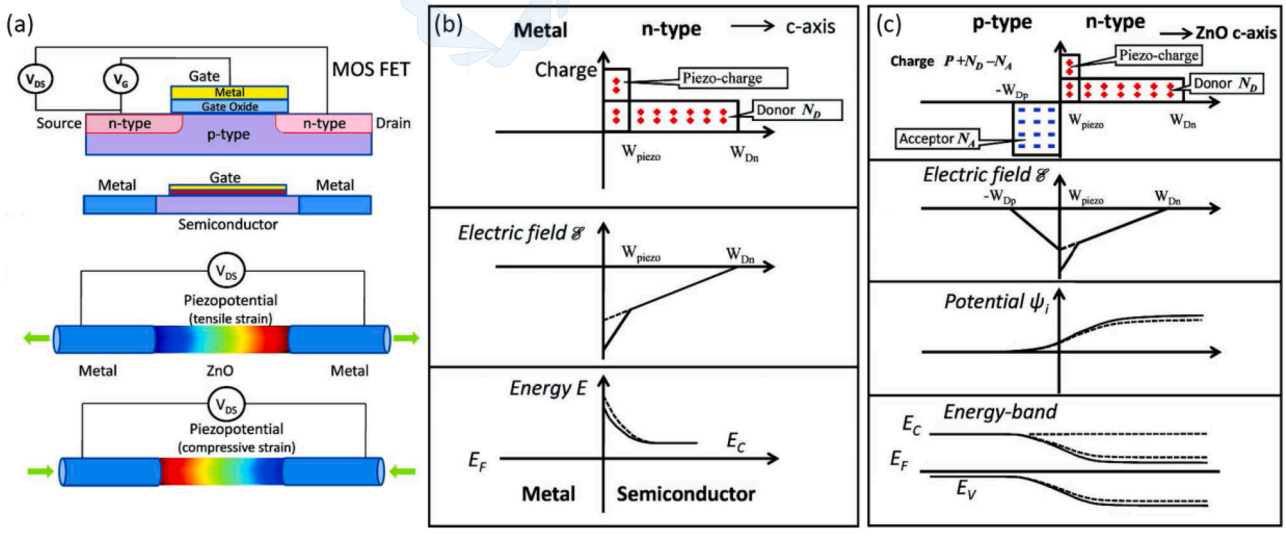

Fig. 10. Fundamental theory of piezotronics [468]. (a) Schematic of an n-channel MOS FET, a semiconductor nanowire FET, and a piezotronic transistor with a tensile strain and a compressive strain, illustrating the piezotronic effect when the gate voltage that controls the channel length is replaced by a piezopotential that controls transport across the M-S interface. (b,c) Charge (top), electric field (middle) and energy (bottom) distributions in an ideal piezoelectric M-S Schottky contact (b) and a p-n junction (c). Reprinted by permission of WILEY-VCH.

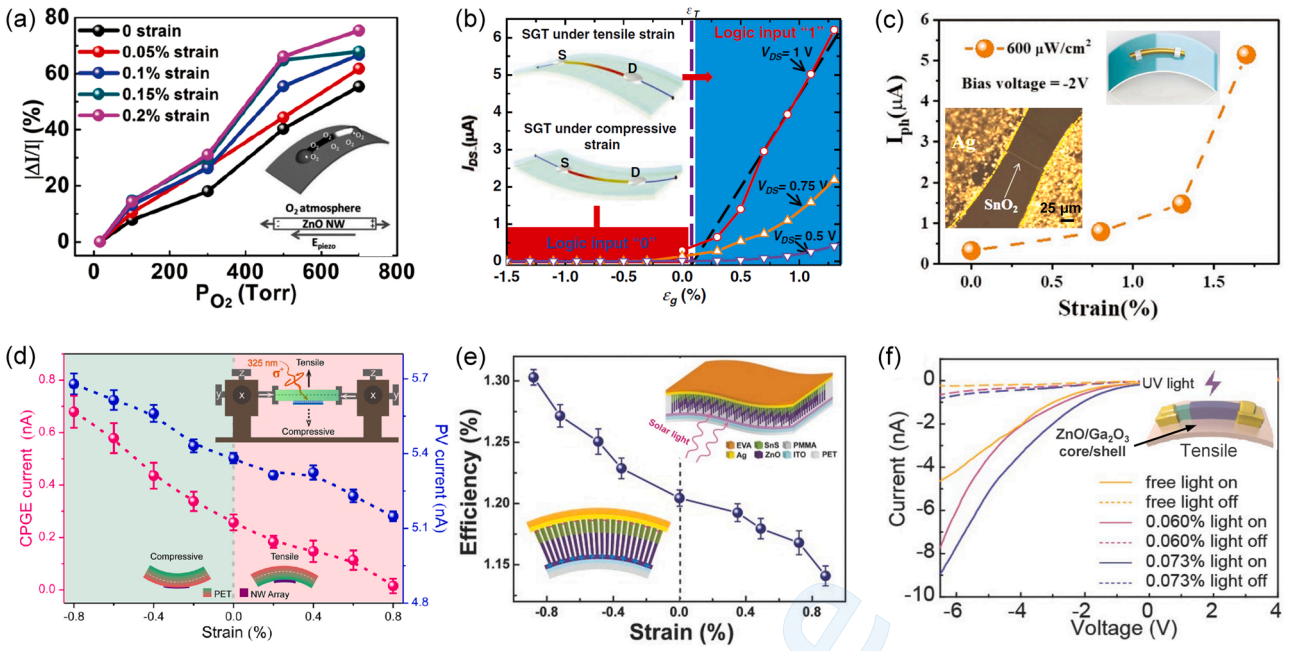

Fig. 11. The piezotronic effect in M-S Schottky contacts (a—c) and the piezo-phototronic effect in heterojunctions (d—f). (a) An individual ZnO nanowire-based oxygen sensor (insets) exhibiting improved device performance (change of current) due to the piezotronic effect [459]. (b) A single ZnO nanowire-based SGT showing that a gating effect is produced by the piezotronic effect [466]. Insets show schematics of the SGT under compressive and tensile strains. (c) Piezo-phototronic effect in a single SnO_2 microwire-based device. Insets show the device structure (top) and an optical image of the device (bottom-right) [191]. (d) A ZnO/P3HT nanowire array structure (top right inset) showing that the CPGE current and the PV current are modulated by the piezotronic effect [505]. Insets show the measurement setup (top-right) and schematics of the device under compressive and tensile strains (bottom). (e) A flexible solar cell based on n-ZnO/p-SnS core-shell nanowire array (top-right inset) showing that the cell efficiency is enhanced by the piezo-phototronic effect [509]. The bottom-left inset shows the device under a compressive strain. (f) A deep UV photodetector based on the ZnO-Ga_2O_3 core-shell heterojunction (top-right inset) showing that its performance is modulated by the piezo-phototronic effect [511]. Reprinted by permission of American Chemical Society, Wiley-VCH and Nature Publishing Group.

polarization charges induced by a tensile strain in the nanowire which attract free electrons towards the M-S interface and decrease the SBHs at both contacts [459]. A similar working mechanism was reported in a ZnO thin film-based UV sensor [487]. When the thickness of ZnO decreases to an atomic scale, e.g., atomically thin ZnO sheets reported by Wang et al., the strain sensitivity can be greatly enhanced [492].

Similar enhancement in performance has been found in devices based on strain gated transistors (SGT) [461, 493–495]. The first mechanical-electronic logic device triggered by piezoelectricity [466] (Fig. 11b) and first resistive switching device [496] based on piezotronic ZnO nanowires have been reported. Fig. 11b shows a gating effect of the logic operations in response to an input strain in the ZnO nanowire SGT and schematic illustrations of the transistor (insets) modulated by the piezoelectric effect. Besides ZnO, the piezo-phototronic effect has been observed in a single SnO_2 microwire-based device [191]. Fig. 11c shows that the photocurrent of the SnO_2 device increases more than one order of magnitude with a strain of 1.7 %.

6.3.2. *p-n junction/heterojunction*

The p-n junction has been widely applied in optoelectronic devices including LEDs [484], solar cells [463,497] and photodetectors [498]. Energy bands at the p-n junction can be tuned by the strain-induced piezoelectric polarization charges as well, thereby effectively controlling the generation, separation, recombination and transport of photo-induced charge carriers at the local hetero-/homojunction of optoelectronic devices [457].

The piezo-phototronic effect has been found to remarkably enhance the light emission intensity of several devices including a n-ZnO nanofilm/p-Si micropillar heterostructure LED array [499], a flexible LED array composed of PEDOT:PSS and patterned ZnO nanowires [467], a pressure-sensitive Si/ZnO nanowires heterostructure matrix LED array [500] and a single n-ZnO nanowire/p-GaN LED [501,502]. It can also enhance the emission efficiency of a hybridized inorganic/organic LED based on a ZnO nanowire/p-polymer structure [503]. A mechanical signal can be recorded by optical means, suggesting the potential application of the piezo-phototronic effect in biological sciences, human-machine interfacing and smart sensors [501].

In solar cells, the piezo-phototronic effect can be used to enhance device performance as has been demonstrated in a flexible heterojunction ZnO/poly(3- hexylthiophene) (P3HT) solar cell (Fig. 11d) [463, 504–506], a flexible ZnO/$CH_3NH_3PbI_3$ perovskite solar cell [507], a Si/ZnO solar cell [508] and a flexible solar cell based on n-ZnO/p-SnS core-shell nanowire array (Fig. 11e) [509]. Fig. 11d shows that a strong Rashba spin-orbit coupling can be induced by the structure inversion asymmetry of the ZnO/P3HT heterointerface and both the circular photogalvanic effect (CPGE) current and the photovoltaic (PV) current in the nanowire array structure increase with decreasing strain, revealing the piezotronic effect [505]. Fig. 11e shows a similar effect in a flexible solar cell based on a n-ZnO/p-SnS core-shell nanowire array (insets of Fig. 11e), which exhibits enhanced efficiency under compressive strain [509].

The piezotronic effect has also been observed in photodetectors, e.g., a p-Si/ZnO nanowires hybridized photodetector [498], a MoS_2- and ZnO-based heterojunction p-n photodiode [510], deep UV photodetectors based on a ZnO-Ga_2O_3 heterojunction (inset of Fig. 11f) [511] and ZnO/ZnS core/shell nanowires [512–514], and a ultraviolet-visible-near infrared (UV-Vis-NIR) photodetector based on a p-ZnO/Al_2O_3/n-Si structure [515]. Fig. 11f shows remarkable enhancement of sensitivity (current on-off ratio) in the ZnO-Ga_2O_3 deep UV photodetector under tensile strain [511]. Additionally, couplings of the piezotronic and piezophototronic effect with a magnetic field (i.e., the piezo-magnetotronic and piezo-photomagnetotronic effect) have also been observed, for example, in ZnO/Co_3O_4 core/shell heterojunction nanowire arrays [516].

6.3.3. Electrolyte-semiconductor contact for catalysis

The interface between an electrolyte and a piezoelectric semiconductor is important in many energy conversion and storage systems [517]. The impact of elastic strain and the piezotronic effect on interface energetics can determine the redox reaction favored at the interface. For instance, experiments have shown evolution of H_2 and O_2 from mechanically agitated piezoelectric $BaTiO_3$ and ZnO microstructures [518] and single-crystalline $Pb(Mg1/3Nb2/3)O_3$-$32PbTiO_3$ [519] in an aqueous sonication bath. Using a piezoelectric ZnO thin film as a photoanode in a photoelectrochemical (PEC) cell, Shi et al. investigated barrier-height engineering by the piezotronic effect and found an increase (decrease) in the photocurrent by a fixed amount under a constant tensile (compressive) strain [415]. Fig. 12a shows the schematic setup of a ZnO-based PEC cell for characterizing water splitting reactions. The *I-V* curves of the cell with and without strain, and the band diagram of the entire PEC system (indium tin oxide (ITO)/ZnO in the dashed ellipse) are shown in Fig. 12b and c, respectively. Under a static tensile or compressive strain, the barrier height changed by ~1.5 mV per 0.1 % strain and the PEC performance improved by ~5 % per 0.1 % tensile strain, as illustrated in Fig. 12d and e, respectively.

By assembling TiO_2 nanoparticles on ZnO monocrystalline nanoplatelets, Wang et al. developed effective piezoelectric semiconductor based hybrid photocatalysts and the piezotronic effect significantly enhanced the photocatalytic performance [520]. Fig. 12f shows the schematics of ZnO/TiO_2 hybrid photocatalysts with and without strain and the simulated potential distribution. Fig. 12g—i illustrate the working mechanism, i.e., band diagrams of the ZnO/TiO_2 heterojunction without (g) and with (h, i) strain via the piezotronic effect. The photogenerated electrons and holes can be effectively separated by strain at the heterojunction interface, i.e., the piezotronic effect, thereby continuously enhancing the photocatalytic performance and providing a strategy for high-performance photocatalysis applications [520]. Similarly, in direct Z-scheme ZnO-WO_{3-x} nanorod arrays and CuS/ZnO nanowires, the photocatalytic efficiencies are enhanced by the piezotronic effect of ZnO, as reported by Chen et al. [521] and Hong et al. [522], respectively.

6.3.4. Challenges and opportunities

The impacts of strain to the performance of electronic and optoelectronic devices, such as LEDs, solar cells, photosensors/photodetectors and PEC cells, have been demonstrated to be significant. By applying a strain of less than 1 %, one can tune the efficiency or power of the devices by up to a few times. If one can extend the laboratory demonstrated concept into large scale systems, these progresses may be harnessed for practical applications.

Although tremendous theoretical and experimental advancements have been made, a systematic and comprehensive understanding of piezotronics and piezo-phototronics and their full potential applications is still necessary. When the size of piezoelectric semiconductors reaches the atomically thin limit, the quantum confinement effect should be considered in existing models of piezotronics and piezo-phototronics. As mentioned in Section 6.1, many low-dimensional binary oxides other than ZnO, e.g., CdO, MgO, TiO_2, ZrO_2, exhibit comparable or better piezoelectric properties. Thus, exploring their piezotronic and piezo-phototronic properties might be a new promising direction for future research.

6.4. Ferroelectricity

Ferroelectricity, used in analogy to ferromagnetism, is a characteristic of particular materials that have a spontaneous and reversible electric polarization [523]. Ferroelectricity was first discovered in Rochelle salt by Valasek in the early 1920s [524]. It has been widely studied for various applications including MEMS, radiofrequency identification (RFID) chips, and semiconductor memory devices [391,525].

Most ferroelectric thin films are perovskite structured materials [526], e.g., PZT [527], $SrBi_2Ta_2O_9$ (SBT) [528], $BaTiO_3$ [178,529] and $SrTiO_3$ [18]. Elastic strain engineering of the perovskite ferroelectric oxides has been well summarized in many review articles [10,19,530,531]. However, these conventional perovskite ferroelectric materials suffer from poor compatibility with silicon technology and CMOS integration. The scaling issue for application of ferroelectric random-access memory (FeRAM) based on perovskite ferroelectric materials is an example of their drawbacks. However, simple binary oxides with

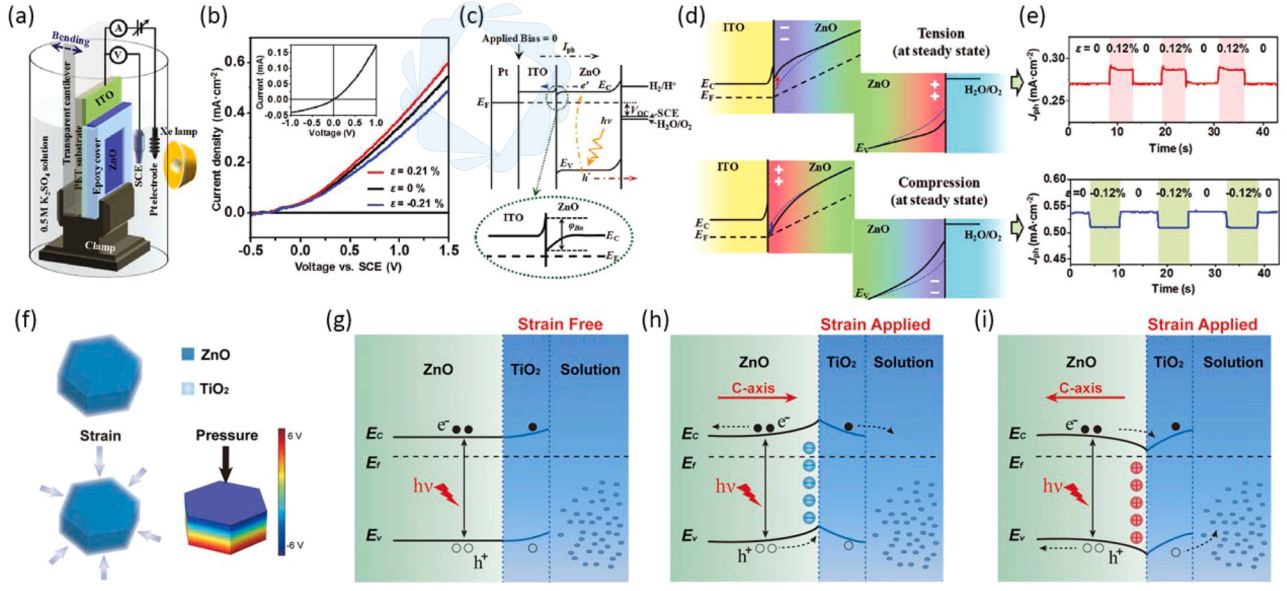

Fig. 12. Piezotronic effect in electrolyte-semiconductor contact for catalysis in ZnO. (a) Schematic setup of a ZnO-based PEC cell for characterizing water splitting reactions. (b) *I-V* curves of the cell with and without strain. (c) Band diagram of the entire PEC system. The schematic in the dashed ellipse shows the detailed band alignment of the ITO/ZnO interface. A Schottky barrier-like n-n junction is formed due to the slightly large work function of ZnO. (d,e) Piezotronic effect on the interface barrier height (d) and photocurrent (e) in the ZnO-based PEC cell [415]. (f—i) Piezotronics and the working mechanism of ZnO/TiO_2 hybrid photocatalysts [520]. (f) Schematics of ZnO/TiO_2 hybrid photocatalysts with and without strain and the simulated potential distribution. (g—i) Band diagrams of the ZnO/TiO_2 heterojunction without (g) and with (h, i) strain via the piezotronic effect. Reprinted by permission of American Chemical Society.

ferroelectric properties have excellent compatibility with silicon technology and are well suited for applications in ferroelectric FETs and capacitors [532–534]. In 2011, Böscke observed ferroelectric behavior in SiO_2-doped HfO_2 thin film [535]. Since then, HfO_2 and its analog ZrO_2 have received a flurry of interest from the ferroelectric community [65, 536]. Ferroelectricity or antiferroelectricity can exist in a wide spectrum of HfO_2-based thin films, such as undoped [537], Si-doped [535], Zr-doped [65,538] and Al-doped HfO_2 [539] as well as Hf doped ZrO_2 [65,538].

Epitaxial strain has often been employed in epitaxial thin films to achieve desired phases and corresponding properties. Analogous to the observation of ferroelectricity in $SrTiO_3$ [18] and $BaTiO_3$ [178] epitaxial thin films under biaxial tensile strain, epitaxial strain may induce ferroelectricity in simple binary oxides as well. ZrO_2 exhibits four experimentally reported phases, as shown in Fig. 13a, among which the orthorhombic ($Pca2_1$) phase, corresponding to a distortion of the high-symmetry cubic phase, is the polar phase [540]. Ferroelectricity in ZrO_2 (or HfO_2) can be achieved by stabilization of this orthorhombic phase via strain engineering.

Müller et al. discovered a field-driven and temperature-dependent ferroelectric phase transition in sub 10 nm pure ZrO_2 thin films and Zr rich HfO_2 $-ZrO_2$ mixed oxides [65]. Fig. 13b shows the polarization−voltage and capacitance−voltage hysteresis for monoclinic HfO_2, orthorhombic HfO_2 $-ZrO_2$ and tetragonal ZrO_2 based metal−insulator−metal capacitors, revealing the stabilization of the composition-dependent ferroelectric phase. Along with temperature dependence of the ferroelectric phase transition, the authors attributed these unusual findings to a size-driven tetragonal to orthorhombic phase transition. The temperature of this phase transition was lowered to room temperature in the sub 10 nm thin films. This size effect on phase transition is also frequently observed in ZrO_2 nanoparticles due to a decrease in their surface strain energy with decreasing size [541,542]. Recently, Bi et al. reported their research on a strained $Hf_{0.5}Zr_{0.5}O_2$ film grown on a highly doped GaN substrate, indicating that interfacial strain plays a key role in the origin of ferroelectricity in the $Hf_{0.5}Zr_{0.5}O_2$ film [543]. Estandía et al. reported that the lattice strain of the epitaxial $La_{0.67}Sr_{0.33}MnO_3$ electrode is critical in the stabilization of the orthorhombic phase of $Hf_{0.5}Zr_{0.5}O_2$ [544]. Cheema reported enhanced ferroelectricity in ultrathin (1 nm thick) $Hf_{0.8}Zr_{0.2}O_2$ film grown by atomic layer deposition on silicon [545]. Their work demonstrated the promising potential for ferroelectric applications in fluorite-structure binary oxides over perovskite-derived complex oxides.

Using DFT calculations, Reyes-Lillo et al. investigated the experimentally reported field-induced phase transition in thin-film ZrO_2 and

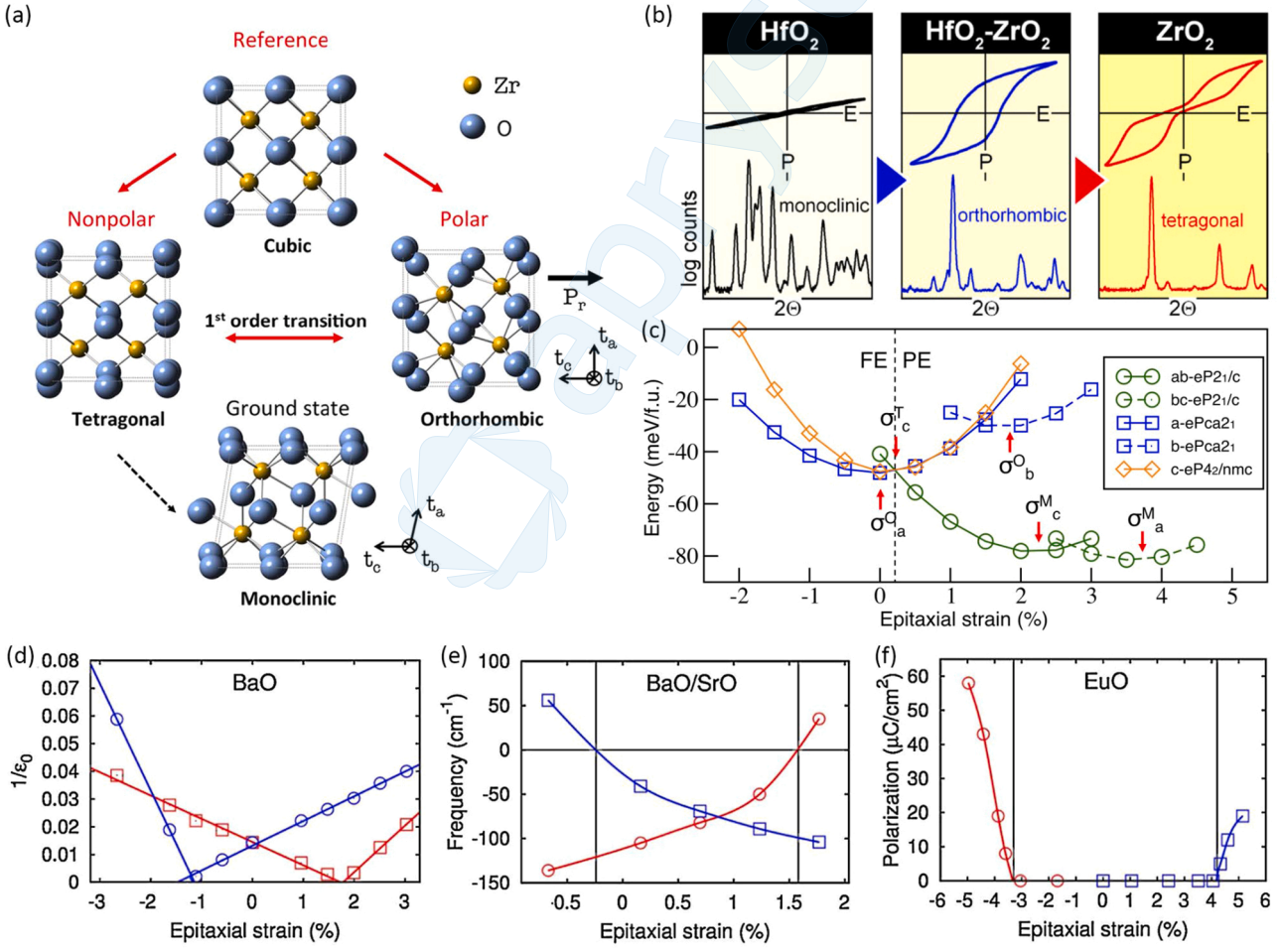

Fig. 13. Effect of elastic strain on ferroelectricity in binary oxides. (a) Unit-cell structures of experimentally reported phases of ZrO_2: cubic (*Fm*-3*m*), tetragonal ($P4_2/nmc$, nonpolar), monoclinic ($P2_1/c$, ground state), orthorhombic ($Pca2_1$, polar). (b) Evolution from paraelectric HfO_2 to ferroelectric HfO_2-ZrO_2 to antiferroelectric-like behavior in ZrO_2. (c) Phase formation energy diagram (as a function of epitaxial strain) of ZrO_2. FE and PE refer to the ferroelectric and paraelectric ground state. (d) Calculated $1/\varepsilon_0$ versus epitaxial strain in BaO ($1/\varepsilon_0^{xx}$ red squares, $1/\varepsilon_0^{zz}$ blue circles). The linear evolution of $1/\varepsilon_0$ is characteristic of a displaced ferroelectric phase transition. (e) Epitaxial strain dependence of the A_{2u} (red circles) and E_u (blue squares) modes of BaO/SrO superlattice. A ferroelectric ground state is expected. (f) Epitaxial strain dependence of the spontaneous polarization of EuO. The polarization can be stabilized with out-of-plane and in-plane orientation by a compressive and tensile epitaxial strain, respectively. Reprinted by permission of American Physical Society and American Chemical Society.
(a) and (c) are adapted from Ref. [546], (d—f) are adapted from Ref. [66], (b) is adapted from Ref. [65].

found a small energy difference between the nonpolar tetragonal and polar orthorhombic structure [546]. The authors further predicted that epitaxial strain could stabilize the ferroelectric phase of ZrO_2, suggesting an alternative stabilization mechanism other than the continuous substitution of Zr by Hf. Fig. 13c shows the calculated epitaxial strain and the energy diagram of ZrO_2 indicating that the stabilization of ferroelectricity can be expected at accessible values of compressive strain. This was experimentally demonstrated by Fan et al. who reported that an epitaxial strain, induced by the lattice mismatch between the ZrO_2 film and the TiN/MgO (001) substrate, stabilized the orthorhombic phase and ferroelectricity was achieved in the strained (111)-textured ZrO_2 film [547].

In addition to ZrO_2, using first-principles DFT calculations, Bousquet et al. predicted that an appropriate epitaxial strain could induce ferroelectricity in simple alkaline-earth-metal binary oxides such as barium oxide (BaO) [66]. Recently, Yang et al. also investigated the effect of epitaxial strain on the spontaneous polarization in alkaline-earth-metal binary oxides (MgO, CaO, SrO and BaO) using DFT calculations [548]. The authors found a linear increase in polarization for both tensile and compressive strains, with the polarization being as large as ~100 μCcm^{-2} at a compressive strain of − 8%. Similarly, using analytical calculations performed within the Landau-Ginzburg-Devonshire theory, Morozovska et al. predicted that a ferroelectric phase could be induced in otherwise non-ferroelectric binary oxides (BaO, EuO, MgO and Er_2O_3) by bending their cylindrical nanoparticles and nanowires [549]. Fig. 13d shows the calculated linear evolution of $1/\varepsilon_0$ (ε_0 is static dielectric tensor) with epitaxial strain in BaO, which is characteristic of a displaced ferroelectric phase transition temperature. Inspired by ferroelectricity in perovskite oxide superlattices [550], ferroelectric superlattices may also be constructed from alkaline-earth-metal binary oxides due to their tendency to exhibit ferroelectricity. Fig. 13e shows the calculated evolution of the A_{2u} and E_u modes of BaO/SrO superlattice with epitaxial strain, indicating that a ferroelectric ground state is expected irrespective of the epitaxial strain. In the ferromagnetic binary oxide EuO, the amplitude of polarization can reach sizable values (60 $\mu C/cm^2$ at −5.5 % of strain) with either an out-of-plane or an in-plane orientation due to both compressive and tensile epitaxial strains, as illustrated in Fig. 13 f. Djermouni et al. also investigated strain effects on ferromagnetism and ferroelectricity in EuO by using DFT+U-based first principles calculations and presented similar predictions i.e., a spontaneous polarization of the order of P_s(EuO) = 57.50 $\mu C/cm^2$ with a strain of 5 % [551]. Recently, by using infrared reflectance spectroscopy, Goian et al. provided experimental indications of the ferroelectric phase induced by epitaxial tensile strain (6.4 %) in EuO [210].

The excellent compatibility of simple binary oxides with silicon technology makes them highly attractive for commercial applications in devices. However, most binary oxides are expected to exhibit a centrosymmetric crystal structure and therewith a linear dielectric characteristic at room temperature. Nevertheless, the ferroelectric phase can be stabilized by elastic strain engineering, as reviewed above for ZrO_2. As predicted by theoretical calculations, the realization of ferroelectricity in other binary oxides can be possible with a large epitaxial strain. Additionally, further experimental and theoretical studies of ferroelectric nanowires and nanocrystals of binary oxides, which have strain states different from thin films, are also necessary for a more complete exploration of strain-dependent ferroelectricity in binary oxides.

6.5. Metal-insulator transition

Metal-insulator transition is a phase transition that is accompanied by a huge resistivity change in many condensed-matter systems. The early theoretical description of metals and insulators was based on the filling of electronic bands while neglecting electron interactions, i.e., bands are partially filled in a metal while completely filled in an insulator. However, the classic band picture cannot explain the poor conduction in many transition-metal oxides with a partially filled *d*-electron band, as reported by de Boer and Verwey in 1937 [552]. The insulating behavior may be attributed to strong Coulombic repulsion between electrons (electron-electron correlation), as stated by Mott and Peierls in the same year [553]. Since then, great efforts and much progress have been made in both experimental and theoretical studies to understand the metal-insulator transition in such strongly correlated electronic systems [554]. In particular, transition-metal oxides were extensively studied in the early years [555] and have regained interest in recent decades due to remarkable discoveries of colossal magnetoresistance in manganites [556] and high-temperature superconductivity in cuprates [557].

Among transition-metal oxides, VO_2 is a typical example that undergoes a first-order metal-insulator transition at 341 K with a change in conductivity by several orders of magnitude [558]. The metal-insulator transition in VO_2 is accompanied by a structural phase transition from the high-temperature tetragonal phase to the low-temperature monoclinic phase and an abrupt change in the lattice constant of about 1% along the tetragonal *c*-axis [559]. Thus, a tensile or compressive elastic strain along the tetragonal *c*-axis can drive the transition from metal to insulator or insulator to metal [56]. Here, we mainly focus on the effect of elastic strain on the metal-insulator transition in VO_2 in this section.

6.5.1. Mechanism of metal-insulator transition

The mechanism of metal-insulator transition in VO_2, i.e., whether the transition is of a Mott (electron-electron correlation) [560] or a Peierls (electron-lattice interaction) [561] type, has been long debated [562–564]. The low-temperature insulating phase of VO_2 is not a conventional Mott insulator and should be considered as a Peierls-Mott insulator wherein both electron-electron and electron-lattice interactions can contribute to the opening of an insulating band gap. Based on cluster dynamical mean-field theory, Biermann et al. found that the dimerization of vanadium atoms due to strong Coulomb correlations plays a crucial role for the opening of a Peierls gap in the metal-insulator transition of VO_2 [565]. Using soft-X-ray absorption spectroscopy, Haverkort reported direct experimental evidence for orbital switching in the V 3*d* states during the metal-insulator transition, suggesting an orbital-driven Peierls-like transition [566]. A giant transfer of spectral weight across the metal-insulator transition in VO_2 single crystals was observed by Koethe et al., signaling that the transition is neither of the standard Peierls nor the single-band Mott type [567].

Taking moderate values of strain into account, Aetukuri recently reported that in the metallic phase of strained VO_2 thin films, orbital occupations triggered the transition and the T_{MIT} (transition temperature) varied with over a range of 60 K, while orbital occupations in the insulating state changed little with strain, indicating the importance of orbital occupancy in the metallic state of VO_2 in governing the metal-insulator transition [329]. A similar metal-insulator transition induced by orbital-driven Peierls state with tetramer ordering was suggested in spinals, such as $CuIr_2S_4$, $MgTi_2O_4$ and $NaTiO_2$ [568], and experimentally observed in Fe_3O_4 [569]. In addition, using a combination of soft X-ray spectroscopies, Laverock et al. showed that electron-lattice interaction was involved in the metal-insulator transition of moderately strained VO_2 and revealed strain dependence of the V-O hybridization that was not anticipated by the band theory [570].

However, in highly strained VO_2 films, the T_{MIT} and some of the electronic interband transitions differ substantially from bulk values, while the lattice dynamics remain largely unchanged, highlighting the important role of electronic correlations in driving the metal-insulator transition [571]. The epitaxial strain in VO_2/TiO_2 films can suppress the structural phase transition in a temperature range in the vicinity of the metal-insulator transition [572] and modulate the electron correlation effects inducing an orbital selective Mott transition [573], suggesting that an electronic transition triggers the metal-insulator transition. Using spectromicroscopy, Laverock et al. observed that periodic modulations in both crystal symmetry and V-V dimerization occur

near the metal-insulator transition of strained VO_2, while a homogeneous conductivity transition occurs within a narrow temperature range, supporting the effect of the strong electron correlation on the metal-insulator transition [574]. In an epitaxial bilayer on a TiO_2 (001) substrate, consisting of slightly oxygen-deficient $VO_{2-\delta}$ and stoichiometric VO_2 layers, Lee et al. demonstrated an isostructural, purely electronically driven metal-insulator transition in VO_2 [575].

In single-domain VO_2 nanobeams, an equilibrium carrier density and an activation energy corresponding to an optical gap in the insulating phase were observed, indicating that electron-electron interactions play a driving role in the metal-insulator transition [576]. From a theoretical point of view, by using cluster-dynamic mean field theory calculations, Lazarovits et al. studied the elastic strain effect on the electronic structure of VO_2 in both the metal and the insulator phase. The authors found that the increase of bandwidth induced by compressive strain along the rutile *c*-axis was more important for the metal-insulator transition than the Peierls bonding-antibonding splitting [577]. Later, the same group presented a photoemission spectroscopic study and observed a crossover from Peierls- to Mott-like transitions with increasing compressive strain along the rutile *c*-axis. Thus, the Mott type transition appears to be the dominant mechanism in the highly strained VO_2. Additionally, experimental evidence has shown that excited carrier density in the insulator phase of VO_2 plays an important role when the metal-insulator transition is induced optically [292,578,579]. The effect of elastic strain on the metal-insulator transition of VO_2 is further reviewed in the next sections.

6.5.2. *Metal-insulator transition in strained VO_2 thin films*

Elastic strain plays a fundamental role in the metal-insulator transition behavior of VO_2. In VO_2 thin films, epitaxial elastic strain is given by

$$\varepsilon_{\mathrm{EPI}} = \frac{d_f - d_b}{d_b} \times 100\% \tag{8}$$

where d_f is the lattice constant of the thin film and d_b is the lattice constant of the bulk counterpart. Elastic strains can be introduced in VO_2 thin films via many approaches. Compressively strained VO_2 thin films that can be grown on TiO_2 (011) [580],TiO_2 (001) [570, 581–584], quartz [571], MgF_2 [585,586], CaF_2 [281] and Ge (100) [587] have transition temperatures below that of bulk VO_2. Tensile strained VO_2 films can be grown on TiO_2 (110) [570,581], RuO_2 [588] and Al_2O_3 (001) [319,589,590], resulting in a shift of both the metal-insulator transition and the accompanying structural phase transition towards higher temperatures. Recently, Guo et al. found that the epitaxial strain of VO_2 films can be partially released by a graphene buffer layer grown on the Al_2O_3 (001) substrate thereby modifying transport characteristics of the films [591].

The epitaxial elastic strain resulting from lattice mismatch between the film and the substrate depends on film thickness. By varying the thickness of VO_2 films, different values of epitaxial strain can be introduced, modulating the metal-insulator transition behavior, i.e., large compressive (tensile) strains lead to a low (high) T_{MIT} [583,584,589, 592,593]. It is suggested that with increasing film thickness, the compressive (tensile) strain at the interface would be smaller and the T_{MIT} would be higher (lower). Based on interfacial strain dynamics determined by means of synchrotron radiation and theoretical calculations, Fan et al. claimed that the epitaxial strain in an ultrathin VO_2 film on a TiO_2 substrate strongly affects the electronic orbital occupancy and the electron-electron correlation as well, thus changing the T_{MIT} [583]. Besides, an abrupt change in T_{MIT} can be induced by epitaxial strain in ultrathin VO_2 films with a thickness of 4.1 nm on a TiO_2 (001) substrate [582]. With increasing film thickness, the domain size decreases, causing a broad metal-insulator transition behavior with respect to temperature due to increased cracks and dislocations in the domain boundary [584]. Yang et al. reported phase transformation of a (001)-VO_2/TiO_2 film from the rutile phase, i.e., the tetragonal-like phase, to the monoclinic M1 phase with increasing film thickness due to thickness-dependent epitaxial strains [593].

The epitaxial strain can be further controlled by introducing a buffer layer between the substrate and the overlying film. Aetukuri et al. reported that different epitaxial strains, induced by varying the thickness of a RuO_2 buffer layer, changed the metal-insulator transition temperature of VO_2 (001) thin films on TiO_2 substrates from ~285 to ~345 K continuously [329]. Recently, by using a TiO_2 layer as a buffer layer (similar to the RuO_2 buffer), strained VO_2 films with a metal-insulator transition temperature of ~317 K have been grown on Al_2O_3 (100) substrates [170]. It has been suggested that the metal-insulator transition behavior of VO_2 films can be effectively tuned by the specific microstructure of the TiO_2 buffer layer which in turn can be controlled by the growth parameters.

In contrast to conventional thin film epitaxy, a buffer layer with a large lattice mismatch has also been employed to modify the metal-insulator transition characteristics of VO_2. Use of a SnO_2 buffer layer with a large lattice mismatch of 4% relieved the interfacial strain energy between the VO_2 film and the TiO_2 substrate and resulted in a much sharper metal-insulator transition in VO_2 films as compared to those grown without the SnO_2 buffer layer [207]. In addition, the epitaxial strain in the highly mismatched VO_2/Al_2O_3 heterostructures can also be influenced by the surface growth mode of VO_2 thereby affecting its metal-insulator transition behavior [319]. Elastic strain engineering can also be introduced by ion implantation, enabling a 3D local manipulation of the metal-insulator transition of VO_2 films with a lateral spatial resolution of a micrometer scale [331].

In addition to the static-strain effect, the metal-insulator transition can also be influenced dynamically via a dynamic strain. Kikuzuki et al. have studied the dynamic effect of strain states on the metal-insulator transition in VO_2 thin films by using a low-frequency crystal bending stage, showing that the resistance response of the film to strain excitation is determined by the nucleation lifetime and growth lifetime of a domain but limited by the presence of grain boundaries [594]. Using a piezoelectric PMN-PT substrate, Petraru et al. have showed that the biaxial strain in VO_2 films can be tuned by simply applying an external voltage to the piezoelectric substrate, thereby lowering the T_{MIT} [279].

6.5.3. *Metal-insulator transition in strained VO_2 nanobeams*

In VO_2 epitaxial thin films, microscopic domain structures can form and affect strain distribution due to the possible presence of misfit dislocations and grain boundaries, complicating the interpretation of experimental results. Specifically in polycrystalline VO_2 films, a phase coexistence and percolation across a temperature range near T_{MIT} was observed by using scanning near-field infrared microscopy [578]. A similar effect of microscopic domain structures on the local strain distribution was also seen in VO_2 nanocrystals and larger microcrystals [595,596]. In VO_2 nanoparticles, the size or volume can significantly affect the metal-insulator transition behavior, e.g., a broadened hysteresis width is seen with a reduced volume, which can be correlated with defects such as grain boundaries and dislocations [597–600]. Fadlelmula et al. studied the effects of thickness on metal-insulator transition in freestanding VO_2 nanocrystals by using argon ion-beam milling, showing that even below a thickness of 4 nm, the metal-insulator transition persisted and the T_{MIT} decreased as the crystal got thinner [601]. Additionally, Cao et al. have shown that a uniform and continuously tunable uniaxial strain over 2% can be introduced in freestanding VO_2 beams without fracturing and the metal-insulator temperature can be effectively tuned up to the room temperature [198].

Wu et al. have observed that the resistivity in a freestanding single-crystal VO_2 nanobeam changed abruptly within a temperature range of less than 0.1 °C at the T_{MIT} [602]. Further, the authors investigated the effect of strain on the metal-insulator transition in single-crystal VO_2 nanobeams and found that fully clamped samples on a SiO_2 surface exhibited a remarkably different resistivity compared with freestanding

ones. Uniaxial strain in elastic-misfit heterostructures led to the formation of periodic metal-insulator domains near T_{MIT} [602,603]. The authors proposed that the energy of the nanobeam depends on the spatial period of the domains as

$$E(\lambda) = \frac{\lambda\epsilon}{\pi^3}\sum_{j=0}^{\infty}\frac{1-e^{-2(2j+1)\pi t/\lambda}}{(2j+1)^3}+\frac{\gamma t}{\lambda}+\frac{(f_M+f_I)t}{2} \quad (9)$$

where, λ is the spatial period of the domain pattern, $\epsilon = \frac{Y_{eff}\varepsilon_{MI}^2}{2(1-\nu^2)}$ is the volume density of the elastic misfit energy, Y_{eff} is the effective Young's modulus of the system, $\varepsilon_{MI} = \frac{\Delta c}{c} \approx 0.011$ is the elongation percentage of the c-axis of VO_2 during the metal-insulator transition, ν is the Poisson's ratio, γ is the domain wall energy per unit domain wall area, t is the nanobeam thickness and f_M and f_I are the free energy densities of the metal and insulator phases respectively. Thus, the equilibrium spatial period of domains (obtained by minimizing energy) is determined by a tradeoff between the elastic misfit energy (the first term) and the domain wall energy (the second term) with the period decreasing with an increase in the Young's modulus of the substrate. Parikh et al. proposed a similar model to determine the energy of a VO_2 nanobeam/SiO_2 substrate and obtained the fraction of the transformed phase as

$$x_M = \frac{H}{Y_{eff}\varepsilon_{MI}{}^2 T_{MIT_0}}(T-T_{MIT}) \quad (10)$$

where H is the latent heat of transition, T_{MIT_0} is the equilibrium phase transition temperature and the temperature T_{MIT} at which the phase transition starts is given by

$$T_{MIT} = \frac{\varepsilon_P\varepsilon_{MI}Y_{eff}T_{MIT_0}}{H}+T_{MIT_0} \quad (11)$$

where ε_P is the pre-strain before transition [280]. Hence, compressive (tensile) strains stabilize the metallic (insulating) phase and lower (increase) the phase transition temperature [613]. Other approaches adopted to introduce strain in VO_2 nanobeams and to thus modulate the metal-insulator transition include the misfit in VO_2/TiO_2 core/shell nanostructures [604], hydrogen doping in individual VO_2 single-crystalline nanobeams on Au-coated Si substrates [605], and controlling diameters in single-phase VO_2 wires [606]. Recently, Pendse et al. demonstrated van der Waals epitaxy and chemical epitaxy of VO_2 nanowires on h-BN and c-plane sapphire, respectively, revealing distinct metal-insulator phase transition kinetics resulting from each type growth [607].

In addition to interfacial strain, externally applied mechanical strain, tunable over a wide range of values can influence the metallic and insulating domains along single-crystal VO_2 nanobeams, and reduce the T_{MIT} to room temperature [198,576,608]. Critical stress σ_c needed to trigger a transition at T_{MIT} is given by the uniaxial Clapeyron equation [833]

$$\frac{d\sigma_c}{dT_{MIT}} = \frac{H}{\varepsilon_0 T_{MIT}}. \quad (12)$$

Considering the above experimental observations, it is necessary to understand thermodynamics of the phase transition under different strain conditions. Gu et al. constructed a phenomenological thermodynamic potential and calculated the phase diagram of VO_2 under different strain conditions, which agrees well with existing experimental data [449,581,609,610], hence emphasizing the strong dependence of T_{MIT} on the strain condition in both VO_2 films and nanobeams [611].

By using strain, Cao reported the propagation of metallic and insulating domains during the metal-insulator transition and the stress-temperature phase diagram for VO_2 [198]. In order to precisely study the phase transition experimentally in an in situ manner, Park et al. used a home-built nanomechanical strain apparatus to investigate the metal-insulator transition in single-crystal VO_2 nanobeams [264]. Recently, Shi et al. reported that single-crystalline VO_2 actuators exhibited excellent performance resulting from internally lateral and gradual strain engineering [612].

6.5.4. Strain-induced M2 phase of VO_2

In VO_2, strain can enrich the phase space and induce another monoclinic structure, the M2 phase [609]. M2 structure was widely observed in Cr-doped VO_2 [559] and Al-doped VO_2 [613] in the early days. The monoclinic M2 phase is a known Mott insulator suggesting that electron-electron interactions may play an important role in determining the mechanism of the metal-insulator transition [563,609]. Within the framework of the Ginzburg-Landau formalism, the M2 phase can appear under a small perturbation of the M1 structure induced by doping or stress [614].

In VO_2 thin films, the M2 phase has been observed when using substrates with a mismatched symmetry, e.g., Al_2O_3 (001). Strain states in these films can contribute to stabilization of the M2 phase [615,616]. In order to understand how the M2 phase can be stabilized by epitaxial strain, Quackenbush et al. studied high quality epitaxial VO_2 films on TiO_2 (001) and (100) oriented substrates [617]. The authors found that tensile strain along the c-axis of the R phase in epitaxial VO_2 films raised the T_{MIT} and indeed stabilized the intermediate monoclinic M2 phase.

In strained VO_2 nanobeams or nanowires, the M2 phase can act as a transitional structure between the M1 and the R phase during metal-insulator transition [157,198,449,596,618,619]. A strain of about 0.5–1% can induce a reversible phase transition from M1 to M2 [362,450] and in epitaxially grown single crystal VO_2 nanowires, the insulating M1 and M2 phases were seen to coexist during transition from the M1 phase to the R phase at atmospheric pressure [157]. Using electromechanical resonators, Parikh et al. dynamically tracked strain across the metal-insulator transition in a VO_2 nanobeam and the M1-M2 and M2-R phase transitions by simultaneous resistance and resonance measurements [280]. A triclinic T phase, which is a continuously distorted variant of the M1 monoclinic phase, was identified during a discontinuous transition from both the M1 and T phases into the M2 phase [619].

Doping-induced chemical strain in VO_2 nanostructures can also stabilize the monoclinic M2 phase. Strelcov reported the temperature-doping level phase diagram for freestanding VO_2 nanostructures, revealing a remarkable change of domain patterns (insets) and phases depending on the dopant (Al) concentration [620].

6.5.5. Metal-insulator transition-based devices

Based on the unique characteristics of the metal-insulator transition and properties of the various phases in low-dimensional VO_2, novel nanodevices have been fabricated, e.g., sensors and switches, as summarized in a recent review article by Liu et al. [621]. By utilizing the phase transition between M1 and M2 phases, a freestanding VO_2 nanobeam has been used to fabricate a flexible strain sensor, as reported by Hu et al. and shown in the inset of Fig. 14a [622]. A localized M2 phase is formed due to a preloaded tensile strain which in turn originates from the electrostatic interaction between the nanobeam and the plastic substrate and can be detected by Raman spectroscopy. By loading tensile and compressive strains, the phase transition between M1 and M2 phases can be tuned, as shown in the inset of Fig. 14b, resulting in a change in the resistance of the device, as illustrated in both Fig. 14a and b. The VO_2 nanobeam based device showed a high gauge factor and a fast response (not shown here) in low strain ranges suggesting its potential application as a flexible strain sensor [622]. In order to expand the application of VO_2 based nanodevices, the same group fabricated a single domain switch, as shown in the insets of Fig. 14c [623]. The metal-insulator transition in this single domain device can be tuned by coupling self-heating with external strain, exhibiting great controllability and quick switching [623]. Fig. 14c shows *I-V* curves of the device under different axial compressive strains. It can be observed that the current and threshold voltage gradually decrease with increasing compressive strain.

In addition to VO_2, strain effects on the metal-insulator transition

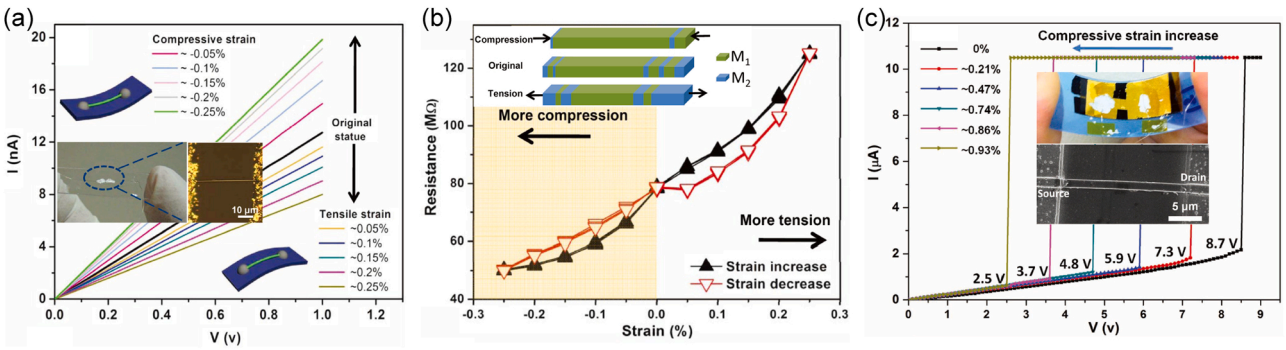

Fig. 14. Effect of elastic strain on the performance of metal-insulator transition-based devices. (a) *I-V* curves under different tensile and compressive strains in a VO_2 nanobeam-based flexible strain sensor. Insets show an as-fabricated flexible strain sensor (middle left) and schematic illustrations of the device under strain (top left and bottom right). (b) Resistance of the sensor dependent on external strain. Inset shows the transition between M1 and M2 phases in the presence of tensile and compressive strain. Insets show schematics of the domain pattern under compression, in the original state and under tension. (c) *I-V* curves of a packaged VO_2 nanobeam (insets) under different axial compressive strains. It can be seen that the current and threshold voltage decrease with increasing compressive strain. Reprinted by permission of Wiley-VCH.
(a) and (b) are adapted from Ref. [622], (c) is adapted from Ref. [623].

behavior have also been observed in other oxides. In perovskite manganite oxides, e.g., $La_{1-x-y}Pr_yCa_xMnO_3$, Ahn et al. reported that strain induced the coexistence of distinct metallic and insulating electronic phases [624]. In V_2O_3 thin films, epitaxial strains can stabilize a metallic phase when the films are grown on Al_2O_3 (0001) substrates [625], increase the T_{MIT} when the films are grown on $LiTaO_3$ (0001) substrates [626], and induce local insulating regions within a metallic phase when the films are doped with Cr [627]. In hexagonal-phase bilayers of ScO_2, using DFT calculations under the generalized-gradient approximation with on-site Coulomb interactions, Loh and Pandey theoretically reported a metal-semiconductor-metal transition under a large tensile strain [628].

Strain can play an important role in determining a structural phase transition, inducing a variation in the metal-insulator transition behavior as reviewed in the case of VO_2. New phases can also be induced under high tensile strains, e.g., the metallic monoclinic X phase of VO_2 as reported by Bai et al. [629]. However, epitaxial strains in VO_2 films or mechanically loaded tensile strains in single crystal VO_2 nanobeams are normally less than ~1 %. The abrupt change in the lattice constant of VO_2 (1 % along the tetragonal *c*-axis) during its metal-insulator transition, which can be triggered by external stimulations (e.g., temperature), may be used to generate strain in materials bonded with VO_2 leading to observation of various new phenomena [282–284]. Furthermore, the strain-related properties in rare earth metal oxides such as EuO which may also exhibit a metal-insulator transition may be explored following strain engineering strategies similar to those used in VO_2 [630].

6.6. Band gap engineering

Strain serves as a unique tool to modify the band structure and hence numerous band-gap related properties of semiconductors. The following sections illustrate strain-based band-gap engineering of various low-dimensional binary oxides.

6.6.1. PL and CL of ZnO

The band structure of low-dimensional forms of ZnO has been found to be sensitive to misfit strain as reflected in the PL and CL spectra. Makino et al. presented have comparative studies of ZnO and GaN epitaxial films grown on sapphire (0001) and demonstrated that ZnO-based quantum well structures not only show a shift in their energy levels due to the epitaxial strain but their optoelectronic properties are also largely modified due to a piezoelectric field induced by the misfit strain [631].

In individual ZnO nanowires, elastic strains can be generated by manipulating the nanowire into different shapes, e.g., L-shape and S-shape, as reported by Han et al. [271]. Fig. 15a and c show a ZnO nanowire bent into an L-shape and an S-shape, respectively. Low-temperature (81 K) CL of ZnO nanowires (both L- and S- shaped) revealed a significant reduction in bandgap due to tensile strain, as shown in Fig. 15b and d, respectively. The observed phenomenon, i.e., a reduction in bandgap by the introduction of tensile strain, was explained theoretically by both first-principles DFT and effective-mass envelope function theory calculations. Similarly, using spatially resolved low-temperature PL, Dietrich et al. studied the effect of uniaxial stress on the PL properties of ZnO microwires [632]. The authors determined maximum energy shifts of $\pm$ 30 meV corresponding to tensile and compressive strain of up to 1.5% along the *c*-axis.

In addition to elastic strain, strain gradients can also be introduced by bending ZnO nanowires. Han et al. investigated the spatial distribution of exciton spectra in bent ZnO microwires and found a significant effect of strain gradient on the energy bandgap [633]. Fig. 15e and f show the strain gradient in a bent ZnO microwire and CL spectra collected along the bent ZnO microwire on the strain-neutral middle--plane, respectively. The authors observed that the red shift of free exciton energy was proportional to the strain gradient between the region with tensile strain and the neutral region. The total red-shift at $r \geq 0$ (along the highest strain-gradient direction) was found to be

$$\Delta E = \frac{\hbar c}{a_0}\alpha\varepsilon + \hbar c\beta g \tag{13}$$

where α (<0) is the strain coefficient, $a_0 = 5.29177 \times 10^{-11}$ m is the Bohr constant, β is the coefficient of the linear strain gradient effect, $c = 1.23982$ eV·μm is the product of the Planck's constant with the speed of light and g is the constant strain gradient across the neutral plane (mid-plane) in the nanowire [633]. Later, Fu et al. reported direct observation of the dynamics of exciton transport in a ZnO microwire under a purely elastic bending strain [634]. The authors demonstrated that the gradient due to inhomogeneous strain fields effectively drifts excitons [272] and modifies electron-hole interactions as well as the fine structures of bound exciton states [635,636]. Xu et al. reported that the distribution of photon carriers may be affected by the piezoelectric field in bent ZnO nanowires, leading to a net redshift of the free exciton PL emission [637].

Along with bending and shaping, the size effect can simultaneously contribute to the elastic strain effect on PL of low-dimensional materials. Wei et al. reported that a ZnO nanowire with a diameter of 100 nm can sustain a maximum elastic strain of 7.3 % using a uniaxial tensile loading setup, as shown in the inset of Fig. 15g [152]. Combining the

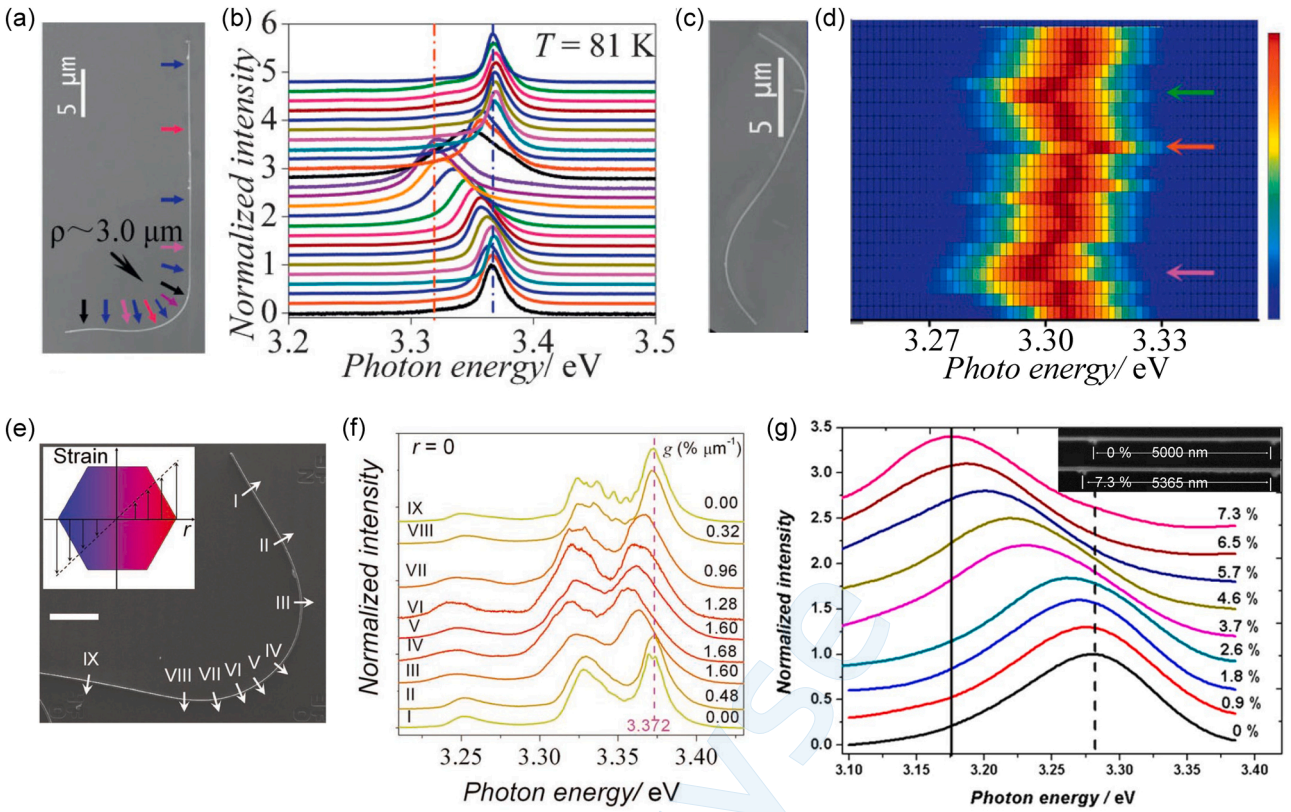

Fig. 15. Effect of elastic strain and strain gradient on the CL and PL of ZnO nanowires. (a—d) SEM images of an L-shaped (a) and an S-shaped (c) ZnO nanowire and corresponding CL spectra along the bent nanowire in (b) and (d), respectively. The colored arrows in (a) represent the measurement positions in (b). The vertical axes in (c) and (d) are consistent. A significant reduction in bandgap with strain is observed. (e,f) Strain gradient (inset of e) in a bent nanowire (e) and CL spectra collected along the bent ZnO microwire on the strain-neutral middle-plane (f) showing the effect of the strain-gradient on CL. (g) Effect of tensile strain on PL in a ZnO 100 nm nanowire. Inset shows that the tensile loading induces a maximum elastic strain of 7.3% in the nanowire. Reprinted by permission of Wiley-VCH. (a—d) are adapted from Ref. [271]. (g) are adapted from Ref. [152]. (e,f) are adapted from Ref. [633].

uniaxial tensile loading setup with a CL spectroscope, the authors quantified the effect of size of the ZnO nanowire on its energy bandgap. They observed that the critical strain, i.e., the strain at which there was a change in the slope of the energy-strain curve, moved toward a higher value with decreasing diameter of the nanowire. Fig. 15g shows the variation in the near band edge emission peaks of a 100 nm nanowire with increasing strain up to 7.3 %. This demonstrates that the size-effect contributes to the effect of strain on the energy bandgap. The authors modeled the total bandgap shift as

$$\Delta E = A_1[\varepsilon_1 - \varepsilon_c(D)] + A_2[\varepsilon_2 - \varepsilon_c(D)] \quad (14)$$

where A_1 and A_2 are the deformation potentials in low- and high-stress stages, ε_1 and ε_2 are tensile strains in low- and high-stress stages and $\varepsilon_c(D)$ is the size dependent critical strain.

Shifts in the band gap of ZnO due to elastic strain have also been theoretically investigated for the bulk, the nanowire and the monolayer forms [638–643]. Tse and Yu performed a series of computational simulations when applying a compressive or tensile strain up to 5 % on the crystal lattice, and provided a systematic explanation of the electronic and optical properties for bent ZnO nanowires [644]. Fu et al. studied the dependence of band gap deformation potential on the strain mode of ZnO micro/nanowires under both uniaxial tensile and bending strains at room temperature [645]. The authors showed that the deformation potential under uniaxial tensile strains varied between − 10.6 to − 30.6 meV/% depending on the diameter of the nanowire. For bending, the value was 27 meV/%.

6.6.2. Optical band gap of SnO_2

Similar to ZnO, effect of strain on low-dimensional SnO_2 has been widely studied. Saniz et al. theoretically calculated the effect of uniaxial strain on the band gap of SnO_2 using the GW approximation [646]. The authors pointed out that the band gap of SnO_2 increases under uniaxial compressive strain along the *c*-axis at a rate of 27 meV/GPa. Similarly, using DFT within LDA, Mounkachi et al. recently studied the effect of external pressure and internal strain on the band gap of bulk SnO_2 and SnO_2 thin films [647].

In SnO_2 epitaxial thin films, biaxial epitaxial strain is normally used to tune the band gap and optical properties. Zhou et al. experimentally observed that the optical band gap in a SnO_2 epitaxial thin film grown on an Al_2O_3 (0001) substrate significantly decreased with decreasing film thickness, i.e., with increasing biaxial tensile strain in the *bc* plane [648]. The same phenomenon, i.e., the variation of optical band gap of SnO_2 with epitaxial strain, was also reported by Rus et al. [649]. Their experimental results showed that compressive out-of-plane strain of SnO_2 films decreased with increasing film thickness, resulting in shrinking of the band gap at a rate of 0.38 eV per 1% strain.

However, band structure engineering based on epitaxial strain is severely limited by the availability of suitable substrates and the band gap can only be modified in a discrete manner. Recently, helium ion implantation into an epitaxial oxide film has been found to be an effective method that can continuously induce a single axis lattice strain along the out-of-plane lattice direction without changing the in-plane lattice constants [216]. Herklotz et al. reported that the optical band gap of the prototypical semiconducting oxide SnO_2 can be continuously controlled by a single axis lattice strain induced by low-energy helium implantation [182]. Fig. 16a and the inset show optical properties of SnO_2 thin films and the extrapolated optical band gaps with increasing single axis lattice strain, respectively. As compared to the effect of

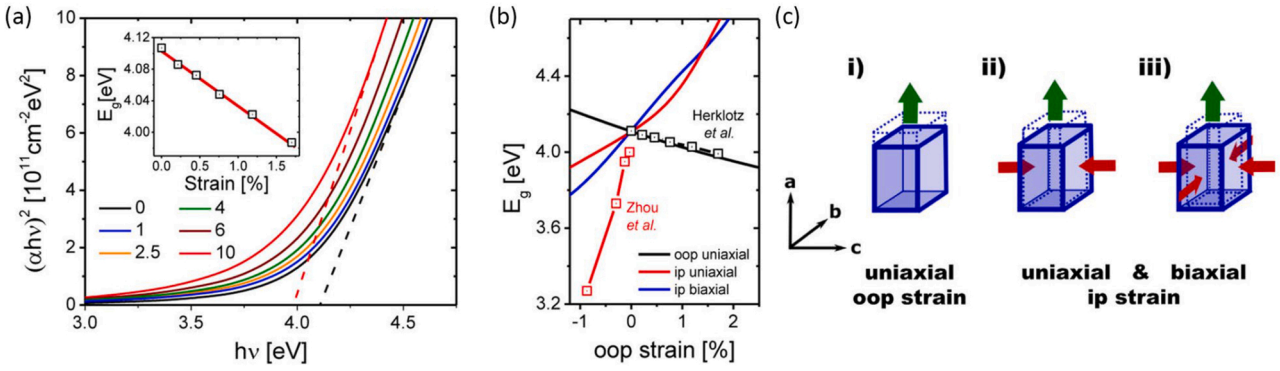

Fig. 16. Effect of elastic strain induced by helium ion implantation on the optical properties of SnO_2 [182]. (a) Variation of the optical band gap with single axis lattice strain (dependent on the helium dose). (b) Band gap as a function of the out-of-plane (oop) and in-plane (ip) strain calculated by DFT (solid lines), experimental data on the opp uniaxial strain (black symbols) and the ip uniaxial strain (red symbols) published by Zhou et al. [648] for comparison. (c) Schematics of three different strain scenarios: uniaxial oop strain, uniaxial and biaxial ip strain. Reprinted by permission of American Chemical Society.

traditional biaxial strain induced by epitaxy and reported in ref. [648] (red symbols in Fig. 16b), extrapolated data from Fig. 16a (black symbols) along with DFT calculations (solid lines in Fig. 16b) demonstrated that uniaxial strain leads to a fundamentally different effect on both the band structure and the crystal structure, as shown in Fig. 16b and c, respectively.

6.6.3. Other oxides

Few experimental studies of the effect of elastic strain on the band gap of binary oxides other than ZnO and SnO_2 have also been reported. In HfO_2 thin films, changes in the optical band gap with increasing epitaxial strain are not very significant, as reported by Bharathi et al. [171]. By taking advantage of the two-way shape memory effect of a TiNiNb substrate and in-situ mechanical bending, Du et al. experimentally reported narrowing of the band gap of both rutile and anatase TiO_2 films under the tensile strain [650].

Recently, Yang et al. investigated the band gap of alkaline-earth-metal binary oxides (MgO, CaO, SrO and BaO) under epitaxial strain using a DFT approach [548]. The authors revealed that the optical band gaps of CaO, SrO and BaO decreased with increasing tensile as well as compressive strain. Using DFT, Yin et al. have calculated that the band gap of TiO_2 in the anatase phase can be effectively tuned by applying stress along a soft direction (low Young's modulus) [651]. Kelaidis et al. obtained similar results for TiO_2 using DFT with the introduction of the Hubbard + U model [652]. In MoO_3, contrary to TiO_2 and RuO_2, Dandogbessi et al. reported that the calculated band gap increased as the strain changed from compressive to tensile [653]. In an octahedral-phase bilayer of ScO_2, Loh et al. theoretically reported that the band gap increased and then decreased with increasing tensile strain [628].

Low-dimensional materials with a high surface-to-volume ratio exhibit a band structure different from their bulk counterparts due to different strain states and deformation potentials on the surface. The effect of strain on optical properties in atomically thin layers, e.g., MoS_2 grown on flexible substrates [238], has been widely investigated, suggesting the potential application of two-dimensional crystals in flexible electronics and optoelectronics. Along similar lines, low-dimensional binary oxides (thin film or nanostructure) that exhibit optical properties tunable by strain serve as attractive candidates for similar applications.

6.7. Magnetic properties

The coupling of elastic strain to magnetism in multiferroic oxide heterostructures has been widely investigated, especially in perovskite oxides [10, 654–657]. Elastic strain tuning of magnetic properties in binary oxides has been reported in only a few systems.

EuO is one of the initially discovered ferromagnetic semiconductors [658] that has recently received renewed focus [30,87,88]. The successful integration of EuO with Si and GaN has created interest in increasing the Curie temperature (T_C) of EuO to room temperature for spintronic applications [659]. Cation and anion doping have been reported to be an effective means to increase the T_C of stoichiometric EuO from 69 K [660] up to 200 K [659,661,662]. A similar effect on T_C can be obtained by applying a biaxial strain in an epitaxial EuO film, as theoretically calculated by Ingle and Elfimov [663]. The authors pointed out that decreasing the lattice parameters was an effective method to increase the T_C, as shown in Fig. 17a with experimental data from references [664–666] (solid circles and triangles) for comparison. Additionally, compressive strain induced by substitution of Eu^{2+} ions with smaller ions such as Gd^{3+} (introduced by co-evaporation during MBE) can play an important role in enhancing the T_C of an epitaxial EuO thin film, as reported by Altendorf et. al [662]. Melville et al. calculated the effect of biaxial strain on the T_C of EuO, specifically for biaxially strained EuO/$LuAlO_3$, revealing an enhancement of T_C under a high compressive strain, as shown in Fig. 17b [330]. The authors experimentally observed a systematically lower T_C in EuO/$LuAlO_3$ films with decreasing film thickness, as shown in Fig. 17c. The lowered T_C can be attributed to the + 1.0% lattice mismatch and the resulting biaxial tensile strain in the EuO/$LuAlO_3$ system as opposed to the complete lattice matching in the EuO/YSZ system [667–669].

CoO, an antiferromagnetic material with a Neel temperature (T_N) of 293 K and a magnetic moment of 3.98 μ_B, is a promising candidate for spintronic applications [670]. Due to the easily accessible ordering temperature and the high-quality growth of a CoO film, CoO can serve as a great model system to study the exchange coupling effect in a ferromagnetic/antiferromagnetic system. Csiszar et al. studied magnetic properties of CoO thin films epitaxially grown on MnO(100) and Ag (100) [671]. The authors found that the magnitude and orientation of magnetic moments strongly depend on the epitaxial strain in CoO films. Lamirand et al. found that in a strained ultrathin CoO/PtFe double layer with a perpendicular magnetic anisotropy, a robust perpendicular shift of the exchange bias was present up to the antiferromagnetic ordering temperature, i.e., the room temperature, which may be attributed to the coupling of the distorted CoO hexagonal layer with the perpendicular magnetic anisotropy of the PtFe layer [672]. Later, the same group reported that the strain related monoclinic distortion of ultrathin CoO films in the exchange-coupled CoO/FePt/Pt(001) system led to a stable Co^{2+} spin configuration within the plane of the film, indicating the effective role of strain in stabilizing the magnetic properties of the system [673].

In a single-crystalline Fe/CoO/MgO(001) system, Zhu et al. reported that strain in the CoO layer can be transferred by magnetostriction through a field cooling process, inducing volume anisotropy of the Fe

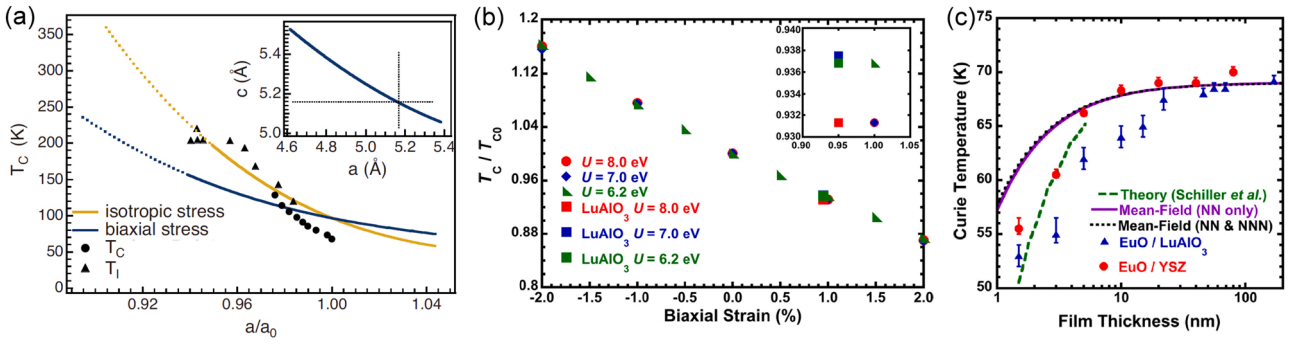

Fig. 17. Effect of elastic strain on the magnetic properties of EuO. (a) Effect of isotropic and biaxial strain in EuO on the calculated mean field T_C [663] and experimental T_C [664] (solid circles) and T_I (tracks T_C) [665,666] (solid triangles). At insulator-to-metal transition, both solid lines change to dashed lines. (b) Calculated biaxial strain effect on the T_C of EuO in the specific case of biaxially strained EuO/$LuAlO_3$ [330]. (c) Film thickness dependence of T_C in EuO/YSZ (red circles) and EuO/$LuAlO_3$ (blue triangles). Theoretical calculation presented by Schiller et al. [667] is shown as a green dashed line and the mean-field approximations [668,669] are shown as a purple solid line and a black dashed line. The vertical dashed lines indicate experimental values of the axial ratio without strain. Reprinted by permission of American Chemical Society and American Physical Society.
(a) is adapted from Ref. [663]. (b,c) are adapted from Ref. [330].

layer and controlling the exchange coupling effect [674]. The same group further investigated the relationship among strain, antiferromagnetic spin orientation and anisotropy in a single-crystalline Fe/CoO/MnO/MgO(001) system [675]. By varying the MnO layer thickness, the authors found that the transition of in-plane strain in the CoO film from compression to expansion induced an antiferromagnetic CoO spin reorientation transition, modifying the exchange coupling in the ferromagnetic/antiferromagnetic bilayer. Fontaina-Troitino et al. reported that in CoO octahedron-shaped nanoparticles, a weak room-temperature ferromagnetism was observed, which was attributed to a thin surface layer of Co_3O_4 and the strain at the CoO/Co_3O_4 interface [676].

Similar phenomena of antiferromagnetic spin orientation modulated by strain were observed in NiO films grown on Ag(001) and MgO(001) [677,678]. Different antiferromagnetic spin alignments could be attributed to epitaxial strain in the NiO films grown on different substrates, e.g., the compressive and tensile strains introduced by Ag(001) and MgO(001) substrates, respectively. Huang et al. investigated the phase transition in beta-MnO_2 under negative pressure and external strain by using DFT calculations and demonstrated the formation of a ferromagnetic phase due to external strain. [679]. In epitaxial Mn_2O_3 thin films grown on a MgO(001) substrate, Dang Duc et al. reported that a compressive epitaxial strain changed the antiferromagnetic ordering seen in the bulk material with a Curie temperature T_C of less than 90 K to ferromagnetic ordering with a T_C of 175 K [680].

In corundum-type antiferromagnets Cr_2O_3 and Fe_2O_3, Kota et al. theoretically studied the effect of strain on the T_N [681]. The authors calculated exchange coupling constants up to the fifth-nearest neighbors by using first-principles DFT and the T_N by using a Monte Carlo simulation. The simulated T_N increased (decreased) with tensile (compressive) strain along the *c*-axis for both Cr_2O_3 and Fe_2O_3. The strong effect of strain on the first- and second-nearest neighbor exchange coupling constants of Cr_2O_3 implies that strain engineering can be an effective tool for improving the thermal stability of Cr_2O_3 based magnetoelectric devices [682]. Recently, by using X-ray photoemission spectroscopy, Pinho et al. quantified the impact of epitaxial strain on crystal field splitting of α-Cr_2O_3 thin films [683]. Vila et al. fabricated epitaxial Cr_2O_3 thin films on α-Al_2O_3 and $SrTiO_3$ substrates and reported a strain-induced soft ferromagnetic response with both films exhibiting a similar coercive field [684].

Punugupati et al. experimentally studied the magnetic properties of antiferromagnetic and magnetoelectric Cr_2O_3 thin films deposited on cubic-YSZ/Si(001) using PLD [685]. The authors found that although bulk Cr_2O_3 is antiferromagnetic with a T_N of 307 K, the deposited thin films exhibited ferromagnetism like hysteresis loops with high saturations up to 400 K. The authors attributed the ferromagnetism in Cr_2O_3 thin films to oxygen related defects induced by strain [685]. Effects of strain on spin reorientation transition, i.e., the so-called Morin transition, were comprehensively studied by Park et al. in α-Fe_2O_3(0001) films grown on Al_2O_3(0001) substrates with a Cr_2O_3 buffer layer [686]. Compressive strain in the α-Fe_2O_3(0001) films was modulated by thickness of the Cr_2O_3 buffer layer on the Al_2O_3(0001) substrates, hence controlling the Morin transition temperature and the T_N.

Intriguing physical phenomena, e.g., a giant magnetoelectric effect, can be induced by an interplay between spin and lattice, thus attracting physicists to study the spin-lattice coupling in materials, especially in multiferroic compounds. Among binary oxides, EuO is a promising material for spintronic devices due to its thermodynamic stability in contact with silicon [61], pronounced metal-insulator transition induced by ferromagnetism [687], and high spin polarization [88]. The T_C of EuO can be increased by reducing the distance between the magnetic 4*f* electrons. Therefore, a large compressive strain in low-dimensional EuO may need to be achieved for further enhancing the T_C.

6.8. *Chemical reactivity*

Lattice strain has been known to affect chemical reactions [688–690]. In theory, an applied strain can change the energy landscape of a reaction, e.g., turn an endothermic reaction into an exothermic one and reduce energy barriers (i.e., mechano-chemical coupling) [691]. An example that demonstrates this coupling in a chain of polymeric molecules is the application of spatially precise forces on bonds between single molecules by using an AFM tip, hence affecting the chemical reactions of the polymer [692,693]. Another example, which originates from the experimental work of Gsell et al. [694] and theoretical work of Mavrikakis et al. [248], is associated with the investigation of the relationship between chemisorption on a metal surface and lattice strain. Gsell et al. reported that lattice strain modified the chemisorption properties of a Ru(0001) metal surface considerably [694]. Mavrikakis et al. used DFT to assess how elastic strain changed the reactivity of a thin metal surface by altering adsorption energies, activation energy barriers and electronic structures [248].

The coupling of lattice strain to ion conduction and surface reaction kinetics of low-dimensional oxides has attracted interest recently in the context of oxygen transport and electrode reactions in solid oxide fuel cells (SOFC) and electrolysis cells [219, 695–697]. As compared to metals, surface reactivity of strained metal oxides is more complex due to the increased chemical, electronic, and structural complexity. For

instance, applying a elastic strain on the non-stoichiometric oxygen structure can result in elemental segregation and phase separation [698, 699]. However, the possibility of modifying reactivity and ion transport properties of oxides with elastic strain is worth studying further. The perovskite family of oxides, such as $La_{1-x}Sr_xMnO_3$ [700], $LaCoO_3$ [701, 702] and $La_{1-x}Sr_xCoO_3$ [250,703], has been widely studied in terms of surface reactions and electrocatalytic activity under strain for use as SOFC cathode materials [704].

With respect to low-dimensional binary oxide materials, titanium dioxide (TiO_2) has attracted much attention due to its promising application in photocatalysis [705,706]. However, the area of the most reactive (001) surface is only a few percent of the total surface area of anatase TiO_2 in equilibrium, which greatly limits the surface reactivity [707]. Theoretical calculations suggested that external strain may be used to change the band gap [651,708,709] as well as the formation energy of surface oxygen vacancies in TiO_2 [710,711]. Experimental work on rutile TiO_2 nanostructures reported by Cha et al. showed that the strain field of dislocations can indeed modify the band gap and enhance photocatalytic activity [712]. Thus, fraction of the reactive surface may be increased by a suitable external strain.

Jia et al. studied the equilibrium shape of anatase TiO_2 under an applied strain via DFT calculations based on the bulk and surface elastic properties of TiO_2 [249]. Fig. 18a shows that the fraction of the (001) surface can be dramatically increased by a biaxial compressive strain along the *a*-axes. Different area ratios lead to different behaviors under different strains as can be understood from Fig. 18b. According to the rule of Wulff construction [713], an increase in $1/\cos\theta$ (θ is the angle formed by the (101) and (001) surfaces) and a decrease in $\gamma_{(001)}/\gamma_{(101)}$ with increasing biaxial compressive strain, as shown in Fig. 18b, suggest an increase in the proportion of the (001) surface. A systematic study of anatase TiO_2(001)-(1 ×4) surface using first-principles calculations has also been reported by Shi et al., showing that tensile stress plays a crucial role in determining surface reactivity [714].

Ceria (CeO_2) is a technologically important catalyst, catalyst support, and ion transport membrane material [715,716]. By performing atomistic calculations, Sayle et al. revealed that tensile strain in CeO_2 nanorods can lead to extraction of oxygen from their surface and increase their tendency to oxidize CO to CO_2. [717]. Based on a DFT study corrected for on-site Coulomb interactions, Wu et al. reported that strain can shift the Ce 4 f orbital energy in CeO_2(111), hence improving its capacity for the electrocatalytic water splitting [718]. Another CeO_2--based study was carried out by Zhang et al. where strain-engineered polaronic defects were studied by using first-principles calculations [719]. Additionally, it has been found that kinetics of point-defect reactions in Gd-doped CeO_2 (GDC) thin films can be affected by thermally induced strain [720,721]. Recently, Gopal et al. studied the oxygen redox chemistry in $CeO_{2-\delta}$ films under large biaxial compressive and tensile strains and revealed a non-monotonic effect of biaxial strain on the equilibrium oxygen storage capacity of $CeO_{2-\delta}$ [722]. This non-monotonicity was attributed to a tetragonal distortion under the large biaxial strain. The inset of Fig. 18c shows a schematic image of the unit cell of CeO_2 in the absence of strain (green), under compression (blue) and under tension (red). Fig. 18c illustrates the tetragonal distortion of CeO_2 under biaxial strain and Fig. 18d shows the vacancy formation energy (E_{vac}) as a function of relative volume with respect to the unstrained bulk for $CeO_{1.97}$ and $CeO_{1.50}$.

Effect of elastic strain on chemical reactions is also seen in piezoelectric materials, e.g., ZnO, where elastic strain can be used to tune reactions occurring at the piezoelectric component–solvent interface, a phenomenon termed as piezocatalysis [723]. Theoretical analysis of piezocatalysis has indicated that a high piezoelectric coupling coefficient and a low electrical conductivity as well as an optimized electrical permittivity can enable high electrochemical activity [723].

Great progress has been made in the area of strain-controlled electrocatalysis on metal surfaces, as recently reviewed by Luo et al. [724]. In oxides, especially in low-dimensional binary oxides, systematic experimental and theoretical investigations are needed to determine the mechanism behind the effects of elastic strain on the surface reactivity of different crystallographic planes.

6.9. Ionic conductivity

Since elastic strain affects reaction and diffusion kinetics via a number of parameters like adsorption energy, oxygen defect formation enthalpy, migration energy barrier, charge transfer barrier and the dissociation barrier, ionic conductivity in oxides can be tuned with elastic strain engineering. [691]. The migration energy barrier for oxygen diffusion is a critical factor affecting ion conductivity in oxide electrolytes. Lattice strain can reduce oxygen migration energy barriers in oxide electrolytes for SOFCs, e.g., GDC or Sm-doped ceria (SDC) with an energy barrier of 0.9—1.16 eV and YSZ with an energy barrier of 1.0—1.2 eV [725], leading to fast diffusion [696,726]. From an atomic-scale point of view, coupling of the strain field with dopant segregation around crystal defects such as dislocations may lead to

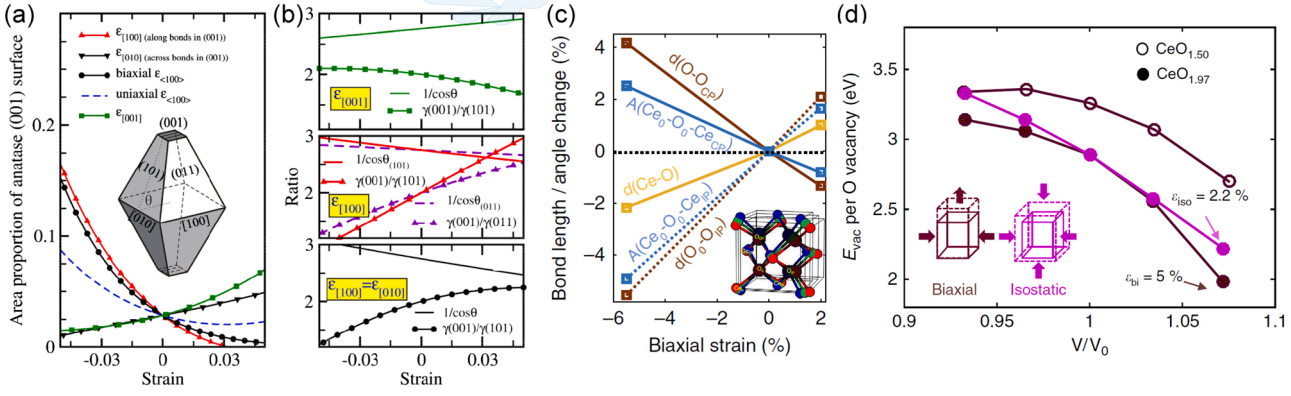

Fig. 18. Effect of elastic strain on the chemical reactivity of TiO_2 (a,b) and CeO_2 (c,d). (a) Area percentage of anatase (001) facets as a function of external strains present uniaxially along [100], [010], < 100 > (average), [001] and biaxially along < 100 > . (b) Surface energy ratio $\gamma_{(001)}$ to $\gamma_{(101)}$ and the ratio $1/\cos\theta$ as a function of strain. The anatase (001) surface appears only when the surface energy ratio is smaller than $1/\cos\theta$. (c) Effect of biaxial strain on tetragonal distortion of CeO_2 (change of bond lengths Ce-O, O_0-O_{IP} and O_0-O_{CP} and angles Ce_0-O_0-Ce_{IP} and Ce_0-O_0-Ce_{CP}, where subscripts 'IP', 'CP' and '0' denote in-plane, cross-plane, and reference species, respectively). Inset shows a schematic structure of the unit cell of ceria in the absence of strain (green), under compression (blue) and under tension (red). (d) Effect of biaxial and isostatic strain (relative volume with respect to the unstrained bulk) on energy of vacancy formation (E_{vac}) per oxygen released in bulk ceria for $CeO_{1.97}$ and $CeO_{1.50}$. Reprinted by permission of American Physical Society, and Nature Research.
(a,b) are adapted From Ref. [249]. (c,d) are adapted from Ref. [722].

formation of faster ionic conduction pathways resulting in an enhancement of ionic conductivity [727]. In Table 5, we summarize typical experimental results from the literature on strain introduced in thin films and multilayers of CeO_2 and ZrO_2 and the corresponding relative change in conductivity and activation energy. This table is included as a complementary and updated version to the table reported in the review articles Ref. [691] and Ref. [728], with the addition of recent relevant reports and the lattice strain and activation energy values presented within them.

6.9.1. CeO_2

In 1993, Adler et al. studied the influence of yttria doping in YDC thin films and reported that long-range forces resulting from the doping can play an important role in ion transport in the films [729]. A study on GDC thin films reported that tuning the grain size can increase the ionic conductivity of the film [730]. The influence of grain size as well as micro strain on ionic conductivity in GDC was further investigated by Rupp et al. [731,732] and Karageorgakis et al. [734].

Using static lattice simulation techniques, De Souza et al. predicted that a biaxial, tensile strain of 4 % can increase the in-plane conductivity of fluorite-structured CeO_2 at $T = 500$ K by close to four orders of magnitude [735]. Later, using DFT calculations, the same group studied the effect of different strain states (uniaxial, biaxial and isotropic) and strain magnitudes (up to $\pm$ 7 %) on the migration of oxygen vacancies in fluorite-structured CeO_2 [736]. For a tensile strain ($\varepsilon > 0$), the authors predicted the activation enthalpy of migration for oxygen vacancies to be lower for the [100] orientation, suggesting a higher ionic conductivity in strained thin films of [100]-oriented CeO_2.

Experimentally, a change in conduction by as much as three orders of magnitude for strained thin films based on CeO_2 was confirmed [691, 757,758]. In epitaxial $Ce_{0.9}Gd_{0.1}O_{2-\delta}$ thin films deposited on MgO(001) with $SrTiO_3$ buffer layers, compressive out-of-plane strains up to 1.9 % and tensile in-plane strains were introduced by varying the thickness of the $SrTiO_3$ buffer layers, resulting in an enhancement of in-plane ionic conductivity [175]. Fluri et al. attached a multi-beam optical stress sensor (MOSS) into a PLD system to enable measurement of stress during growth of oxide thin films, as shown in Fig. 19a. The authors achieved different tensile strains in SDC thin films on different substrates, e.g., single-crystal MgO, $NdGaO_3$ (NGO) and $LaAlO_3$ (LAO). The inset of Fig. 19b shows a typical cross-sectional TEM image of an SDC film grown on an MgO substrate with $SrTiO_3$ and $BaZrO_3$ as buffer layers. Temperature-dependent ion conductivity (Fig. 19b) was measured for SDC films grown on different substrates and hence experiencing different values of strain. The authors found that an increase in tensile strain lowered the activation energy for charge transport via oxygen ion conduction (Fig. 19c) [740]. By using different dopants and keeping a constant film thickness, Shen et al. reported the effect of different interfacial strains on the oxygen ion conductivity of CeO_2 films deposited on Al_2O_3 substrates and doped with Y_2O_3, Gd_2O_3, or La_2O_3. [739]. Recently, Ahn et al. reported the effect of in-plane tensile strain on the ionic conductivity of $Ce_{0.9}Gd_{0.1}O_{2-\delta}$ (100) thin films [741,759]. The ionic conductivity, which was measured in the out-of-plane direction by electrochemical impedance spectroscopy analysis to avoid any interference from defects perpendicular to the surface, showed an enhancement by approximately two orders of magnitude.

Elastic strains can also be introduced in epitaxial CeO_2 films by using metal substrates to improve ionic conductivity. Examples include CeO_2/Cu(111) with reported in-plane compressive strains of 5 % [760] and 3.2 % [761] and CeO_2/Pt(111) with an in-plane compressive strain of 3.3 % [762]. Similar to heterostructures that show increased (decreased) ionic conductivity due a tensile (compressive) strain, multilayers have also been shown to exhibit strain-dependent ionic conductivity, e.g., tensile SDC/YSZ multilayers [733] and biaxially compressed YDC/$Ce_{1-x}Zr_xO$ multilayers [738]. Schweiger et al. fabricated multilayer microdot

Table 5
Summary of selected reports from the literature on relative increase in conductivity and activation energy, as a result of elastic strain in thin films and multilayers. Symbol "-" denotes that data is not available in literature.

Year	Material	Structure	Elastic strain (%)	T (K)	Increase in conductivity	Activation energy (eV)	Ref.
CeO_2 based materials							
1993	Yttria-doped CeO_2 (YDC)	Thin film	–	~400—1000	~10	0.81—0.94	[729]
2002	GDC/Al_2O_3	Thin film	0.015—1	~800—1100	~1—10	1.0—1.3	[730]
2006	GDC/Al_2O_3	Thin film	0.2—1.2	~773	~1.5	0.77—1.04	[731,732]
2010	SDC/YSZ	Multilayer	~6	673—1073	~10	0.76—1.09	[733]
2011	GDC/Al_2O_3	Thin film	0.1—0.4	~673—1273	~10—10^2	~0.8—2.2	[734]
2012	GDC/STO/MgO	Thin film	0.7—1.9	723—1123	3—10	0.93—0.94	[175]
2012	CeO_2	Bulk	-6—5	500	~10^4	0—1.1	[735]
2013	CeO_2	Bulk	-7—7	–	–	0—1.1	[736]
2013	Gd and Y co-doped CeO_2	bulk	-2.5—2.5	973—1873	–	0.70—0.75	[737]
2014	YDC/CZO	Multilayer	1.5—2.2	723—923	10^1—$10^{1.5}$	0.84—0.95	[738]
2014	Doped CeO_2/MgO	Thin film	1.2—1.7	673—873	10	0.74—1.53	[184]
2014	GDC/Er_2O_3	Thin film	1.16	638—873	~7	0.75—1.06	[174]
2014	YDC, GDC/Al_2O_3	Thin film	-2—4.6	776—872	2	0.85—1.0	[739]
2015	GDC	Thin film	0.46—2.7	293—873	–	0.93—1.01	[6]
2016	SDC/MgO(BZO,STO)	Thin film	0—0.35	573—1000	2	0.71—0.76	[740]
2018	GDC	Thin film	0—0.83	373—498	10^2	0.91—0.96	[741]
2019	Rare-earth doped CeO_2	Thin film	-0.5—0	293—773	~0.1	0.70—0.97	[742]
ZrO_2 based materials							
2003	YTZ	Thin film	0—270 MPa (stress)	423—523	4.7—7.9 (resistivity)		[743]
2005	YSZ on MgO	Thin film	–	673—1073	~10—10^2	0.62—1.09	[744]
2007	CSZ/Al_2O_3	Multilayer	–	623—973	~60	0.91—1.6	[745]
2008	YSZ/Y_2O_3	Multilayer	0.5—3.8	623—973	1.4—20	~0.99—1.13	[746]
2008	YSZ/STO	Multilayer	7	357—531	10^8	~0.45—1.1	[169]
2009	YSZ/STO	Multilayer	7	357—531	–	~0.64	[747]
2009	YSZ/Y_2O_3(Lu_2O_3, Sc_2O_3)	Multilayer	-4.28—3.09	833	~0.6—1.5	0.99—1.27	[748]
2010	YSZ	bulk	0—8	400—1000	$10^{2.5}$—$10^{3.8}$	0.1—0.5	[749]
2010	YSZ/MgO	Thin film	1	423—773	$10^{3.5}$	0.89—1.24	[750]
2012	YSZ/CeO_2	Multilayer	0—5	673—973	1	1.07	[751]
2013	YSZ/GdZrO	Multilayer	3	550—750	10^2	–	[752]
2013	YSZ/Y_2O_3	Multilayer	3.04	793	2	–	[753]
2013	YSZ on Al_2O_3	Thin film	1—2	573—923	$10^{0.5}$—$10^{1.5}$	0.79—0.99	[754]
2017	YSZ/MgO(Al_2O_3)	Thin film	0.5—2.5	573—823	~0.03—0.3	1.3—1.5	[755]
2018	YSZ/SNDC	Nanowire	–	400—600	2.5	0.86—0.90	[756]

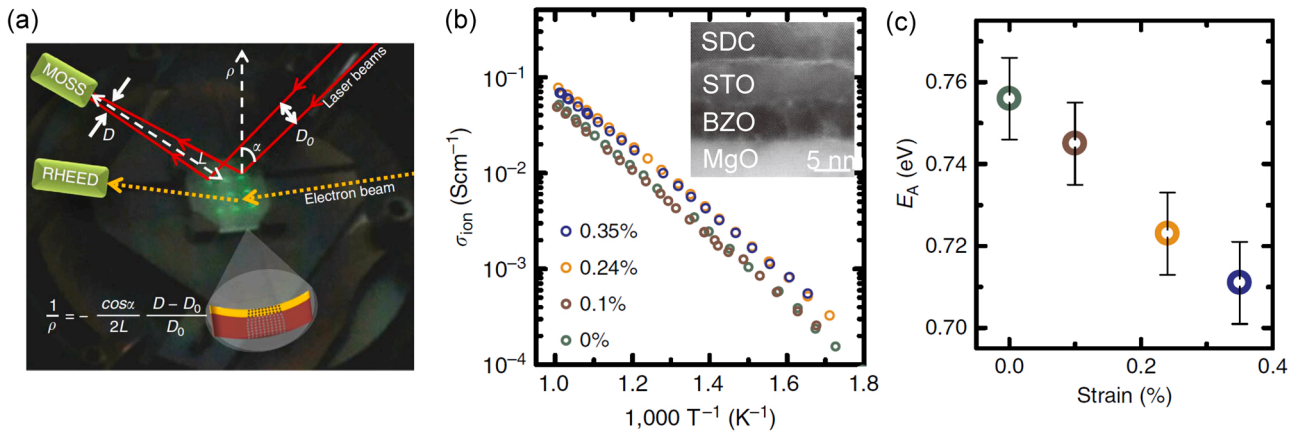

Fig. 19. Effect of elastic strain on the ionic conductivity of CeO_2. (a) A PLD system equipped with MOSS and RHEED. A strained layer changes the curvature ($1/\rho$) of the substrate and the direction of the reflected laser beams. The change of curvature is expressed as: $1/\rho = -(\cos\alpha/2\,L)\times(D\text{-}D_0)/D_0$, where α is the incident angle, L is the optical path length and $(D\text{-}D_0)/D_0$ is the change of relative distance between the laser beams. (b,c) Effect of the epitaxial tensile strain on ionic conductivity (b) and activation energy for ion migration (c). Inset of (b) is a TEM image of the SDC film on MgO with buffer layers of $SrTiO_3$ (STO) and $BaZrO_3$ (BZO). Epitaxial strain is induced by using different substrates [740]. Reprinted by permission of American Physical Society.
(a—c) are adapted from [740].

devices based on the multilayer heterostructure $Gd_{0.1}Ce_{0.9}O_{2-\delta}/Er_2O_3$ and demonstrated that a compressive strain of up to 1.16 % altered the activation energy of the devices by 0.31 eV, hence tuning their resistive response and ionic transport [174]. Recently, Shi et al. reported a large biaxial strain of ~5 % in ultrathin CeO_2 films grown on YSZ [153] and studied their growth mode [763]. Such high epitaxial strain calls for a systematic investigation into the effect of elastic strain on ionic transport properties of CeO_2. While epitaxy is one approach to introduce strain, post annealing in acceptor doped ceria films can introduce strain as well, thereby significantly modifying the oxygen ion conductivity [184].

Strain induced by twisting can also affect the association/migration energies of oxygen ions in freestanding polycrystalline membranes of doped CeO_2 in an in-situ manner. Shi et al. fabricated a freestanding electrochemical membrane device based on a $Ce_{0.2}Gd_{0.8}O_{1.9-x}$ thin film [6]. Using different Pt microelectrode designs, the authors studied the electro-chemo-mechanical coupling in the films and observed that the ionic transport could be tuned by varying compressive strain. For different microelectrode designs and electrodes tested with freestanding and substrate-supported $Ce_{0.2}Gd_{0.8}O_{1.9-x}$ films, it can be found that with increasing effective strain, the activation energy increases. The authors also suggested that maximizing lattice tensile strain in the out-of-plane direction of GDC film electrolytes could be a potential direction of research to accelerate ionic diffusion in future micro electrochemical conversion devices. Schweiger et al. fabricated a strain-modulated memristive device based on the $Gd_{0.1}Ce_{0.9}O_{2-\delta}/Er_2O_3$ model system [764]. The authors engineered the R_{off}/R_{on} ratio and the persistence of the system by modulating the interfacial strain.

6.9.2. ZrO_2

In polycrystalline zirconia, it has been reported that an external mechanical load can lead to variation in bulk and grain boundary ionic transport [743]. Kosacki reported that the ionic conductivity of YSZ thin films deposited on a MgO substrate was enhanced significantly at a thickness less than 60 nm [744]. In multilayer systems such as CSZ/Al_2O_3 [745] and YSZ/Y_2O_3 [746], with decreasing thickness of the individual CSZ or YSZ layers, the oxygen ionic conductivity increased and the corresponding activation energy decreased, which may be attributed to strain at the interface.

In epitaxial $YSZ/SrTiO_3$ heterostructures, Garcia-Barriocanal et al. reported a high lateral ionic conductivity enhanced by up to eight orders of magnitude near room temperature [169]. A large interfacial strain was introduced in the $YSZ/SrTiO_3$ heterostructures, providing both a large number of carriers and a high-mobility plane. With decreasing YSZ thickness, the conductivity remarkably increased. However, the observed enhancement of conductivity and the exact nature of conductance (ionic or electronic) induced in the vicinity of the YSZ/STO interface were debatable [747]. Nevertheless, this result attracted great interest in studying the effect of lattice strain on ion conduction, especially in YSZ/STO heterostructures [765].

In YSZ thin films grown on a MgO substrate, Sillassen et al. reported that the low temperature ionic conductivity was enhanced by more than three orders of magnitude as compared to bulk YSZ, due to a combination of elastic strain and misfit dislocation density at the interface [750]. In multilayered $YSZ/Gd_2Zr_2O_7$ (GZO) films, a tensile strain of 3 % resulting from lattice mismatch enhanced the oxygen ion conductivity by two orders of magnitude as compared to that in the bulk YSZ [752]. An increased ionic conductivity and a reduced activation energy were observed in strained YSZ thin films on (0001) Al_2O_3 substrates as well [754]. Aydin et al. determined the oxygen ion diffusion coefficient for transport in strained YSZ/Y_2O_3 multilayers and attributed an increase in the coefficient with decreasing YSZ thickness to lattice mismatch strain [753]. Zhang et al. fabricated composite Sm-Nd codoped CeO_2 film electrolytes with YSZ nanowires to introduce a tensile strain, showing great long term chemical stability with excellent conductivity at intermediate temperatures [756].

Theoretical studies have explained some of the effects of strain on ionic transport in ZrO_2. Schichtel et al. introduced a qualitative model for estimating the influence of local lattice strain on the interfacial ionic conductivity of ionic conductors [748]. By using DFT and the nudged elastic band method, Kushima and Yildiz investigated the effect of lattice strain on oxygen vacancy migration paths and barriers in YSZ, revealing the underlying microscopic mechanism and the extent of increase in oxygen ion conductivity of YSZ under biaxial lattice strain [749]. Strain can lead to a more open migration pathway and a decrease in the O-C bond strength thereby reducing the migration barrier and increasing oxygen diffusivity. The authors found that the optimum biaxial lattice strain to attain maximum benefit in terms of an enhanced oxygen diffusivity in the material system was around 4 % in YSZ and the diffusivity was higher at lower temperatures.

However, the large increase in conductivity can also be attributed to conduction pathways along dislocation lines. Since a large dislocation density was consistently found at interfaces with increased oxygen-ion conductivity [748,750], the dominant reason for enhanced oxygen-ion conductivity is still controversial. Using DFT calculations, Pennycook et al. investigated the order of magnitude of ionic conductivity that was possible in YSZ/STO multilayers [766]. The authors found that the

colossal ionic conductivity could be explained in terms of a combination of lattice mismatch strain and O-sublattice incompatibility, as shown in Fig. 20a-b. By applying 7 % strain to YSZ, it can be found that significant O-sublattice disorder occurs as low as 1000 K, as shown in Fig. 20b. The extreme O-sublattice disorder at the YSZ/STO interface at room temperature is comparable to the disorder found in strained bulk vacancy-doped ZrO_2 at 2000 K. This disorder originates from the 7 % lattice strain as well as the incompatibility of oxygen sublattices. Thus, the low temperature conductivity of strained multilayers can be estimated to be 10^6 times higher than that of unstrained bulk ZrO_2.

As stated earlier, the mechanism behind enhancement of ionic conductivity, i.e., whether the interfacial strain or the dislocation density plays a dominant role, has not been fully understood yet. Meanwhile, Pergolesi reported experimental evidence that lattice strain, grain boundary conduction pathways or misfit dislocation conducting planes cannot affect oxygen ion transport in multilayered YSZ/CeO_2 [751]. Sun et al. theoretically studied the effect of dislocations on diffusion kinetics in strained CeO_2 using atomistic simulations and revealed that an edge dislocation slowed down oxide ion transport [767]. To unambiguously identify the effect of interfacial strain on ionic conductivity, high-quality uniform interfaces may be essential.

In addition to the epitaxial strain in heterostructures, new approaches for manipulating strain states in thin films are expected, e.g., mechanical twisting in oxygen ion conducting membranes reported by Shi et al. [6]. The range of elastic strain values achieved in CeO_2, ZrO_2 and other binary oxides may be expanded, which can probably lead to new understanding on the phenomenon of ion transport.

6.10. Others - thermoelectric effect, pyroelectric effect, flexoelectric effect

6.10.1. Thermoelectric effect

Elastic strain plays an important role in many functionalities of low-dimensional binary oxides, beyond those mentioned in Sections 6.1 through 6.9. For example, elastic strain also affects the thermoelectric properties of materials. The thermoelectric effect is the direct conversion of a temperature gradient to an electric voltage and vice versa [768]. Thus, a thermoelectric device is able to convert heat directly into electricity. The conversion performance of thermoelectric devices is defined by their figure-of-merit (ZT).

$$ZT = S^2\sigma/\kappa, \quad (15)$$

where S, σ and κ are the Seebeck coefficient, the electrical conductivity and the thermal conductivity, respectively. Low-dimensional materials have shown great potential for thermal management and thermoelectric energy generation [769–772]. Elastic strain engineering can tune electronic and thermal properties in low-dimensional materials, further enhancing their ZT, as reviewed by Zhang et al. for 2D materials [773].

Most oxides are poor thermoelectric materials because of their high lattice thermal conductivity due to tightly bounded light oxygen ions and relatively low electrical conductivity. However, there are exceptions. Low-dimensional oxides with promising thermoelectric properties include the family of misfit layered cobaltates [774,775], $SrTiO_3$ [769, 776], $CaMnO_3$ [777] and $La_2NiO_{4+\delta}$ [778]. Simple binary oxides, such as TiO_2 [779] and ZnO [780], are potential thermoelectric materials for high-temperature power generation [781,782]. However, so far there has been only limited research based on the effect of elastic strain on thermoelectric properties of binary oxides. This research field is still unexplored, calling for further studies to unravel new opportunities.

6.10.2. Pyroelectric effect and pyro-phototronic effect

Pyroelectric effect describes the time-domain temperature fluctuation response of the polarization in polar materials. In the recent years, pyroelectric effect has attracted researchers' attention due to its potential for waste energy conversion [783,784]. Pyro-phototronic effect is a coupling effect of pyroelectric effect and photoelectric effect, which is first proposed by Wang et al. [785,786]. Wang et al. utilized this pyro-phototronic effect to achieve high-performance photo sensing in ZnO/perovskite-heterostructured photodetector [786] and ZnO/Ag Schottky junction-based photodetector [785]. Explicit external strain effect on the pyroelectric effect or pyro-phototronic effect in low-dimensional materials has yet to be investigated. However, the theory of pyroelectricity suggests that [787] one may expect a strong strain dependence of pyroelectric effect and pyro-phototronic effect in low-dimensional materials.

6.10.3. Flexoelectric effect and flexoelectronics

Flexoelectric effect describes the generation of a spontaneous polarization by a strain gradient. In semiconductors, the flexoelectric polarization can modulate the metal-semiconductor interface for tuning the transport properties. This mechanism is termed as flexoelectronics [788]. Wang et al. reported a giant flexoelectronic effect in centrosymmetric semiconductors such as Si, TiO_2 and Nb-$SrTiO_3$ [788]. Using the flexoelectronic effect, the authors achieved high sensitivity, high resolution and fast response in centrosymmetric semiconductor-based

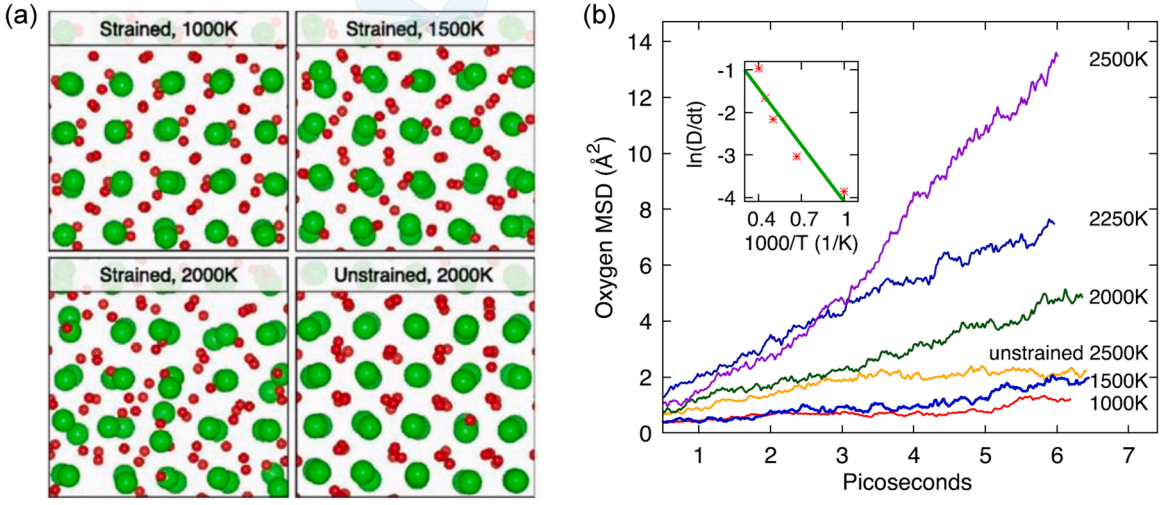

Fig. 20. Origin of the effect of elastic strain on ionic conductivity of ZrO_2. (a) Strained structures of ZrO_2 at three temperatures (1000 K, top left, 1500 K, top right, 2000 K bottom left), unstrained cubic ZrO_2 at 2000 K (bottom right) based on quantum mechanical simulation. (b) Mean-square-displacement (MSD) of oxygen atoms as a function of time at various temperatures based on molecular dynamics simulations. The inset shows an Arrhenius plot of diffusivity (D) from the strained MSDs. (a,b) is adapted from Ref. [766]. Reprinted by permission of American Physical Society.

electronic devices. Similarly, Kumar et al. reported a strong enhancement in the self-powered UV response of the TiO_2-based Schottky photodetector by taking advantage of the flexoelectronic effect [789]. Since large strain gradients up to 10^{-6} m^{-1} can be sustained in low-dimensional materials [284], the flexoelectric and flexoelectronic effects may greatly modulate materials' properties. These effects on low-dimensional materials, especially binary oxides, have been rarely reported so far and need more investigations.

7. Challenges and perspectives

7.1. Challenges and unsolved issues

Although many studies and significant progresses have been made during the last few decades related to the elastic strain engineering of low-dimensional binary oxides, there are experimental challenges and unsolved issues that remain. These mainly include: (1) synthesis of low-dimensional binary oxides (especially freestanding thin films) approaching the dimensional limit; (2) controllable dynamic strain/strain gradient manipulation in thin films; (3) fast and convenient strain characterization at the nanoscale.

Over the past decades, the semiconductor industry has witnessed the success of thin film epitaxy especially since thin film morphology is preferred in device applications. However, in the case of conventional epitaxial thin films, the maximum elastic strain that can be achieved is limited to about 1 %, which is far from the elastic strain limit. Hence, there is plenty of room to introduce and sustain larger elastic strains in thin films and thereby enable new functional properties. Commonly, epitaxial strains are static. By utilizing phase transitions [283] or ferroelastic strain [279] from substrates, epitaxial strain in thin films may be dynamically controlled. However, this technique is limited to material systems that exhibit a favorable phase-transition.

Another feasible but challenging solution is the synthesis of freestanding thin films. Although quasi-one-dimensional nanowires of binary oxides have been widely synthesized, two-dimensional freestanding thin films are difficult to obtain. Strictly speaking, conventional epitaxial thin films might not be in the scope of two-dimensional materials due to strong bonding at the interface between the epitaxial thin film and the substrate. Due to the recent development of epitaxy techniques, e.g., vdW epitaxy [312,790], epitaxy using a water-soluble buffer layer [791,792] and remote epitaxy using a graphene buffer layer [591, 793–795], epitaxial thin films with thicknesses approaching even the monolayer limit can be separated from the underlying substrates and freestanding or quasi-freestanding thin films can be fabricated. Freestanding films enable the possibility of manipulating strain by using irreversible or dynamic approaches allowing strains and strain gradients much larger than those obtained in heteroepitaxy. A recent work reporting a uniaxial tensile strain exceeding 8% in freestanding nanoscale $La_{0.7}Ca_{0.3}MnO_3$ membranes is an exciting example [189]. Moreover, strain gradients and their effects on material properties have received less attention due to the complexity and uncontrollability associated with strain gradients. However, large strain gradients can be induced in low-dimensional materials, breaking their symmetry and yielding flexoelectricity [788,796] or the flexo-photovoltaic effect [284,797] even in centrosymmetric crystals. The phase stability of these two-dimensional freestanding thin films is a serious issue that needs to be explored both theoretically and experimentally.

A number of challenges also remain to be solved regarding the characterization of strain. Although electron-diffraction-based techniques can directly yield 2D strain mapping of a thin film with an atomic-scale resolution, a TEM sample is not representative of the film used in a functional device and the sample preparation is time consuming. Photon-based techniques, such as Raman and PL measurements, are fast and convenient but are limited to a micrometer resolution due to the wavelength of photons used in these techniques. Coherent X-ray diffraction is currently one of the best techniques for 3D strain mapping of samples (or devices) at the nanoscale. However, access to coherent X-ray beam sources is limited. A lab-scale source of coherent X-ray beams is highly desired for fast and convenient characterization of strain.

7.2. Perspectives

The motivation behind this review is to shed light on the advantages of low-dimensional binary oxides and to highlight how their properties can be controlled by elastic strain engineering. The reported values of elastic strain in many low-dimensional materials, measured by different experimental methods have been summarized along with many effective strain engineering approaches, strain characterization techniques and related theoretical calculations. Due to the unique advantages of low-dimensional binary oxides over other materials systems, tuning of their functionalities and applications based on elastic strain is intriguing and has been comprehensively reviewed. These functionalities and applications include piezoelectricity, the piezoresistive effect, piezotronic and piezo-phototronic effects, ferroelectricity, metal-insulator transition, band gap engineering, magnetic properties, chemical reactivity and ionic conductivity.

Piezoelectricity has been widely studied in the ZnO system. Since elastic strain can enhance piezoelectricity [183], effective approaches to increase the maximum elastic strain sustained by ZnO nanostructures, may further enhance piezoelectricity in ZnO. In addition to ZnO, the low-dimensional CdO can be another good candidate for future nanoscale piezoelectric applications due to its much higher in-plane piezoelectric coefficient than that of ZnO [420] and reasonably low formation energy relative to its bulk structure [425]. Low-dimensional transition metal dioxides, e.g., TiO_2 and ZrO_2, may be promising candidates for studying piezoelectric properties as well.

The piezoresistive effect has been most widely investigated in ZnO and SnO_2. Because elastic strain changes electronic band structure, the piezoresistive effect could be universal in materials. In low-dimensional binary oxides, the underlying mechanism of the piezoresistive effect still requires systematic theoretical investigation. When the sample size approaches the regime of the quantum confinement effect, both band structure and surface modification can affect the piezoresistive coefficient. The quantum confinement effect in materials with their characteristic dimensions close or below their Bohr radii may play a dominant role. Giant piezoresistance might be observed in nanostructures as a result of both surface states and the quantum confinement effect.

The piezotronic and piezo-phototronic effects have been extensively studied in ZnO-based nanodevices by experimental as well as theoretical means. Increasing the maximum elastic strain that can be sustained in ZnO may further enhance the piezotronic effect and thereby the device performance. Besides, low-dimensional binary oxides other than ZnO, e.g., CdO, MgO, TiO_2, ZrO_2, that have piezoelectric properties better than or comparable to those of ZnO might also exhibit promising piezotronic and piezo-phototronic effects. In piezoelectric semiconductors with dimensions of a few nanometers, the quantum confinement effect should be considered in the existing models of piezotronics and piezo-phototronics, which might bring new understanding to the current experimental observations.

Research on ferroelectricity in strained low-dimensional binary oxides is limited and mainly focuses on strained ZrO_2, because most binary oxides are expected to exhibit a centrosymmetric crystal structure and therewith linear dielectric characteristics at room temperature. Theoretical calculations have predicted that ferroelectricity can be realized in centrosymmetric binary oxides with certain epitaxial strains. Therefore, ferroelectricity in strained MgO, CaO, SrO, BaO and related superlattices or nanostructures is worth an experimental exploration. Recently, an unexpected giant polarization has been reported in a freestanding crystalline oxide perovskite approaching the monolayer limit [792]. Whether ferroelectricity can exist in a monolayer binary oxide and how it would behave are still open questions that remain to be answered.

The metal-insulator transition has been extensively studied in strained VO_2 thin films and nanobeams/microbeams. Epitaxial strains sustained in VO_2 thin films and compressive and tensile strains sustained in VO_2 beams can be further increased by decreasing the thickness of films or the size of beams to the atomic scale. The abrupt change in the lattice constant of VO_2 upon phase transition (1 % along the tetragonal *c*-axis), which can be triggered by external stimulations such as temperature, can be used to generate strain in a material grown or transferred on VO_2. In addition, possible robust metal-insulator transition behaviors might be observed in other low-dimensional binary oxides.

Studies on band gap engineering modulated by elastic strain have focused on strained ZnO and SnO_2. Optical properties can be universally modified by elastic strain for all materials, especially for semiconductors, since a change in the lattice constant under elastic strain leads to a modified band structure. The band structure of a low-dimensional material with a high surface-to-volume ratio is different from that of its bulk counterpart due to surface strain states and different deformation potentials. Therefore, binary oxide thin films or atomic-scale nanostructures that exhibit promising optical properties are suitable candidates for further investigation of strain related band gap engineering.

Magnetic properties of binary oxides are widely studied in terms of spin-lattice coupling in strained CoO and EuO. EuO is a promising material for spintronic devices due to its thermodynamic stability in contact with silicon and a metal-insulator transition induced by pronounced ferromagnetism and high spin polarization. To enhance T_C in low-dimensional EuO, large compressive strains are required. In-situ studies on magnetic properties of single-crystal oxide nanostructures under an external strain may be highly desirable.

Studies on the chemical reactivity of strained binary oxides mainly focus on the TiO_2 system. Syntheses of nanoscale strained samples without dislocations, first principles-based computational predictions and systematic investigations to precisely determine the effect of elastic strain on the surface reactivity of different crystallographic planes, especially those of binary oxides, are desirable.

Ionic conductivity is being currently studied with a focus on strained CeO_2 and ZrO_2. Atomically thin films or nanostructures with large strains are essential for the enhancement of the ionic conductivity. More systematic studies on the mechanism of the effect of strain on oxygen ion transport are required. New methods for manipulating strain states in thin films may also need to be designed.

As reviewed in this article, one can find that ZnO and VO_2 have been extensively studied, while SnO_2, ZrO_2, TiO_2 and CeO_2 have been moderately explored, along with few studies on CoO and EuO. Future research in this field may be on newly designed ZnO and VO_2 based heterostructure devices and their commercial applications, systematic studies of elastic strain engineering in SnO_2, ZrO_2, TiO_2, CeO_2, CoO and EuO, and initial attempts of theoretical and experimental exploration of elastic strain engineering in MgO, CdO, BaO, CrO, BeO and GeO_2. Moreover, elastic strains experimentally achieved in low-dimensional binary oxides may be further increased to explore new functional properties.

It can be found that among all the mentioned methods of introducing elastic strain in low-dimensional materials, creating heterostructures is one of the most effective ways of introducing a large static elastic strain in a nanostructure via interfacial bonding between two materials [7, 153, 168, 176–178, 202, 204, 205, 234, 283, 291, 305–310, 320, 322]. However, such a strain is irreversible while in many electrical (e.g., pressure-enabled logic devices [798]) and optical devices (e.g., piezo-phototronic luminescence devices [17,799]), a reversible elastic strain is necessary to dynamically control and tune the properties of the semiconductor. Therefore, from the point of view of prospective applications, obtaining control over elastic strain or the elastic strain pattern in semiconductor devices in a dynamic and in-situ manner may be the next upcoming research field [282–284]. One may name it as dynamic strain engineering. Also, further efforts may be allocated on understanding the role of external elastic strain on the tuning of internal strain and phonon dynamics [784].

It is our hope that this review can inspire more scientists to explore the untapped but rich field of low-dimensional, strained binary oxides to seek both new scientific understanding as well as technological breakthroughs.

Declaration of Competing Interest

The authors declare that they have no known competing financial interests or personal relationships that could have appeared to influence the work reported in this paper.

Data availability

Data will be made available on request.

Acknowledgments

We thank the fund support from the Air Force Office of Scientific Research under award number FA9550–18-1–0116 and the NYSTAR Focus Center at Rensselaer Polytechnic Institute under award number C180117. We also thank the supports from National Science Foundatoin awards under 2031692 and 2024972.

References

[1] L. Zhang, Y. Wang, J. Lv, Y. Ma, Materials discovery at high pressures, Nat. Rev. Mater. 2 (2017) 17005, https://doi.org/10.1038/natrevmats.2017.5.
[2] Y.V. Milman, I. Gridneva, A. Golubenko, Construction of stress-strain curves for brittle materials by indentation in a wide temperature range, Sci. Sinter. 39 (2007) 67–75, https://doi.org/10.2298/SOS0701067M.
[3] J. Song, X. Wang, E. Riedo, Z.L. Wang, Elastic property of vertically aligned nanowires, Nano Lett. 5 (2005) 1954–1958, https://doi.org/10.1021/nl051334v.
[4] Z. Liu, M. Amani, S. Najmaei, Q. Xu, X. Zou, W. Zhou, T. Yu, C. Qiu, A. G. Birdwell, F.J. Crowne, R. Vajtai, B.I. Yakobson, Z. Xia, M. Dubey, P.M. Ajayan, J. Lou, Strain and structure heterogeneity in MoS_2 atomic layers grown by chemical vapour deposition, Nat. Commun. 5 (2014) 5246, https://doi.org/10.1038/ncomms6246.
[5] J. Feng, X.F. Qian, C.W. Huang, J. Li, Strain-engineered artificial atom as a broad-spectrum solar energy funnel, Nat. Photonics 6 (2012) 865–871, https://doi.org/10.1038/nphoton.2012.285.
[6] Y.U. Shi, A.H. Bork, S. Schweiger, J.L.M. Rupp, The effect of mechanical twisting on oxygen ionic transport in solid-state energy conversion membranes, Nat. Mater. 14 (2015) 721–727, https://doi.org/10.1038/nmat4278.
[7] H. Zheng, J. Wang, S.E. Lofland, Z. Ma, L. Mohaddes-Ardabili, T. Zhao, L. Salamanca-Riba, S.R. Shinde, S.B. Ogale, F. Bai, D. Viehland, Y. Jia, D. G. Schlom, M. Wuttig, A. Roytburd, R. Ramesh, Multiferroic $BaTiO_3$-$CoFe_2O_4$ nanostructures, Science 303 (2004) 661–663, https://doi.org/10.1126/science.1094207.
[8] Z.L. Wang, From nanogenerators to piezotronics-A decade-long study of ZnO nanostructures, MRS Bull. 37 (2012) 814–827, https://doi.org/10.1557/mrs.2012.186.
[9] C. Pan, M. Chen, R. Yu, Q. Yang, Y. Hu, Y. Zhang, Z.L. Wang, Progress in piezo-phototronic-effect-enhanced light-emitting diodes and pressure imaging, Adv. Mater. 28 (2016) 1535–1552, https://doi.org/10.1002/adma.201503500.
[10] D.G. Schlom, L.-Q. Chen, C.J. Fennie, V. Gopalan, D.A. Muller, X. Pan, R. Ramesh, R. Uecker, Elastic strain engineering of ferroic oxides, MRS Bull. 39 (2014) 118–130, https://doi.org/10.1557/mrs.2014.1.
[11] B. You, M.T. Tang, C. Tsai, F. Abild-Pedersen, X. Zheng, H. Li, Enhancing electrocatalytic water pplitting by strain engineering, Adv. Mater. 31 (2019), 1807001, https://doi.org/10.1002/adma.201807001.
[12] R. Roldán, A. Castellanos-Gomez, E. Cappelluti, F. Guinea, Strain engineering in semiconducting two-dimensional crystals, J. Phys.: Condens. Matter 27 (2015), 313201, https://doi.org/10.1088/0953-8984/27/31/313201.
[13] C. Si, Z. Sun, F. Liu, Strain engineering of graphene: a review, Nanoscale 8 (2016) 3207–3217, https://doi.org/10.1039/C5NR07755A.
[14] M. Chu, Y.K. Sun, U. Aghoram, S.E. Thompson, Strain: a solution for higher carrier mobility in nanoscale MOSFETs, Annu. Rev. Mater. Res. 39 (2009) 203–229.
[15] T. Makino, G. Skretas, G. Georgiou, Strain engineering for improved expression of recombinant proteins in bacteria, Microb. Cell Factor. 10 (2011) 32, https://doi.org/10.1186/1475-2859-10-32.
[16] A.I. Hochbaum, P. Yang, Semiconductor nanowires for energy conversion, Chem. Rev. 110 (2010) 527–546, https://doi.org/10.1021/cr900075v.
[17] W.Z. Wu, Z.L. Wang, Piezotronics and piezo-phototronics for adaptive electronics and optoelectronics, Nat. Rev. Mater. 1 (2016) 16031, https://doi.org/10.1038/natrevmats.2016.31.

[18] J.H. Haeni, P. Irvin, W. Chang, R. Uecker, P. Reiche, Y.L. Li, S. Choudhury, W. Tian, M.E. Hawley, B. Craigo, A.K. Tagantsev, X.Q. Pan, S.K. Streiffer, L. Q. Chen, S.W. Kirchoefer, J. Levy, D.G. Schlom, Room-temperature ferroelectricity in strained $SrTiO_3$, Nature 430 (2004) 758–761, https://doi.org/10.1038/nature02773.

[19] A.R. Damodaran, J.C. Agar, S. Pandya, Z. Chen, L. Dedon, R. Xu, B. Apgar, S. Saremi, L.W. Martin, New modalities of strain-control of ferroelectric thin films, J. Phys.: Condens. Matter 28 (2016), 263001, https://doi.org/10.1088/0953-8984/28/26/263001.

[20] Z.W. Pan, Z.R. Dai, Z.L. Wang, Nanobelts of semiconducting oxides, Science 291 (2001) 1947–1949, https://doi.org/10.1126/science.1058120.

[21] P.X. Gao, W. Mai, Z.L. Wang, Superelasticity and nanofracture mechanics of ZnO nanohelices, Nano Lett. 6 (2006) 2536–2543, https://doi.org/10.1021/nl061943i.

[22] S.L. Mensah, V.K. Kayastha, I.N. Ivanov, D.B. Geohegan, Y.K. Yap, Formation of single crystalline ZnO nanotubes without catalysts and templates, Appl. Phys. Lett. 90 (2007), 113108, https://doi.org/10.1063/1.2714186.

[23] C. Tusche, H.L. Meyerheim, J. Kirschner, Observation of depolarized ZnO(0001) monolayers: formation of unreconstructed planar sheets, Phys. Rev. Lett. 99 (2007), 026102, https://doi.org/10.1103/PhysRevLett.99.026102.

[24] L. Hu, M. Chen, W. Shan, T. Zhan, M. Liao, X. Fang, X. Hu, L. Wu, Stacking-order-dependent optoelectronic properties of bilayer nanofilm photodetectors made from hollow ZnS and ZnO microspheres, Adv. Mater. 24 (2012) 5872–5877, https://doi.org/10.1002/adma.201202749.

[25] K. Nomura, H. Ohta, A. Takagi, T. Kamiya, M. Hirano, H. Hosono, Room-temperature fabrication of transparent flexible thin-film transistors using amorphous oxide semiconductors, Nature 432 (2004) 488, https://doi.org/10.1038/nature03090.

[26] R. John, High dielectric constant gate oxides for metal oxide Si transistors, Rep. Prog. Phys. 69 (2006) 327, https://doi.org/10.1088/0034-4885/69/2/R02.

[27] D.G. Schlom, S. Guha, S. Datta, Gate oxides beyond SiO_2, MRS Bull. 33 (2011) 1017–1025, https://doi.org/10.1557/mrs2008.221.

[28] H.S.P. Wong, H.Y. Lee, S. Yu, Y.S. Chen, Y. Wu, P.S. Chen, B. Lee, F.T. Chen, M. J. Tsai, Metal–oxide RRAM, Proc. IEEE 100 (2012) 1951–1970, https://doi.org/10.1109/JPROC.2012.2190369.

[29] X. Rocquefelte, K. Schwarz, P. Blaha, S. Kumar, J. van den Brink, Room-temperature spin-spiral multiferroicity in high-pressure cupric oxide, Nat. Commun. 4 (2013) 2511, https://doi.org/10.1038/ncomms3511.

[30] W.-Y. Tong, H.-C. Ding, Y.-C. Gao, S.-J. Gong, X. Wan, C.-G. Duan, Spin-dependent optical response of multiferroic EuO: first-principles DFT calculations, Phys. Rev. B 89 (2014), 064404, https://doi.org/10.1103/PhysRevB.89.064404.

[31] T. Kimura, Y. Sekio, H. Nakamura, T. Siegrist, A.P. Ramirez, Cupric oxide as an induced-multiferroic with high-T_C, Nat. Mater. 7 (2008) 291, https://doi.org/10.1038/nmat2125.

[32] M.D. Uchic, D.M. Dimiduk, J.N. Florando, W.D. Nix, Sample dimensions influence strength and crystal plasticity, Science 305 (2004) 986–989, https://doi.org/10.1126/science.1098993.

[33] A.D. Yoffe, Low-dimensional systems: quantum size effects and electronic properties of semiconductor microcrystallites (zero-dimensional systems) and some quasi-two-dimensional systems, Adv. Phys. 42 (1993) 173–262, https://doi.org/10.1080/00018739300101484.

[34] M. Lorenzo, A. Giovanni, B. Elisa, G. Diego, P. Andrea, G. Erik, L. Carlo, Low-dimensional systems investigated by x-ray absorption spectroscopy: a selection of 2D, 1D and 0D cases, J. Phys. D: Appl. Phys. 46 (2013), 423001, https://doi.org/10.1088/0022-3727/46/42/423001.

[35] L. Esaki, R. Tsu, Superlattice and negative differential conductivity in semiconductors, IBM J. Res. Dev. 14 (1970) 61–65, https://doi.org/10.1147/rd.141.0061.

[36] L.L. Chang, L. Esaki, R. Tsu, Resonant tunneling in semiconductor double barriers, Appl. Phys. Lett. 24 (1974) 593–595, https://doi.org/10.1063/1.1655067.

[37] J.P. van der Ziel, R. Dingle, R.C. Miller, W. Wiegmann, W.A. Nordland Jr., Laser oscillation from quantum states in very thin GaAs−Al0.2Ga0.8As multilayer structures, Appl. Phys. Lett. 26 (1975) 463–465, https://doi.org/10.1063/1.88211.

[38] A.H. Cottrell, Dislocations and plastic flow in crystals, Am. J. Phys. 22 (1954) 242–243, https://doi.org/10.1119/1.1933704.

[39] P. Hiralal, H.E. Unalan, G.A.J. Amaratunga, Nanowires for energy generation, Nanotechnology 23 (2012), 194002, https://doi.org/10.1088/0957-4484/23/19/194002.

[40] L. Sun, A.V. Krasheninnikov, T. Ahlgren, K. Nordlund, F. Banhart, Plastic deformation of single nanometer-sized crystals, Phys. Rev. Lett. 101 (2008), 156101, https://doi.org/10.1103/PhysRevLett.101.156101.

[41] D.P. Norton, Synthesis and properties of epitaxial electronic oxide thin-film materials, Mater. Sci. Eng. R: Rep. 43 (2004) 139–247, https://doi.org/10.1016/j.mser.2003.12.002.

[42] L.S. Dubrovinsky, N.A. Dubrovinskaia, V. Swamy, J. Muscat, N.M. Harrison, R. Ahuja, B. Holm, B. Johansson, Materials science: the hardest known oxide, Nature 410 (2001) 653–654, https://doi.org/10.1038/35070650.

[43] D. Lee, H. Lu, Y. Gu, S.Y. Choi, S.D. Li, S. Ryu, T.R. Paudel, K. Song, E. Mikheev, S. Lee, S. Stemmer, D.A. Tenne, S.H. Oh, E.Y. Tsymbal, X. Wu, L.Q. Chen, A. Gruverman, C.B. Eom, Emergence of room-temperature ferroelectricity at reduced dimensions, Science 349 (2015) 1314–1317, https://doi.org/10.1126/science.aaa6442.

[44] Y. Saito, H. Takao, T. Tani, T. Nonoyama, K. Takatori, T. Homma, T. Nagaya, M. Nakamura, Lead-free piezoceramics, Nature 432 (2004) 84–87, https://doi.org/10.1038/nature03028.

[45] J.M.D. Coey, M. Venkatesan, C.B. Fitzgerald, Donor impurity band exchange in dilute ferromagnetic oxides, Nat. Mater. 4 (2005) 173, https://doi.org/10.1038/nmat1310.

[46] S. Sun, H. Zeng, D.B. Robinson, S. Raoux, P.M. Rice, S.X. Wang, G. Li, Monodisperse MFe_2O_4 (M = Fe, Co, Mn) nanoparticles, J. Am. Chem. Soc. 126 (2004) 273–279, https://doi.org/10.1021/ja0380852.

[47] J.A. Mundy, C.M. Brooks, M.E. Holtz, J.A. Moyer, H. Das, A.F. Rebola, J.T. Heron, J.D. Clarkson, S.M. Disseler, Z.Q. Liu, A. Farhan, R. Held, R. Hovden, E. Padgett, Q.Y. Mao, H. Paik, R. Misra, L.F. Kourkoutis, E. Arenholz, A. Scholl, J.A. Borchers, W.D. Ratcliff, R. Ramesh, C.J. Fennie, P. Schiffer, D.A. Muller, D.G. Schlom, Atomically engineered ferroic layers yield a room - temperature magnetoelectric multiferroic, Nature 537 (2016) 523–527, https://doi.org/10.1038/nature19343.

[48] L.W. Martin, Y.H. Chu, R. Ramesh, Advances in the growth and characterization of magnetic, ferroelectric, and multiferroic oxide thin films, Mater. Sci. Eng. R: Rep. 68 (2010) 89–133, https://doi.org/10.1016/j.mser.2010.03.001.

[49] E. Fortunato, P. Barquinha, R. Martins, Oxide semiconductor thin-film transistors: a review of recent advances, Adv. Mater. 24 (2012) 2945–2986, https://doi.org/10.1002/adma.201103228.

[50] U. Ozgür, Y.I. Alivov, C. Liu, A. Teke, M.A. Reshchikov, S. Doğan, V. Avrutin, S. J. Cho, H. Morkoç, A comprehensive review of ZnO materials and devices, J. Appl. Phys. 98 (2005), 041301, https://doi.org/10.1063/1.1992666.

[51] M. Batzill, U. Diebold, The surface and materials science of tin oxide, Prog. Surf. Sci. 79 (2005) 47–154, https://doi.org/10.1016/j.progsurf.2005.09.002.

[52] S. Das, V. Jayaraman, SnO_2: a comprehensive review on structures and gas sensors, Prog. Mater. Sci. 66 (2014) 112–255, https://doi.org/10.1016/j.pmatsci.2014.06.003.

[53] U. Diebold, The surface science of titanium dioxide, Surf. Sci. Rep. 48 (2003) 53–229, https://doi.org/10.1016/s0167-5729(02)00100-0.

[54] B.K. Meyer, A. Polity, D. Reppin, M. Becker, P. Hering, P.J. Klar, T. Sander, C. Reindl, J. Benz, M. Eickhoff, C. Heiliger, M. Heinemann, J. Bläsing, A. Krost, S. Shokovets, C. Müller, C. Ronning, Binary copper oxide semiconductors: from materials towards devices, Phys. Status Solidi (b) 249 (2012) 1487–1509, https://doi.org/10.1002/pssb.201248128.

[55] A. Sawa, Resistive switching in transition metal oxides, Mater. Today 11 (2008) 28–36, https://doi.org/10.1016/s1369-7021(08)70119-6.

[56] J.B. Cao, J.Q. Wu, Strain effects in low-dimensional transition metal oxides, Mater. Sci. Eng. R: Rep. 71 (2011) 35–52, https://doi.org/10.1016/j.mser.2010.08.001.

[57] C.G. Granqvist, Electrochromic tungsten oxide films: review of progress 1993-1998, Sol. Energy Mater. Sol. Cells 60 (2000) 201–262, https://doi.org/10.1016/s0927-0248(99)00088-4.

[58] N. Nuraje, K. Su, Perovskite ferroelectric nanomaterials, Nanoscale 5 (2013) 8752–8780, https://doi.org/10.1039/c3nr02543h.

[59] P.M. Rorvik, T. Grande, M.A. Einarsrud, One-dimensional nanostructures of ferroelectric perovskites, Adv. Mater. 23 (2011) 4007–4034, https://doi.org/10.1002/adma.201004676.

[60] J.G. Wu, D.Q. Xiao, J.G. Zhu, Potassium-sodium niobate lead-free piezoelectric materials: past, present, and future of phase boundaries, Chem. Rev. 115 (2015) 2559–2595, https://doi.org/10.1021/cr5006809.

[61] K.J. Hubbard, D.G. Schlom, Thermodynamic stability of binary oxides in contact with silicon, J. Mater. Res. 11 (1996) 2757–2776, https://doi.org/10.1557/jmr.1996.0350.

[62] W. Tian, H. Lu, L. Li, Nanoscale ultraviolet photodetectors based on onedimensional metal oxide nanostructures, Nano Res. 8 (2015) 382–405, https://doi.org/10.1007/s12274-014-0661-2.

[63] J. Jiang, F. Heck, D.M. Hofmann, M. Eickhoff, Synthesis of SnO2 nanowires using SnI2 as precursor and their application as high-performance self-powered ultraviolet photodetectors, Physica Status Solidi (b) 255 (2017), 1700426, https://doi.org/10.1002/pssb.201700426.

[64] D.J. Gargas, H. Gao, H. Wang, P. Yang, High quantum efficiency of band-edge emission from ZnO nanowires, Nano Lett. 11 (2011) 3792–3796, https://doi.org/10.1021/nl201850k.

[65] J. Muller, T.S. Boscke, U. Schroder, S. Mueller, D. Brauhaus, U. Bottger, L. Frey, T. Mikolajick, Ferroelectricity in simple binary ZrO_2 and HfO_2, Nano Lett. 12 (2012) 4318–4323, https://doi.org/10.1021/nl302049k.

[66] E. Bousquet, N.A. Spaldin, P. Ghosez, Strain-induced ferroelectricity in simple rocksalt binary oxides, Phys. Rev. Lett. 104 (2010), 037601, https://doi.org/10.1103/PhysRevLett.104.037601.

[67] Z.L. Wang, J.H. Song, Piezoelectric nanogenerators based on zinc oxide nanowire arrays, Science 312 (2006) 242–246, https://doi.org/10.1126/science.1124005.

[68] B.L. Cushing, V.L. Kolesnichenko, C.J. O'Connor, Recent advances in the liquid-phase syntheses of inorganic nanoparticles, Chem. Rev. 104 (2004) 3893–3946, https://doi.org/10.1021/cr030027b.

[69] J.-J. Wu, S.-C. Liu, Low-temperature growth of well-aligned ZnO nanorods by chemical vapor deposition, Adv. Mater. 14 (2002) 215, https://doi.org/10.1002/1521-4095(20020205)14:3<215::AID-ADMA215>3.0.CO;2-J.

[70] Z. Fan, J.G. Lu, Zinc oxide nanostructures: synthesis and properties, J. Nanosci. Nanotechnol. 5 (2005) 1561–1573, https://doi.org/10.1166/jnn.2005.182.

[71] M. Laurenti, S. Stassi, G. Canavese, V. Cauda, Surface engineering of nanostructured ZnO surfaces, Adv. Mater. Interfaces 4 (2017), 1600758, https://doi.org/10.1002/admi.201600758.

[72] Z.L. Wang, ZnO nanowire and nanobelt platform for nanotechnology, Mater. Sci. Eng. R: Rep. 64 (2009) 33–71, https://doi.org/10.1016/j.mser.2009.02.001.

[73] R.S. Devan, R.A. Patil, J.-H. Lin, Y.-R. Ma, One-dimensional metal-oxide nanostructures: recent developments in synthesis, characterization, and

applications, Adv. Funct. Mater. 22 (2012) 3326–3370, https://doi.org/10.1002/adfm.201201008.
[74] X. Xia, J. Tu, Y. Zhang, X. Wang, C. Gu, X.-b Zhao, H.J. Fan, High-quality metal oxide core/shell nanowire arrays on conductive substrates for electrochemical energy storage, ACS Nano (2012) 5531–5538, https://doi.org/10.1021/nn301454q.
[75] S. Hirano, N. Takeuchi, S. Shimada, K. Masuya, K. Ibe, H. Tsunakawa, M. Kuwabara, Room-temperature nanowire ultraviolet lasers: An aqueous pathway for zinc oxide nanowires with low defect density, J. Appl. Phys. 98 (2005), 094305, https://doi.org/10.1063/1.2113418.
[76] G. Hautier, A. Miglio, D. Waroquiers, G.-M. Rignanese, X. Gonze, How does chemistry influence electron effective mass in oxides? A high-throughput computational analysis, Chem. Mater. 26 (2014) 5447–5458, https://doi.org/10.1021/cm404079a.
[77] I.G. Baek, M.S. Lee, S. Seo, M.J. Lee, D.H. Seo, D.S. Suh, J.C. Park, S.O. Park, H.S. Kim, I.K. Yoo, U.I. Chung, J.T. Moon, Highly scalable nonvolatile resistive memory using simple binary oxide driven by asymmetric unipolar voltage pulses, IEDM Technical Digest. In: Proceedings of the IEEE International Electron Devices Meeting, 2004., vol 04, 2004, pp. 587–590.
[78] J.S. Suehle, R.E. Cavicchi, M. Gaitan, S. Semancik, Tin oxide gas sensor fabricated using CMOS micro-hotplates and in-situ processing, IEEE Electron Device Lett. 14 (1993) 118–120, https://doi.org/10.1109/55.215130.
[79] Z. Wang, P.K. Nayak, J.A. Caraveo-Frescas, H.N. Alshareef, Recent developments in p-Type oxide semiconductor materials and devices, Adv. Mater. 28 (2016) 3831–3892, https://doi.org/10.1002/adma.201503080.
[80] F.M. Hossain, J. Nishii, S. Takagi, A. Ohtomo, T. Fukumura, H. Fujioka, H. Ohno, H. Koinuma, M. Kawasaki, Modeling and simulation of polycrystalline ZnO thin-film transistors, J. Appl. Phys. 94 (2003) 7768–7777, https://doi.org/10.1063/1.1628834.
[81] K. Park, D.-K. Lee, B.-S. Kim, H. Jeon, N.-E. Lee, D. Whang, H.-J. Lee, Y.J. Kim, J.-H. Ahn, Stretchable, transparent zinc oxide thin film transistors, Adv. Funct. Mater. 20 (2010) 3577–3582, https://doi.org/10.1002/adfm.201001107.
[82] E.N. Dattoli, Q. Wan, W. Guo, Y. Chen, X. Pan, W. Lu, Fully transparent thin-film transistor devices based on SnO_2 nanowires, Nano Lett. 7 (2007) 2463–2469, https://doi.org/10.1021/nl0712217.
[83] K. Matsuzaki, K. Nomura, H. Yanagi, T. Kamiya, M. Hirano, H. Hosono, Epitaxial growth of high mobility Cu_2O thin films and application to p-channel thin film transistor, Appl. Phys. Lett. 93 (2008), 202107, https://doi.org/10.1063/1.3026539.
[84] J.A. Caraveo-Frescas, P.K. Nayak, H.A. Al-Jawhari, D.B. Granato, U. Schwingenschlögl, H.N. Alshareef, Record mobility in transparent p-type tin monoxide films and devices by phase engineering, ACS Nano 7 (2013) 5160–5167, https://doi.org/10.1021/nn400852r.
[85] Y. Ogo, H. Hiramatsu, K. Nomura, H. Yanagi, T. Kamiya, M. Hirano, H. Hosono, p-channel thin-film transistor using p-type oxide semiconductor, SnO, Appl. Phys. Lett. 93 (2008), 032113, https://doi.org/10.1063/1.2964197.
[86] H. Yabuta, N. Kaji, R. Hayashi, H. Kumomi, K. Nomura, T. Kamiya, M. Hirano, H. Hosono, Sputtering formation of p-type SnO thin-film transistors on glass toward oxide complimentary circuits, Appl. Phys. Lett. 97 (2010), 072111, https://doi.org/10.1063/1.3478213.
[87] M.J. Bierman, K.M. Van Heuvelen, D. Schmeißer, T.C. Brunold, S. Jin, Ferromagnetic semiconducting EuO nanorods, Adv. Mater. 19 (2007) 2677–2681, https://doi.org/10.1002/adma.200602612.
[88] P.G. Steeneken, L.H. Tjeng, I. Elfimov, G.A. Sawatzky, G. Ghiringhelli, N. B. Brookes, D.J. Huang, Exchange splitting and charge carrier spin polarization in EuO, Phys. Rev. Lett. 88 (2002), 047201, https://doi.org/10.1103/PhysRevLett.88.047201.
[89] Z. Wang, N. Qureshi, S. Yasin, A. Mukhin, E. Ressouche, S. Zherlitsyn, Y. Skourski, J. Geshev, V. Ivanov, M. Gospodinov, V. Skumryev, Magnetoelectric effect and phase transitions in CuO in external magnetic fields, Nat. Commun. 7 (2016), 10295, https://doi.org/10.1038/ncomms10295.
[90] G. Quirion, M.L. Plumer, Landau theory of the magnetic phase diagram of monoclinic multiferroics: application to $MnWO_4$ and CuO, Phys. Rev. B 87 (2013), 174428, https://doi.org/10.1103/PhysRevB.87.174428.
[91] S.K.V. Farahani, V. Muñoz-Sanjosé, J. Zúñiga-Pérez, C.F. McConville, T.D. Veal, Temperature dependence of the direct bandgap and transport properties of CdO, Appl. Phys. Lett. 102 (2013), 022102, https://doi.org/10.1063/1.4775691.
[92] D. Groh, R. Pandey, M.B. Sahariah, E. Amzallag, I. Baraille, M. Rérat, First-principles study of the optical properties of BeO in its ambient and high-pressure phases, J. Phys. Chem. Solids 70 (2009) 789–795, https://doi.org/10.1016/j.jpcs.2009.03.013.
[93] J. Berashevich, O. Semeniuk, J.A. Rowlands, A. Reznik, Anisotropy of the carrier effective masses in bulk α -PbO, Europhys. Lett. 99 (2012), 47005, https://doi.org/10.1209/0295-5075/99/47005.
[94] A. Murat, J.E. Medvedeva, Electronic properties of layered multicomponent wide-band-gap oxides: a combinatorial approach, Phys. Rev. B 85 (2012), 155101, https://doi.org/10.1103/PhysRevB.85.155101.
[95] D.M. Roessler, W.C. Walker, Electronic spectrum and ultraviolet optical properties of crystalline MgO, Phys. Rev. 159 (1967) 733–738, https://doi.org/10.1103/PhysRev.159.733.
[96] J.E. Medvedeva, E.N. Teasley, M.D. Hoffman, Electronic band structure and carrier effective mass in calcium aluminates, Phys. Rev. B 76 (2007), 155107, https://doi.org/10.1103/PhysRevB.76.155107.
[97] S.C. Choi, K. Koumoto, H. Yanagida, Electrical conduction and effective mass of a hole in single-crystal NiO, J. Mater. Sci. 21 (1986) 1947–1950, https://doi.org/10.1007/BF00547931.
[98] G.A. Sawatzky, J.W. Allen, Magnitude and origin of the band gap in NiO, Phys. Rev. Lett. 53 (1984) 2339–2342, https://doi.org/10.1103/PhysRevLett.53.2339.
[99] C. Rödl, A. Schleife, Photoemission spectra and effective masses of n- and p-type oxide semiconductors from first principles: ZnO, CdO, SnO2, MnO, and NiO, Phys. Status Solidi A 211 (2014) 74–81, https://doi.org/10.1002/pssa.201330181.
[100] V.I. Anisimov, M.A. Korotin, E.Z. Kurmaev, Band-structure description of Mott insulators (NiO, MnO, FeO, CoO), J. Phys.: Condens. Matter 2 (1990) 3973, https://doi.org/10.1088/0953-8984/2/17/008.
[101] R.M. Xavier, On the magnetic properties of divalent europium compounds, Phys. Lett. A 25 (1967) 244–245, https://doi.org/10.1016/0375-9601(67)90882-1.
[102] Y. Shapira, S. Foner, T.B. Reed, I. EuO, Resistivity and hall effect in fields up to 150 kOe, Phys. Rev. B 8 (1973) 2299–2315, https://doi.org/10.1103/PhysRevB.8.2299.
[103] W. Mindt, Electrical properties of electrodeposited PbO_2 films, J. Electrochem. Soc. 116 (1969) 1076–1080, https://doi.org/10.1149/1.2412217.
[104] F. Zhang, S.-W. Chan, J.E. Spanier, E. Apak, Q. Jin, R.D. Robinson, I.P. Herman, Cerium oxide nanoparticles: size-selective formation and structure analysis, Appl. Phys. Lett. 80 (2002) 127–129, https://doi.org/10.1063/1.1430502.
[105] L. Kavan, M. Grätzel, S.E. Gilbert, C. Klemenz, H.J. Scheel, Electrochemical and photoelectrochemical investigation of single-crystal anatase, J. Am. Chem. Soc. 118 (1996) 6716–6723, https://doi.org/10.1021/ja954172l.
[106] J. Zhang, P. Zhou, J. Liu, J. Yu, New understanding of the difference of photocatalytic activity among anatase, rutile and brookite TiO_2, Phys. Chem. Chem. Phys. 16 (2014) 20382–20386, https://doi.org/10.1039/C4CP02201G.
[107] B. Enright, D. Fitzmaurice, Spectroscopic determination of electron and hole effective masses in a nanocrystalline semiconductor film, J. Phys. Chem. 100 (1996) 1027–1035, https://doi.org/10.1021/jp951142w.
[108] S. Monaghan, P.K. Hurley, K. Cherkaoui, M.A. Negara, A. Schenk, Determination of electron effective mass and electron affinity in HfO_2 using MOS and MOSFET structures, Solid-State Electron. 53 (2009) 438–444, https://doi.org/10.1016/j.sse.2008.09.018.
[109] F.L. Martínez, M. Toledano-Luque, J.J. Gandía, J. Cárabe, W. Bohne, J. Röhrich, E. Strub, I. Mártil, Optical properties and structure of HfO_2 thin films grown by high pressure reactive sputtering, J. Phys. D: Appl. Phys. 40 (2007) 5256, https://doi.org/10.1088/0022-3727/40/17/037.
[110] A.V. Shaposhnikov, D.V. Gritsenko, I.P. Petrenko, O.P. Pchelyakov, V. A. Gritsenko, S.B. Érenburg, N.V. Bausk, A.M. Badalyan, Y.V. Shubin, T. P. Smirnova, H. Wong, C.W. Kim, The atomic and electron structure of ZrO_2, J. Exp. Theor. Phys. 102 (2006) 799–809, https://doi.org/10.1134/S1063776106050128.
[111] K.J. Button, C.G. Fonstad, W. Dreybrodt, Determination of the electron masses in stannic oxide by submillimeter cyclotron resonance, Phys. Rev. B 4 (1971) 4539–4542, https://doi.org/10.1103/PhysRevB.4.4539.
[112] T.V. Perevalov, A.V. Shaposhnikov, V.A. Gritsenko, H. Wong, J.H. Han, C.W. Kim, Electronic structure of α-Al_2O_3: Ab initio simulations and comparison with experiment, JETP Lett. 85 (2007) 165–168, https://doi.org/10.1134/S0021364007030071.
[113] W.Y. Ching, Y.-N. Xu, First-principles calculation of electronic, optical, and structural properties of α-Al_2O_3, J. Am. Ceram. Soc. 77 (1994) 404–411, https://doi.org/10.1111/j.1151-2916.1994.tb07008.x.
[114] K. Irmscher, Z. Galazka, M. Pietsch, R. Uecker, R. Fornari, Electrical properties of β-Ga_2O_3 single crystals grown by the Czochralski method, J. Appl. Phys. 110 (2011), 063720, https://doi.org/10.1063/1.3642962.
[115] N. Preissler, O. Bierwagen, A.T. Ramu, J.S. Speck, Electrical transport, electrothermal transport, and effective electron mass in single-crystalline In_2O_3 films, Phys. Rev. B 88 (2013), 085305, https://doi.org/10.1103/PhysRevB.88.085305.
[116] P.D.C. King, T.D. Veal, F. Fuchs, C.Y. Wang, D.J. Payne, A. Bourlange, H. Zhang, G.R. Bell, V. Cimalla, O. Ambacher, R.G. Egdell, F. Bechstedt, C.F. McConville, Band gap, electronic structure, and surface electron accumulation of cubic and rhombohedral In_2O_3, Phys. Rev. B 79 (2009), 205211, https://doi.org/10.1103/PhysRevB.79.205211.
[117] P.P. Edwards, A. Porch, M.O. Jones, D.V. Morgan, R.M. Perks, Basic materials physics of transparent conducting oxides, Dalton Trans. (2004) 2995–3002, https://doi.org/10.1039/B408864F.
[118] D. Bagayoko, G.L. Zhao, J.D. Fan, J.T. Wang, Ab initio calculations of the electronic structure and optical properties of ferroelectric tetragonal $BaTiO_3$, J. Phys.: Condens. Matter 10 (1998) 5645, https://doi.org/10.1088/0953-8984/10/25/014.
[119] W. Setyawan, R.M. Gaume, R.S. Feigelson, S. Curtarolo, Comparative study of nonproportionality and electronic band structures features in scintillator materials, IEEE Trans. Nucl. Sci. 56 (2009) 2989–2996, https://doi.org/10.1109/TNS.2009.2027019.
[120] H. Mizoguchi, T. Kamiya, S. Matsuishi, H. Hosono, A germanate transparent conductive oxide, Nat. Commun. 2 (2011) 470, https://doi.org/10.1038/ncomms1484.
[121] S.J. Allen, S. Raghavan, T. Schumann, K.M. Law, S. Stemmer, Conduction band edge effective mass of La-doped $BaSnO_3$, Appl. Phys. Lett. 108 (2016) 4, https://doi.org/10.1063/1.4954671.
[122] H. Kozuka, K. Ohbayashi, K. Koumoto, Electronic conduction in La-based perovskite-type oxides, Sci. Technol. Adv. Mater. 16 (2015) 16, https://doi.org/10.1088/1468-6996/16/2/026001.
[123] N. Ueda, H. Hosono, H. Kawazoe, Noble transparent semiconductor: MgIn2O4, Solid State Phenom. 51 (1996) 317–322.

[124] W.P. Mulligan, T.J. Coutts, Measurement of the effective mass of transparent conducting films of cadmium tin oxide, MRS Online Proceedings Library 471 (2011) 117. ⟨https://doi.org/10.1557/PROC-471–117⟩.

[125] K.G. Godinho, B.J. Morgan, J.P. Allen, D.O. Scanlon, G.W. Watson, Chemical bonding in copper-based transparent conducting oxides: $CuMO_2$ (M = In, Ga, Sc), J. Phys.: Condens. Matter 23 (2011), 334201, https://doi.org/10.1088/0953-8984/23/33/334201.

[126] B. Yang, Y. He, A. Polity, B.K. Meyer, Structural, optical and electrical properties of transparent conducting $CuInO_2$ thin films prepared by RF sputtering, MRS Online Proceedings Library 865 (2011) F14.17. ⟨https://doi.org/10.1557/PROC-865-F14.7⟩.

[127] Y. Kakehi, K. Satoh, T. Yotsuya, K. Masuko, T. Yoshimura, A. Ashida, N. Fujimura, Optical and electrical properties of $CuScO_2$ epitaxial films prepared by combining two-step deposition and post-annealing techniques, J. Cryst. Growth 311 (2009) 1117–1122, https://doi.org/10.1016/j.jcrysgro.2008.11.060.

[128] G. Hautier, A. Miglio, G. Ceder, G.-M. Rignanese, X. Gonze, Identification and design principles of low hole effective mass p-type transparent conducting oxides, Nat. Commun. 4 (2013) 2292, https://doi.org/10.1038/ncomms3292.

[129] A. Kudo, H. Yanagi, H. Hosono, H. Kawazoe, $SrCu_2O_2$: a p-type conductive oxide with wide band gap, Appl. Phys. Lett. 73 (1998) 220–222, https://doi.org/10.1063/1.121761.

[130] N. Mansourian-Hadavi, S. Wansom, N.H. Perry, A.R. Nagaraja, T.O. Mason, L.-h Ye, A.J. Freeman, Transport and band structure studies of crystalline ZnRh2O4, in: Physical Review B, 81, 2010, https://doi.org/10.1103/PhysRevB.81.075112.

[131] H. Uwe, J. Kinoshita, K. Yoshihiro, C. Yamanouchi, T. Sakudo, Evidence for light and heavy conduction electrons at the zone center in $KTaO_3$, Phys. Rev. B 19 (1979) 3041–3044, https://doi.org/10.1103/PhysRevB.19.3041.

[132] D.J. Singh, Stability and phonons of $KTaO_3$, Phys. Rev. B 53 (1996) 176–180, https://doi.org/10.1103/PhysRevB.53.176.

[133] F. Michel-Calendini, L. Castet, Band structure, optical and transport properties of $KTaO_3$, $KNbO_3$ and $BaTiO_3$ in the paraelectric phase, Ferroelectrics 13 (1976) 367–370, https://doi.org/10.1080/00150197608236614.

[134] H. Wen, P. Chen, M.P. Cosgriff, D.A. Walko, J.H. Lee, C. Adamo, R.D. Schaller, J. F. Ihlefeld, E.M. Dufresne, D.G. Schlom, P.G. Evans, J.W. Freeland, Y. Li, Electronic origin of ultrafast photoinduced strain in $BiFeO_3$, Phys. Rev. Lett. 110 (2013), 037601, https://doi.org/10.1103/PhysRevLett.110.037601.

[135] J.F. Scott, Applications of modern ferroelectrics, Science 315 (2007) 954–959, https://doi.org/10.1126/science.1129564.

[136] T. Zhu, J. Li, Ultra-strength materials, Prog. Mater. Sci. 55 (2010) 710–757, https://doi.org/10.1016/j.pmatsci.2010.04.001.

[137] J. Li, Z. Shan, E. Ma, Elastic strain engineering for unprecedented materials properties, MRS Bull. 39 (2014) 108–114, https://doi.org/10.1557/mrs.2014.3.

[138] F. Sansoz, K. Lu, T. Zhu, A. Misra, Strengthening and plasticity in nanotwinned metals, MRS Bull. 41 (2016) 292–297, https://doi.org/10.1557/mrs.2016.60.

[139] E.J. Guo, R. Roth, A. Herklotz, D. Hesse, K. Dorr, Ferroelectric 180 degrees domain wall motion controlled by biaxial strain, Adv. Mater. 27 (2015) 1615–1618, https://doi.org/10.1002/adma.201405205.

[140] Z. Wu, R.E. Cohen, Pressure-induced anomalous phase transitions and colossal enhancement of piezoelectricity in $PbTiO_3$, Phys. Rev. Lett. 95 (2005), 037601, https://doi.org/10.1103/PhysRevLett.95.037601.

[141] H. Zheng, A. Cao, C.R. Weinberger, J.Y. Huang, K. Du, J. Wang, Y. Ma, Y. Xia, S. X. Mao, Discrete plasticity in sub-10-nm-sized gold crystals, Nat. Commun. 1 (2010) 144, https://doi.org/10.1038/ncomms1149.

[142] G. Williamson, R. Smallman, III. Dislocation densities in some annealed and cold-worked metals from measurements on the X-ray debye-scherrer spectrum, Philos. Mag. 1 (1956) 34–46, https://doi.org/10.1080/14786435608238074.

[143] S.M. Wiederhorn, Brittle fracture and toughening mechanisms in ceramics, Annu. Rev. Mater. Sci. 14 (1984) 373–403, https://doi.org/10.1146/annurev.ms.14.080184.002105.

[144] T. Zhu, J. Li, A. Samanta, A. Leach, K. Gall, Temperature and strain-rate dependence of surface dislocation nucleation, Phys. Rev. Lett. 100 (2008), 025502, https://doi.org/10.1103/PhysRevLett.100.025502.

[145] M.D. Uchic, P.A. Shade, D.M. Dimiduk, Plasticity of micrometer-scale single crystals in compression, Annu. Rev. Mater. Res. vol 39 (2009) 361–386.

[146] S. Yip, Nanocrystals: the strongest size, Nature 391 (1998) 532–533, https://doi.org/10.1038/35254.

[147] R. Maaß, S. Van Petegem, D. Ma, J. Zimmermann, D. Grolimund, F. Roters, H. Van Swygenhoven, D. Raabe, Smaller is stronger: the effect of strain hardening, Acta Mater. 57 (2009) 5996–6005, https://doi.org/10.1016/j.actamat.2009.08.024.

[148] T. Zhu, J. Li, S. Ogata, S. Yip, Mechanics of ultra-strength materials, MRS Bull. 34 (2009) 167–172, https://doi.org/10.1557/mrs2009.47.

[149] Y.H. Yue, P. Liu, Z. Zhang, X.D. Han, E. Ma, Approaching the theoretical elastic strain limit in copper nanowires, Nano Lett. 11 (2011) 3151–3155, https://doi.org/10.1021/nl201233u.

[150] J.W. Wang, F. Sansoz, C. Deng, G. Xu, G.R. Han, S.X. Mao, Strong hall-petch type behavior in the elastic strain limit of nanotwinned gold nanowires, Nano Lett. 15 (2015) 3865–3870, https://doi.org/10.1021/acs.nanolett.5b00694.

[151] S. Narayanan, G.M. Cheng, Z. Zeng, Y. Zhu, T. Zhu, Strain hardening and size effect in five-fold twinned Ag nanowires, Nano Lett. 15 (2015) 4037–4044, https://doi.org/10.1021/acs.nanolett.5b01015.

[152] B. Wei, K. Zheng, Y. Ji, Y. Zhang, Z. Zhang, X. Han, Size-dependent bandgap modulation of ZnO nanowires by tensile strain, Nano Lett. 12 (2012) 4595–4599, https://doi.org/10.1021/nl301897q.

[153] Y. Shi, S.C. Lee, M. Monti, C. Wang, Z.A. Feng, W.D. Nix, M.F. Toney, R. Sinclair, W.C. Chueh, Growth of highly strained CeO_2 ultrathin films, ACS Nano 10 (2016) 9938–9947, https://doi.org/10.1021/acsnano.6b04081.

[154] H.T. Zhang, J. Tersoff, S. Xu, H.X. Chen, Q.B. Zhang, K.L. Zhang, Y. Yang, C. S. Lee, K.N. Tu, J. Li, Y. Lu, Approaching the ideal elastic strain limit in silicon nanowires, Sci. Adv. 2 (2016), e1501382, https://doi.org/10.1126/sciadv.1501382.

[155] J.W. Wang, F. Sansoz, J.Y. Huang, Y. Liu, S.H. Sun, Z. Zhang, S.X. Mao, Near-ideal theoretical strength in gold nanowires containing angstrom scale twins, Nat. Commun. 4 (2013) 1742, https://doi.org/10.1038/ncomms2768.

[156] Q.Q. Qin, S. Yin, G.M. Cheng, X.Y. Li, T.H. Chang, G. Richter, Y. Zhu, H.J. Gao, Recoverable plasticity in penta-twinned metallic nanowires governed by dislocation nucleation and retraction, Nat. Commun. 6 (2015) 5983, https://doi.org/10.1038/ncomms6983.

[157] J.I. Sohn, H.J. Joo, K.S. Kim, H.W. Yang, A.R. Jang, D. Ahn, H.H. Lee, S. Cha, D. J. Kang, J.M. Kim, M.E. Welland, Stress-induced domain dynamics and phase transitions in epitaxially grown VO_2 nanowires, Nanotechnology 23 (2012), 205707, https://doi.org/10.1088/0957-4484/23/20/205707.

[158] S. Hoffmann, F. Östlund, J. Michler, H.J. Fan, M. Zacharias, S.H. Christiansen, C. Ballif, Fracture strength and Young's modulus of ZnO nanowires, Nanotechnology 18 (2007), 205503, https://doi.org/10.1088/0957-4484/18/20/205503.

[159] L.H. Wang, D.L. Kong, T.J. Xin, X.Y. Shu, K. Zheng, L.R. Xiao, X.C. Sha, Y. Lu, Z. Zhang, X.D. Han, J. Zou, Deformation mechanisms of bent Si nanowires governed by the sign and magnitude of strain, Appl. Phys. Lett. 108 (2016), 151903, https://doi.org/10.1063/1.4946855.

[160] D.-M. Tang, C.-L. Ren, M.-S. Wang, X. Wei, N. Kawamoto, C. Liu, Y. Bando, M. Mitome, N. Fukata, D. Golberg, Mechanical properties of Si nanowires as revealed by in situ transmission electron microscopy and molecular dynamics simulations, Nano Lett. 12 (2012) 1898–1904, https://doi.org/10.1021/nl204282y.

[161] J.O. Island, A. Kuc, E.H. Diependaal, R. Bratschitsch, H.S.J. van der Zant, T. Heine, A. Castellanos-Gomez, Precise and reversible band gap tuning in single-layer $MoSe_2$ by uniaxial strain, Nanoscale 8 (2016) 2589–2593, https://doi.org/10.1039/c5nr08219f.

[162] G. da Cunha Rodrigues, P. Zelenovskiy, K. Romanyuk, S. Luchkin, Y. Kopelevich, A. Kholkin, Strong piezoelectricity in single-layer graphene deposited on SiO_2 grating substrates, Nat. Commun. 6 (2015) 7572, https://doi.org/10.1038/ncomms8572.

[163] H.J. Conley, B. Wang, J.I. Ziegler, R.F. Haglund, S.T. Pantelides, K.I. Bolotin, Bandgap engineering of strained monolayer and bilayer MoS_2, Nano Lett. 13 (2013) 3626–3630, https://doi.org/10.1021/nl4014748.

[164] S.J. Hao, L.S. Cui, D.Q. Jiang, X.D. Han, Y. Ren, J. Jiang, Y.N. Liu, Z.Y. Liu, S. C. Mao, Y.D. Wang, Y. Li, X.B. Ren, X.D. Ding, S. Wang, C. Yu, X.B. Shi, M.S. Du, F. Yang, Y.J. Zheng, Z. Zhang, X.D. Li, D.E. Brown, J. Li, A transforming metal nanocomposite with large elastic strain, low modulus, and high strength, Science 339 (2013) 1191–1194, https://doi.org/10.1126/science.1228602.

[165] S. Wang, L.S. Cui, S.J. Hao, D.Q. Jiang, Y.N. Liu, Z.Y. Liu, S.C. Mao, X.D. Han, Y. Ren, Locality and rapidity of the ultra-large elastic deformation of Nb nanowires in a NiTi phase-transforming matrix, Sci. Rep. 4 (2014) 6753, https://doi.org/10.1038/srep06753.

[166] D. Jung, J. Faucher, S. Mukherjee, A. Akey, D.J. Ironside, M. Cabral, X. Sang, J. Lebeau, S.R. Bank, T. Buonassisi, O. Moutanabbir, M.L. Lee, Highly tensile-strained Ge/InAlAs nanocomposites, Nat. Commun. 8 (2017) 14204, https://doi.org/10.1038/ncomms14204.

[167] S. Lee, W.R. Zhang, F. Khatkhatay, Q.X. Jia, H.Y. Wang, J.L. MacManus-Driscoll, Strain tuning and strong enhancement of ionic conductivity in $SrZrO_3$-RE_2O_3 (RE = Sm, Eu, Gd, Dy, and Er) nanocomposite films, Adv. Funct. Mater. 25 (2015) 4328–4333, https://doi.org/10.1002/adfm.201404420.

[168] S.A. Harrington, J. Zhai, S. Denev, V. Gopalan, H. Wang, Z. Bi, S.A.T. Redfern, S.-H. Baek, C.W. Bark, C.-B. Eom, Q. Jia, M.E. Vickers, J.L. MacManus-Driscoll, Thick lead-free ferroelectric films with high Curie temperatures through nanocomposite-induced strain, Nat. Nanotechnol. 6 (2011) 491–495, https://doi.org/10.1038/nnano.2011.98.

[169] J. Garcia-Barriocanal, A. Rivera-Calzada, M. Varela, Z. Sefrioui, E. Iborra, C. Leon, S.J. Pennycook, J. Santamaria, Colossal ionic conductivity at interfaces of epitaxial ZrO_2:Y_2O_3/$SrTiO_3$ heterostructures, Science 321 (2008) 676–680, https://doi.org/10.1126/science.1156393.

[170] E. Breckenfeld, H. Kim, K. Burgess, N. Charipar, S.-F. Cheng, R. Stroud, A. Pique, Strain effects in epitaxial VO_2 thin films on columnar buffer-layer TiO_2/Al_2O_3 virtual substrates, ACS Appl. Mater. Interfaces 9 (2017) 1577–1584, https://doi.org/10.1021/acsami.6b13112.

[171] K.K. Bharathi, N.R. Kalidindi, C.V. Ramana, Grain size and strain effects on the optical and electrical properties of hafnium oxide nanocrystalline thin films, J. Appl. Phys. 108 (2010), 083529, https://doi.org/10.1063/1.3499325.

[172] G. Signorello, S. Karg, M.T. Björk, B. Gotsmann, H. Riel, Tuning the light emission from GaAs nanowires over 290 meV with uniaxial strain, Nano Lett. 13 (2013) 917–924, https://doi.org/10.1021/nl303694c.

[173] Y. Huo, H. Lin, R. Chen, M. Makarova, Y. Rong, M. Li, T.I. Kamins, J. Vuckovic, J. S. Harris, Strong enhancement of direct transition photoluminescence with highly tensile-strained Ge grown by molecular beam epitaxy, Appl. Phys. Lett. 98 (2011), 011111, https://doi.org/10.1063/1.3534785.

[174] S. Schweiger, M. Kubicek, F. Messerschmitt, C. Murer, J.L.M. Rupp, A microdot multilayer oxide device: Let us tune the strain-ionic transport interaction, ACS Nano 8 (2014) 5032–5048, https://doi.org/10.1021/nn501128y.

[175] K.M. Kant, V. Esposito, N. Pryds, Strain induced ionic conductivity enhancement in epitaxial Ce0.9Gd0.1O2−δ thin films, Appl. Phys. Lett. 100 (2012), 033105, https://doi.org/10.1063/1.3676659.

[176] J.R. Petrie, C. Mitra, H. Jeen, W.S. Choi, T.L. Meyer, F.A. Reboredo, J. W. Freeland, G. Eres, H.N. Lee, Strain control of oxygen vacancies in epitaxial strontium cobaltite films, Adv. Funct. Mater. 26 (2016) 1564–1570, https://doi.org/10.1002/adfm.201504868.
[177] M.P. Warusawithana, C. Cen, C.R. Sleasman, J.C. Woicik, Y. Li, L.F. Kourkoutis, J. A. Klug, H. Li, P. Ryan, L.-P. Wang, M. Bedzyk, D.A. Muller, L.-Q. Chen, J. Levy, D. G. Schlom, A ferroelectric oxide made directly on silicon, Science 324 (2009) 367–370, https://doi.org/10.1126/science.1169678.
[178] K.J. Choi, M. Biegalski, Y.L. Li, A. Sharan, J. Schubert, R. Uecker, P. Reiche, Y. B. Chen, X.Q. Pan, V. Gopalan, L.-Q. Chen, D.G. Schlom, C.B. Eom, Enhancement of ferroelectricity in strained $BaTiO_3$ thin films, Science 306 (2004) 1005–1009, https://doi.org/10.1126/science.1103218.
[179] M.D. Biegalski, L. Qiao, Y. Gu, A. Mehta, Q. He, Y. Takamura, A. Borisevich, L.-Q. Chen, Impact of symmetry on the ferroelectric properties of $CaTiO_3$ thin films, Appl. Phys. Lett. 106 (2015), 162904, https://doi.org/10.1063/1.4918805.
[180] J.H. Lee, L. Fang, E. Vlahos, X.L. Ke, Y.W. Jung, L.F. Kourkoutis, J.W. Kim, P. J. Ryan, T. Heeg, M. Roeckerath, V. Goian, M. Bernhagen, R. Uecker, P. C. Hammel, K.M. Rabe, S. Kamba, J. Schubert, J.W. Freeland, D.A. Muller, C. J. Fennie, P. Schiffer, V. Gopalan, E. Johnston-Halperin, D.G. Schlom, A strong ferroelectric ferromagnet created by means of spin-lattice coupling, Nature 466 (2010) 954–958, https://doi.org/10.1038/nature09331.
[181] A. Azcatl, X.Y. Qin, A. Prakash, C.X. Zhang, L.X. Cheng, Q.X. Wang, N. Lu, M. J. Kim, J. Kim, K. Cho, R. Addou, C.L. Hinkle, J. Appenzeller, R.M. Wallace, Covalent nitrogen doping and compressive strain in MoS_2 by remote N-2 plasma exposure, Nano Lett. 16 (2016) 5437–5443, https://doi.org/10.1021/acs.nanolett.6b01853.
[182] A. Herklotz, S.F. Rus, T.Z. Ward, Continuously controlled optical band gap in oxide semiconductor thin films, Nano Lett. 16 (2016) 1782–1786, https://doi.org/10.1021/acs.nanolett.5b04815.
[183] Y. Zhang, C. Liu, J. Liu, J. Xiong, J. Liu, K. Zhang, Y. Liu, M. Peng, A. Yu, A. Zhang, Y. Zhang, Z. Wang, J. Zhai, Z.L. Wang, Lattice strain induced remarkable enhancement in piezoelectric performance of ZnO-based flexible nanogenerators, ACS Appl. Mater. Interfaces 8 (2016) 1381–1387, https://doi.org/10.1021/acsami.5b10345.
[184] J.L.M. Rupp, E. Fabbri, D. Marrocchelli, J.-W. Han, D. Chen, E. Traversa, H. L. Tuller, B. Yildiz, Scalable oxygen-ion transport kinetics in metal-oxide films: impact of thermally induced lattice compaction in acceptor doped ceria films, Adv. Funct. Mater. 24 (2014) 1562–1574, https://doi.org/10.1002/adfm.201302117.
[185] C. Lee, X. Wei, J.W. Kysar, J. Hone, Measurement of the elastic properties and intrinsic strength of monolayer graphene, Science 321 (2008) 385–388, https://doi.org/10.1126/science.1157996.
[186] A. Cao, P.L. Dickrell, W.G. Sawyer, M.N. Ghasemi-Nejhad, P.M. Ajayan, Super-compressible foamlike carbon nanotube films, Science 310 (2005) 1307–1310, https://doi.org/10.1126/science.1118957.
[187] A. Domenicucci, S. Bedell, R. Roy, D.K. Sadana, A. Mocuta, Use of moire fringe patterns to map relaxation in SiGe on insulator structures fabricated on SIMOX substrates, in: A.G.A.G. Cullis, J.L.J.L. Hutchison (Eds.), Microscopy of Semiconducting Materials: Proceedings of the 14th Conference, Springer Berlin Heidelberg, Oxford, UK, 2005, pp. 89–92.
[188] S.S. Brenner, Growth and properties of "Whiskers", Science 128 (1958) 569–575, https://doi.org/10.1126/science.128.3324.569.
[189] S.S. Hong, M. Gu, M. Verma, V. Harbola, B.Y. Wang, D. Lu, A. Vailionis, Y. Hikita, R. Pentcheva, J.M. Rondinelli, H.Y. Hwang, Extreme tensile strain states in La0.7Ca0.3MnO3 membranes, Science 368 (2020) 71–76, https://doi.org/10.1126/science.aax9753.
[190] L. Tian, Y.Q. Cheng, Z.W. Shan, J. Li, C.C. Wang, X.D. Han, J. Sun, E. Ma, Approaching the ideal elastic limit of metallic glasses, Nat. Commun. 3 (2012) 609, https://doi.org/10.1038/ncomms1619.
[191] L. Li, W. Gao, H. Chen, K. Zhao, P. Wen, Y. Yang, X. Wang, Z. Wei, N. Huo, J. Li, Strong anisotropy and piezo-phototronic effect in SnO_2 microwires, Adv. Electron. Mater. 6 (2020), 1901441, https://doi.org/10.1002/aelm.201901441.
[192] J. Quereda, P. San-Jose, V. Parente, L. Vaquero-Garzon, A.J. Molina-Mendoza, N. Agraït, G. Rubio-Bollinger, F. Guinea, R. Roldán, A. Castellanos-Gomez, Strong modulation of optical properties in black phosphorus through strain-engineered rippling, Nano Lett. 16 (2016) 2931–2937, https://doi.org/10.1021/acs.nanolett.5b04670.
[193] S.X. Yang, C. Wang, H. Sahin, H. Chen, Y. Li, S.S. Li, A. Suslu, F.M. Peeters, Q. Liu, J.B. Li, S. Tongay, Tuning the optical, magnetic, and electrical properties of $ReSe_2$ by nanoscale strain engineering, Nano Lett. 15 (2015) 1660–1666, https://doi.org/10.1021/nl504276u.
[194] D. Lloyd, X. Liu, J.W. Christopher, L. Cantley, A. Wadehra, B.L. Kim, B. B. Goldberg, A.K. Swan, J.S. Bunch, Band gap engineering with ultralarge biaxial strains in suspended monolayer MoS_2, Nano Lett. 16 (2016) 5836–5841, https://doi.org/10.1021/acs.nanolett.6b02615.
[195] Y. Sun, W.M. Choi, H. Jiang, Y.Y. Huang, J.A. Rogers, Controlled buckling of semiconductor nanoribbons for stretchable electronics, Nat. Nanotechnol. 1 (2006) 201, https://doi.org/10.1038/nnano.2006.131.
[196] D.A. Walters, L.M. Ericson, M.J. Casavant, J. Liu, D.T. Colbert, K.A. Smith, R. E. Smalley, Elastic strain of freely suspended single-wall carbon nanotube ropes, Appl. Phys. Lett. 74 (1999) 3803–3805, https://doi.org/10.1063/1.124185.
[197] S. Bertolazzi, J. Brivio, A. Kis, Stretching and breaking of ultrathin MoS_2, ACS Nano 5 (2011) 9703–9709, https://doi.org/10.1021/nn203879f.
[198] J. Cao, E. Ertekin, V. Srinivasan, W. Fan, S. Huang, H. Zheng, J.W.L. Yim, D. R. Khanal, D.F. Ogletree, J.C. Grossmanan, J. Wu, Strain engineering and one-dimensional organization of metal-insulator domains in single-crystal vanadium dioxide beams, Nat. Nanotechnol. 4 (2009) 732–737, https://doi.org/10.1038/nnano.2009.266.
[199] J. Wang, Z. Zeng, C.R. Weinberger, Z. Zhang, T. Zhu, S.X. Mao, In situ atomic-scale observation of twinning-dominated deformation in nanoscale body-centred cubic tungsten, Nat. Mater. 14 (2015) 594–600, https://doi.org/10.1038/nmat4228.
[200] Y.-B. Wang, L.-F. Wang, H.J. Joyce, Q. Gao, X.-Z. Liao, Y.-W. Mai, H.H. Tan, J. Zou, S.P. Ringer, H.-J. Gao, C. Jagadish, Super deformability and Young's modulus of GaAs nanowires, Adv. Mater. 23 (2011) 1356–1360, https://doi.org/10.1002/adma.201004122.
[201] A. Lai, Z. Du, C.L. Gan, C.A. Schuh, Shape memory and superelastic ceramics at small scales, Science 341 (2013) 1505–1508, https://doi.org/10.1126/science.1239745.
[202] J. Zhang, X. Ke, G. Gou, J. Seidel, B. Xiang, P. Yu, W.-I. Liang, A.M. Minor, Y.-h Chu, G. Van Tendeloo, X. Ren, R. Ramesh, A nanoscale shape memory oxide, Nat. Commun. 4 (2013) 2768, https://doi.org/10.1038/ncomms3768.
[203] J.F. Gómez-Cortés, M.L. Nó, I. López-Ferreño, J. Hernández-Saz, S.I. Molina, A. Chuvilin, J.M. San Juan, Size effect and scaling power-law for superelasticity in shape-memory alloys at the nanoscale, Nat. Nanotechnol. 12 (2017) 790, https://doi.org/10.1038/nnano.2017.91.
[204] J.L. MacManus-Driscoll, P. Zerrer, H. Wang, H. Yang, J. Yoon, A. Fouchet, R. Yu, M.G. Blamire, Q. Jia, Strain control and spontaneous phase ordering in vertical nanocomposite heteroepitaxial thin films, Nat. Mater. 7 (2008) 314–320, https://doi.org/10.1038/nmat2124.
[205] C. Cantoni, Y.F. Gao, S.H. Wee, E.D. Specht, J. Gazquez, J.Y. Meng, S. J. Pennycook, A. Goyal, Strain-driven oxygen deficiency in self-assembled, nanostructured, composite oxide films, ACS Nano 5 (2011) 4783–4789, https://doi.org/10.1021/nn2007628.
[206] T. Amrillah, Y. Bitla, K. Shin, T. Yang, Y.-H. Hsieh, Y.-Y. Chiou, H.-J. Liu, T.H. Do, D. Su, Y.-C. Chen, S.-U. Jen, L.-Q. Chen, K.H. Kim, J.-Y. Juang, Y.-H. Chu, Flexible multiferroic bulk heterojunction with giant magnetoelectric coupling via van der Waals epitaxy, ACS Nano 11 (2017) 6122–6130, https://doi.org/10.1021/acsnano.7b02102.
[207] D. Lee, J. Lee, K. Song, F. Xue, S.-Y. Choi, Y. Ma, J. Podkaminer, D. Liu, S.-C. Liu, B. Chung, W. Fan, S.J. Cho, W. Zhou, J. Lee, L.-Q. Chen, S.H. Oh, Z. Ma, C.-B. Eom, Sharpened VO_2 phase transition via controlled release of epitaxial strain, Nano Lett. 17 (2017) 5614–5619, https://doi.org/10.1021/acs.nanolett.7b02482.
[208] S. Kittiwatanakul, S.A. Wolf, J. Lu, Large epitaxial bi-axial strain induces a Mott-like phase transition in VO_2, Appl. Phys. Lett. 105 (2014), 073112, https://doi.org/10.1063/1.4893326.
[209] J. Laverock, A.R.H. Preston, D. Newby, K.E. Smith, S. Sallis, L.F.J. Piper, S. Kittiwatanakul, J.W. Lu, S.A. Wolf, M. Leandersson, T. Balasubramanian, Photoemission evidence for crossover from Peierls-like to Mott-like transition in highly strained VO_2, Phys. Rev. B 86 (2012), 195124, https://doi.org/10.1103/PhysRevB.86.195124.
[210] V. Goian, R. Held, E. Bousquet, Y. Yuan, A. Melville, H. Zhou, V. Gopalan, P. Ghosez, N.A. Spaldin, D.G. Schlom, S. Kamba, Making EuO multiferroic by epitaxial strain engineering, Commun. Mater. 1 (2020) 74, https://doi.org/10.1038/s43246-020-00075-1.
[211] R.J. Zeches, M.D. Rossell, J.X. Zhang, A.J. Hatt, Q. He, C.-H. Yang, A. Kumar, C. H. Wang, A. Melville, C. Adamo, G. Sheng, Y.-H. Chu, J.F. Ihlefeld, R. Erni, C. Ederer, V. Gopalan, L.Q. Chen, D.G. Schlom, N.A. Spaldin, L.W. Martin, R. Ramesh, A strain-driven morphotropic phase boundary in $BiFeO_3$, Science 326 (2009) 977–980, https://doi.org/10.1126/science.1177046.
[212] D. Lee, A. Yoon, S.Y. Jang, J.G. Yoon, J.S. Chung, M. Kim, J.F. Scott, T.W. Noh, Giant flexoelectric effect in ferroelectric epitaxial thin films, Phys. Rev. Lett. 107 (2011), 057602, https://doi.org/10.1103/PhysRevLett.107.057602.
[213] Y.J. Wang, Y.P. Feng, Y.L. Zhu, Y.L. Tang, L.X. Yang, M.J. Zou, W.R. Geng, M. J. Han, X.W. Guo, B. Wu, X.L. Ma, Polar meron lattice in strained oxide ferroelectrics, Nat. Mater. 19 (2020) 881–886, https://doi.org/10.1038/s41563-020-0694-8.
[214] C. Sohn, X. Gao, R.K. Vasudevan, S.M. Neumayer, N. Balke, J.M. Ok, D. Lee, E. Skoropata, H.Y. Jeong, Y.-M. Kim, H.N. Lee, Strain-driven autonomous control of cation distribution for artificial ferroelectrics, Sci. Adv. 7 (2021), https://doi.org/10.1126/sciadv.abd7394.
[215] Y. Chen, Y. Lei, Y. Li, Y. Yu, J. Cai, M.-H. Chiu, R. Rao, Y. Gu, C. Wang, W. Choi, H. Hu, C. Wang, Y. Li, J. Song, J. Zhang, B. Qi, M. Lin, Z. Zhang, A.E. Islam, B. Maruyama, S. Dayeh, L.-J. Li, K. Yang, Y.-H. Lo, S. Xu, Strain engineering and epitaxial stabilization of halide perovskites, Nature 577 (2020) 209–215, https://doi.org/10.1038/s41586-019-1868-x.
[216] H. Guo, S. Dong, P.D. Rack, J.D. Budai, C. Beekman, Z. Gai, W. Siemons, C. M. Gonzalez, R. Timilsina, A.T. Wong, A. Herklotz, P.C. Snijders, E. Dagotto, T. Z. Ward, Strain doping: Reversible single-axis control of a complex oxide lattice via helium implantation, Phys. Rev. Lett. 114 (2015), 256801, https://doi.org/10.1103/PhysRevLett.114.256801.
[217] H. Yoon, M. Choi, T.-W. Lim, H. Kwon, K. Ihm, J.K. Kim, S.-Y. Choi, J. Son, Reversible phase modulation and hydrogen storage in multivalent VO_2 epitaxial thin films, Nat. Mater. 15 (2016) 1113, https://doi.org/10.1038/nmat4692.
[218] T. Ling, D.-Y. Yan, H. Wang, Y. Jiao, Z. Hu, Y. Zheng, L. Zheng, J. Mao, H. Liu, X.-W. Du, M. Jaroniec, S.-Z. Qiao, Activating cobalt(II) oxide nanorods for efficient electrocatalysis by strain engineering, Nat. Commun. 8 (2017) 1509, https://doi.org/10.1038/s41467-017-01872-y.
[219] P. Strasser, S. Koh, T. Anniyev, J. Greeley, K. More, C. Yu, Z. Liu, S. Kaya, D. Nordlund, H. Ogasawara, M.F. Toney, A. Nilsson, Lattice-strain control of the

activity in dealloyed core–shell fuel cell catalysts, Nat. Chem. 2 (2010) 454, https://doi.org/10.1038/nchem.623.
[220] L. Balaghi, G. Bussone, R. Grifone, R. Hübner, J. Grenzer, M. Ghorbani-Asl, A. V. Krasheninnikov, H. Schneider, M. Helm, E. Dimakis, Widely tunable GaAs bandgap via strain engineering in core/shell nanowires with large lattice mismatch, Nat. Commun. 10 (2019) 2793, https://doi.org/10.1038/s41467-019-10654-7.
[221] M.V. Fischetti, F. Gámiz, W. Hänsch, On the enhanced electron mobility in strained-silicon inversion layers, J. Appl. Phys. 92 (2002) 7320–7324, https://doi.org/10.1063/1.1521796.
[222] A.R. Damodaran, E. Breckenfeld, Z.H. Chen, S. Lee, L.W. Martin, Enhancement of ferroelectric curie temperature in $BaTiO_3$ films via strain-induced defect dipole alignment, Adv. Mater. 26 (2014) 6341–6347, https://doi.org/10.1002/adma.201400254.
[223] H. Lu, D.J. Kim, C.W. Bark, S. Ryu, C.B. Eom, E.Y. Tsymbal, A. Gruverman, Mechanically-induced resistive switching in ferroelectric tunnel junctions, Nano Lett. 12 (2012) 6289–6292, https://doi.org/10.1021/nl303396n.
[224] J.P. Locquet, J. Perret, J. Fompeyrine, E. Machler, J.W. Seo, G. Van Tendeloo, Doubling the critical temperature of La1.9Sr0.1CuO4 using epitaxial strain, Nature 394 (1998) 453–456, https://doi.org/10.1038/28810.
[225] J.P. Attfield, A.L. Kharlanov, J.A. McAllister, Cation effects in doped La_2CuO_4 superconductors, Nature 394 (1998) 157–159, https://doi.org/10.1038/28120.
[226] E.D. Minot, Y. Yaish, V. Sazonova, J.-Y. Park, M. Brink, P.L. McEuen, Tuning carbon nanotube band gaps with strain, Phys. Rev. Lett. 90 (2003), 156401, https://doi.org/10.1103/PhysRevLett.90.156401.
[227] S.B. Desai, G. Seol, J.S. Kang, H. Fang, C. Battaglia, R. Kapadia, J.W. Ager, J. Guo, A. Javey, Strain-induced indirect to direct bandgap transition in multilayer WSe_2, Nano Lett. 14 (2014) 4592–4597, https://doi.org/10.1021/nl501638a.
[228] S. Zhang, Z. Yan, Y. Li, Z. Chen, H. Zeng, Atomically thin arsenene and antimonene: semimetal–semiconductor and indirect–direct band-gap transitions, Angew. Chem. Int. Ed. 54 (2015) 3112–3115, https://doi.org/10.1002/anie.201411246.
[229] Z. Zhang, L. Li, J. Horng, N.Z. Wang, F. Yang, Y. Yu, Y. Zhang, G. Chen, K. Watanabe, T. Taniguchi, Strain-modulated bandgap and piezo-resistive effect in black phosphorus field-effect transistors, Nano Lett. 17 (2017) 6097–6103, https://doi.org/10.1021/acs.nanolett.7b02624.
[230] W. Yan, W.Y. He, Z.D. Chu, M.X. Liu, L. Meng, R.F. Dou, Y.F. Zhang, Z.F. Liu, J. C. Nie, L. He, Strain and curvature induced evolution of electronic band structures in twisted graphene bilayer, Nat. Commun. 4 (2013) 2159, https://doi.org/10.1038/ncomms3159.
[231] R. He, P. Yang, Giant piezoresistance effect in silicon nanowires, Nat. Nanotechnol. 1 (2006) 42–46, https://doi.org/10.1038/nnano.2006.53.
[232] L. Sun, D.H. Kim, K.H. Oh, R. Agarwal, Strain-induced large exciton energy shifts in buckled CdS nanowires, Nano Lett. 13 (2013) 3836–3842, https://doi.org/10.1021/nl401860f.
[233] M.A. Khan, J.W. Yang, G. Simin, R. Gaska, M.S. Shur, H.-C. Loye, G. Tamulaitis, A. Zukauskas, D.J. Smith, D. Chandrasekhar, R. Bicknell-Tassius, Lattice and energy band engineering in AlInGaN/GaN heterostructures, Appl. Phys. Lett. 76 (2000) 1161–1163, https://doi.org/10.1063/1.125970.
[234] C. Kisielowski, J. Krüger, S. Ruvimov, T. Suski, J.W. Ager, E. Jones, Z. Liliental-Weber, M. Rubin, E.R. Weber, M.D. Bremser, R.F. Davis, Strain-related phenomena in GaN thin films, Phys. Rev. B 54 (1996) 17745–17753, https://doi.org/10.1103/PhysRevB.54.17745.
[235] O. Stier, M. Grundmann, D. Bimberg, Electronic and optical properties of strained quantum dots modeled by 8-band k-p theory, Phys. Rev. B 59 (1999) 5688–5701, https://doi.org/10.1103/PhysRevB.59.5688.
[236] M.E. Aumer, S.F. LeBoeuf, S.M. Bedair, M. Smith, J.Y. Lin, H.X. Jiang, Effects of tensile and compressive strain on the luminescence properties of AlInGaN/InGaN quantum well structures, Appl. Phys. Lett. 77 (2000) 821–823, https://doi.org/10.1063/1.1306648.
[237] E.C. Le Ru, P. Howe, T.S. Jones, R. Murray, Strain-engineered InAs/GaAs quantum dots for long-wavelength emission, Phys. Rev. B 67 (2003), 165303, https://doi.org/10.1103/PhysRevB.67.165303.
[238] K. He, C. Poole, K.F. Mak, J. Shan, Experimental demonstration of continuous electronic structure tuning via strain in atomically thin MoS_2, Nano Lett. 13 (2013) 2931–2936, https://doi.org/10.1021/nl4013166.
[239] F. Boxberg, J. Tulkki, Theory of the electronic structure and carrier dynamics of strain-induced (Ga, In) As quantum dots, Rep. Prog. Phys. 70 (2007) 1425–1471, https://doi.org/10.1088/0034-4885/70/8/r04.
[240] A. Castellanos-Gomez, R. Roldán, E. Cappelluti, M. Buscema, F. Guinea, H.S. van der Zant, G.A. Steele, Local strain engineering in atomically thin MoS_2, Nano Lett. 13 (2013) 5361–5366, https://doi.org/10.1021/nl402875m.
[241] R. Frisenda, M. Drüppel, R. Schmidt, S. Michaelis de Vasconcellos, D. Perez de Lara, R. Bratschitsch, M. Rohlfing, A. Castellanos-Gomez, Biaxial strain tuning of the optical properties of single-layer transition metal dichalcogenides, npj 2D Mater. Appl. 1 (2017) 10, https://doi.org/10.1038/s41699-017-0013-7.
[242] J. Greil, A. Lugstein, C. Zeiner, G. Strasser, E. Bertagnolli, Tuning the electro-optical properties of germanium nanowires by tensile strain, Nano Lett. 12 (2012) 6230–6234, https://doi.org/10.1021/nl303288g.
[243] R.S. Jacobsen, K.N. Andersen, P.I. Borel, J. Fage-Pedersen, L.H. Frandsen, O. Hansen, M. Kristensen, A.V. Lavrinenko, G. Moulin, H. Ou, C. Peucheret, B. Zsigri, A. Bjarklev, Strained silicon as a new electro-optic material, Nature 441 (2006) 199–202, https://doi.org/10.1038/nature04706.
[244] W.S. Choi, J.H. Kwon, H. Jeen, J.E. Hamann-Borrero, A. Radi, S. Macke, R. Sutarto, F.Z. He, G.A. Sawatzky, V. Hinkov, M. Kim, H.N. Lee, Strain-induced spin states in atomically ordered cobaltites, Nano Lett. 12 (2012) 4966–4970, https://doi.org/10.1021/nl302562f.
[245] Y. Kato, R.C. Myers, A.C. Gossard, D.D. Awschalom, Coherent spin manipulation without magnetic fields in strained semiconductors, Nature 427 (2004) 50–53, https://doi.org/10.1038/nature02202.
[246] D.H. Mosca, F. Vidal, V.H. Etgens, Strain engineering of the magnetocaloric effect in MnAs epilayers, Phys. Rev. Lett. 101 (2008), 125503, https://doi.org/10.1103/PhysRevLett.101.125503.
[247] L. Abad, V. Laukhin, S. Valencia, A. Gaup, W. Gudat, L. Balcells, B. Martinez, Interfacial strain: the driving force for selective orbital occupancy in manganite thin films, Adv. Funct. Mater. 17 (2007) 3918–3925, https://doi.org/10.1002/adfm.200700137.
[248] M. Mavrikakis, B. Hammer, J.K. Nørskov, Effect of strain on the reactivity of metal surfaces, Phys. Rev. Lett. 81 (1998) 2819–2822, https://doi.org/10.1103/PhysRevLett.81.2819.
[249] L. Jia, D.J. Shu, M. Wang, Tuning the area percentage of reactive surface of TiO_2 by strain engineering, Phys. Rev. Lett. 109 (2012), 156104, https://doi.org/10.1103/PhysRevLett.109.156104.
[250] M. Kubicek, Z.H. Cai, W. Ma, B. Yildiz, H. Hutter, J. Fleig, Tensile lattice strain accelerates oxygen surface exchange and diffusion in $La_{1-x}Sr_xCoO_{3-\delta}$ thin films, ACS Nano 7 (2013) 3276–3286, https://doi.org/10.1021/nn305987x.
[251] U. Aschauer, N. Vonrueti, N.A. Spaldin, Effect of epitaxial strain on cation and anion vacancy formation in MnO, Phys. Rev. B 92 (2015), 054103, https://doi.org/10.1103/PhysRevB.92.054103.
[252] S.C. Wimbush, M.C. Li, M.E. Vickers, B. Maiorov, D.M. Feldmann, Q.X. Jia, J. L. MacManus-Driscoll, Interfacial strain-induced oxygen disorder as the cause of enhanced critical current density in superconducting thin films, Adv. Funct. Mater. 19 (2009) 835–841, https://doi.org/10.1002/adfm.200801112.
[253] X.Z. Lu, J.M. Rondinelli, Epitaxial-strain-induced polar-to-nonpolar transitions in layered oxides, Nat. Mater. 15 (2016) 951–955, https://doi.org/10.1038/nmat4664.
[254] A. Pratt, L. Lari, O. Hovorka, A. Shah, C. Woffinden, S.P. Tear, C. Binns, R. Kroger, Enhanced oxidation of nanoparticles through strain-mediated ionic transport, Nat. Mater. 13 (2014) 26–30, https://doi.org/10.1038/nmat3785.
[255] J.A. Steele, H. Jin, I. Dovgaliuk, R.F. Berger, T. Braeckevelt, H. Yuan, C. Martin, E. Solano, K. Lejaeghere, S.M.J. Rogge, C. Notebaert, W. Vandezande, K.P. F. Janssen, B. Goderis, E. Debroye, Y.-K. Wang, Y. Dong, D. Ma, M. Saidaminov, H. Tan, Z. Lu, V. Dyadkin, D. Chernyshov, V. Van Speybroeck, E.H. Sargent, J. Hofkens, M.B.J. Roeffaers, Thermal unequilibrium of strained black $CsPbI_3$ thin films, Science 365 (2019) 679–684, https://doi.org/10.1126/science.aax3878.
[256] J. Welser, J.L. Hoyt, J.F. Gibbons, Electron mobility enhancement in strained-Si n-type metal-oxide-semiconductor field-effect transistors, IEEE Electron Device Lett. 15 (1994) 100–102, https://doi.org/10.1109/55.285389.
[257] M. Ieong, B. Doris, J. Kedzierski, K. Rim, M. Yang, Silicon device scaling to the sub-10-nm regime, Science 306 (2004) 2057–2060, https://doi.org/10.1126/science.1100731.
[258] S.E. Thompson, M. Armstrong, C. Auth, S. Cea, R. Chau, G. Glass, T. Hoffman, J. Klaus, M. Zhiyong, B. Mcintyre, A. Murthy, B. Obradovic, L. Shifren, S. Sivakumar, S. Tyagi, T. Ghani, K. Mistry, M. Bohr, Y. El-Mansy, A logic nanotechnology featuring strained-silicon, IEEE Electron Device Lett. 25 (2004) 191–193, https://doi.org/10.1109/LED.2004.825195.
[259] P.R. Chidambaram, C. Bowen, S. Chakravarthi, C. Machala, R. Wise, Fundamentals of silicon material properties for successful exploitation of strain engineering in modern CMOS manufacturing, IEEE Trans. Electron Devices 53 (2006) 944–964, https://doi.org/10.1109/TED.2006.872912.
[260] T. Ghani, M. Armstrong, C. Auth, M. Bost, P. Charvat, G. Glass, T. Hoffmann, K. Johnson, C. Kenyon, J. Klaus, A 90nm high volume manufacturing logic technology featuring novel 45nm gate length strained silicon CMOS transistors, In: Proceedings of the Electron Devices Meeting, 2003. IEDM'03 Technical Digest. IEEE International, IEEE, 2003, pp. 11.16. 11–11.16. 13.
[261] K. Rim, K. Chan, L. Shi, D. Boyd, J. Ott, N. Klymko, F. Cardone, L. Tai, S. Koester, M. Cobb, D. Canaperi, B. To, E. Duch, I. Babich, R. Carruthers, P. Saunders, G. Walker, Y. Zhang, M. Steen, M. Ieong, Fabrication and mobility characteristics of ultra-thin strained Si directly on insulator (SSDOI) MOSFETs, In: Proceedings of the IEEE International Electron Devices Meeting 2003, 2003, pp. 3.1.1–3.1.4.
[262] S.W. Bedell, A. Khakifirooz, D.K. Sadana, Strain scaling for CMOS, MRS Bull. 39 (2014) 131–137, https://doi.org/10.1557/mrs.2014.5.
[263] X.D. Han, K. Zheng, Y.F. Zhang, X.N. Zhang, Z. Zhang, Z.L. Wang, Low-temperature in situ large-strain plasticity of silicon nanowires, Adv. Mater. 19 (2007) 2112–2118, https://doi.org/10.1002/adma.200602705.
[264] J.H. Park, J.M. Coy, T.S. Kasirga, C. Huang, Z. Fei, S. Hunter, D.H. Cobden, Measurement of a solid-state triple point at the metal-insulator transition in VO_2, Nature 500 (2013) 431–434, https://doi.org/10.1038/nature12425.
[265] T. Shokuhfar, G.K. Arumugam, P.A. Heiden, R.S. Yassar, C. Friedrich, Direct compressive measurements of individual titanium dioxide nanotubes, ACS Nano 3 (2009) 3098–3102, https://doi.org/10.1021/nn900202x.
[266] M.-F. Yu, B.S. Files, S. Arepalli, R.S. Ruoff, Tensile loading of ropes of single wall carbon nanotubes and their mechanical properties, Phys. Rev. Lett. 84 (2000) 5552–5555, https://doi.org/10.1103/PhysRevLett.84.5552.
[267] Y.Y. Hui, X. Liu, W. Jie, N.Y. Chan, J. Hao, Y.-T. Hsu, L.-J. Li, W. Guo, S.P. Lau, Exceptional tunability of band energy in a compressively strained trilayer MoS_2 sheet, ACS Nano 7 (2013) 7126–7131, https://doi.org/10.1021/nn4024834.
[268] C. Bousige, F. Balima, D. Machon, G.S. Pinheiro, A. Torres-Dias, J. Nicolle, D. Kalita, N. Bendiab, L. Marty, V. Bouchiat, G. Montagnac, A.G. Souza, P. Poncharal, A. San-Miguel, Biaxial strain transfer in supported graphene, Nano Lett. 17 (2017) 21–27, https://doi.org/10.1021/acs.nanolett.6b02981.

[269] G.Y. Jing, H.L. Duan, X.M. Sun, Z.S. Zhang, J. Xu, Y.D. Li, J.X. Wang, D.P. Yu, Surface effects on elastic properties of silver nanowires: contact atomic-force microscopy, Phys. Rev. B 73 (2006), 235409, https://doi.org/10.1103/PhysRevB.73.235409.

[270] S. Hoffmann, I. Utke, B. Moser, J. Michler, S.H. Christiansen, V. Schmidt, S. Senz, P. Werner, U. Gösele, C. Ballif, Measurement of the bending strength of vapor−liquid−solid grown silicon nanowires, Nano Lett. 6 (2006) 622–625, https://doi.org/10.1021/nl052223z.

[271] X. Han, L. Kou, X. Lang, J. Xia, N. Wang, R. Qin, J. Lu, J. Xu, Z. Liao, X. Zhang, X. Shan, X. Song, J. Gao, W. Guo, D. Yu, Electronic and mechanical coupling in bent ZnO nanowires, Adv. Mater. 21 (2009) 4937–4941, https://doi.org/10.1002/adma.200900956.

[272] X.W. Fu, G. Jacopin, M. Shahmohammadi, R. Liu, M. Benameur, J.D. Ganiere, J. Feng, W.L. Guo, Z.M. Liao, B. Deveaud, D.P. Yu, Exciton drift in semiconductors under uniform strain gradients: application to bent ZnO microwires, Acs Nano 8 (2014) 3412–3420, https://doi.org/10.1021/nn4062353.

[273] M.R. Falvo, G.J. Clary, R.M. Taylor, V. Chi, F.P. Brooks, S. Washburn, R. Superfine, Bending and buckling of carbon nanotubes under large strain, Nature 389 (1997) 582–584, https://doi.org/10.1038/39282.

[274] D.-Y. Khang, H. Jiang, Y. Huang, J.A. Rogers, A stretchable form of single-crystal silicon for high-performance electronics on rubber substrates, Science 311 (2006) 208–212, https://doi.org/10.1126/science.1121401.

[275] Y. Wang, R. Yang, Z. Shi, L. Zhang, D. Shi, E. Wang, G. Zhang, Super-elastic graphene ripples for flexible strain sensors, ACS Nano 5 (2011) 3645–3650, https://doi.org/10.1021/nn103523t.

[276] M.H. Zhao, Z.-Z. Ye, S.X. Mao, Photoinduced stiffening in ZnO nanobelts, Phys. Rev. Lett. 102 (2009), 045502, https://doi.org/10.1103/PhysRevLett.102.045502.

[277] G. Stan, C.V. Ciobanu, P.M. Parthangal, R.F. Cook, Diameter-dependent radial and tangential elastic moduli of ZnO nanowires, Nano Lett. 7 (2007) 3691–3697, https://doi.org/10.1021/nl071986e.

[278] S. Manzeli, A. Allain, A. Ghadimi, A. Kis, Piezoresistivity and strain-induced band gap tuning in atomically thin MoS_2, Nano Lett. 15 (2015) 5330–5335, https://doi.org/10.1021/acs.nanolett.5b01689.

[279] A. Petraru, R. Soni, H. Kohlstedt, Voltage controlled biaxial strain in VO_2 films grown on 0.72Pb($Mg_{1/3}Nb_{2/3}$)-0.28$PbTiO_3$ crystals and its effect on the transition temperature, Appl. Phys. Lett. 105 (2014), 092902, https://doi.org/10.1063/1.4894536.

[280] P. Parikh, C. Chakraborty, T.S. Abhilash, S. Sengupta, C. Cheng, J. Wu, M. M. Deshmukh, Dynamically tracking the strain across the metal insulator transition in VO_2 measured using electromechanical resonators, Nano Lett. 13 (2013) 4685–4689, https://doi.org/10.1021/nl402116f.

[281] J. Sakai, M. Zaghrioui, M. Matsushima, H. Funakubo, K. Okimura, Impact of thermal expansion of substrates on phase transition temperature of VO_2 films, J. Appl. Phys. 116 (2014), 123510, https://doi.org/10.1063/1.4896500.

[282] Y. Wang, X. Sun, Z. Chen, Z. Cai, H. Zhou, T.-M. Lu, J. Shi, Defect-engineered epitaxial VO2±δ in strain engineering of heterogeneous soft crystals, Sci. Adv. 4 (2018), https://doi.org/10.1126/sciadv.aar3679.

[283] Y. Wang, L. Seewald, Y.-Y. Sun, P. Keblinski, X. Sun, S. Zhang, T.-M. Lu, J. M. Johnson, J. Hwang, J. Shi, Nonlinear electron-lattice interactions in a wurtzite semiconductor enabled via strongly correlated oxide, Adv. Mater. 28 (2016) 8975–8982, https://doi.org/10.1002/adma.201602178.

[284] J. Jiang, Z. Chen, Y. Hu, Y. Xiang, L. Zhang, Y. Wang, G.-C. Wang, J. Shi, Flexo-photovoltaic effect in MoS_2, Nat. Nanotechnol. (2021), https://doi.org/10.1038/s41565-021-00919-y.

[285] S.-Y. Chung, S.-Y. Choi, J.-G. Kim, Y.-M. Kim, Quadruple-junction lattice coherency and phase separation in a binary-phase system, Nat. Commun. 6 (2015) 8252, https://doi.org/10.1038/ncomms9252.

[286] D.A. Cogswell, M.Z. Bazant, Coherency strain and the kinetics of phase separation in $LiFePO_4$ nanoparticles, ACS Nano 6 (2012) 2215–2225, https://doi.org/10.1021/nn204177u.

[287] Z. Hiroi, H. Hayamizu, T. Yoshida, Y. Muraoka, Y. Okamoto, J.-I. Yamaura, Y. Ueda, Spinodal decomposition in the TiO_2–VO_2 system, Chem. Mater. 25 (2013) 2202–2210, https://doi.org/10.1021/cm400236p.

[288] S. Nambu, M. Oiji, Coherent phase diagram for spinodal decomposition in the tetragonal titanium dioxide – tin oxide system, J. Am. Ceram. Soc. 74 (1991) 1910–1915, https://doi.org/10.1111/j.1151-2916.1991.tb07808.x.

[289] E.M. Mannebach, R. Li, K.-A. Duerloo, C. Nyby, P. Zalden, T. Vecchione, F. Ernst, A.H. Reid, T. Chase, X. Shen, S. Weathersby, C. Hast, R. Hettel, R. Coffee, N. Hartmann, A.R. Fry, Y. Yu, L. Cao, T.F. Heinz, E.J. Reed, H.A. Dürr, X. Wang, A. M. Lindenberg, Dynamic structural response and deformations of monolayer MoS_2 visualized by femtosecond electron diffraction, Nano Lett. 15 (2015) 6889–6895, https://doi.org/10.1021/acs.nanolett.5b02805.

[290] A.J. McKenna, J.K. Eliason, D.J. Flannigan, Spatiotemporal evolution of coherent elastic strain waves in a single MoS_2 flake, Nano Lett. 17 (2017) 3952–3958, https://doi.org/10.1021/acs.nanolett.7b01565.

[291] Y. Wang, Z. Chen, F. Deschler, X. Sun, T.-M. Lu, E.A. Wertz, J.-M. Hu, J. Shi, Epitaxial halide perovskite lateral double heterostructure, ACS Nano 11 (2017) 3355–3364, https://doi.org/10.1021/acsnano.7b00724.

[292] D.J. Hilton, R.P. Prasankumar, S. Fourmaux, A. Cavalleri, D. Brassard, M.A. El Khakani, J.C. Kieffer, A.J. Taylor, R.D. Averitt, Enhanced photosusceptibility near Tc for the light-induced insulator-to-metal phase transition in vanadium dioxide, Phys. Rev. Lett. 99 (2007), 226401, https://doi.org/10.1103/PhysRevLett.99.226401.

[293] L.Q. Zhang, X.H. Liu, Y. Liu, S. Huang, T. Zhu, L.J. Gui, S.X. Mao, Z.Z. Ye, C. M. Wang, J.P. Sullivan, J.Y. Huang, Controlling the lithiation-induced strain and charging rate in nanowire electrodes by coating, ACS Nano 5 (2011) 4800–4809, https://doi.org/10.1021/nn200770p.

[294] J.Y. Huang, L. Zhong, C.M. Wang, J.P. Sullivan, W. Xu, L.Q. Zhang, S.X. Mao, N. S. Hudak, X.H. Liu, A. Subramanian, H. Fan, L. Qi, A. Kushima, J. Li, In situ observation of the electrochemical lithiation of a single SnO_2 nanowire electrode, Science 330 (2010) 1515–1520, https://doi.org/10.1126/science.1195628.

[295] H. Sun, G. Xin, T. Hu, M. Yu, D. Shao, X. Sun, J. Lian, High-rate lithiation-induced reactivation of mesoporous hollow spheres for long-lived lithium-ion batteries, Nat. Commun. 5 (2014) 4526, https://doi.org/10.1038/ncomms5526.

[296] X.H. Liu, H. Zheng, L. Zhong, S. Huang, K. Karki, L.Q. Zhang, Y. Liu, A. Kushima, W.T. Liang, J.W. Wang, J.-H. Cho, E. Epstein, S.A. Dayeh, S.T. Picraux, T. Zhu, J. Li, J.P. Sullivan, J. Cumings, C. Wang, S.X. Mao, Z.Z. Ye, S. Zhang, J.Y. Huang, Anisotropic swelling and fracture of silicon nanowires during lithiation, Nano Lett. 11 (2011) 3312–3318, https://doi.org/10.1021/nl201684d.

[297] X.H. Liu, L. Zhong, S. Huang, S.X. Mao, T. Zhu, J.Y. Huang, Size-dependent fracture of silicon nanoparticles during lithiation, ACS Nano 6 (2012) 1522–1531, https://doi.org/10.1021/nn204476h.

[298] M.T. McDowell, S.W. Lee, W.D. Nix, Y. Cui, 25th anniversary article: understanding the lithiation of silicon and other alloying anodes for lithium-ion batteries, Adv. Mater. 25 (2013) 4966–4985, https://doi.org/10.1002/adma.201301795.

[299] Y. Liu, H. Zheng, X.H. Liu, S. Huang, T. Zhu, J. Wang, A. Kushima, N.S. Hudak, X. Huang, S. Zhang, S.X. Mao, X. Qian, J. Li, J.Y. Huang, Lithiation-induced embrittlement of multiwalled carbon nanotubes, ACS Nano 5 (2011) 7245–7253, https://doi.org/10.1021/nn202071y.

[300] M. Gu, H. Yang, D.E. Perea, J.-G. Zhang, S. Zhang, C.-M. Wang, Bending-induced symmetry breaking of lithiation in germanium nanowires, Nano Lett. 14 (2014) 4622–4627, https://doi.org/10.1021/nl501680w.

[301] N. Balke, S. Jesse, A.N. Morozovska, E. Eliseev, D.W. Chung, Y. Kim, L. Adamczyk, R.E. García, N. Dudney, S.V. Kalinin, Nanoscale mapping of ion diffusion in a lithium-ion battery cathode, Nat. Nanotechnol. 5 (2010) 749, https://doi.org/10.1038/nnano.2010.174.

[302] Y. Zhu, R.L. Withers, L. Bourgeois, C. Dwyer, J. Etheridge, Direct mapping of Li-enabled octahedral tilt ordering and associated strain in nanostructured perovskites, Nat. Mater. 14 (2015) 1142–1149, https://doi.org/10.1038/nmat4390.

[303] N. Lu, P. Zhang, Q. Zhang, R. Qiao, Q. He, H.-B. Li, Y. Wang, J. Guo, D. Zhang, Z. Duan, Z. Li, M. Wang, S. Yang, M. Yan, E. Arenholz, S. Zhou, W. Yang, L. Gu, C.-W. Nan, J. Wu, Y. Tokura, P. Yu, Electric-field control of tri-state phase transformation with a selective dual-ion switch, Nature 546 (2017) 124–128, https://doi.org/10.1038/nature22389.

[304] H. Jeen, W.S. Choi, M.D. Biegalski, C.M. Folkman, I.C. Tung, D.D. Fong, J. W. Freeland, D. Shin, H. Ohta, M.F. Chisholm, H.N. Lee, Reversible redox reactions in an epitaxially stabilized $SrCoO_x$ oxygen sponge, Nat. Mater. 12 (2013) 1057, https://doi.org/10.1038/nmat3736.

[305] O.I. Lebedev, J. Verbeeck, G. Van Tendeloo, O. Shapoval, A. Belenchuk, V. Moshnyaga, B. Damashcke, K. Samwer, Structural phase transitions and stress accommodation in (La0.67Ca0.33MnO3)1-x:(MgO)x composite films, Phys. Rev. B 66 (2002), 104421, https://doi.org/10.1103/PhysRevB.66.104421.

[306] S. Kang, A. Goyal, J. Li, A.A. Gapud, P.M. Martin, L. Heatherly, J.R. Thompson, D. K. Christen, F.A. List, M. Paranthaman, D.F. Lee, High-performance high Tc superconducting wires, Science 311 (2006) 1911–1914, https://doi.org/10.1126/science.1124872.

[307] H. Yang, H. Wang, J. Yoon, Y. Wang, M. Jain, D.M. Feldmann, P.C. Dowden, J. L. MacManus-Driscoll, Q. Jia, Vertical interface effect on the physical properties of self-assembled nanocomposite epitaxial films, Adv. Mater. 21 (2009) 3794–3798, https://doi.org/10.1002/adma.200900781.

[308] J.K. Kawasaki, B.D. Schultz, H. Lu, A.C. Gossard, C.J. Palmstrøm, Surface-mediated tunable self-assembly of single crystal semimetallic ErSb/GaSb nanocomposite structures, Nano Lett. 13 (2013) 2895–2901, https://doi.org/10.1021/nl4012563.

[309] S. Lee, W.R. Zhang, F. Khatkhatay, H.Y. Wang, Q.X. Jia, J.L. MacManus-Driscoll, Ionic conductivity increased by two orders of magnitude in micrometer-thick vertical yttria-stabilized ZrO_2 nanocomposite films, Nano Lett. 15 (2015) 7362–7369, https://doi.org/10.1021/acs.nanolett.5b02726.

[310] Y. Wang, Y.-Y. Sun, S. Zhang, T.-M. Lu, J. Shi, Band gap engineering of a soft inorganic compound PbI_2 by incommensurate van der Waals epitaxy, Appl. Phys. Lett. 108 (2016), 013105, https://doi.org/10.1063/1.4939269.

[311] K. Zhang, S. Hu, Y. Zhang, T. Zhang, X. Zhou, Y. Sun, T.-X. Li, H.J. Fan, G. Shen, X. Chen, Self-induced uniaxial strain in MoS_2 monolayers with local van der Waals-stacked interlayer interactions, ACS Nano 9 (2015) 2704–2710, https://doi.org/10.1021/acsnano.5b00547.

[312] J. Jiang, Y. Bitla, C.-W. Huang, T.H. Do, H.-J. Liu, Y.-H. Hsieh, C.-H. Ma, C.-Y. Jang, Y.-H. Lai, P.-W. Chiu, W.-W. Wu, Y.-C. Chen, Y.-C. Zhou, Y.-H. Chu, Flexible ferroelectric element based on van der Waals heteroepitaxy, Sci. Adv. 3 (2017), e1700121, https://doi.org/10.1126/sciadv.1700121.

[313] J.-K. Lee, S. Yamazaki, H. Yun, J. Park, G.P. Kennedy, G.-T. Kim, O. Pietzsch, R. Wiesendanger, S. Lee, S. Hong, U. Dettlaff-Weglikowska, S. Roth, Modification of electrical properties of graphene by substrate-induced nanomodulation, Nano Lett. 13 (2013) 3494–3500, https://doi.org/10.1021/nl400827p.

[314] M. Ishigami, J.H. Chen, W.G. Cullen, M.S. Fuhrer, E.D. Williams, Atomic structure of graphene on SiO_2, Nano Lett. 7 (2007) 1643–1648, https://doi.org/10.1021/nl070613a.

[315] L.M. Rodriguez-Martinez, J.P. Attfield, Cation disorder and size effects in magnetoresistive manganese oxide perovskites, Phys. Rev. B 54 (1996) R15622–R15625, https://doi.org/10.1103/PhysRevB.54.R15622.

[316] N.S. Ramgir, Y.K. Hwang, I.S. Mulla, J.S. Chang, Effect of particle size and strain in nanocrystalline SnO_2 according to doping concentration of ruthenium, Solid State Sci. 8 (2006) 359–362, https://doi.org/10.1016/j.solidstatesciences.2006.02.008.
[317] R.C. Haislmaier, E.D. Grimley, M.D. Biegalski, J.M. LeBeau, S. Trolier-McKinstry, V. Gopalan, R. Engel-Herbert, Unleashing strain induced ferroelectricity in complex oxide thin films via precise stoichiometry control, Adv. Funct. Mater. 26 (2016) 7271–7279, https://doi.org/10.1002/adfm.201602767.
[318] C.V. Ramana, K.K. Bharathi, A. Garcia, A.L. Campbell, Growth behavior, lattice expansion, strain, and surface morphology of nanocrystalline, monoclinic HfO_2 thin films, J. Phys. Chem. C 116 (2012) 9955–9960, https://doi.org/10.1021/jp211109h.
[319] M. Yang, Y. Yang, B. Hong, L. Wang, Z. Luo, X. Li, C. Kang, M. Li, H. Zong, C. Gao, Surface-growth-mode-induced strain effects on the metal-insulator transition in epitaxial vanadium dioxide thin films, RSC Adv. 5 (2015) 80122–80128, https://doi.org/10.1039/c5ra13490k.
[320] S.R. Spurgeon, J.D. Sloppy, D.M. Kepaptsoglou, P.V. Balachandran, S. Nejati, J. Karthik, A.R. Damodaran, C.L. Johnson, H. Ambaye, R. Goyette, V. Lauter, Q. M. Ramasse, J.C. Idrobo, K.K.S. Lau, S.E. Lofland, J.M. Rondinelli, L.W. Martin, M.L. Taheri, Thickness-dependent crossover from charge- to strain-mediated magnetoelectric coupling in ferromagnetic/piezoelectric oxide heterostructures, ACS Nano 8 (2014) 894–903, https://doi.org/10.1021/nn405636c.
[321] Z.H. Ni, T. Yu, Y.H. Lu, Y.Y. Wang, Y.P. Feng, Z.X. Shen, Uniaxial strain on graphene: Raman spectroscopy study and band-gap opening, ACS Nano 2 (2008) 2301–2305, https://doi.org/10.1021/nn800459e.
[322] J.X. Zhang, B. Xiang, HeQ, J. Seidel, R.J. Zeches, YuP, S.Y. Yang, C.H. Wang, Y. H. Chu, L.W. Martin, A.M. Minor, R. Ramesh, Large field-induced strains in a lead-free piezoelectric material, Nat. Nanotechnol. 6 (2011) 98–102, https://doi.org/10.1038/nnano.2010.265.
[323] A. Kumar, F. Ciucci, A.N. Morozovska, S.V. Kalinin, S. Jesse, Measuring oxygen reduction/evolution reactions on the nanoscale, Nat. Chem. 3 (2011) 707, https://doi.org/10.1038/nchem.1112.
[324] X. Ren, Large electric-field-induced strain in ferroelectric crystals by point-defect-mediated reversible domain switching, Nat. Mater. 3 (2004) 91–94, https://doi.org/10.1038/nmat1051.
[325] E. Szilagyi, J.S. Wittenberg, T.A. Miller, K. Lutker, F. Quirin, H. Lemke, D.L. Zhu, M. Chollet, J. Robinson, H.D. Wen, K. Sokolowski-Tinten, A.M. Lindenberg, Visualization of nanocrystal breathing modes at extreme strains, Nat. Commun. 6 (2015), https://doi.org/10.1038/ncomms7577.
[326] D.R. Cremons, D.A. Plemmons, D.J. Flannigan, Femtosecond electron imaging of defect-modulated phonon dynamics, Nat. Commun. 7 (2016) 11230, https://doi.org/10.1038/ncomms11230.
[327] L.Y. Beaulieu, K.W. Eberman, R.L. Turner, L.J. Krause, J.R. Dahn, Colossal reversible volume changes in lithium alloys, Electrochem. Solid-State Lett. 4 (2001) A137–A140, https://doi.org/10.1149/1.1388178.
[328] B.B. Nelson-Cheeseman, H. Zhou, P.V. Balachandran, G. Fabbris, J. Hoffman, D. Haskel, J.M. Rondinelli, A. Bhattacharya, Polar cation ordering: A route to introducing > 10% bond strain into layered oxide films, Adv. Funct. Mater. 24 (2014) 6884–6891, https://doi.org/10.1002/adfm.201401077.
[329] N.B. Aetukuri, A.X. Gray, M. Drouard, M. Cossale, L. Gao, A.H. Reid, R. Kukreja, H. Ohldag, C.A. Jenkins, E. Arenholz, K.P. Roche, H.A. Duerr, M.G. Samant, S.S. P. Parkin, Control of the metal-insulator transition in vanadium dioxide by modifying orbital occupancy, Nat. Phys. 9 (2013) 661–666, https://doi.org/10.1038/nphys2733.
[330] A. Melville, T. Mairoser, A. Schmehl, T. Birol, T. Heeg, B. Hollander, J. Schubert, C.J. Fennie, D.G. Schlom, Effect of film thickness and biaxial strain on the curie temperature of EuO, Appl. Phys. Lett. 102 (2013), 062404, https://doi.org/10.1063/1.4789972.
[331] Q. Jia, J. Grenzer, H. He, W. Anwand, Y. Ji, Y. Yuan, K. Huang, T. You, W. Yu, W. Ren, X. Chen, M. Liu, S. Facsko, X. Wang, X. Ou, 3D local manipulation of the metal–insulator transition behavior in VO_2 thin film by defect-induced lattice engineering, Adv. Mater. Interfaces 5 (2018), 1701268, https://doi.org/10.1002/admi.201701268.
[332] I.A. Blech, E.S. Meieran, Enhanced X-ray diffraction from substrate crystals containing discontinuous surface films, J. Appl. Phys. 38 (1967) 2913–2919, https://doi.org/10.1063/1.1710023.
[333] A. Segmüller, J. Angilelo, S.J.La Placa, Automatic X-ray diffraction measurement of the lattice curvature of substrate wafers for the determination of linear strain patterns, J. Appl. Phys. 51 (1980) 6224–6230, https://doi.org/10.1063/1.327606.
[334] S. Schmidt, S.F. Nielsen, C. Gundlach, L. Margulies, X. Huang, D.J. Jensen, Watching the growth of bulk grains during recrystallization of deformed metals, Science 305 (2004) 229–232, https://doi.org/10.1126/science.1098627.
[335] B.C. Larson, W. Yang, G.E. Ice, J.D. Budai, J.Z. Tischler, Three-dimensional X-ray structural microscopy with submicrometre resolution, Nature 415 (2002) 887–890, https://doi.org/10.1038/415887a.
[336] I. Robinson, R. Harder, Coherent X-ray diffraction imaging of strain at the nanoscale, Nat. Mater. 8 (2009) 291–298, https://doi.org/10.1038/nmat2400.
[337] D.M. Fritz, D.A. Reis, B. Adams, R.A. Akre, J. Arthur, C. Blome, P.H. Bucksbaum, A.L. Cavalieri, S. Engemann, S. Fahy, R.W. Falcone, P.H. Fuoss, K.J. Gaffney, M. J. George, J. Hajdu, M.P. Hertlein, P.B. Hillyard, M. Horn-von Hoegen, M. Kammler, J. Kaspar, R. Kienberger, P. Krejcik, S.H. Lee, A.M. Lindenberg, B. McFarland, D. Meyer, T. Montagne, É.D. Murray, A.J. Nelson, M. Nicoul, R. Pahl, J. Rudati, H. Schlarb, D.P. Siddons, K. Sokolowski-Tinten, T. Tschentscher, D. von der Linde, J.B. Hastings, Ultrafast bond softening in bismuth: Mapping a solid's interatomic potential with X-rays, in: Science, 315, 2007, pp. 633–636, https://doi.org/10.1126/science.1135009.
[338] H. Ade, H. Stoll, Near-edge X-ray absorption fine-structure microscopy of organic and magnetic materials, Nat. Mater. 8 (2009) 281–290, https://doi.org/10.1038/nmat2399.
[339] J.L. Taraci, M.J. Hytch, T. Clement, P. Peralta, M.R. McCartney, J. Drucker, S. T. Picraux, Strain mapping in nanowires, Nanotechnology 16 (2005) 2365–2371, https://doi.org/10.1088/0957-44/16/10/062.
[340] M.J. Hÿtch, E. Snoeck, R. Kilaas, Quantitative measurement of displacement and strain fields from HREM micrographs, Ultramicroscopy 74 (1998) 131–146, https://doi.org/10.1016/S0304-3991(98)00035-7.
[341] R. Bierwolf, M. Hohenstein, F. Phillipp, O. Brandt, G.E. Crook, K. Ploog, Direct measurement of local lattice distortions in strained layer structures by HREM, Ultramicroscopy 49 (1993) 273–285, https://doi.org/10.1016/0304-3991(93)90234-O.
[342] M.R. McCartney, D.J. Smith, Electron holography: phase imaging with nanometer resolution, Annu. Rev. Mater. Res. 37 (2007) 729–767, https://doi.org/10.1146/annurev.matsci.37.052506.084219.
[343] P.A. Midgley, R.E. Dunin-Borkowski, Electron tomography and holography in materials science, Nat. Mater. 8 (2009) 271–280, https://doi.org/10.1038/nmat2406.
[344] K.W. Urban, Studying atomic structures by aberration-corrected transmission electron microscopy, Science 321 (2008) 506–510, https://doi.org/10.1126/science.1152800.
[345] M. Hytch, F. Houdellier, F. Hue, E. Snoeck, Nanoscale holographic interferometry for strain measurements in electronic devices, Nature 453 (2008) 1086–1089, https://doi.org/10.1038/nature07049.
[346] A. Armigliato, R. Balboni, G.P. Carnevale, G. Pavia, D. Piccolo, S. Frabboni, A. Benedetti, A.G. Cullis, Application of convergent beam electron diffraction to two-dimensional strain mapping in silicon devices, Appl. Phys. Lett. 82 (2003) 2172–2174, https://doi.org/10.1063/1.1565181.
[347] P.M. Jones, G.M. Rackham, J.W. Steeds, Higher order laue zone effects in electron diffraction and their use in lattice parameter determination, Proc. R. Soc. A: Math. Phys. Eng. Sci. 354 (1977) 197–222, https://doi.org/10.1098/rspa.1977.0064.
[348] F. Uesugi, A. Hokazono, S. Takeno, Evaluation of two-dimensional strain distribution by STEM/NBD, Ultramicroscopy 111 (2011) 995–998, https://doi.org/10.1016/j.ultramic.2011.01.035.
[349] K. Usuda, T. Numata, T. Irisawa, N. Hirashita, S. Takagi, Strain characterization in SOI and strained-Si on SGOI MOSFET channel using nano-beam electron diffraction (NBD, Mater. Sci. Eng.: B 124–125 (2005) 143–147, https://doi.org/10.1016/j.mseb.2005.08.062.
[350] R. Maaß, S. Van Petegem, D. Grolimund, H. Van Swygenhoven, D. Kiener, G. Dehm, Crystal rotation in Cu single crystal micropillars: in situ Laue and electron backscatter diffraction, Appl. Phys. Lett. 92 (2008), 071905, https://doi.org/10.1063/1.2884688.
[351] B. Clausen, T. Lorentzen, T. Leffers, Self-consistent modelling of the plastic deformation of f.c.c. polycrystals and its implications for diffraction measurements of internal stresses, Acta Mater. 46 (1998) 3087–3098, https://doi.org/10.1016/S1359-6454(98)00014-7.
[352] W. Ingrid De, Micro-Raman spectroscopy to study local mechanical stress in silicon integrated circuits, Semicond. Sci. Technol. 11 (1996) 139, https://doi.org/10.1088/0268-1242/11/2/001.
[353] D.T. Cassidy, S.K.K. Lam, B. Lakshmi, D.M. Bruce, Strain mapping by measurement of the degree of polarization of photoluminescence, Appl. Opt. 43 (2004) 1811–1818, https://doi.org/10.1364/AO.43.001811.
[354] H.-Y. Hwang, H. Baek, G.-C. Yi, H.-C. Kim, Y.-D. Jho, Distinctive mapping of strain and quantum size effects using depth-resolved photoluminescence in ZnO nanoneedles, AIP Adv. 6 (2016), 045021, https://doi.org/10.1063/1.4948452.
[355] W. Tong, An evaluation of digital image correlation criteria for strain mapping applications, Strain 41 (2005) 167–175, https://doi.org/10.1111/j.1475-1305.2005.00227.x.
[356] Q. Yu, Z.-W. Shan, J. Li, X. Huang, L. Xiao, J. Sun, E. Ma, Strong crystal size effect on deformation twinning, Nature 463 (2010) 335–338, https://doi.org/10.1038/nature08692.
[357] L. Tian, J. Li, J. Sun, E. Ma, Z.-W. Shan, Visualizing size-dependent deformation mechanism transition in Sn, Sci. Rep. 3 (2013) 2113, https://doi.org/10.1038/srep02113.
[358] Z.W. Shan, R.K. Mishra, S.A. Syed Asif, O.L. Warren, A.M. Minor, Mechanical annealing and source-limited deformation in submicrometre-diameter Ni crystals, Nat. Mater. 7 (2008) 115–119, https://doi.org/10.1038/nmat2085.
[359] A.M. Minor, S.A. Syed Asif, Z. Shan, E.A. Stach, E. Cyrankowski, T.J. Wyrobek, O. L. Warren, A new view of the onset of plasticity during the nanoindentation of aluminium, Nat. Mater. 5 (2006) 697–702, https://doi.org/10.1038/nmat1714.
[360] M. Legros, D.S. Gianola, C. Motz, Quantitative in situ mechanical testing in electron microscopes, MRS Bull. 35 (2011) 354–360, https://doi.org/10.1557/mrs2010.567.
[361] D. Kiener, A.M. Minor, Source truncation and exhaustion: insights from quantitative in situ TEM tensile testing, Nano Lett. 11 (2011) 3816–3820, https://doi.org/10.1021/nl201890s.
[362] H. Guo, K. Chen, Y. Oh, K. Wang, C. Dejoie, S.A.S. Asif, O.L. Warren, Z.W. Shan, J. Wu, A.M. Minor, Mechanics and dynamics of the strain-induced M1-M2 structural phase transition in individual VO_2 nanowires, Nano Lett. 11 (2011) 3207–3213, https://doi.org/10.1021/nl201460v.
[363] A. Kushima, J.Y. Huang, J. Li, Quantitative fracture strength and plasticity measurements of lithiated silicon nanowires by in situ TEM tensile experiments, ACS Nano 6 (2012) 9425–9432, https://doi.org/10.1021/nn3037623.

[364] A.H. Zewail, Four-dimensional electron microscopy, Science 328 (2010) 187–193, https://doi.org/10.1126/science.1166135.
[365] A.J. Wilkinson, T.B. Britton, Strains, planes, and EBSD in materials science, Mater. Today 15 (2012) 366–376, https://doi.org/10.1016/S1369-7021(12)70163-3.
[366] G.-C. Wang, T.-M. Lu, Strain measurement of ultrathin epitaxial films using electron diffraction techniques, J. Appl. Phys. 125 (2019), 082401, https://doi.org/10.1063/1.5049357.
[367] D. Karpov, E. Fohtung, Bragg coherent diffractive imaging of strain at the nanoscale, J. Appl. Phys. 125 (2019), 121101, https://doi.org/10.1063/1.5054294.
[368] O. Kraynis, E. Makagon, E. Mishuk, M. Hartstein, E. Wachtel, I. Lubomirsky, T. Livneh, Suitability of Raman spectroscopy for assessing anisotropic strain in thin films of doped ceria, Adv. Funct. Mater. 29 (2019), 1804433, https://doi.org/10.1002/adfm.201804433.
[369] J. Curie, P. Curie, Phénomènes électriques des cristaux hémièdres à faces inclinées, J. Theor. Appl. Phys. 1 (1882) 245–251, https://doi.org/10.1051/jphystap:018820010024500.
[370] D.A. Skoog, F.J. Holler, S.R. Crouch, Principles of Instrumental Analysis, Thomson Brooks/Cole,, 2007.
[371] C. Constantin, L. Paul, Production of submarine signals and the location of suemarine orjects, Google Patents, 1923.
[372] R. Arshadi, R.S.C. Cobbold, A pioneer in the development of modern ultrasound: Robert William Boyle (1883-1955), Ultrasound Med. Biol. 33 (2007) 3–14, https://doi.org/10.1016/j.ultrasmedbio.2006.07.030.
[373] W.G. Cady, The piezo-electric resonator, Proceedings of the Institute of Radio Engineers 10 (1922) 83–114. ⟨https://doi.org/10.1109/JRPROC.1922.219800⟩.
[374] A. von Hippel, Ferroelectricity, domain structure, and phase transitions of barium titanate, Rev. Mod. Phys. 22 (1950) 221–237, https://doi.org/10.1103/RevModPhys.22.221.
[375] G. Shirane, E. Sawaguchi, Y. Takagi, Dielectric properties of lead zirconate, Phys. Rev. 84 (1951) 476–481, https://doi.org/10.1103/PhysRev.84.476.
[376] M.-H. Zhao, Z.-L. Wang, S.X. Mao, Piezoelectric characterization of individual zinc oxide nanobelt probed by piezoresponse force microscope, Nano Lett. 4 (2004) 587–590, https://doi.org/10.1021/nl035198a.
[377] M. Minary-Jolandan, R.A. Bernal, I. Kuljanishvili, V. Parpoil, H.D. Espinosa, Individual GaN nanowires exhibit strong piezoelectricity in 3D, Nano Lett. 12 (2012) 970–976, https://doi.org/10.1021/nl204043y.
[378] T.D. Nguyen, J.M. Nagarah, Y. Qi, S.S. Nonnenmann, A.V. Morozov, S. Li, C. B. Arnold, M.C. McAlpine, Wafer-scale nanopatterning and translation into high-performance piezoelectric nanowires, Nano Lett. 10 (2010) 4595–4599, https://doi.org/10.1021/nl102619c.
[379] S. Xu, B.J. Hansen, Z.L. Wang, Piezoelectric-nanowire-enabled power source for driving wireless microelectronics, Nat. Commun. 1 (2010) 93, https://doi.org/10.1038/ncomms1098.
[380] X. Chen, S. Xu, N. Yao, Y. Shi, 1.6 v nanogenerator for mechanical energy harvesting using pzt nanofibers, Nano Lett. 10 (2010) 2133–2137, https://doi.org/10.1021/nl100812k.
[381] Z. Wang, J. Hu, A.P. Suryavanshi, K. Yum, M.-F. Yu, Voltage generation from individual $BaTiO_3$ nanowires under periodic tensile mechanical load, Nano Lett. 7 (2007) 2966–2969, https://doi.org/10.1021/nl070814e.
[382] K.-I. Park, S. Xu, Y. Liu, G.-T. Hwang, S.-J.L. Kang, Z.L. Wang, K.J. Lee, Piezoelectric $BaTiO_3$ thin film nanogenerator on plastic substrates, Nano Lett. 10 (2010) 4939–4943, https://doi.org/10.1021/nl102959k.
[383] H. Liu, H. Wu, K.P. Ong, T. Yang, P. Yang, P.K. Das, X. Chi, Y. Zhang, C. Diao, W. K.A. Wong, E.P. Chew, Y.F. Chen, C.K.I. Tan, A. Rusydi, M.B.H. Breese, D.J. Singh, L.-Q. Chen, S.J. Pennycook, K. Yao, Giant piezoelectricity in oxide thin films with nanopillar structure, Science 369 (2020) 292–297, https://doi.org/10.1126/science.abb3209.
[384] J.H. Jung, M. Lee, J.-I. Hong, Y. Ding, C.-Y. Chen, L.-J. Chou, Z.L. Wang, Lead-free $NaNbO_3$ nanowires for a high output piezoelectric nanogenerator, ACS Nano 5 (2011) 10041–10046, https://doi.org/10.1021/nn2039033.
[385] G. Lazovski, E. Wachtel, I. Lubomirsky, Detection of a piezoelectric effect in thin films of thermally grown SiO_2 via lock-in ellipsometry, Appl. Phys. Lett. 100 (2012), 262905, https://doi.org/10.1063/1.4731287.
[386] A. Apte, K. Mozaffari, F.S. Samghabadi, J.A. Hachtel, L. Chang, S. Susarla, J. C. Idrobo, D.C. Moore, N.R. Glavin, D. Litvinov, P. Sharma, A.B. Puthirath, P. M. Ajayan, 2D electrets of ultrathin MoO_2 with apparent piezoelectricity, Adv. Mater. 32 (2020), 2000006, https://doi.org/10.1002/adma.202000006.
[387] M.B. Ghasemian, A. Zavabeti, R. Abbasi, P.V. Kumar, N. Syed, Y. Yao, J. Tang, Y. Wang, A. Elbourne, J. Han, M. Mousavi, T. Daeneke, K. Kalantar-Zadeh, Ultra-thin lead oxide piezoelectric layers for reduced environmental contamination using a liquid metal-based process, J. Mater. Chem. A 8 (2020) 19434–19443, https://doi.org/10.1039/D0TA06379G.
[388] C. Mart, T. Kämpfe, R. Hoffmann, S. Eßlinger, S. Kirbach, K. Kühnel, M. Czernohorsky, L.M. Eng, W. Weinreich, Piezoelectric response of polycrystalline silicon-doped hafnium oxide thin films determined by rapid temperature cycles, Adv. Electron. Mater. 6 (2020), 1901015, https://doi.org/10.1002/aelm.201901015.
[389] H.D. Espinosa, R.A. Bernal, M. Minary-Jolandan, A review of mechanical and electromechanical properties of piezoelectric nanowires, Adv. Mater. 24 (2012) 4656–4675, https://doi.org/10.1002/adma.201104810.
[390] X. Xin, P. Alexis, S. Rudeesun, L. Jae Woo, B. Bogdan, B. Thierry, S. Bassem, M. Laurent, An improved AFM cross-sectional method for piezoelectric nanostructures properties investigation: application to GaN nanowires, Nanotechnology 22 (2011), 105704, https://doi.org/10.1088/0957-4484/22/10/105704.
[391] D. Dragan, Ferroelectric, dielectric and piezoelectric properties of ferroelectric thin films and ceramics, Rep. Prog. Phys. 61 (1998) 1267, https://doi.org/10.1088/0034-4885/61/9/002.
[392] H.J. Fan, W. Lee, R. Hauschild, M. Alexe, G. LeRhun, R. Scholz, A. Dadgar, K. Nielsch, H. Kalt, A. Krost, M. Zacharias, U. Gösele, Template-assisted large-scale ordered arrays of ZnO pillars for optical and piezoelectric applications, Small 2 (2006) 561–568, https://doi.org/10.1002/smll.200500331.
[393] D.A. Scrymgeour, J.W.P. Hsu, Correlated piezoelectric and electrical properties in individual ZnO nanorods, Nano Lett. 8 (2008) 2204–2209, https://doi.org/10.1021/nl080704n.
[394] P.X. Gao, Y. Ding, W. Mai, W.L. Hughes, C. Lao, Z.L. Wang, Conversion of zinc oxide nanobelts into superlattice-structured nanohelices, Science 309 (2005) 1700–1704, https://doi.org/10.1126/science.1116495.
[395] P.X. Gao, Y. Ding, Z.L. Wang, Electronic transport in superlattice-structured ZnO nanohelix, Nano Lett. 9 (2009) 137–143, https://doi.org/10.1021/nl802682c.
[396] F. Boxberg, N. Søndergaard, H.Q. Xu, Photovoltaics with piezoelectric core−shell nanowires, Nano Lett. 10 (2010) 1108–1112, https://doi.org/10.1021/nl9040934.
[397] J. Shi, P. Zhao, X.D. Wang, Piezoelectric-polarization-enhanced photovoltaic performance in depleted-heterojunction quantum-dot solar cells, Adv. Mater. 25 (2013) 916–921, https://doi.org/10.1002/adma.201203021.
[398] J. Zhou, Y. Gu, P. Fei, W. Mai, Y. Gao, R. Yang, G. Bao, Z.L. Wang, Flexible piezotronic strain sensor, Nano Lett. 8 (2008) 3035–3040, https://doi.org/10.1021/nl802367t.
[399] X.Q. Liao, Q.L. Liao, Z. Zhang, X.Q. Yan, Q.J. Liang, Q.Y. Wang, M.H. Li, Y. Zhang, A highly stretchable ZnO@fiber-based multifunctional nanosensor for strain/temperature/UV detection, Adv. Funct. Mater. 26 (2016) 3074–3081, https://doi.org/10.1002/adfm.201505223.
[400] S. Xu, Y. Qin, C. Xu, Y. Wei, R. Yang, Z.L. Wang, Self-powered nanowire devices, Nat. Nanotechnol. 5 (2010) 366–373, https://doi.org/10.1038/nnano.2010.46.
[401] Y. Qi, N.T. Jafferis, K. Lyons, C.M. Lee, H. Ahmad, M.C. McAlpine, Piezoelectric ribbons printed onto rubber for flexible energy conversion, Nano Lett. 10 (2010) 524–528, https://doi.org/10.1021/nl903377u.
[402] C. Chang, V.H. Tran, J. Wang, Y.-K. Fuh, L. Lin, Direct-write piezoelectric polymeric nanogenerator with high energy conversion efficiency, Nano Lett. 10 (2010) 726–731, https://doi.org/10.1021/nl9040719.
[403] Y. Gao, Z.L. Wang, Electrostatic potential in a bent piezoelectric nanowire. The fundamental theory of nanogenerator and nanopiezotronics, Nano Lett. 7 (2007) 2499–2505, https://doi.org/10.1021/nl071310j.
[404] Y. Gao, Z.L. Wang, Equilibrium potential of free charge carriers in a bent piezoelectric semiconductive nanowire, Nano Lett. 9 (2009) 1103–1110, https://doi.org/10.1021/nl803547f.
[405] X. Wang, J. Song, J. Liu, Z.L. Wang, Direct-current nanogenerator driven by ultrasonic waves, Science 316 (2007) 102–105, https://doi.org/10.1126/science.1139366.
[406] J. Liu, P. Fei, J. Song, X. Wang, C. Lao, R. Tummala, Z.L. Wang, Carrier density and schottky barrier on the performance of DC nanogenerator, Nano Lett. 8 (2008) 328–332, https://doi.org/10.1021/nl0728470.
[407] P.X. Gao, J. Song, J. Liu, Z.L. Wang, Nanowire piezoelectric nanogenerators on plastic substrates as flexible power sources for nanodevices, Adv. Mater. 19 (2007) 67–72, https://doi.org/10.1002/adma.200601162.
[408] Y. Hu, Y. Zhang, C. Xu, G. Zhu, Z.L. Wang, High-output nanogenerator by rational unipolar assembly of conical nanowires and its application for driving a small liquid crystal display, Nano Lett. 10 (2010) 5025–5031, https://doi.org/10.1021/nl103203u.
[409] Y. Hu, Y. Zhang, C. Xu, L. Lin, R.L. Snyder, Z.L. Wang, Self-powered system with wireless data transmission, Nano Lett. 11 (2011) 2572–2577, https://doi.org/10.1021/nl201505c.
[410] G. Zhu, A.C. Wang, Y. Liu, Y. Zhou, Z.L. Wang, Functional electrical stimulation by nanogenerator with 58V output voltage, Nano Lett. 12 (2012) 3086–3090, https://doi.org/10.1021/nl300972f.
[411] M. Lee, J. Bae, J. Lee, C.-S. Lee, S. Hong, Z.L. Wang, Self-powered environmental sensor system driven by nanogenerators, Energy Environ. Sci. 4 (2011) 3359–3363, https://doi.org/10.1039/C1EE01558C.
[412] Y. Hu, C. Xu, Y. Zhang, L. Lin, R.L. Snyder, Z.L. Wang, A nanogenerator for energy harvesting from a rotating tire and its application as a self-powered pressure/speed sensor, Adv. Mater. 23 (2011) 4068–4071, https://doi.org/10.1002/adma.201102067.
[413] S. Lee, S.-H. Bae, L. Lin, Y. Yang, C. Park, S.-W. Kim, S.N. Cha, H. Kim, Y.J. Park, Z.L. Wang, Super-flexible nanogenerator for energy harvesting from gentle wind and as an active deformation sensor, Adv. Funct. Mater. 23 (2013) 2445–2449, https://doi.org/10.1002/adfm.201202867.
[414] S. Lee, R. Hinchet, Y. Lee, Y. Yang, Z.-H. Lin, G. Ardila, L. Montès, M. Mouis, Z. L. Wang, Ultrathin nanogenerators as self-powered/active skin sensors for tracking eye ball motion, Adv. Funct. Mater. 24 (2014) 1163–1168, https://doi.org/10.1002/adfm.201301971.
[415] J. Shi, M.B. Starr, H. Xiang, Y. Hara, M.A. Anderson, J.H. Seo, Z.Q. Ma, X. D. Wang, Interface engineering by piezoelectric potential in ZnO-based photoelectrochemical anode, Nano Lett. 11 (2011) 5587–5593, https://doi.org/10.1021/nl203729j.
[416] H.J. Xiang, J. Yang, J.G. Hou, Q. Zhu, Piezoelectricity in ZnO nanowires: a first-principles study, Appl. Phys. Lett. 89 (2006), 223111, https://doi.org/10.1063/1.2397013.
[417] R. Agrawal, H.D. Espinosa, Giant piezoelectric size effects in zinc oxide and gallium nitride nanowires. A first principles investigation, Nano Lett. 11 (2011) 786–790, https://doi.org/10.1021/nl104004d.

[418] D. Shuangxing, L.D. Martin, S.P. Harold, Piezoelectric constants for ZnO calculated using classical polarizable core–shell potentials, Nanotechnology 21 (2010), 445707, https://doi.org/10.1088/0957-4484/21/44/445707.
[419] C.L. Sun, J.A. Shi, X.D. Wang, Fundamental study of mechanical energy harvesting using piezoelectric nanostructures, J. Appl. Phys. 108 (2010), 034309, https://doi.org/10.1063/1.3462468.
[420] M.N. Blonsky, H.L. Zhuang, A.K. Singh, R.G. Hennig, Ab Initio prediction of piezoelectricity in two-dimensional materials, ACS Nano 9 (2015) 9885–9891, https://doi.org/10.1021/acsnano.5b03394.
[421] M.M. Alyoruk, Piezoelectric properties of monolayer II-VI group oxides by first-principles calculations, Phys. Status Solidi B-Basic Solid State Phys. 253 (2016) 2534–2539, https://doi.org/10.1002/pssb.201600387.
[422] R. Bechmann, Elastic and piezoelectric constants of alpha-quartz, Phys. Rev. 110 (1958) 1060–1061, https://doi.org/10.1103/PhysRev.110.1060.
[423] C.M. Lueng, H.L.W. Chan, C. Surya, C.L. Choy, Piezoelectric coefficient of aluminum nitride and gallium nitride, J. Appl. Phys. 88 (2000) 5360–5363, https://doi.org/10.1063/1.1317244.
[424] M.M. Alyörük, Y. Aierken, D. Çakır, F.M. Peeters, C. Sevik, Promising piezoelectric performance of single layer transition-metal dichalcogenides and dioxides, J. Phys. Chem. C 119 (2015) 23231–23237, https://doi.org/10.1021/acs.jpcc.5b06428.
[425] H.L. Zhuang, R.G. Hennig, Computational identification of single-layer CdO for electronic and optical applications, Appl. Phys. Lett. 103 (2013), 212102, https://doi.org/10.1063/1.4831972.
[426] A.A. Barlian, W.T. Park, J.R. Mallon, A.J. Rastegar, B.L. Pruitt, Review: Semiconductor piezoresistance for microsystems, In: Proceedings of the IEEE 97 (2009) 513–552. ⟨https://doi.org/10.1109/JPROC.2009.2013612⟩.
[427] H. Rolnick, Tension coefficient of resistance of metals, Phys. Rev. 36 (1930) 506–512, https://doi.org/10.1103/PhysRev.36.506.
[428] Y. Yang, W. Guo, J. Qi, Y. Zhang, Flexible piezoresistive strain sensor based on single Sb-doped ZnO nanobelts, Appl. Phys. Lett. 97 (2010), 223107, https://doi.org/10.1063/1.3522885.
[429] W. Thomson, On the electro-dynamic qualities of metals:–effects of magnetization on the electric conductivity of nickel and of iron, Proc. R. Soc. Lond. 8 (1856) 546–550, https://doi.org/10.1098/rspl.1856.0144.
[430] J.W. Cookson, Theory of the piezo-resistive effect, Phys. Rev. 47 (1935) 194–195, https://doi.org/10.1103/PhysRev.47.194.2.
[431] J. Bardeen, W. Shockley, Deformation potentials and mobilities in non-polar crystals, Phys. Rev. 80 (1950) 72–80, https://doi.org/10.1103/PhysRev.80.72.
[432] C.S. Smith, Piezoresistance effect in germanium and silicon, Phys. Rev. 94 (1954) 42–49, https://doi.org/10.1103/PhysRev.94.42.
[433] C. Herring, E. Vogt, Transport and deformation-potential theory for many-valley semiconductors with anisotropic scattering, Phys. Rev. 101 (1956) 944–961, https://doi.org/10.1103/PhysRev.101.944.
[434] R. Oberhuber, G. Zandler, P. Vogl, Subband structure and mobility of two-dimensional holes in strained Si/SiGe MOSFET's, Phys. Rev. B 58 (1998) 9941–9948, https://doi.org/10.1103/PhysRevB.58.9941.
[435] M.V. Fischetti, Z. Ren, P.M. Solomon, M. Yang, K. Rim, Six-band k·p calculation of the hole mobility in silicon inversion layers: Dependence on surface orientation, strain, and silicon thickness, J. Appl. Phys. 94 (2003) 1079–1095, https://doi.org/10.1063/1.1585120.
[436] J.X. Cao, X.G. Gong, R.Q. Wu, Giant piezoresistance and its origin in Si(111) nanowires: first-principles calculations, Phys. Rev. B 75 (2007), 233302, https://doi.org/10.1103/PhysRevB.75.233302.
[437] O.N. Tufte, P.W. Chapman, D. Long, Silicon diffused-element piezoresistive diaphragms, J. Appl. Phys. 33 (1962) 3322–3327, https://doi.org/10.1063/1.1931164.
[438] K.E. Petersen, Silicon as a mechanical material, In: Proceedings of the IEEE 70 (1982) 420–457. ⟨https://doi.org/10.1109/PROC.1982.12331⟩.
[439] O. Paul, J. Gaspar, P. Ruther, Advanced silicon microstructures, sensors, and systems, IEEJ Trans. Electr. Electron. Eng. 2 (2007) 199–215, https://doi.org/10.1002/tee.20155.
[440] R. Zhu, R.S. Yang, Separation of the piezotronic and piezoresistive effects in a zinc oxide nanowire, Nanotechnology 25 (2014) 6, https://doi.org/10.1088/0957-4484/25/34/345702.
[441] X. Han, G. Jing, X. Zhang, R. Ma, X. Song, J. Xu, Z. Liao, N. Wang, D. Yu, Bending-induced conductance increase in individual semiconductor nanowires and nanobelts, Nano Res. 2 (2009) 553–557, https://doi.org/10.1007/s12274-009-9053-4.
[442] X.G. Wang, K. Chen, Y.Q. Zhang, J.C. Wan, O.L. Warren, J. Oh, J. Li, E. Ma, Z. W. Shan, Growth conditions control the elastic and electrical properties of ZnO nanowires, Nano Lett. 15 (2015) 7886–7892, https://doi.org/10.1021/acs.nanolett.5b02852.
[443] J.-H. He, J.-J. Ke, P.-H. Chang, K.-T. Tsai, P.C. Yang, I.M. Chan, Development of Ohmic nanocontacts via surface modification for nanowire-based electronic and optoelectronic devices: ZnO nanowires as an example, Nanoscale 4 (2012) 3399–3404, https://doi.org/10.1039/C2NR30688C.
[444] G.W.A. Cardoso, G. Leal, A.S.D. Sobrinho, M.A. Fraga, M. Massi, Evaluation of piezoresistivity properties of sputtered ZnO thin films, Mater. Res. -Ibero-Am. J. Mater. 17 (2014) 588–592, https://doi.org/10.1590/s1516-14392014005000080.
[445] A. Sutka, M. Timusk, N. Dobelin, R. Parna, M. Visnapuu, U. Joost, T. Kaambre, V. Kisand, K. Saal, M. Knite, A straightforward and "green" solvothermal synthesis of Al doped zinc oxide plasmonic nanocrystals and piezoresistive elastomer nanocomposite, RSC Adv. 5 (2015) 63846–63852, https://doi.org/10.1039/c5ra11910c.
[446] C.O. Chey, X.J. Liu, H. Alnoor, O. Nur, M. Willander, Fast piezoresistive sensor and UV photodetector based on Mn-doped ZnO nanorods, Phys. Status Solidi-Rapid Res. Lett. 9 (2015) 87–91, https://doi.org/10.1002/pssr.201409453.
[447] P. Ray, V.R. Rao, Al-doped ZnO thin-film transistor embedded micro-cantilever as a piezoresistive sensor, Appl. Phys. Lett. 102 (2013), 064101, https://doi.org/10.1063/1.4792062.
[448] X. Li, Z. Yin, X. Zhang, Y. Wang, D. Wang, M. Gao, J. Meng, J. Wu, J. You, Epitaxial liftoff of wafer-scale VO_2 nanomembranes for flexible, ultrasensitive tactile sensors, Adv. Mater. Technol. 0 (2019), 1800695, https://doi.org/10.1002/admt.201800695.
[449] J. Cao, Y. Gu, W. Fan, L.Q. Chen, D.F. Ogletree, K. Chen, N. Tamura, M. Kunz, C. Barrett, J. Seidel, J. Wu, Extended mapping and exploration of the vanadium dioxide stress-temperature phase diagram, Nano Lett. 10 (2010) 2667–2673, https://doi.org/10.1021/nl101457k.
[450] A. Sedlmayr, R. Moenig, S.T. Boles, G. Kilibarda, O. Kraft, Strain-induced phase transformation and piezoresistivity in VO_2 nanowires, MRS Commun. 2 (2012) 41–45, https://doi.org/10.1557/mrc.2012.5.
[451] Y. Onuma, Z.H. Wang, H. Ito, H. Nakao, K. Kamimura, Preparation and piezoresistive properties of polycrystalline SnO_2 films, Jpn. J. Appl. Phys. Part 1 (37) (1998) 963–964, https://doi.org/10.1143/jjap.37.963.
[452] M. Sakurai, K. Liu, M. Aono, Reversible and nonvolatile modulation of electrical resistance in SnO_2 by external strain, Appl. Phys. Express 7 (2014), 031101, https://doi.org/10.7567/apex.7.031101.
[453] F. Li, Z. Chen, Tuning electronic and magnetic properties of MoO_3 sheets by cutting, hydrogenation, and external strain: a computational investigation, Nanoscale 5 (2013) 5321–5333, https://doi.org/10.1039/c3nr33009e.
[454] X. Wen, W. Yang, Y. Ding, S. Niu, Z.L. Wang, Piezoresistive effect in MoO_3 nanobelts and its application in strain-enhanced oxygen sensors, Nano Res. 7 (2014) 180–189, https://doi.org/10.1007/s12274-013-0385-8.
[455] H.W. Wu, S.Y. Lee, W.C. Lu, K.S. Chang, Piezoresistive effects enhanced the photocatalytic properties of Cu_2O/CuO nanorods, Appl. Surf. Sci. 344 (2015) 236–241, https://doi.org/10.1016/j.apsusc.2015.03.122.
[456] T. Kuykendall, P.J. Pauzauskie, Y. Zhang, J. Goldberger, D. Sirbuly, J. Denlinger, P. Yang, Crystallographic alignment of high-density gallium nitride nanowire arrays, Nat. Mater. 3 (2004) 524, https://doi.org/10.1038/nmat1177.
[457] Z.L. Wang, Piezopotential gated nanowire devices: Piezotronics and piezo-phototronics, Nano Today 5 (2010) 540–552, https://doi.org/10.1016/j.nantod.2010.10.008.
[458] Z.L. Wang, Nanopiezotronics, Adv. Mater. 19 (2007) 889–892, https://doi.org/10.1002/adma.200602918.
[459] S. Niu, Y. Hu, X. Wen, Y. Zhou, F. Zhang, L. Lin, S. Wang, Z.L. Wang, Enhanced performance of flexible ZnO nanowire based room-temperature oxygen sensors by piezotronic effect, Adv. Mater. 25 (2013) 3701–3706, https://doi.org/10.1002/adma.201301262.
[460] R. Yu, C. Pan, Z.L. Wang, High performance of ZnO nanowire protein sensors enhanced by the piezotronic effect, Energy Environ. Sci. 6 (2013) 494–499, https://doi.org/10.1039/C2EE23718K.
[461] W.H. Han, Y.S. Zhou, Y. Zhang, C.Y. Chen, L. Lin, X. Wang, S.H. Wang, Z.L. Wang, Strain-gated piezotronic transistors based on vertical zinc oxide nanowires, ACS Nano 6 (2012) 3760–3766, https://doi.org/10.1021/nn301277m.
[462] C. Pan, Y. Fang, H. Wu, M. Ahmad, Z. Luo, Q. Li, J. Xie, X. Yan, L. Wu, Z.L. Wang, J. Zhu, Generating electricity from biofluid with a nanowire-based biofuel cell for self-powered nanodevices, Adv. Mater. 22 (2010) 5388–5392, https://doi.org/10.1002/adma.201002519.
[463] Y. Yang, W. Guo, Y. Zhang, Y. Ding, X. Wang, Z.L. Wang, Piezotronic effect on the output voltage of P3HT/ZnO micro/nanowire heterojunction solar cells, Nano Lett. 11 (2011) 4812–4817, https://doi.org/10.1021/nl202648p.
[464] Q. Yang, X. Guo, W. Wang, Y. Zhang, S. Xu, D.H. Lien, Z.L. Wang, Enhancing sensitivity of a single ZnO micro-/nanowire photodetector by piezo-phototronic effect, ACS Nano 4 (2010) 6285–6291, https://doi.org/10.1021/nn1022878.
[465] R. Yu, C. Pan, Y. Hu, L. Li, H. Liu, W. Liu, S. Chua, D. Chi, Z.L. Wang, Enhanced performance of GaN nanobelt-based photodetectors by means of piezotronic effects, Nano Res. 6 (2013) 758–766, https://doi.org/10.1007/s12274-013-0354-2.
[466] W. Wu, Y. Wei, Z.L. Wang, Strain-gated piezotronic logic nanodevices, Adv. Mater. 22 (2010) 4711–4715, https://doi.org/10.1002/adma.201001925.
[467] R. Bao, C. Wang, L. Dong, R. Yu, K. Zhao, Z.L. Wang, C. Pan, Flexible and controllable piezo-phototronic pressure mapping sensor matrix by ZnO NW/p-polymer LED array, Adv. Funct. Mater. 25 (2015) 2884–2891, https://doi.org/10.1002/adfm.201500801.
[468] Y. Zhang, Y. Liu, Z.L. Wang, Fundamental theory of piezotronics, Adv. Mater. 23 (2011) 3004–3013, https://doi.org/10.1002/adma.201100906.
[469] J. Shi, M.B. Starr, X. Wang, Band structure engineering at heterojunction interfaces via the piezotronic effect, Adv. Mater. 24 (2012) 4683–4691, https://doi.org/10.1002/adma.201104386.
[470] Y. Liu, Y. Zhang, Q. Yang, S. Niu, Z.L. Wang, Fundamental theories of piezotronics and piezo-phototronics, Nano Energy 14 (2015) 257–275, https://doi.org/10.1016/j.nanoen.2014.11.051.
[471] Y. Zhang, Z.L. Wang, Theory of piezo-phototronics for light-emitting diodes, Adv. Mater. 24 (2012) 4712–4718, https://doi.org/10.1002/adma.201104263.
[472] Y. Liu, S. Niu, Q. Yang, B.D.B. Klein, Y.S. Zhou, Z.L. Wang, Theoretical study of piezo-phototronic nano-LEDs, Adv. Mater. 26 (2014) 7209–7216, https://doi.org/10.1002/adma.201402328.
[473] Y. Liu, Q. Yang, Y. Zhang, Z. Yang, Z.L. Wang, Nanowire piezo-phototronic photodetector: theory and experimental design, Adv. Mater. 24 (2012) 1410–1417, https://doi.org/10.1002/adma.201104333.

[474] X. Wen, W. Wu, C. Pan, Y. Hu, Q. Yang, Z.L. Wang, Development and progress in piezotronics, Nano Energy 14 (2015) 276–295, https://doi.org/10.1016/j.nanoen.2014.10.037.
[475] X.D. Wang, Piezotronics: A new field of strain-engineered functional semiconductor devices, Am. Ceram. Soc. Bull. 92 (2013) 18–23.
[476] Z.L. Wang, X.D. Wang, Nanogenerators and piezotronics, Nano Energy 14 (2015) 1–2, https://doi.org/10.1016/j.nanoen.2015.01.011.
[477] Z.L. Wang, W. Wu, Piezotronics and piezo-phototronics: fundamentals and applications, Natl. Sci. Rev. 1 (2014) 62–90, https://doi.org/10.1093/nsr/nwt002.
[478] C. Pan, J. Zhai, Z.L. Wang, Piezotronics and piezo-phototronics of third generation semiconductor nanowires, Chem. Rev. 119 (2019) 9303–9359, https://doi.org/10.1021/acs.chemrev.8b00599.
[479] R.T. Tung, Recent advances in Schottky barrier concepts, Mater. Sci. Eng. R: Rep. 35 (2001) 1–138, https://doi.org/10.1016/S0927-796X(01)00037-7.
[480] Y. Hu, Y. Zhang, Y. Chang, R.L. Snyder, Z.L. Wang, Optimizing the power output of a ZnO photocell by piezopotential, ACS Nano 4 (2010) 4220–4224, https://doi.org/10.1021/nn1010045.
[481] J. Zhou, P. Fei, Y. Gu, W. Mai, Y. Gao, R. Yang, G. Bao, Z.L. Wang, Piezoelectric-potential-controlled polarity-reversible Schottky diodes and switches of ZnO wires, Nano Lett. 8 (2008) 3973–3977, https://doi.org/10.1021/nl802497e.
[482] J.S. Milne, I. Favorskiy, A.C.H. Rowe, S. Arscott, C. Renner, Piezoresistance in silicon at uniaxial compressive stresses up to 3GPa, Phys. Rev. Lett. 108 (2012), 256801, https://doi.org/10.1103/PhysRevLett.108.256801.
[483] W. Wu, X. Wen, Z.L. Wang, Taxel-addressable matrix of vertical-nanowire piezotronic transistors for active and adaptive tactile imaging, Science 340 (2013) 952–957, https://doi.org/10.1126/science.1234855.
[484] Q. Yang, Y. Wu, Y. Liu, C. Pan, Z.L. Wang, Features of the piezo-phototronic effect on optoelectronic devices based on wurtzite semiconductor nanowires, Phys. Chem. Chem. Phys. 16 (2014) 2790–2800, https://doi.org/10.1039/C3CP53737D.
[485] X. Han, W. Du, R. Yu, C. Pan, Z.L. Wang, Piezo-phototronic enhanced UV sensing based on a nanowire photodetector array, Adv. Mater. 27 (2015) 7963–7969, https://doi.org/10.1002/adma.201502579.
[486] Z. Zhang, Q. Liao, Y. Yu, X. Wang, Y. Zhang, Enhanced photoresponse of ZnO nanorods-based self-powered photodetector by piezotronic interface engineering, Nano Energy 9 (2014) 237–244, https://doi.org/10.1016/j.nanoen.2014.07.019.
[487] X. Wen, W. Wu, Y. Ding, Z.L. Wang, Piezotronic effect in flexible thin-film based devices, Adv. Mater. 25 (2013) 3371–3379, https://doi.org/10.1002/adma.201300296.
[488] C. Pan, R. Yu, S. Niu, G. Zhu, Z.L. Wang, Piezotronic effect on the sensitivity and signal level of Schottky contacted proactive micro/nanowire nanosensors, ACS Nano 7 (2013) 1803–1810, https://doi.org/10.1021/nn306007p.
[489] Q. Yu, R. Ge, J. Wen, T. Du, J. Zhai, S. Liu, L. Wang, Y. Qin, Highly sensitive strain sensors based on piezotronic tunneling junction, Nat. Commun. 13 (2022) 778, https://doi.org/10.1038/s41467-022-28443-0.
[490] R. Zhou, G. Hu, R. Yu, C. Pan, Z.L. Wang, Piezotronic effect enhanced detection of flammable/toxic gases by ZnO micro/nanowire sensors, Nano Energy 12 (2015) 588–596, https://doi.org/10.1016/j.nanoen.2015.01.036.
[491] X.T. Cao, X. Cao, H.J. Guo, T. Li, Y. Jie, N. Wang, Z.L. Wang, Piezotronic effect enhanced label-free detection of DNA using a Schottky-contacted ZnO nanowire biosensor, ACS Nano 10 (2016) 8038–8044, https://doi.org/10.1021/acsnano.6b04121.
[492] L. Wang, S. Liu, Z. Zhang, X. Feng, L. Zhu, H. Guo, W. Ding, L. Chen, Y. Qin, Z. L. Wang, 2D piezotronics in atomically thin zinc oxide sheets: Interfacing gating and channel width gating, Nano Energy 60 (2019) 724–733, https://doi.org/10.1016/j.nanoen.2019.03.076.
[493] K.C. Pradel, W. Wu, Y. Zhou, X. Wen, Y. Ding, Z.L. Wang, Piezotronic effect in solution-grown p-type ZnO nanowires and films, Nano Lett. 13 (2013) 2647–2653, https://doi.org/10.1021/nl400792w.
[494] S. Liu, L. Wang, X. Feng, Z. Wang, Q. Xu, S. Bai, Y. Qin, Z.L. Wang, Ultrasensitive 2D ZnO piezotronic transistor array for high resolution tactile imaging, Adv. Mater. 29 (2017), 1606346, https://doi.org/10.1002/adma.201606346.
[495] L. Wang, S. Liu, X. Feng, Q. Xu, S. Bai, L. Zhu, L. Chen, Y. Qin, Z.L. Wang, Ultrasensitive vertical piezotronic transistor based on ZnO twin nanoplatelet, ACS Nano 11 (2017) 4859–4865, https://doi.org/10.1021/acsnano.7b01374.
[496] W. Wu, Z.L. Wang, Piezotronic nanowire-based resistive switches as programmable electromechanical memories, Nano Lett. 11 (2011) 2779–2785, https://doi.org/10.1021/nl201074a.
[497] C. Xu, C. Pan, Y. Liu, Z.L. Wang, Hybrid cells for simultaneously harvesting multi-type energies for self-powered micro/nanosystems, Nano Energy 1 (2012) 259–272, https://doi.org/10.1016/j.nanoen.2012.01.002.
[498] Z. Wang, R. Yu, X. Wen, Y. Liu, C. Pan, W. Wu, Z.L. Wang, Optimizing performance of silicon-based p-n junction photodetectors by the piezo-phototronic effect, ACS Nano 8 (2014) 12866–12873, https://doi.org/10.1021/nn506427p.
[499] X. Li, M. Chen, R. Yu, T. Zhang, D. Song, R. Liang, Q. Zhang, S. Cheng, L. Dong, A. Pan, Z.L. Wang, J. Zhu, C. Pan, Enhancing light emission of ZnO-nanofilm/Si-micropillar heterostructure arrays by piezo-phototronic effect, Adv. Mater. 27 (2015) 4447–4453, https://doi.org/10.1002/adma.201501121.
[500] M. Chen, C. Pan, T. Zhang, X. Li, R. Liang, Z.L. Wang, Tuning light emission of a pressure-sensitive silicon/ZnO nanowires heterostructure matrix through piezo-phototronic effects, ACS Nano 10 (2016) 6074–6079, https://doi.org/10.1021/acsnano.6b01666.
[501] C. Pan, L. Dong, G. Zhu, S. Niu, R. Yu, Q. Yang, Y. Liu, Z.L. Wang, High-resolution electroluminescent imaging of pressure distribution using a piezoelectric nanowire LED array, Nat. Photonics 7 (2013) 752–758, https://doi.org/10.1038/nphoton.2013.191.
[502] Q. Yang, W. Wang, S. Xu, Z.L. Wang, Enhancing light emission of ZnO microwire-based diodes by piezo-phototronic effect, Nano Lett. 11 (2011) 4012–4017, https://doi.org/10.1021/nl202619d.
[503] Q. Yang, Y. Liu, C. Pan, J. Chen, X. Wen, Z.L. Wang, Largely enhanced efficiency in ZnO nanowire/p-polymer hybridized inorganic/organic ultraviolet light-emitting diode by piezo-phototronic effect, Nano Lett. 13 (2013) 607–613, https://doi.org/10.1021/nl304163n.
[504] X. Wen, W. Wu, Z.L. Wang, Effective piezo-phototronic enhancement of solar cell performance by tuning material properties, Nano Energy 2 (2013) 1093–1100, https://doi.org/10.1016/j.nanoen.2013.08.008.
[505] L. Zhu, Y. Zhang, P. Lin, Y. Wang, L. Yang, L. Chen, L. Wang, B. Chen, Z.L. Wang, Piezotronic effect on Rashba spin–orbit coupling in a ZnO/P3HT nanowire array structure, ACS Nano 12 (2018) 1811–1820, https://doi.org/10.1021/acsnano.7b08618.
[506] Y. Zhang, Y. Yang, Z.L. Wang, Piezo-phototronics effect on nano/microwire solar cells, Energy Environ. Sci. 5 (2012) 6850–6856, https://doi.org/10.1039/C2EE00057A.
[507] G. Hu, W. Guo, R. Yu, X. Yang, R. Zhou, C. Pan, Z.L. Wang, Enhanced performances of flexible ZnO/perovskite solar cells by piezo-phototronic effect, Nano Energy 23 (2016) 27–33, https://doi.org/10.1016/j.nanoen.2016.02.057.
[508] L. Zhu, L. Wang, C. Pan, L. Chen, F. Xue, B. Chen, L. Yang, L. Su, Z.L. Wang, Enhancing the efficiency of silicon-based solar cells by the piezo-phototronic effect, ACS Nano 11 (2017) 1894–1900, https://doi.org/10.1021/acsnano.6b07960.
[509] L. Zhu, L. Wang, F. Xue, L. Chen, J. Fu, X. Feng, T. Li, Z.L. Wang, Piezo-phototronic effect enhanced flexible solar cells based on n-ZnO/p-SnS core–shell nanowire array, Adv. Sci. 4 (2017), 1600185, https://doi.org/10.1002/advs.201600185.
[510] F. Xue, L. Chen, J. Chen, J. Liu, L. Wang, M. Chen, Y. Pang, X. Yang, G. Gao, J. Zhai, Z.L. Wang, p-Type MoS_2 and n-Type ZnO diode and its performance enhancement by the piezophototronic effect, Adv. Mater. 28 (2016) 3391–3398, https://doi.org/10.1002/adma.201506472.
[511] M. Chen, B. Zhao, G. Hu, X. Fang, H. Wang, L. Wang, J. Luo, X. Han, X. Wang, C. Pan, Z.L. Wang, Piezo-phototronic effect modulated deep UV photodetector based on ZnO-Ga_2O_3 heterojuction microwire, Adv. Funct. Mater. 28 (2018), 1706379, https://doi.org/10.1002/adfm.201706379.
[512] S. Jeong, M.W. Kim, Y.-R. Jo, T.-Y. Kim, Y.-C. Leem, S.-W. Kim, B.-J. Kim, S.-J. Park, Crystal-structure-dependent piezotronic and piezo-phototronic effects of ZnO/ZnS core/shell nanowires for enhanced electrical transport and photosensing performance, ACS Appl. Mater. Interfaces 10 (2018) 28736–28744, https://doi.org/10.1021/acsami.8b06192.
[513] F. Zhang, Y. Ding, Y. Zhang, X. Zhang, Z.L. Wang, Piezo-phototronic effect enhanced visible and ultraviolet photodetection using a ZnO–CdS core–shell micro/nanowire, ACS Nano 6 (2012) 9229–9236, https://doi.org/10.1021/nn3035765.
[514] S.C. Rai, K. Wang, Y. Ding, J.K. Marmon, M. Bhatt, Y. Zhang, W. Zhou, Z.L. Wang, Piezo-phototronic effect enhanced UV/visible photodetector based on fully wide band gap type-II ZnO/ZnS core/shell nanowire Array, ACS Nano 9 (2015) 6419–6427, https://doi.org/10.1021/acsnano.5b02081.
[515] Z. Huo, Y. Zhang, X. Han, W. Wu, W. Yang, X. Wang, M. Zhou, C. Pan, Piezo-phototronic effect enhanced performance of a p-ZnO NW based UV–Vis–NIR photodetector, Nano Energy 86 (2021), 106090, https://doi.org/10.1016/j.nanoen.2021.106090.
[516] S. Yan, Z. Zheng, S. Rai, M.A. Retana, M. Bhatt, L. Malkinski, W. Zhou, Coupling effect of magnetic fields on piezotronic and piezophototronic properties of ZnO and ZnO/Co_3O_4 core/shell nanowire arrays, ACS Appl. Nano Mater. 1 (2018) 6897–6903, https://doi.org/10.1021/acsanm.8b01707.
[517] N. Sato, Electrochemistry at Metal and Semiconductor Electrodes, Elsevier,, 1998.
[518] K.-S. Hong, H. Xu, H. Konishi, X. Li, Direct water splitting through vibrating piezoelectric microfibers in water, J. Phys. Chem. Lett. 1 (2010) 997–1002, https://doi.org/10.1021/jz100027t.
[519] M.B. Starr, J. Shi, X. Wang, Piezopotential-driven redox reactions at the surface of piezoelectric materials, Angew. Chem. Int. Ed. 51 (2012) 5962–5966, https://doi.org/10.1002/anie.201201424.
[520] L. Wang, S. Liu, Z. Wang, Y. Zhou, Y. Qin, Z.L. Wang, Piezotronic effect enhanced photocatalysis in strained anisotropic ZnO/TiO_2 nanoplatelets via thermal stress, ACS Nano 10 (2016) 2636–2643, https://doi.org/10.1021/acsnano.5b07678.
[521] Y. Chen, L. Wang, R. Gao, Y.-C. Zhang, L. Pan, C. Huang, K. Liu, X.-Y. Chang, X. Zhang, J.-J. Zou, Polarization-enhanced direct Z-scheme ZnO-WO_{3-x} nanorod arrays for efficient piezoelectric-photoelectrochemical Water splitting, Appl. Catal. B: Environ. 259 (2019), 118079, https://doi.org/10.1016/j.apcatb.2019.118079.
[522] D. Hong, W. Zang, X. Guo, Y. Fu, H. He, J. Sun, L. Xing, B. Liu, X. Xue, High piezo-photocatalytic efficiency of CuS/ZnO nanowires using both solar and mechanical energy for degrading organic dye, ACS Appl. Mater. Interfaces 8 (2016) 21302–21314, https://doi.org/10.1021/acsami.6b05252.
[523] W. Känzig, Ferroelectrics and antiferroeletrics, in: F. Seitz, D. Turnbull (Eds.), Solid State Physics, 4, Academic Press, 1957, pp. 1–197.
[524] J. Valasek, Piezo-electric and allied phenomena in rochelle salt, Phys. Rev. 17 (1921) 475–481, https://doi.org/10.1103/PhysRev.17.475.
[525] J.F. Scott, P. De Araujo, A. Carlos, Ferroelectric memories, Science 246 (1989) 1400–1405, https://doi.org/10.1126/science.246.4936.1400.

[526] C.H. Ahn, K.M. Rabe, J.-M. Triscone, Ferroelectricity at the nanoscale: Local polarization in oxide thin films and heterostructures, Science 303 (2004) 488–491, https://doi.org/10.1109/IEDM.2004.1419228.

[527] R. Takayama, Y. Tomita, Preparation of epitaxial $Pb(Zr_xTi_{1-x})O_3$ thin films and their crystallographic, pyroelectric, and ferroelectric properties, J. Appl. Phys. 65 (1989) 1666–1670, https://doi.org/10.1063/1.342936.

[528] K. Amanuma, T. Hase, Y. Miyasaka, Preparation and ferroelectric properties of $SrBi_2Ta_2O_9$ thin films, Appl. Phys. Lett. 66 (1995) 221–223, https://doi.org/10.1063/1.113140.

[529] W.S. Yun, J.J. Urban, Q. Gu, H. Park, Ferroelectric properties of individual barium titanate nanowires investigated by scanned probe microscopy, Nano Lett. 2 (2002) 447–450, https://doi.org/10.1021/nl015702g.

[530] P.-E. Janolin, Strain on ferroelectric thin films, J. Mater. Sci. 44 (2009) 5025–5048, https://doi.org/10.1007/s10853-009-3553-1.

[531] L.W. Martin, A.M. Rappe, Thin-film ferroelectric materials and their applications, Nat. Rev. Mater. 2 (2016) 16087, https://doi.org/10.1038/natrevmats.2016.87.

[532] T. Böscke, J. Müller, D. Bräuhaus, U. Schröder, U. Böttger, Ferroelectricity in hafnium oxide: CMOS compatible ferroelectric field effect transistors, In: Proceedings of the 2011 International Electron Devices Meeting, IEEE, 2011, pp. 24.25. 21–24.25. 24.

[533] S. Kundu, D. Maurya, M. Clavel, Y. Zhou, N.N. Halder, M.K. Hudait, P. Banerji, S. Priya, Integration of lead-free ferroelectric on HfO_2/Si (100) for high performance non-volatile memory applications, Sci. Rep. 5 (2015) 8494, https://doi.org/10.1038/srep08494.

[534] M.H. Park, Y.H. Lee, H.J. Kim, Y.J. Kim, T. Moon, K. Do Kim, J. Muller, A. Kersch, U. Schroeder, T. Mikolajick, C.S. Hwang, Ferroelectricity and antiferroelectricity of doped thin HfO_2-based films, Adv. Mater. 27 (2015) 1811–1831, https://doi.org/10.1002/adma.201404531.

[535] T.S. Böscke, J. Müller, D. Bräuhaus, U. Schröder, U. Böttger, Ferroelectricity in hafnium oxide thin films, Appl. Phys. Lett. 99 (2011), 102903, https://doi.org/10.1063/1.3634052.

[536] C. Wiemer, A. Debernardi, A. Lamperti, A. Molle, O. Salicio, L. Lamagna, M. Fanciulli, Influence of lattice parameters on the dielectric constant of tetragonal ZrO_2 and La-doped ZrO_2 crystals in thin films deposited by atomic layer deposition on Ge(001), Appl. Phys. Lett. 99 (2011), 232907, https://doi.org/10.1063/1.3666237.

[537] P. Polakowski, J. Muller, Ferroelectricity in undoped hafnium oxide, Appl. Phys. Lett. 106 (2015), 232905, https://doi.org/10.1063/1.4922272.

[538] M.H. Park, H.J. Kim, Y.J. Kim, T. Moon, K.D. Kim, C.S. Hwang, Thin $Hf_xZr_{1-x}O_2$ films: a new lead-free system for electrostatic supercapacitors with large energy storage density and robust thermal stability, Adv. Energy Mater. 4 (2014), 1400610, https://doi.org/10.1002/aenm.201400610.

[539] S. Mueller, J. Mueller, A. Singh, S. Riedel, J. Sundqvist, U. Schroeder, T. Mikolajick, Incipient ferroelectricity in Al-doped HfO_2 thin films, Adv. Funct. Mater. 22 (2012) 2412–2417, https://doi.org/10.1002/adfm.201103119.

[540] E.H. Kisi, C.J. Howard, R.J. Hill, Crystal structure of orthorhombic zirconia in partially stabilized zirconia, J. Am. Ceram. Soc. 72 (1989) 1757–1760, https://doi.org/10.1111/j.1151-2916.1989.tb06322.x.

[541] S. Shukla, S. Seal, R. Vij, S. Bandyopadhyay, Z. Rahman, Effect of nanocrystallite morphology on the metastable tetragonal phase stabilization in zirconia, Nano Lett. 2 (2002) 989–993, https://doi.org/10.1021/nl025660b.

[542] P. Shen, W.H. Lee, (111)-specific coalescence twinning and martensitic transformation of tetragonal ZrO_2 condensates, Nano Lett. 1 (2001) 707–711, https://doi.org/10.1021/nl010058r.

[543] H. Bi, Q. Sun, X. Zhao, W. You, D.W. Zhang, R. Che, Microstructure research for ferroelectric origin in the strained Hf0.5Zr0.5O2 thin film via geometric phase analysis, Appl. Phys. Lett. 112 (2018), 143503, https://doi.org/10.1063/1.5013093.

[544] S. Estandía, N. Dix, J. Gazquez, I. Fina, J. Lyu, M.F. Chisholm, J. Fontcuberta, F. Sánchez, Engineering ferroelectric Hf0.5Zr0.5O2 thin films by epitaxial stress, ACS Appl. Electron. Mater. 1 (2019) 1449–1457, https://doi.org/10.1021/acsaelm.9b00256.

[545] S.S. Cheema, D. Kwon, N. Shanker, R. dos Reis, S.-L. Hsu, J. Xiao, H. Zhang, R. Wagner, A. Datar, M.R. McCarter, C.R. Serrao, A.K. Yadav, G. Karbasian, C.-H. Hsu, A.J. Tan, L.-C. Wang, V. Thakare, X. Zhang, A. Mehta, E. Karapetrova, R. V. Chopdekar, P. Shafer, E. Arenholz, C. Hu, R. Proksch, R. Ramesh, J. Ciston, S. Salahuddin, Enhanced ferroelectricity in ultrathin films grown directly on silicon, Nature 580 (2020) 478–482, https://doi.org/10.1038/s41586-020-2208-x.

[546] S.E. Reyes-Lillo, K.F. Garrity, K.M. Rabe, Antiferroelectricity in thin-film ZrO_2 from first principles, Phys. Rev. B 90 (2014), 140103, https://doi.org/10.1103/PhysRevB.90.140103.

[547] Z. Fan, J.Y. Deng, J.X. Wang, Z.Y. Liu, P. Yang, J.X. Xiao, X.B. Yan, Z.L. Dong, J. Wang, J.S. Chen, Ferroelectricity emerging in strained (111)-textured ZrO_2 thin films, Appl. Phys. Lett. 108 (2016), 012906, https://doi.org/10.1063/1.4939660.

[548] X. Yang, Y. Wang, H.Y. Yan, Y.F. Chen, Effects of epitaxial strains on spontaneous polarizations and band gaps of alkaline-earth-metal oxides MO (M = Mg, Ca, Sr, Ba), Comput. Mater. Sci. 121 (2016) 61–66, https://doi.org/10.1016/j.commatsci.2016.04.021.

[549] A.N. Morozovska, E.A. Eliseev, M.D. Glinchuk, R. Blinc, Analytical prediction of size-induced ferroelectricity in BaO nanowires under stress, Phys. Rev. B 81 (2010), 092101, https://doi.org/10.1103/PhysRevB.81.092101.

[550] E. Bousquet, M. Dawber, N. Stucki, C. Lichtensteiger, P. Hermet, S. Gariglio, J. M. Triscone, P. Ghosez, Improper ferroelectricity in perovskite oxide artificial superlattices, Nature 452 (2008) 732–736, https://doi.org/10.1038/nature06817.

[551] M. Djermouni, A. Zaoui, S. Kacimi, N. Benayad, A. Boukortt, Ferromagnetism and ferroelectricity in EuX (X = O, S): pressure effects, Eur. Phys. J. B 91 (2018) 28, https://doi.org/10.1140/epjb/e2017-80604-7.

[552] J.H. de Boer, E.J.W. Verwey, Semi-conductors with partially and with completely filled 3d -lattice bands, Proc. Phys. Soc. 49 (1937) 59, https://doi.org/10.1088/0959-5309/49/4S/307.

[553] N.F. Mott, R. Peierls, Discussion of the paper by de Boer and Verwey, Proceedings of the Physical Society 49 (1937) 72. https://doi.org/10.1088/0959–5309/49/4S/308.

[554] M. Imada, A. Fujimori, Y. Tokura, Metal-insulator transitions, Rev. Mod. Phys. 70 (1998) 1039–1263, https://doi.org/10.1103/RevModPhys.70.1039.

[555] J.M. Honig, L.L.V. Zandt, The metal-insulator transition in selected oxides, Annu. Rev. Mater. Sci. 5 (1975) 225–278, https://doi.org/10.1146/annurev.ms.05.080175.001301.

[556] A.J. Millis, B.I. Shraiman, R. Mueller, Dynamic Jahn-Teller effect and colossal magnetoresistance in $La_{1-x}Sr_xMnO_3$, Phys. Rev. Lett. 77 (1996) 175–178, https://doi.org/10.1103/PhysRevLett.77.175.

[557] M.K. Wu, J.R. Ashburn, C.J. Torng, P.H. Hor, R.L. Meng, L. Gao, Z.J. Huang, Y. Q. Wang, C.W. Chu, Superconductivity at 93K in a new mixed-phase Y-Ba-Cu-O compound system at ambient pressure, Phys. Rev. Lett. 58 (1987) 908–910, https://doi.org/10.1103/PhysRevLett.58.908.

[558] C.N. Berglund, H.J. Guggenheim, Electronic properties of VO_2 near the semiconductor-metal transition, Phys. Rev. 185 (1969) 1022–1033, https://doi.org/10.1103/PhysRev.185.1022.

[559] M. Marezio, D.B. McWhan, J.P. Remeika, P.D. Dernier, Structural aspects of the metal-insulator transitions in Cr-Doped VO_2, Phys. Rev. B 5 (1972) 2541–2551, https://doi.org/10.1103/PhysRevB.5.2541.

[560] A. Zylbersztejn, N.F. Mott, Metal-insulator transition in vanadium dioxide, Phys. Rev. B 11 (1975) 4383–4395, https://doi.org/10.1103/PhysRevB.11.4383.

[561] J.B. Goodenough, The two components of the crystallographic transition in VO_2, J. Solid State Chem. 3 (1971) 490–500, https://doi.org/10.1016/0022-4596(71)90091-0.

[562] R.M. Wentzcovitch, W.W. Schulz, P.B. Allen, VO_2: Peierls or Mott-Hurbbard? A view from band theory, Phys. Rev. Lett. 72 (1994) 3389–3392, https://doi.org/10.1103/PhysRevLett.72.3389.

[563] T.M. Rice, H. Launois, J.P. Pouget, Comment on "VO_2: Peierls or Mott-Hubbard? A view from band theory", Phys. Rev. Lett. 73 (1994), https://doi.org/10.1103/PhysRevLett.73.3042.

[564] M. Abbate, F.M.F. de Groot, J.C. Fuggle, Y.J. Ma, C.T. Chen, F. Sette, A. Fujimori, Y. Ueda, K. Kosuge, Soft-x-ray-absorption studies of the electronic-structure changes through the VO_2 phase transition, Phys. Rev. B 43 (1991) 7263–7266, https://doi.org/10.1103/PhysRevB.43.7263.

[565] S. Biermann, A. Poteryaev, A.I. Lichtenstein, A. Georges, Dynamical singlets and correlation-assisted peierls transition in VO_2, Phys. Rev. Lett. 94 (2005), 026404, https://doi.org/10.1103/PhysRevLett.94.026404.

[566] M.W. Haverkort, Z. Hu, A. Tanaka, W. Reichelt, S.V. Streltsov, M.A. Korotin, V. I. Anisimov, H.H. Hsieh, H.J. Lin, C.T. Chen, D.I. Khomskii, L.H. Tjeng, Orbital-assisted metal-insulator transition in VO_2, Phys. Rev. Lett. 95 (2005), 196404, https://doi.org/10.1103/PhysRevLett.95.196404.

[567] T.C. Koethe, Z. Hu, M.W. Haverkort, C. Schüßler-Langeheine, F. Venturini, N. B. Brookes, O. Tjernberg, W. Reichelt, H.H. Hsieh, H.J. Lin, C.T. Chen, L.H. Tjeng, Transfer of spectral weight and symmetry across the metal-insulator transition in VO_2, Phys. Rev. Lett. 97 (2006), 116402, https://doi.org/10.1103/PhysRevLett.97.116402.

[568] D.I. Khomskii, T. Mizokawa, Orbitally induced peierls state in spinels, Phys. Rev. Lett. 94 (2005), 156402, https://doi.org/10.1103/PhysRevLett.94.156402.

[569] M.S. Senn, J.P. Wright, J.P. Attfield, Charge order and three-site distortions in the Verwey structure of magnetite, Nature 481 (2012) 173–176, https://doi.org/10.1038/nature10704.

[570] J. Laverock, L.F.J. Piper, A.R.H. Preston, B. Chen, J. McNulty, K.E. Smith, S. Kittiwatanakul, J.W. Lu, S.A. Wolf, P.A. Glans, J.H. Guo, Strain dependence of bonding and hybridization across the metal-insulator transition of VO_2, Phys. Rev. B 85 (2012), 081104, https://doi.org/10.1103/PhysRevB.85.081104.

[571] T.J. Huffman, P. Xu, A.J. Hollingshad, M.M. Qazilbash, L. Wang, R.A. Lukaszew, S. Kittiwatanakul, J. Lu, S.A. Wolf, Modification of electronic structure in compressively strained vanadium dioxide films, Phys. Rev. B 91 (2015), 205140, https://doi.org/10.1103/PhysRevB.91.205140.

[572] M. Yang, Y. Yang, B. Hong, L. Wang, K. Hu, Y. Dong, H. Xu, H. Huang, J. Zhao, H. Chen, L. Song, H. Ju, J. Zhu, J. Bao, X. Li, Y. Gu, T. Yang, X. Gao, Z. Luo, C. Gao, Suppression of structural phase transition in VO_2 by epitaxial strain in vicinity of metal-insulator transition, Sci. Rep. 6 (2016) 23119, https://doi.org/10.1038/srep23119.

[573] S. Mukherjee, N.F. Quackenbush, H. Paik, C. Schlueter, T.L. Lee, D.G. Schlom, L.F. J. Piper, W.-C. Lee, Tuning a strain-induced orbital selective Mott transition in epitaxial VO_2, Phys. Rev. B 93 (2016), 241110, https://doi.org/10.1103/PhysRevB.93.241110.

[574] J. Laverock, V. Jovic, A.A. Zakharov, Y.R. Niu, S. Kittiwatanakul, B. Westhenry, J. W. Lu, S.A. Wolf, K.E. Smith, Observation of weakened V-V dimers in the monoclinic metallic phase of strained VO_2, Phys. Rev. Lett. 121 (2018), 256403, https://doi.org/10.1103/PhysRevLett.121.256403.

[575] D. Lee, B. Chung, Y. Shi, G.-Y. Kim, N. Campbell, F. Xue, K. Song, S.-Y. Choi, J. P. Podkaminer, T.H. Kim, P.J. Ryan, J.-W. Kim, T.R. Paudel, J.-H. Kang, J. W. Spinuzzi, D.A. Tenne, E.Y. Tsymbal, M.S. Rzchowski, L.Q. Chen, J. Lee, C. B. Eom, Isostructural metal-insulator transition in VO_2, Science 362 (2018) 1037–1040, https://doi.org/10.1126/science.aam9189.

[576] J. Wei, Z. Wang, W. Chen, D.H. Cobden, New aspects of the metal-insulator transition in single-domain vanadium dioxide nanobeams, Nat. Nanotechnol. 4 (2009) 420–424, https://doi.org/10.1038/nnano.2009.141.

[577] B. Lazarovits, K. Kim, K. Haule, G. Kotliar, Effects of strain on the electronic structure of VO_2, Phys. Rev. B 81 (2010), 115117, https://doi.org/10.1103/PhysRevB.81.115117.

[578] M.M. Qazilbash, M. Brehm, B.-G. Chae, P.C. Ho, G.O. Andreev, B.-J. Kim, S. J. Yun, A.V. Balatsky, M.B. Maple, F. Keilmann, H.-T. Kim, D.N. Basov, Mott transition in VO_2 revealed by infrared spectroscopy and nano-imaging, Science 318 (2007) 1750–1753, https://doi.org/10.1126/science.1150124.

[579] P. Baum, D.-S. Yang, A.H. Zewail, 4D visualization of transitional structures in phase transformations by electron diffraction, Science 318 (2007) 788–792, https://doi.org/10.1126/science.1147724.

[580] J. Lu, K.G. West, S.A. Wolf, Very large anisotropy in the dc conductivity of epitaxial VO_2 thin films grown on (011) rutile TiO_2 substrates, Appl. Phys. Lett. 93 (2008), 262107, https://doi.org/10.1063/1.3058769.

[581] Y. Muraoka, Z. Hiroi, Metal–insulator transition of VO_2 thin films grown on TiO_2 (001) and (110) substrates, Appl. Phys. Lett. 80 (2002) 583–585, https://doi.org/10.1063/1.1446215.

[582] N.F. Quackenbush, J.W. Tashman, J.A. Mundy, S. Sallis, H. Paik, R. Misra, J. A. Moyer, J.H. Guo, D.A. Fischer, J.C. Woicik, D.A. Muller, D.G. Schlom, L.F. J. Piper, Nature of the metal insulator transition in ultrathin epitaxial vanadium dioxide, Nano Lett. 13 (2013) 4857–4861, https://doi.org/10.1021/nl402716d.

[583] L.L. Fan, S. Chen, Z.L. Luo, Q.H. Liu, Y.F. Wu, L. Song, D.X. Ji, P. Wang, W.S. Chu, C. Gao, C.W. Zou, Z.Y. Wu, Strain dynamics of ultrathin VO_2 film grown on TiO_2 (001) and the associated phase transition modulation, Nano Lett. 14 (2014) 4036–4043, https://doi.org/10.1021/nl501480f.

[584] K. Kawatani, T. Kanki, H. Tanaka, Formation mechanism of a microscale domain and effect on transport properties in strained VO_2 thin films on TiO_2(001), Phys. Rev. B 90 (2014), 054203, https://doi.org/10.1103/PhysRevB.90.054203.

[585] L.L. Fan, S. Chen, Q.H. Liu, G.M. Liao, Y.L. Chen, H. Ren, C.W. Zou, The epitaxial growth and interfacial strain study of VO_2/MgF_2 (001) films by synchrotron based grazing incidence X-ray diffraction, J. Alloy. Compd. 678 (2016) 312–316, https://doi.org/10.1016/j.jallcom.2016.03.277.

[586] S.A. Howard, E. Evlyukhin, G. Páez Fajardo, H. Paik, D.G. Schlom, L.F.J. Piper, Digital tuning of the transition temperature of epitaxial VO_2 thin films on MgF_2 substrates by strain engineering, Adv. Mater. Interfaces 8 (2021), 2001790, https://doi.org/10.1002/admi.202001790.

[587] Z. Yang, C. Ko, S. Ramanathan, Metal-insulator transition characteristics of VO_2 thin films grown on Ge(100) single crystals, J. Appl. Phys. 108 (2010), 073708, https://doi.org/10.1063/1.3492716.

[588] S. Fischer, J.-O. Krisponeit, M. Foerster, L. Aballe, J. Falta, J.I. Flege, Massively strained VO_2 thin film growth on RuO_2, Cryst. Growth Des. 20 (2020) 2734–2741, https://doi.org/10.1021/acs.cgd.0c00120.

[589] V. Thery, A. Boulle, A. Crunteanu, J.C. Orlianges, A. Beaumont, R. Mayet, A. Mennai, F. Cosset, A. Bessaudou, M. Fabert, Role of thermal strain in the metal-insulator and structural phase transition of epitaxial VO_2 films, Phys. Rev. B 93 (2016), 184106, https://doi.org/10.1103/PhysRevB.93.184106.

[590] C. Chen, Y. Zhu, Y. Zhao, J.H. Lee, H. Wang, A. Bernussi, M. Holtz, Z. Fan, VO_2 multidomain heteroepitaxial growth and terahertz transmission modulation, Appl. Phys. Lett. 97 (2010), 211905, https://doi.org/10.1063/1.3519361.

[591] Y. Guo, X. Sun, J. Jiang, B. Wang, X. Chen, X. Yin, W. Qi, L. Gao, L. Zhang, Z. Lu, R. Jia, S. Pendse, Y. Hu, Z. Chen, E. Wertz, D. Gall, J. Feng, T.-M. Lu, J. Shi, A reconfigurable remotely epitaxial VO_2 electrical heterostructure, Nano Lett. 20 (2020) 33–42, https://doi.org/10.1021/acs.nanolett.9b02696.

[592] J. Jian, X. Wang, L. Li, M. Fan, W. Zhang, J. Huang, Z. Qi, H. Wang, Continuous tuning of phase transition temperature in VO_2 thin films on c-Cut sapphire substrates via strain variation, ACS Appl. Mater. Interfaces 9 (2017) 5319–5327, https://doi.org/10.1021/acsami.6b13217.

[593] Y. Yang, X. Mao, Y. Yao, H. Huang, Y. Lu, L. Luo, X. Zhang, G. Yin, T. Yang, X. Gao, Thickness effects on the epitaxial strain states and phase transformations in (001)-VO_2/TiO_2 thin films, J. Appl. Phys. 125 (2019), 082508, https://doi.org/10.1063/1.5049551.

[594] T. Kikuzuki, R. Takahashi, M. Lippmaa, Strained state dynamics in a VO_2 thin film, Phys. Rev. B 82 (2010), 144113, https://doi.org/10.1103/PhysRevB.82.144113.

[595] A. Tselev, E. Strelcov, I.A. Luk'yanchuk, J.D. Budai, J.Z. Tischler, I.N. Ivanov, K. Jones, R. Proksch, S.V. Kalinin, A. Kolmakov, Interplay between ferroelastic and metal-insulator phase transitions in strained quasi-two-dimensional VO_2 nanoplatelets, Nano Lett. 10 (2010) 2003–2011, https://doi.org/10.1021/nl1008794.

[596] A.C. Jones, S. Berweger, J. Wei, D. Cobden, M.B. Raschke, Nano-optical investigations of the metal-insulator phase behavior of individual VO_2 microcrystals, Nano Lett. 10 (2010) 1574–1581, https://doi.org/10.1021/nl903765h.

[597] K. Appavoo, D.Y. Lei, Y. Sonnefraud, B. Wang, S.T. Pantelides, S.A. Maier, R. F. Haglund, Role of defects in the phase transition of VO_2 nanoparticles probed by plasmon resonance spectroscopy, Nano Lett. 12 (2012) 780–786, https://doi.org/10.1021/nl203782y.

[598] E.U. Donev, R. Lopez, L.C. Feldman, R.F. Haglund, Confocal raman microscopy across the metal−insulator transition of single vanadium dioxide nanoparticles, Nano Lett. 9 (2009) 702–706, https://doi.org/10.1021/nl8031839.

[599] K. Appavoo, R.F. Haglund, Detecting nanoscale size dependence in VO_2 phase transition using a split-ring resonator metamaterial, Nano Lett. 11 (2011) 1025–1031, https://doi.org/10.1021/nl103842v.

[600] R. Lopez, L.C. Feldman, R.F. Haglund, Size-dependent optical properties of VO_2 nanoparticle arrays, Phys. Rev. Lett. 93 (2004), 177403, https://doi.org/10.1103/PhysRevLett.93.177403.

[601] M.M. Fadlelmula, E.C. Sürmeli, M. Ramezani, T.S. Kasırga, Effects of thickness on the metal–insulator transition in free-standing vanadium dioxide nanocrystals, Nano Lett. 17 (2017) 1762–1767, https://doi.org/10.1021/acs.nanolett.6b05067.

[602] J. Wu, Q. Gu, B.S. Guiton, N.P. de Leon, O. Lian, H. Park, Strain-induced self organization of metal-insulator domains in single-crystalline VO_2 nanobeams, Nano Lett. 6 (2006) 2313–2317, https://doi.org/10.1021/nl061831r.

[603] Q. Gu, A. Falk, J. Wu, L. Ouyang, H. Park, Current-driven phase oscillation and domain-wall propagation in $W_xV_{1-x}O_2$ nanobeams, Nano Lett. 7 (2007) 363–366, https://doi.org/10.1021/nl0624768.

[604] Y. Li, S. Ji, Y. Gao, H. Luo, P. Jin, Modification of Mott phase transition characteristics in VO_2@TiO_2 core/shell nanostructures by misfit-strained heteroepitaxy, ACS Appl. Mater. Interfaces 5 (2013) 6603–6614, https://doi.org/10.1021/am401297g.

[605] S.-J. Chang, J.B. Park, G. Lee, H.J. Kim, J.-B. Lee, T.-S. Bae, Y.-K. Han, T.J. Park, Y.S. Huh, W.-K. Hong, In situ probing of doping- and stress-mediated phase transitions in a single-crystalline VO_2 nanobeam by spatially resolved Raman spectroscopy, Nanoscale 6 (2014) 8068–8074, https://doi.org/10.1039/c4nr01118j.

[606] M.-W. Kim, S.-S. Ha, O. Seo, D.Y. Noh, B.-J. Kim, Real-time structural and electrical characterization of metal-insulator transition in strain-modulated single-phase VO_2 wires with controlled diameters, Nano Lett. 16 (2016) 4074–4081, https://doi.org/10.1021/acs.nanolett.6b00719.

[607] S. Pendse, J. Jiang, L. Zhang, Y. Guo, Z. Chen, Y. Hu, Z. Lu, S. Li, J. Feng, T.-M. Lu, J. Shi, Tuning phase transition kinetics via van der Waals epitaxy of single crystalline VO_2 on hexagonal-BN, J. Cryst. Growth 543 (2020), 125699, https://doi.org/10.1016/j.jcrysgro.2020.125699.

[608] W. Fan, S. Huang, J. Cao, E. Ertekin, C. Barrett, D.R. Khanal, J.C. Grossman, J. Wu, Superelastic metal-insulator phase transition in single-crystal VO_2 nanobeams, Phys. Rev. B 80 (2009), 241105, https://doi.org/10.1103/PhysRevB.80.241105.

[609] J.P. Pouget, H. Launois, J.P. D'Haenens, P. Merenda, T.M. Rice, Electron localization induced by uniaxial stress in pure VO_2, Phys. Rev. Lett. 35 (1975) 873–875, https://doi.org/10.1103/PhysRevLett.35.873.

[610] K. Nagashima, T. Yanagida, H. Tanaka, T. Kawai, Interface effect on metal-insulator transition of strained vanadium dioxide ultrathin films, J. Appl. Phys. 101 (2007), 026103, https://doi.org/10.1063/1.2424321.

[611] Y. Gu, J. Cao, J. Wu, L.-Q. Chen, Thermodynamics of strained vanadium dioxide single crystals, J. Appl. Phys. 108 (2010), 083517, https://doi.org/10.1063/1.3499349.

[612] R. Shi, X. Cai, W. Wang, J. Wang, D. Kong, N. Cai, P. Chen, P. He, Z. Wu, A. Amini, N. Wang, C. Cheng, Single-crystalline vanadium dioxide actuators, Adv. Funct. Mater. 29 (2019), 1900527, https://doi.org/10.1002/adfm.201900527.

[613] M. Ghedira, H. Vincent, M. Marezio, J.C. Launay, Structural aspects of the metal-insulator transitions in V0.985Al0.015O2, J. Solid State Chem. 22 (1977) 423–438, https://doi.org/10.1016/0022-4596(77)90020-2.

[614] A. Tselev, I.A. Luk'yanchuk, I.N. Ivanov, J.D. Budai, J.Z. Tischler, E. Strelcov, A. Kolmakov, S.V. Kalinin, Symmetry relationship and strain-induced transitions between insulating M1 and M2 and metallic R phases of vanadium dioxide, Nano Lett. 10 (2010) 4409–4416, https://doi.org/10.1021/nl1020443.

[615] N.H. Azhan, K. Su, K. Okimura, M. Zaghrioui, J. Sakai, Appearance of large crystalline domains in VO_2 films grown on sapphire (001) and their phase transition characteristics, J. Appl. Phys. 117 (2015), 245314, https://doi.org/10.1063/1.4923223.

[616] Y. Ji, Y. Zhang, M. Gao, Z. Yuan, Y. Xia, C. Jin, B. Tao, C. Chen, Q. Jia, Y. Lin, Role of microstructures on the M1-M2 phase transition in epitaxial VO_2 thin films, Sci. Rep. 4 (2014) 4854, https://doi.org/10.1038/srep04854.

[617] N.F. Quackenbush, H. Paik, M.J. Wahila, S. Sallis, M.E. Holtz, X. Huang, A. Ganose, B.J. Morgan, D.O. Scanlon, Y. Gu, F. Xue, L.Q. Chen, G.E. Sterbinsky, C. Schlueter, T.L. Lee, J.C. Woicik, J.H. Guo, J.D. Brock, D.A. Muller, D.A. Arena, D.G. Schlom, L.F.J. Piper, Stability of the M2 phase of vanadium dioxide induced by coherent epitaxial strain, Phys. Rev. B 94 (2016), 085105, https://doi.org/10.1103/PhysRevB.94.085105.

[618] S. Zhang, J.Y. Chou, L.J. Lauhon, Direct correlation of structural domain formation with the metal insulator transition in a VO_2 nanobeam, Nano Lett. 9 (2009) 4527–4532, https://doi.org/10.1021/nl9028973.

[619] J.M. Atkin, S. Berweger, E.K. Chavez, M.B. Raschke, J. Cao, W. Fan, J. Wu, Strain and temperature dependence of the insulating phases of VO_2 near the metal-insulator transition, Phys. Rev. B 85 (2012), 020101, https://doi.org/10.1103/PhysRevB.85.020101.

[620] E. Strelcov, A. Tselev, I. Ivanov, J.D. Budai, J. Zhang, J.Z. Tischler, I. Kravchenko, S.V. Kalinin, A. Kolmakov, Doping-sased stabilization of the M2 phase in free-standing VO_2 nanostructures at room temperature, Nano Lett. 12 (2012) 6198–6205, https://doi.org/10.1021/nl303065h.

[621] K. Liu, S. Lee, S. Yang, O. Delaire, J. Wu, Recent progresses on physics and applications of vanadium dioxide, Mater. Today 21 (2018) 875–896, https://doi.org/10.1016/j.mattod.2018.03.029.

[622] B. Hu, Y. Ding, W. Chen, D. Kulkarni, Y. Shen, V.V. Tsukruk, Z.L. Wang, External-strain induced insulating phase transition in VO_2 nanobeam and its application as flexible strain sensor, Adv. Mater. 22 (2010) 5134–5139, https://doi.org/10.1002/adma.201002868.

[623] B. Hu, Y. Zhang, W. Chen, C. Xu, Z.L. Wang, Self-heating and external strain coupling induced phase transition of VO_2 nanobeam as single domain switch, Adv. Mater. 23 (2011) 3536–3541, https://doi.org/10.1002/adma.201101731.

[624] K.H. Ahn, T. Lookman, A.R. Bishop, Strain-induced metal–insulator phase coexistence in perovskite manganites, Nature 428 (2004) 401, https://doi.org/10.1038/nature02364.

[625] S. Autier-Laurent, B. Mercey, D. Chippaux, P. Limelette, C. Simon, Strain-induced pressure effect in pulsed laser deposited thin films of the strongly correlated oxide V_2O_3, Phys. Rev. B 74 (2006), https://doi.org/10.1103/PhysRevB.74.195109.

[626] S. Yonezawa, Y. Muraoka, Y. Ueda, Z. Hiroi, Epitaxial strain effects on the metal-insulator transition in V_2O_3 thin films, Solid State Commun. 129 (2004) 245–248, https://doi.org/10.1016/j.ssc.2003.10.024.

[627] A.I. Frenkel, D.M. Pease, J.I. Budnick, P. Metcalf, E.A. Stern, P. Shanthakumar, T. Huang, Strain-induced bond buckling and its role in insulating properties of Cr-Doped V_2O_3, Phys. Rev. Lett. 97 (2006), 195502, https://doi.org/10.1103/PhysRevLett.97.195502.

[628] G.C. Loh, R. Pandey, Versatile electronic properties of atomically layered ScO_2, J. Mater. Chem. C. 3 (2015) 6627–6644, https://doi.org/10.1039/c5tc01096a.

[629] L. Bai, Q. Li, S.A. Corr, Y. Meng, C. Park, S.V. Sinogeikin, C. Ko, J. Wu, G. Shen, Pressure-induced phase transitions and metallization in VO_2, Phys. Rev. B 91 (2015), 104110, https://doi.org/10.1103/PhysRevB.91.104110.

[630] P. Sinjukow, W. Nolting, Metal-insulator transition in EuO, Phys. Rev. B 68 (2003), 125107, https://doi.org/10.1103/PhysRevB.68.125107.

[631] T. Makino, T. Yasuda, Y. Segawa, A. Ohtomo, K. Tamura, M. Kawasaki, H. Koinuma, Strain effects on exciton resonance energies of ZnO epitaxial layers, Appl. Phys. Lett. 79 (2001) 1282–1284, https://doi.org/10.1063/1.1398328.

[632] C.P. Dietrich, M. Lange, F.J. Klüpfel, Hv Wenckstern, R. Schmidt-Grund, M. Grundmann, Strain distribution in bent ZnO microwires, Appl. Phys. Lett. 98 (2011), 031105, https://doi.org/10.1063/1.3544939.

[633] X. Han, L. Kou, Z. Zhang, Z. Zhang, X. Zhu, J. Xu, Z. Liao, W. Guo, D. Yu, Strain-gradient effect on energy bands in bent ZnO microwires, Adv. Mater. 24 (2012) 4707–4711, https://doi.org/10.1002/adma.201104372.

[634] X.W. Fu, C. Su, Q. Fu, X.L. Zhu, R. Zhu, C.P. Liu, Z.M. Liao, J. Xu, W.L. Guo, J. Feng, J. Li, D.P. Yu, Tailoring exciton dynamics by elastic strain- gradient in semiconductors, Adv. Mater. 26 (2014) 2572–2579, https://doi.org/10.1002/adma.201305058.

[635] Z.-M. Liao, H.-C. Wu, Q. Fu, X. Fu, X. Zhu, J. Xu, I.V. Shvets, Z. Zhang, W. Guo, Y. Leprince-Wang, Q. Zhao, X. Wu, D.-P. Yu, Strain induced exciton fine-structure splitting and shift in bent ZnO microwires, Sci. Rep. 2 (2012) 452, https://doi.org/10.1038/srep00452.

[636] X.W. Fu, C.Z. Li, L. Fang, D.M. Liu, J. Xu, D.P. Yu, Z.M. Liao, Strain-gradient modulated exciton emission in bent ZnO wires probed by cathodoluminescence, ACS Nano 10 (2016) 11469–11474, https://doi.org/10.1021/acsnano.6b07206.

[637] S. Xu, W. Guo, S. Du, M.M.T. Loy, N. Wang, Piezotronic effects on the optical properties of ZnO nanowires, Nano Lett. 12 (2012) 5802–5807, https://doi.org/10.1021/nl303132c.

[638] S. Li, Q. Jiang, G.W. Yang, Uniaxial strain modulated band gap of ZnO nanostructures, Appl. Phys. Lett. 96 (2010), 213101, https://doi.org/10.1063/1.3435479.

[639] S.K. Yadav, T. Sadowski, R. Ramprasad, Density functional theory study of ZnX (X⎓O, S, Se, Te) under uniaxial strain, Phys. Rev. B 81 (2010), 144120, https://doi.org/10.1103/PhysRevB.81.144120.

[640] Q. Yan, P. Rinke, M. Winkelnkemper, A. Qteish, D. Bimberg, M. Scheffler, C. G. Van de Walle, Strain effects and band parameters in MgO, ZnO, and CdO, Appl. Phys. Lett. 101 (2012), https://doi.org/10.1063/1.4759107.

[641] R. Chaurasiya, A. Dixit, R. Pandey, Strain-driven thermodynamic stability and electronic transitions in ZnX (X = O, S, Se, and Te) monolayers, J. Appl. Phys. 125 (2019), 082540, https://doi.org/10.1063/1.5053680.

[642] W. Yu, Y. He, G. Ouyang, Surface gradient dependence of bandgap energy and dielectric constant of ZnO tapered nanowires, J. Appl. Phys. 122 (2017), 094307, https://doi.org/10.1063/1.4996239.

[643] A. Vazinishayan, D.R. Lambada, S. Yang, G. Zhang, B. Cheng, Y.T. Woldu, S. Shafique, Y. Wang, N. Anastase, Effects of mechanical strain on optical properties of ZnO nanowire, AIP Adv. 8 (2018), 025306, https://doi.org/10.1063/1.5016995.

[644] G. Tse, D.P. Yu, The bandgap distribution investigated across the strain-induced bending ZnO nanowire, Mod. Phys. Lett. B 30 (2016), 1650048, https://doi.org/10.1142/S0217984916500482.

[645] X.W. Fu, Z.M. Liao, R. Liu, F. Lin, J. Xu, R. Zhu, W. Zhong, Y.K. Liu, W.L. Guo, D. P. Yu, Strain loading mode dependent bandgap deformation potential in ZnO micro/nanowires, ACS Nano 9 (2015) 11960–11967, https://doi.org/10.1021/acsnano.5b04617.

[646] R. Saniz, H. Dixit, D. Lamoen, B. Partoens, Quasiparticle energies and uniaxial pressure effects on the properties of SnO_2, Appl. Phys. Lett. 97 (2010), 261901, https://doi.org/10.1063/1.3532109.

[647] O. Mounkachi, E. Salmani, M. Lakhal, H. Ez-Zahraouy, M. Hamedoun, M. Benaissa, A. Kara, A. Ennaoui, A. Benyoussef, Band-gap engineering of SnO2, Sol. Energy Mater. Sol. Cells 148 (2016) 34–38, https://doi.org/10.1016/j.solmat.2015.09.062.

[648] W. Zhou, Y. Liu, Y. Yang, P. Wu, Band gap engineering of SnO_2 by epitaxial strain: experimental and theoretical investigations, J. Phys. Chem. C 118 (2014) 6448–6453, https://doi.org/10.1021/jp500546r.

[649] S.F. Rus, T.Z. Ward, A. Herklotz, Strain-induced optical band gap variation of SnO_2 films, Thin Solid Films 615 (2016) 103–106, https://doi.org/10.1016/j.tsf.2016.06.057.

[650] M. Du, L. Cui, Q. Wan, Tensile strain induced narrowed bandgap of TiO_2 films: utilizing the two-way shape memory effect of TiNiNb substrate and in-situ mechanical bending, Mater. Sci. Eng.: B 207 (2016) 7–12, https://doi.org/10.1016/j.mseb.2016.01.012.

[651] W.-J. Yin, S. Chen, J.-H. Yang, X.-G. Gong, Y. Yan, S.-H. Wei, Effective band gap narrowing of anatase TiO_2 by strain along a soft crystal direction, Appl. Phys. Lett. 96 (2010), 221901, https://doi.org/10.1063/1.3430005.

[652] N. Kelaidis, A. Kordatos, S.R.G. Christopoulos, A. Chroneos, A roadmap of strain in doped anatase TiO_2, Sci. Rep. 8 (2018) 12790, https://doi.org/10.1038/s41598-018-30747-5.

[653] B.S. Dandogbessi, O. Akin-Ojo, First principles prediction of the electronic structure and carrier mobilities of biaxially strained molybdenum trioxide (MoO_3), J. Appl. Phys. 120 (2016), 055105, https://doi.org/10.1063/1.4960142.

[654] J.X. Zhang, Q. He, M. Trassin, W. Luo, D. Yi, M.D. Rossell, P. Yu, L. You, C. H. Wang, C.Y. Kuo, J.T. Heron, Z. Hu, R.J. Zeches, H.J. Lin, A. Tanaka, C.T. Chen, L.H. Tjeng, Y.H. Chu, R. Ramesh, Microscopic origin of the giant ferroelectric polarization in tetragonal-like $BiFeO_3$, Phys. Rev. Lett. 107 (2011), 147602, https://doi.org/10.1103/PhysRevLett.107.147602.

[655] K.-T. Ko, M.H. Jung, Q. He, J.H. Lee, C.S. Woo, K. Chu, J. Seidel, B.-G. Jeon, Y. S. Oh, K.H. Kim, W.-I. Liang, H.-J. Chen, Y.-H. Chu, Y.H. Jeong, R. Ramesh, J.-H. Park, C.-H. Yang, Concurrent transition of ferroelectric and magnetic ordering near room temperature, Nat. Commun. 2 (2011) 567, https://doi.org/10.1038/ncomms1576.

[656] Q. He, Y.H. Chu, J.T. Heron, S.Y. Yang, W.I. Liang, C.Y. Kuo, H.J. Lin, P. Yu, C. W. Liang, R.J. Zeches, W.C. Kuo, J.Y. Juang, C.T. Chen, E. Arenholz, A. Scholl, R. Ramesh, Electrically controllable spontaneous magnetism in nanoscale mixed phase multiferroics, Nat. Commun. 2 (2011) 225, https://doi.org/10.1038/ncomms1221.

[657] R. Ramesh, N.A. Spaldin, Multiferroics: progress and prospects in thin films, Nat. Mater. 6 (2007) 21–29, https://doi.org/10.1038/nmat1805.

[658] B.T. Matthias, R.M. Bozorth, J.H.Van Vleck, Ferromagnetic interaction in EuO, Phys. Rev. Lett. 7 (1961) 160–161, https://doi.org/10.1103/PhysRevLett.7.160.

[659] A. Schmehl, V. Vaithyanathan, A. Herrnberger, S. Thiel, C. Richter, M. Liberati, T. Heeg, M. Rockerath, L.F. Kourkoutis, S. Muhlbauer, P. Boni, D.A. Muller, Y. Barash, J. Schubert, Y. Idzerda, J. Mannhart, D.G. Schlom, Epitaxial integration of the highly spin-polarized ferromagnetic semiconductor EuO with silicon and GaN, Nat. Mater. 6 (2007) 882–887, https://doi.org/10.1038/nmat2012.

[660] T.R. McGuire, M.W. Shafer, Ferromagnetic europium compounds, J. Appl. Phys. 35 (1964) 984–988, https://doi.org/10.1063/1.1713568.

[661] H. Miyazaki, H.J. Im, K. Terashima, S. Yagi, M. Kato, K. Soda, T. Ito, S. Kimura, La-doped EuO: a rare earth ferromagnetic semiconductor with the highest Curie temperature, Appl. Phys. Lett. 96 (2010), 232503, https://doi.org/10.1063/1.3416911.

[662] S.G. Altendorf, N. Hollmann, R. Sutarto, C. Caspers, R.C. Wicks, Y.Y. Chin, Z. Hu, H. Kierspel, I.S. Elfimov, H.H. Hsieh, H.J. Lin, C.T. Chen, L.H. Tjeng, Spectroscopic observation of strain-assisted T_C enhancement in EuO upon Gd doping, Phys. Rev. B 85 (2012), 081201, https://doi.org/10.1103/PhysRevB.85.081201.

[663] N.J.C. Ingle, I.S. Elfimov, Influence of epitaxial strain on the ferromagnetic semiconductor EuO: first-principles calculations, Phys. Rev. B 77 (2008), 121202, https://doi.org/10.1103/PhysRevB.77.121202.

[664] D.B. McWhan, P.C. Souers, G. Jura, Magnetic and structural properties of europium metal and europium monoxide at high pressure, Phys. Rev. 143 (1966) 385–389, https://doi.org/10.1103/PhysRev.143.385.

[665] H.G. Zimmer, K. Takemura, K. Syassen, K. Fischer, Insulator-metal transition and valence instability in EuO near 130 kbar, Phys. Rev. B 29 (1984) 2350–2352, https://doi.org/10.1103/PhysRevB.29.2350.

[666] D. DiMarzio, M. Croft, N. Sakai, M.W. Shafer, Effect of pressure on the electrical resistance of EuO, Phys. Rev. B 35 (1987) 8891–8893, https://doi.org/10.1103/PhysRevB.35.8891.

[667] R. Schiller, W. Nolting, Thickness dependent Curie temperatures of ferromagnetic Heisenberg films, Solid State Commun. 110 (1999) 121–125, https://doi.org/10.1016/S0038-1098(98)00593-6.

[668] M. Müller, G.-X. Miao, J.S. Moodera, Thickness dependence of ferromagnetic- and metal-insulator transition in thin EuO films, J. Appl. Phys. 105 (2009) 07C917, https://doi.org/10.1063/1.3063673.

[669] M. Barbagallo, T. Stollenwerk, J. Kroha, N.J. Steinke, N.D.M. Hine, J.F.K. Cooper, C.H.W. Barnes, A. Ionescu, P.M.D.S. Monteiro, J.Y. Kim, K.R.A. Ziebeck, C. J. Kinane, R.M. Dalgliesh, T.R. Charlton, S. Langridge, Thickness-dependent magnetic properties of oxygen-deficient EuO, Phys. Rev. B 84 (2011), 075219, https://doi.org/10.1103/PhysRevB.84.075219.

[670] W.L. Roth, Magnetic structures of MnO, FeO, CoO, and NiO, Phys. Rev. 110 (1958) 1333–1341, https://doi.org/10.1103/PhysRev.110.1333.

[671] S.I. Csiszar, M.W. Haverkort, Z. Hu, A. Tanaka, H.H. Hsieh, H.J. Lin, C.T. Chen, T. Hibma, L.H. Tjeng, Controlling orbital moment and spin orientation in CoO layers by strain, Phys. Rev. Lett. 95 (2005), 187205, https://doi.org/10.1103/PhysRevLett.95.187205.

[672] A.D. Lamirand, M.M. Soares, A.Y. Ramos, H.C.N. Tolentino, M. De Santis, J. C. Cezar, A. de Siervo, M. Jamet, Robust perpendicular exchange coupling in an ultrathin CoO/PtFe double layer: Strain and spin orientation, Phys. Rev. B 88 (2013), 140401, https://doi.org/10.1103/PhysRevB.88.140401.

[673] A.D. Lamirand, M.M. Soares, M. De Santis, A.Y. Ramos, S. Grenier, H.C. N. Tolentino, Strain driven monoclinic distortion of ultrathin CoO films in the exchange-coupled CoO/FePt/Pt(001) system, J. Phys. -Condens. Matter 27 (2015), 085001, https://doi.org/10.1088/0953-8984/27/8/085001.

[674] J. Zhu, Q. Li, J.X. Li, Z. Ding, C.Y. Won, Y.Z. Wu, Volume contribution of exchange-coupling-induced uniaxial anisotropy in Fe/CoO/MgO(001) system, J. Appl. Phys. 114 (2013), https://doi.org/10.1063/1.4829009.

[675] J. Zhu, Q. Li, J.X. Li, Z. Ding, C.Y. Hua, M.J. Huang, H.J. Lin, Z. Hu, C. Won, Y. Z. Wu, Strain-modulated antiferromagnetic spin orientation and exchange coupling in Fe/CoO(001), J. Appl. Phys. 115 (2014), 193903, https://doi.org/10.1063/1.4876907.

[676] N. Fontaina-Troitino, S. Liebana-Vinas, B. Rodriguez-Gonzalez, Z.-A. Li, M. Spasova, M. Farle, V. Salgueirino, Room-temperature ferromagnetism in antiferromagnetic cobalt oxide nanooctahedra, Nano Lett. 14 (2014) 640–647, https://doi.org/10.1021/nl4038533.

[677] J. Li, E. Arenholz, Y. Meng, A. Tan, J. Park, E. Jin, H. Son, J. Wu, C.A. Jenkins, A. Scholl, H.W. Zhao, C. Hwang, Z.Q. Qiu, Continuous spin reorientation transition in epitaxial antiferromagnetic NiO thin films, Phys. Rev. B 84 (2011), 012406, https://doi.org/10.1103/PhysRevB.84.012406.

[678] W. Kim, E. Jin, J. Wu, J. Park, E. Arenholz, A. Scholl, C. Hwang, Z.Q. Qiu, Effect of NiO spin orientation on the magnetic anisotropy of the Fe film in epitaxially grown Fe/NiO/Ag(001) and Fe/NiO/MgO(001), Phys. Rev. B 81 (2010), 174416, https://doi.org/10.1103/PhysRevB.81.174416.

[679] X. Huang, X.H. Yan, Y. Xiao, Y.D. Guo, Z.H. Zhu, C.J. Dai, Strain-induced phase transition in beta-MnO_2, Europhys. Lett. 99 (2012) 27005, https://doi.org/10.1209/0295-5075/99/27005.

[680] D. Dang Duc, T. Duong Van, D.A. Tuan, S. Cho, Strain effects in epitaxial Mn_2O_3 thin film grown on MgO(100), J. Appl. Phys. 113 (2013) 17A314, https://doi.org/10.1063/1.4794720.

[681] Y. Kota, H. Imamura, M. Sasaki, Strain-induced Neel temperature enhancement in corundum-type Cr_2O_3 and Fe_2O_3, Appl. Phys. Express 6 (2013), 113007, https://doi.org/10.7567/apex.6.113007.

[682] Y. Kota, H. Imamura, M. Sasaki, Effect of lattice deformation on exchange coupling constants in Cr_2O_3, J. Appl. Phys. 115 (2014) 17D719, https://doi.org/10.1063/1.4865780.

[683] P.V.B. Pinho, A. Chartier, F. Miserque, D. Menut, J.-B. Moussy, Impact of epitaxial strain on crystal field splitting of α-Cr_2O_3(0001) thin films quantified by X-ray photoemission spectroscopy, Mater. Res. Lett. 9 (2021) 163–168, https://doi.org/10.1080/21663831.2020.1863877.

[684] M. Vila, J. Rubio-Zuazo, I. Lucas, C. Magén, A. Prados, E. Salas-Colera, I. Arnay, G.R. Castro, Ferromagnetic epitaxial Cr_2O_3 thin films grown on oxide substrates by pulsed laser deposition, Appl. Surf. Sci. 534 (2020), 147638, https://doi.org/10.1016/j.apsusc.2020.147638.

[685] S. Punugupati, J. Narayan, F. Hunte, Strain induced ferromagnetism in epitaxial Cr_2O_3 thin films integrated on Si(001), Appl. Phys. Lett. 105 (2014), 132401, https://doi.org/10.1063/1.4896975.

[686] S. Park, H. Jang, J.Y. Kim, B.G. Park, T.Y. Koo, J.H. Park, Strain control of Morin temperature in epitaxial alpha-Fe_2O_3(0001) film, Europhys. Lett. 103 (2013) 27007, https://doi.org/10.1209/0295-5075/103/27007.

[687] G. Petrich, S. von Molnár, T. Penney, Exchange-induced autoionization in Eu-Rich EuO, Phys. Rev. Lett. 26 (1971) 885–888, https://doi.org/10.1103/PhysRevLett.26.885.

[688] D.A. Davis, A. Hamilton, J. Yang, L.D. Cremar, D. Van Gough, S.L. Potisek, M. T. Ong, P.V. Braun, T.J. Martinez, S.R. White, J.S. Moore, N.R. Sottos, Force-induced activation of covalent bonds in mechanoresponsive polymeric materials, Nature 459 (2009) 68–72, https://doi.org/10.1038/nature07970.

[689] C.R. Hickenboth, J.S. Moore, S.R. White, N.R. Sottos, J. Baudry, S.R. Wilson, Biasing reaction pathways with mechanical force, Nature 446 (2007) 423–427, https://doi.org/10.1038/nature05681.

[690] L. Grabow, Y. Xu, M. Mavrikakis, Lattice strain effects on CO oxidation on Pt (111), Phys. Chem. Chem. Phys. 8 (2006) 3369–3374, https://doi.org/10.1039/B606131A.

[691] B. Yildiz, "Stretching" the energy landscape of oxides – effects on electrocatalysis and diffusion, MRS Bull. 39 (2014) 147–156, https://doi.org/10.1557/mrs.2014.8.

[692] S.L. Craig, Mechanochemistry: a tour of force, Nature 487 (2012) 176–177, https://doi.org/10.1038/487176a.

[693] S. Akbulatov, Y. Tian, R. Boulatov, Force–reactivity property of a single monomer is sufficient to predict the micromechanical behavior of its polymer, J. Am. Chem. Soc. 134 (2012) 7620–7623, https://doi.org/10.1021/ja301928d.

[694] M. Gsell, P. Jakob, D. Menzel, Effect of substrate strain on adsorption, Science 280 (1998) 717–720, https://doi.org/10.1126/science.280.5364.717.

[695] M.A. Habib, M. Nemitallah, R. Ben-Mansour, Recent development in oxy-combustion technology and its applications to gas turbine combustors and ITM reactors, Energy Fuels 27 (2013) 2–19, https://doi.org/10.1021/ef301266j.

[696] A. Chroneos, B. Yildiz, A. Tarancon, D. Parfitt, J.A. Kilner, Oxygen diffusion in solid oxide fuel cell cathode and electrolyte materials: mechanistic insights from atomistic simulations, Energy Environ. Sci. 4 (2011) 2774–2789, https://doi.org/10.1039/C0EE00717J.

[697] B.C.H. Steele, A. Heinzel, Materials for fuel-cell technologies, Nature 414 (2001) 345–352, https://doi.org/10.1038/35104620.

[698] W. Lee, J.W. Han, Y. Chen, Z. Cai, B. Yildiz, Cation size mismatch and charge interactions drive dopant segregation at the surfaces of manganite perovskites, J. Am. Chem. Soc. 135 (2013) 7909–7925, https://doi.org/10.1021/ja3125349.

[699] M. Kubicek, A. Limbeck, T. Frömling, H. Hutter, J. Fleig, Relationship between cation segregation and the electrochemical oxygen reduction kinetics of La0.6Sr0.4CoO3−δ thin film electrodes, J. Electrochem. Soc. 158 (2011) B727–B734, https://doi.org/10.1149/1.3581114.

[700] H. Jalili, J.W. Han, Y. Kuru, Z. Cai, B. Yildiz, New insights into the strain coupling to surface chemistry, electronic structure, and reactivity of La0.7Sr0.3MnO3, J. Phys. Chem. Lett. 2 (2011) 801–807, https://doi.org/10.1021/jz200160b.

[701] W.T. Hong, M. Gadre, Y.-L. Lee, M.D. Biegalski, H.M. Christen, D. Morgan, Y. Shao-Horn, Tuning the spin state in $LaCoO_3$ thin films for enhanced high-temperature oxygen electrocatalysis, J. Phys. Chem. Lett. 4 (2013) 2493–2499, https://doi.org/10.1021/jz401271m.

[702] A. Kushima, S. Yip, B. Yildiz, Competing strain effects in reactivity of $LaCoO_3$ with oxygen, Phys. Rev. B 82 (2010), 115435, https://doi.org/10.1103/PhysRevB.82.115435.

[703] Z. Cai, Y. Kuru, J.W. Han, Y. Chen, B. Yildiz, Surface electronic structure transitions at high temperature on perovskite oxides: the case of strained La0.8Sr0.2CoO3 thin films, J. Am. Chem. Soc. 133 (2011) 17696–17704, https://doi.org/10.1021/ja2059445.

[704] M.M. Kuklja, E.A. Kotomin, R. Merkle, Y.A. Mastrikov, J. Maier, Combined theoretical and experimental analysis of processes determining cathode performance in solid oxide fuel cells, Phys. Chem. Chem. Phys. 15 (2013) 5443–5471, https://doi.org/10.1039/C3CP44363A.

[705] R. Asahi, T. Morikawa, T. Ohwaki, K. Aoki, Y. Taga, Visible-light photocatalysis in nitrogen-doped titanium oxides, Science 293 (2001) 269–271, https://doi.org/10.1126/science.1061051.

[706] O. Bikondoa, C.L. Pang, R. Ithnin, C.A. Muryn, H. Onishi, G. Thornton, Direct visualization of defect-mediated dissociation of water on TiO_2(110), Nat. Mater. 5 (2006) 189, https://doi.org/10.1038/nmat1592.

[707] M. Lazzeri, A. Vittadini, A. Selloni, Structure and energetics of stoichiometric TiO_2 anatase surfaces, Phys. Rev. B 63 (2001), 155409, https://doi.org/10.1103/PhysRevB.63.155409.

[708] L. Thulin, J. Guerra, Calculations of strain-modified anatase TiO_2 band structures, Phys. Rev. B 77 (2008), 195112, https://doi.org/10.1103/PhysRevB.77.195112.

[709] Z. Liu, C. Menéndez, J. Shenoy, J.N. Hart, C.C. Sorrell, C. Cazorla, Strain engineering of oxide thin films for photocatalytic applications, Nano Energy 72 (2020), 104732, https://doi.org/10.1016/j.nanoen.2020.104732.

[710] D.-J. Shu, S.-T. Ge, M. Wang, N.-B. Ming, Interplay between external strain and oxygen vacancies on a rutile TiO_2 surface, Phys. Rev. Lett. 101 (2008), 116102, https://doi.org/10.1103/PhysRevLett.101.116102.

[711] Z.-W. Wang, D.-J. Shu, M. Wang, N.-B. Ming, Diffusion of oxygen vacancies on a strained rutile TiO_2(110) surface, Phys. Rev. B 82 (2010), 165309, https://doi.org/10.1103/PhysRevB.82.165309.

[712] S.I. Cha, K.H. Hwang, Y.H. Kim, M.J. Yun, S.H. Seo, Y.J. Shin, J.H. Moon, D. Y. Lee, Crystal splitting and enhanced photocatalytic behavior of TiO_2 rutile nano-belts induced by dislocations, Nanoscale 5 (2013) 753–758, https://doi.org/10.1039/C2NR33028H.

[713] A. Zangwill, Physics at Surfaces, Cambridge University Press,, 1988.

[714] Y. Shi, H. Sun, W.A. Saidi, M.C. Nguyen, C.Z. Wang, K. Ho, J. Yang, J. Zhao, Role of surface stress on the reactivity of anatase TiO_2(001), J. Phys. Chem. Lett. 8 (2017) 1764–1771, https://doi.org/10.1021/acs.jpclett.7b00181.

[715] A. Migani, G.N. Vayssilov, S.T. Bromley, F. Illas, K.M. Neyman, Dramatic reduction of the oxygen vacancy formation energy in ceria particles: a possible key to their remarkable reactivity at the nanoscale, J. Mater. Chem. 20 (2010) 10535–10546, https://doi.org/10.1039/C0JM01908A.

[716] T.X.T. Sayle, S.C. Parker, D.C. Sayle, Oxidising CO to CO_2 using ceria nanoparticles, Phys. Chem. Chem. Phys. 7 (2005) 2936–2941, https://doi.org/10.1039/B506359K.

[717] T.X.T. Sayle, M. Cantoni, U.M. Bhatta, S.C. Parker, S.R. Hall, G. Moebus, M. Molinari, D. Reid, S. Seal, D.C. Sayle, Strain and architecture-tuned reactivity in ceria nanostructures; enhanced catalytic oxidation of CO to CO_2, Chem. Mater. 24 (2012) 1811–1821, https://doi.org/10.1021/cm3003436.

[718] T. Wu, T. Vegge, H.A. Hansen, Improved electrocatalytic water splitting reaction on CeO_2(111) by strain engineering: a DFT+U study, ACS Catal. 9 (2019) 4853–4861, https://doi.org/10.1021/acscatal.9b00203.

[719] L. Zhang, L. Sun, Q. Meng, J. Wu, X. Hao, S. Zhai, W. Dou, Y. Jia, M. Zhou, Strain-engineered formation, migration, and electronic properties of polaronic defects in CeO2, Phys. Status Solidi (b) 258 (2021), 2100020, https://doi.org/10.1002/pssb.202100020.

[720] A. Kossoy, Y. Feldman, R. Korobko, E. Wachtel, I. Lubomirsky, J. Maier, Influence of point-defect reaction kinetics on the lattice parameter of Ce0.8Gd0.2O1.9, Adv. Funct. Mater. 19 (2009) 634–641, https://doi.org/10.1002/adfm.200801162.

[721] A. Kossoy, A.I. Frenkel, Q. Wang, E. Wachtel, I. Lubomirsky, Local structure and strain-induced distortion in Ce0.8Gd0.2O1.9, Adv. Mater. 22 (2010) 1659–1662, https://doi.org/10.1002/adma.200902041.

[722] C. Balaji Gopal, M. García-Melchor, S.C. Lee, Y. Shi, A. Shavorskiy, M. Monti, Z. Guan, R. Sinclair, H. Bluhm, A. Vojvodic, W.C. Chueh, Equilibrium oxygen storage capacity of ultrathin $CeO_{2-\delta}$ depends non-monotonically on large biaxial strain, Nat. Commun. 8 (2017) 15360, https://doi.org/10.1038/ncomms15360.

[723] M.B. Starr, X.D. Wang, Fundamental analysis of piezocatalysis process on the surfaces of strained piezoelectric materials, Sci. Rep. 3 (2013) 2160, https://doi.org/10.1038/srep02160.

[724] M. Luo, S. Guo, Strain-controlled electrocatalysis on multimetallic nanomaterials, Nat. Rev. Mater. 2 (2017) 17059, https://doi.org/10.1038/natrevmats.2017.59.

[725] J.A. Kilner, Ionic conductors: feel the strain, Nat. Mater. 7 (2008) 838–839, https://doi.org/10.1038/nmat2314.

[726] V.V. Kharton, F.M.B. Marques, A. Atkinson, Transport properties of solid oxide electrolyte ceramics: a brief review, Solid State Ion. 174 (2004) 135–149, https://doi.org/10.1016/j.ssi.2004.06.015.

[727] B. Feng, R. Ishikawa, A. Kumamoto, N. Shibata, Y. Ikuhara, Atomic scale origin of enhanced ionic conductivity at crystal defects, Nano Lett. 19 (2019) 2162–2168, https://doi.org/10.1021/acs.nanolett.9b00506.

[728] K. Wen, W. Lv, W. He, Interfacial lattice-strain effects on improving the overall performance of micro-solid oxide fuel cells, J. Mater. Chem. A 3 (2015) 20031–20050, https://doi.org/10.1039/C5TA03009A.

[729] S.B. Adler, J.W. Smith, Effects of long-range forces on oxygen transport in yttria-doped ceria: simulation and theory, J. Chem. Soc., Faraday Trans. 89 (1993) 3123–3128, https://doi.org/10.1039/FT9938903123.

[730] T. Suzuki, I. Kosacki, H.U. Anderson, Microstructure–electrical conductivity relationships in nanocrystalline ceria thin films, Solid State Ion. 151 (2002) 111–121, https://doi.org/10.1016/S0167-2738(02)00589-1.

[731] J.L.M. Rupp, A. Infortuna, L.J. Gauckler, Microstrain and self-limited grain growth in nanocrystalline ceria ceramics, Acta Mater. 54 (2006) 1721–1730, https://doi.org/10.1016/j.actamat.2005.11.032.

[732] J.L.M. Rupp, L.J. Gauckler, Microstructures and electrical conductivity of nanocrystalline ceria-based thin films, Solid State Ion. 177 (2006) 2513–2518, https://doi.org/10.1016/j.ssi.2006.07.033.

[733] S. Sanna, V. Esposito, A. Tebano, S. Licoccia, E. Traversa, G. Balestrino, Enhancement of ionic conductivity in Sm-doped ceria/yttria-stabilized zirconia heteroepitaxial structures, Small 6 (2010) 1863–1867, https://doi.org/10.1002/smll.200902348.

[734] N.I. Karageorgakis, A. Heel, J.L.M. Rupp, M.H. Aguirre, T. Graule, L.J. Gauckler, Properties of flame sprayed Ce0.8Gd0.2O1.9-δ electrolyte thin films, Adv. Funct. Mater. 21 (2011) 532–539, https://doi.org/10.1002/adfm.201001622.

[735] R.A. De Souza, A. Ramadan, S. Horner, Modifying the barriers for oxygen-vacancy migration in fluorite-structured CeO_2 electrolytes through strain: a computer simulation study, Energy Environ. Sci. 5 (2012) 5445–5453, https://doi.org/10.1039/C2EE02508F.

[736] J. Hinterberg, T. Zacherle, R.A. De Souza, Activation volume tensor for oxygen-vacancy migration in strained CeO_2 electrolytes, Phys. Rev. Lett. 110 (2013), 205901, https://doi.org/10.1103/PhysRevLett.110.205901.

[737] M.J.D. Rushton, A. Chroneos, S.J. Skinner, J.A. Kilner, R.W. Grimes, Effect of strain on the oxygen diffusion in yttria and gadolinia co-doped ceria, Solid State Ion. 230 (2013) 37–42, https://doi.org/10.1016/j.ssi.2012.09.015.

[738] W. Shen, J. Jiang, J.L. Hertz, Reduced ionic conductivity in biaxially compressed ceria, RSC Adv. 4 (2014) 21625–21630, https://doi.org/10.1039/c4ra00820k.

[739] W. Shen, J. Jiang, J.L. Hertz, Beneficial lattice strain in heterogeneously doped ceria, J. Phys. Chem. C 118 (2014) 22904–22912, https://doi.org/10.1021/jp506554z.

[740] A. Fluri, D. Pergolesi, V. Roddatis, A. Wokaun, T. Lippert, In situ stress observation in oxide films and how tensile stress influences oxygen ion conduction, Nat. Commun. 7 (2016), 10692, https://doi.org/10.1038/ncomms10692.

[741] J. Ahn, H.W. Jang, H. Ji, H. Kim, K.J. Yoon, J.-W. Son, B.-K. Kim, H.-W. Lee, J.-H. Lee, Identification of an actual strain-induced effect on fast ion conduction in a thin-film electrolyte, Nano Lett. 18 (2018) 2794–2801, https://doi.org/10.1021/acs.nanolett.7b04952.

[742] G.F. Harrington, L. Sun, B. Yildiz, K. Sasaki, N.H. Perry, H.L. Tuller, The interplay and impact of strain and defect association on the conductivity of rare-earth substituted ceria, Acta Mater. 166 (2019) 447–458, https://doi.org/10.1016/j.actamat.2018.12.058.

[743] J.-C. M'Peko, M.Fd Souza, Ionic transport in polycrystalline zirconia and Frenkel's space-charge layer postulation, Appl. Phys. Lett. 83 (2003) 737–739, https://doi.org/10.1063/1.1595729.

[744] I. Kosacki, C.M. Rouleau, P.F. Becher, J. Bentley, D.H. Lowndes, Nanoscale effects on the ionic conductivity in highly textured YSZ thin films, Solid State Ion. 176 (2005) 1319–1326, https://doi.org/10.1016/j.ssi.2005.02.021.

[745] A. Peters, C. Korte, D. Hesse, N. Zakharov, J. Janek, Ionic conductivity and activation energy for oxygen ion transport in superlattices – the multilayer system CSZ (ZrO_2 + CaO) / Al_2O_3, Solid State Ion. 178 (2007) 67–76, https://doi.org/10.1016/j.ssi.2006.12.004.

[746] C. Korte, A. Peters, J. Janek, D. Hesse, N. Zakharov, Ionic conductivity and activation energy for oxygen ion transport in superlattices-the semicoherent multilayer system YSZ (ZrO_2 + 9.5 mol% Y_2O_3)/Y_2O_3, Phys. Chem. Chem. Phys. 10 (2008) 4623–4635, https://doi.org/10.1039/B801675E.

[747] X. Guo, Comment on "colossal ionic conductivity at interfaces of epitaxial ZrO_2:Y_2O_3/$SrTiO_3$ heterostructures", Science 324 (2009) https://doi.org/10.1126/science.1168940.

[748] N. Schichtel, C. Korte, D. Hesse, J. Janek, Elastic strain at interfaces and its influence on ionic conductivity in nanoscaled solid electrolyte thin films-theoretical considerations and experimental studies, Phys. Chem. Chem. Phys. 11 (2009) 3043–3048, https://doi.org/10.1039/b900148d.

[749] A. Kushima, B. Yildiz, Oxygen ion diffusivity in strained yttria stabilized zirconia: where is the fastest strain? J. Mater. Chem. 20 (2010) 4809–4819, https://doi.org/10.1039/C000259C.

[750] M. Sillassen, P. Eklund, N. Pryds, E. Johnson, U. Helmersson, J. Bøttiger, Low-temperature superionic conductivity in strained yttria-stabilized zirconia, Adv. Funct. Mater. 20 (2010) 2071–2076, https://doi.org/10.1002/adfm.201000071.

[751] D. Pergolesi, E. Fabbri, S.N. Cook, V. Roddatis, E. Traversa, J.A. Kilner, Tensile lattice distortion does not affect oxygen transport in yttria-stabilized zirconia–CeO_2 heterointerfaces, ACS Nano 6 (2012) 10524–10534, https://doi.org/10.1021/nn302812m.

[752] B. Li, J. Zhang, T. Kaspar, V. Shutthanandan, R.C. Ewing, J. Lian, Multilayered YSZ/GZO films with greatly enhanced ionic conduction for low temperature solid oxide fuel cells, Phys. Chem. Chem. Phys. 15 (2013) 1296–1301, https://doi.org/10.1039/C2CP42964K.

[753] H. Aydin, C. Korte, M. Rohnke, J. Janek, Oxygen tracer diffusion along interfaces of strained Y_2O_3/YSZ multilayers, Phys. Chem. Chem. Phys. 15 (2013) 1944–1955, https://doi.org/10.1039/C2CP43231E.

[754] J. Jiang, X. Hu, W. Shen, C. Ni, J.L. Hertz, Improved ionic conductivity in strained yttria-stabilized zirconia thin films, Appl. Phys. Lett. 102 (2013), 143901, https://doi.org/10.1063/1.4801649.

[755] G.F. Harrington, A. Cavallaro, D.W. McComb, S.J. Skinner, J.A. Kilner, The effects of lattice strain, dislocations, and microstructure on the transport properties of YSZ films, Phys. Chem. Chem. Phys. 19 (2017) 14319–14336, https://doi.org/10.1039/C7CP02017A.

[756] M. Zhang, T. Li, Z. Li, Y. Xing, X. Zhao, M. Shahid, Y. Yuan, H. Nishijima, W. Pan, Enhanced oxygen ion conductivity in composite film electrolytes with aligned nanowires, Adv. Mater. Interfaces 5 (2018), 1800098, https://doi.org/10.1002/admi.201800098.

[757] J.L.M. Rupp, Ionic diffusion as a matter of lattice-strain for electroceramic thin films, Solid State Ion. 207 (2012) 1–13, https://doi.org/10.1016/j.ssi.2011.09.009.

[758] C. Korte, J. Keppner, A. Peters, N. Schichtel, H. Aydin, J. Janek, Coherency strain and its effect on ionic conductivity and diffusion in solid electrolytes - an improved model for nanocrystalline thin films and a review of experimental data, Phys. Chem. Chem. Phys. 16 (2014) 24575–24591, https://doi.org/10.1039/C4CP03055A.

[759] J. Ahn, S. Choi, K.J. Yoon, J.-W. Son, B.-K. Kim, J.-H. Lee, H.W. Jang, H. Kim, Strain-induced tailoring of oxygen-ion transport in highly doped CeO_2 electrolyte: effects of biaxial extrinsic and local lattice strain, ACS Appl. Mater. Interfaces 9 (2017) 42415–42419, https://doi.org/10.1021/acsami.7b13440.

[760] K. Mašek, J. Beran, V. Matolín, RHEED study of the growth of cerium oxide on Cu (111), Appl. Surf. Sci. 259 (2012) 34–38, https://doi.org/10.1016/j.apsusc.2012.06.014.

[761] L. Szabová, O. Stetsovych, F. Dvořák, M. Farnesi Camellone, S. Fabris, J. Mysliveček, V. Matolín, Distinct physicochemical properties of the first ceria monolayer on Cu(111), J. Phys. Chem. C 116 (2012) 6677–6684, https://doi.org/10.1021/jp211955v.

[762] P. Luches, F. Pagliuca, S. Valeri, F. Boscherini, Structure of ultrathin CeO_2 films on Pt(111) by polarization-dependent X-ray absorption fine structure, J. Phys. Chem. C 117 (2013) 1030–1036, https://doi.org/10.1021/jp310375t.

[763] Y. Shi, K.H. Stone, Z. Guan, M. Monti, C. Cao, F. El Gabaly, W.C. Chueh, M. F. Toney, Surface structure of coherently strained ceria ultrathin films, Phys. Rev. B 94 (2016), 205420, https://doi.org/10.1103/PhysRevB.94.205420.

[764] S. Schweiger, R. Pfenninger, W.J. Bowman, U. Aschauer, J.L.M. Rupp, Designing strained interface heterostructures for memristive devices, Adv. Mater. 29 (2017), 1605049, https://doi.org/10.1002/adma.201605049.

[765] R.A. De Souza, A.H.H. Ramadan, Ionic conduction in the $SrTiO_3$|YSZ=$SrTiO_3$ heterostructure, Phys. Chem. Chem. Phys. 15 (2013) 4505–4509, https://doi.org/10.1039/C3CP44399J.

[766] T.J. Pennycook, M.J. Beck, K. Varga, M. Varela, S.J. Pennycook, S.T. Pantelides, Origin of colossal ionic conductivity in oxide multilayers: interface induced sublattice disorder, Phys. Rev. Lett. 104 (2010), 115901, https://doi.org/10.1103/PhysRevLett.104.115901.

[767] L. Sun, D. Marrocchelli, B. Yildiz, Edge dislocation slows down oxide ion diffusion in doped CeO_2 by segregation of charged defects, Nat. Commun. 6 (2015) 6294, https://doi.org/10.1038/ncomms7294.

[768] G. Mahan, Good thermoelectrics, Solid State Phys. 51 (1979) 81–157.

[769] H. Ohta, S. Kim, Y. Mune, T. Mizoguchi, K. Nomura, S. Ohta, T. Nomura, Y. Nakanishi, Y. Ikuhara, M. Hirano, H. Hosono, K. Koumoto, Giant thermoelectric Seebeck coefficient of a two-dimensional electron gas in $SrTiO_3$, Nat. Mater. 6 (2007) 129–134, https://doi.org/10.1038/nmat1821.

[770] J.P. Heremans, M.S. Dresselhaus, L.E. Bell, D.T. Morelli, When thermoelectrics reached the nanoscale, Nat. Nanotechnol. 8 (2013) 471–473, https://doi.org/10.1038/nnano.2013.129.

[771] D.G. Cahill, P.V. Braun, G. Chen, D.R. Clarke, S. Fan, K.E. Goodson, P. Keblinski, W.P. King, G.D. Mahan, A. Majumdar, H.J. Maris, S.R. Phillpot, E. Pop, L. Shi, Nanoscale thermal transport. II. 2003–2012, Appl. Phys. Rev. 1 (2014), 011305, https://doi.org/10.1063/1.4832615.

[772] Y. Qi, Z. Wang, M. Zhang, F. Yang, X. Wang, Thermoelectric devices based on one-dimensional nanostructures, J. Mater. Chem. A 1 (2013) 6110–6124, https://doi.org/10.1039/C3TA01594G.

[773] G. Zhang, Y.W. Zhang, Strain effects on thermoelectric properties of two-dimensional materials, Mech. Mater. 91 (2015) 382–398, https://doi.org/10.1016/j.mechmat.2015.03.009.

[774] B. Rivas-Murias, J. Manuel Vila-Fungueiriño, F. Rivadulla, High quality thin films of thermoelectric misfit cobalt oxides prepared by a chemical solution method, Sci. Rep. 5 (2015) 11889, https://doi.org/10.1038/srep11889.

[775] P. Limelette, V. Hardy, P. Auban-Senzier, D. Jérome, D. Flahaut, S. Hébert, R. Frésard, C. Simon, J. Noudem, A. Maignan, Strongly correlated properties of the thermoelectric cobalt oxide $Ca_3Co_4O_9$, Phys. Rev. B 71 (2005), 233108, https://doi.org/10.1103/PhysRevB.71.233108.

[776] D. Zou, Y. Liu, S. Xie, J. Lin, J. Li, Effect of strain on thermoelectric properties of $SrTiO_3$: first-principles calculations, Chem. Phys. Lett. 586 (2013) 159–163, https://doi.org/10.1016/j.cplett.2013.09.036.

[777] Y. Wang, Y. Sui, H. Fan, X. Wang, Y. Su, W. Su, X. Liu, High temperature thermoelectric response of electron-doped $CaMnO_3$, Chem. Mater. 21 (2009) 4653–4660, https://doi.org/10.1021/cm901766y.

[778] V. Pardo, A.S. Botana, D. Baldomir, Strain effects to optimize thermoelectric properties of hole-doped $La_2NiO_{4+\delta}$ via ab initio calculations, Phys. Rev. B 87 (2013), 125148, https://doi.org/10.1103/PhysRevB.87.125148.
[779] D. Portehault, V. Maneeratana, C. Candolfi, N. Oeschler, I. Veremchuk, Y. Grin, C. Sanchez, M. Antonietti, Facile general route toward tunable magnéli nanostructures and their use as thermoelectric metal oxide/carbon nanocomposites, ACS Nano 5 (2011) 9052–9061, https://doi.org/10.1021/nn203265u.
[780] M. Ohtaki, K. Araki, K. Yamamoto, High thermoelectric performance of dually doped ZnO ceramics, J. Electron. Mater. 38 (2009) 1234–1238, https://doi.org/10.1007/s11664-009-0816-1.
[781] M. Backhaus-Ricoult, J. Rustad, L. Moore, C. Smith, J. Brown, Semiconducting large bandgap oxides as potential thermoelectric materials for high-temperature power generation? Appl. Phys. A 116 (2014) 433–470, https://doi.org/10.1007/s00339-014-8515-z.
[782] J. He, Y. Liu, R. Funahashi, Oxide thermoelectrics: the challenges, progress, and outlook, J. Mater. Res. 26 (2011) 1762–1772, https://doi.org/10.1557/jmr.2011.108.
[783] Y. Yang, W. Guo, K.C. Pradel, G. Zhu, Y. Zhou, Y. Zhang, Y. Hu, L. Lin, Z.L. Wang, Pyroelectric nanogenerators for harvesting thermoelectric energy, Nano Lett. 12 (2012) 2833–2838, https://doi.org/10.1021/nl3003039.
[784] J. Jiang, L. Zhang, C. Ming, H. Zhou, P. Bose, Y. Guo, Y. Hu, B. Wang, Z. Chen, R. Jia, S. Pendse, Y. Xiang, Y. Xia, Z. Lu, X. Wen, Y. Cai, C. Sun, G.-C. Wang, T.-M. Lu, D. Gall, Y.-Y. Sun, N. Koratkar, E. Fohtung, Y. Shi, J. Shi, Giant pyroelectricity in nanomembranes, Nature 607 (2022) 480–485, https://doi.org/10.1038/s41586-022-04850-7.
[785] Y. Wang, L. Zhu, Y. Feng, Z. Wang, Z.L. Wang, Comprehensive pyro-phototronic effect enhanced ultraviolet detector with ZnO/Ag Schottky junction, Adv. Funct. Mater. 29 (2019), 1807111, https://doi.org/10.1002/adfm.201807111.
[786] Z. Wang, R. Yu, C. Pan, Z. Li, J. Yang, F. Yi, Z.L. Wang, Light-induced pyroelectric effect as an effective approach for ultrafast ultraviolet nanosensing, Nat. Commun. 6 (2015) 8401, https://doi.org/10.1038/ncomms9401.
[787] J. Liu, S.T. Pantelides, Mechanisms of pyroelectricity in three- and two-dimensional materials, Phys. Rev. Lett. 120 (2018), 207602, https://doi.org/10.1103/PhysRevLett.120.207602.
[788] L. Wang, S. Liu, X. Feng, C. Zhang, L. Zhu, J. Zhai, Y. Qin, Z.L. Wang, Flexoelectronics of centrosymmetric semiconductors, Nat. Nanotechnol. 15 (2020) 661–667, https://doi.org/10.1038/s41565-020-0700-y.
[789] M. Kumar, J.-Y. Park, H. Seo, Boosting self-powered ultraviolet photoresponse of TiO_2-based heterostructure by flexo-phototronic effects, Adv. Opt. Mater. 10 (2022), 2102532, https://doi.org/10.1002/adom.202102532.
[790] Y. Wang, Y. Shi, G. Xin, J. Lian, J. Shi, Two-dimensional van der Waals epitaxy kinetics in a three-dimensional perovskite halide, Cryst. Growth Des. 15 (2015) 4741–4749, https://doi.org/10.1021/acs.cgd.5b00949.
[791] S.S. Hong, J.H. Yu, D. Lu, A.F. Marshall, Y. Hikita, Y. Cui, H.Y. Hwang, Two-dimensional limit of crystalline order in perovskite membrane films, Sci. Adv. 3 (2017), https://doi.org/10.1126/sciadv.aao5173.
[792] D. Ji, S. Cai, T.R. Paudel, H. Sun, C. Zhang, L. Han, Y. Wei, Y. Zang, M. Gu, Y. Zhang, W. Gao, H. Huyan, W. Guo, D. Wu, Z. Gu, E.Y. Tsymbal, P. Wang, Y. Nie, X. Pan, Freestanding crystalline oxide perovskites down to the monolayer limit, Nature 570 (2019) 87–90, https://doi.org/10.1038/s41586-019-1255-7.
[793] Y. Kim, S.S. Cruz, K. Lee, B.O. Alawode, C. Choi, Y. Song, J.M. Johnson, C. Heidelberger, W. Kong, S. Choi, K. Qiao, I. Almansouri, E.A. Fitzgerald, J. Kong, A.M. Kolpak, J. Hwang, J. Kim, Remote epitaxy through graphene enables two-dimensional material-based layer transfer, Nature 544 (2017) 340, https://doi.org/10.1038/nature22053.
[794] W. Kong, H. Li, K. Qiao, Y. Kim, K. Lee, Y. Nie, D. Lee, T. Osadchy, R.J. Molnar, D. K. Gaskill, R.L. Myers-Ward, K.M. Daniels, Y. Zhang, S. Sundram, Y. Yu, S.-h Bae, S. Rajan, Y. Shao-Horn, K. Cho, A. Ougazzaden, J.C. Grossman, J. Kim, Polarity governs atomic interaction through two-dimensional materials, Nat. Mater. 17 (2018) 999–1004, https://doi.org/10.1038/s41563-018-0176-4.
[795] J. Jiang, X. Sun, X. Chen, B. Wang, Z. Chen, Y. Hu, Y. Guo, L. Zhang, Y. Ma, L. Gao, F. Zheng, L. Jin, M. Chen, Z. Ma, Y. Zhou, N.P. Padture, K. Beach, H. Terrones, Y. Shi, D. Gall, T.-M. Lu, E. Wertz, J. Feng, J. Shi, Carrier lifetime enhancement in halide perovskite via remote epitaxy, Nat. Commun. 10 (2019) 4145, https://doi.org/10.1038/s41467-019-12056-1.
[796] B. Wang, Y. Gu, S. Zhang, L.-Q. Chen, Flexoelectricity in solids: progress, challenges, and perspectives, Prog. Mater. Sci. 106 (2019), https://doi.org/10.1016/j.pmatsci.2019.05.003.
[797] M.-M. Yang, D.J. Kim, M. Alexe, Flexo-photovoltaic effect, Science 360 (2018) 904–907, https://doi.org/10.1126/science.aan3256.
[798] M. Copel, M.A. Kuroda, M.S. Gordon, X.H. Liu, S.S. Mahajan, G.J. Martyna, N. Moumen, C. Armstrong, S.M. Rossnagel, T.M. Shaw, P.M. Solomon, T.N. Theis, J.J. Yurkas, Y. Zhu, D.M. Newns, Giant piezoresistive On/Off ratios in rare-earth chalcogenide thin films enabling nanomechanical switching, Nano Lett. 13 (2013) 4650–4653, https://doi.org/10.1021/nl401710f.
[799] X. Wang, H. Zhang, R. Yu, L. Dong, D. Peng, A. Zhang, Y. Zhang, H. Liu, C. Pan, Z. L. Wang, Dynamic pressure mapping of personalized handwriting by a flexible sensor matrix based on the mechanoluminescence process, Adv. Mater. 27 (2015) 2324–2331, https://doi.org/10.1002/adma.201405826.